

Unravelling gravel

Including stochastic behaviour of granular materials in design of bulk handling equipment

Fransen, M.P.

DOI

[10.4233/uuid:ad7999d2-5058-4a9d-8688-be6c91f41485](https://doi.org/10.4233/uuid:ad7999d2-5058-4a9d-8688-be6c91f41485)

Publication date

2024

Document Version

Final published version

Citation (APA)

Fransen, M. P. (2024). *Unravelling gravel: Including stochastic behaviour of granular materials in design of bulk handling equipment*. [Dissertation (TU Delft), Delft University of Technology].
<https://doi.org/10.4233/uuid:ad7999d2-5058-4a9d-8688-be6c91f41485>

Important note

To cite this publication, please use the final published version (if applicable).
Please check the document version above.

Copyright

Other than for strictly personal use, it is not permitted to download, forward or distribute the text or part of it, without the consent of the author(s) and/or copyright holder(s), unless the work is under an open content license such as Creative Commons.

Takedown policy

Please contact us and provide details if you believe this document breaches copyrights.
We will remove access to the work immediately and investigate your claim.

The background of the entire cover is a light blue-grey gradient. Scattered across this background are numerous small, smooth, rounded stones of various sizes and colors, including shades of grey, tan, and brown. These stones are more densely packed in the bottom-left corner, forming a large pile, and are more sparsely distributed elsewhere.

Unravelling gravel

Including stochastic behaviour of granular materials in design of bulk handling equipment

Marc Fransen

UNRAVELLING GRAVEL

INCLUDING STOCHASTIC BEHAVIOUR OF GRANULAR MATERIALS
IN DESIGN OF BULK HANDLING EQUIPMENT

UNRAVELLING GRAVEL

INCLUDING STOCHASTIC BEHAVIOUR OF GRANULAR MATERIALS
IN DESIGN OF BULK HANDLING EQUIPMENT

Proefschrift

ter verkrijging van de graad van doctor
aan de Technische Universiteit Delft,
op gezag van de Rector Magnificus prof. dr. ir. T. H. J. J. van der Hagen,
voorzitter van het College voor Promoties,
in het openbaar te verdedigen op
dinsdag 14 januari 2025

door

Marc Patrick FRANSEN

Werktuigbouwkundig Ingenieur, Technische Universiteit Delft, Nederland,
geboren te Amstelveen, Nederland.

Dit proefschrift is goedgekeurd door de promotoren.

Samenstelling promotiecommissie:

Rector Magnificus

voorzitter

Prof. dr. ir. D.L. Schott

Technische Universiteit Delft, promotor

Prof. dr. ir. M. Langelaar

Technische Universiteit Delft, promotor

Onafhankelijke leden:

Prof. Dr. -Ing. A. Katterfeld

Otto von Guericke University Magdenburg

Prof. dr. V. Magnanimo

University of Twente

Prof. dr. ing. B. Rosic

University of Twente

Prof. dr. G.D. Weymouth

Technische Universiteit Delft



Keywords: Bulk material, stochastic granular behaviour, bulk handling equipment design, metamodels, calibration, robust design optimization

Printed by: Ridderprint | www.ridderprint.nl

Front & Back: by E. van Weelden

Copyright © 2024 by M.P. Fransen

ISBN 978-94-6506-772-8

An electronic version of this dissertation is available at
<http://repository.tudelft.nl/>.

A seemingly endless story

CONTENTS

Contents	vii
Summary	xi
Samenvatting	xiii
1 Introduction	1
1.1 Research area	1
1.2 Theoretical background.	2
1.3 Research aim and research questions	5
1.4 Methodology	7
1.5 Outline of this thesis	8
2 Experimental study on flow induced hopper vibrations and the relation to geometry	9
2.1 Introduction	10
2.2 Experimental setup	11
2.2.1 Hopper discharge setup	11
2.2.2 Discharging material: Gravel.	13
2.2.3 High speed imaging setup	15
2.3 Data analysis methodology	16
2.3.1 Analysis of load cell data	16
2.3.2 Image analysis using Particle Image Velocimetry (PIV).	19
2.4 Results	19
2.4.1 Discharge rates and impact loads	20
2.4.2 PIV analysis: identifying flow fields in discharging hoppers	21
2.4.3 Comparison load cell to PIV data.	28
2.5 Conclusion	35
2.6 Outlook	36
2.7 Acknowledgements	37
3 Application of DEM-based metamodells in bulk handling equipment design: methodology and DEM case study	39
3.1 Introduction	40
3.2 Metamodelling	43
3.2.1 Sampling and data generation	43
3.2.2 Metamodel selection.	44
3.2.3 Hyper-parameter optimization	46
3.2.4 Metamodel validation	46

3.3	DEM-based metamodel test case: Discharging hopper	47
3.3.1	DEM (object) model	47
3.3.2	DEM data analysis	50
3.3.3	Sampling.	50
3.3.4	Hyper-parameter optimization	51
3.3.5	Verification	53
3.4	Results	53
3.4.1	DEM simulation results	53
3.4.2	Effect of hyper-parameter optimization	56
3.4.3	Metamodel Validation	61
3.4.4	Effect of sample size on accuracy	66
3.4.5	Summary of findings.	68
3.5	Conclusions.	70
4	Including stochastics in metamodel-based DEM model calibration	71
4.1	Introduction	72
4.2	Experimental methods and materials	74
4.2.1	Laboratory scale experiments	75
4.2.2	Large scale hopper experiment	76
4.2.3	Analysis experimental results	76
4.2.4	Experimental results	80
4.3	DEM models	84
4.3.1	DEM model assumptions and material properties	84
4.3.2	Initialisation of DEM models and simulations	85
4.3.3	Analysis simulation results.	89
4.4	Metamodel and calibration methods	90
4.4.1	Bounds of the calibration space	92
4.4.2	Sampling the calibration space	93
4.4.3	Metamodel training	94
4.4.4	Calibration of DEM parameters	96
4.4.5	Verification of DEM parameter sets	98
4.4.6	Validation of Optimal DEM parameter sets for large scale hopper model	98
4.5	Results	98
4.5.1	Metamodels for calibration	99
4.5.2	Calibration results	102
4.5.3	Verification of laboratory scale simulations and validation with experimental results	110
4.5.4	Validation of hopper model	116
4.6	Conclusion	119
5	Deterministic vs. robust design optimization of a discharging hopper: A validated case study	121
5.1	Introduction	122
5.2	Methodology	123

5.3	DEM-based metamodel design optimization for a discharging hopper . . .	126
5.3.1	Experimental setup and DEM model of hopper	126
5.3.2	Analysis of experimental and DEM simulation results	126
5.3.3	Sampling of design space and number of repetitions	127
5.3.4	Metamodel training	128
5.3.5	Formulization Optimization Problem	132
5.3.6	Case studies including verification and validation	133
5.4	Results	133
5.4.1	DEM data and DEM-based metamodel	133
5.4.2	Deterministic vs Robust design optimization	135
5.5	Conclusions.	148
6	Conclusions and Recommendations	149
6.1	Conclusions.	149
6.2	Recommendations	151
A	Appendices to Chapter 2	153
A.1	PIV procedure.	153
A.2	Arching	154
A.3	Reference values discharge rate and impact load	156
B	Appendices to Chapter 5	157
B.1	Arching	157
B.2	Design considerations	157
B.3	Comparing DEM results and Experiments	159
	References	163
	Nomenclature	173
	Acknowledgements	177
	Curriculum Vitæ	179
	List of Publications	181

SUMMARY

Understanding the behaviour of and handling of bulk materials is an essential part of many industrial processes. Small changes in equipment design or the properties of a bulk material can result in drastic changes in performance. To understand these processes, research on the behaviour of granular materials and their interaction with equipment needs to be studied. Research can consist of experimental or numerical work at different scales. The level of particles, the interaction of small agglomerates of particles or the transport of millions of particles. For accurate models it is essential that the variety in shape, size, and other material properties is included. Due to the variety, the behaviour of granular materials is inherently stochastic. Even though this is an important aspect, it is not commonly included in research. In addition to the stochastic behaviour it is essential that detailed modelling techniques like particle based models are used as a tool in the design process of bulk handling equipment. An important method is the Discrete Element Method (DEM) which can model the interaction between particles and particles and equipment in high detail. However, in the optimization of bulk handling equipment designs it is difficult to include these models directly because of the high computational cost. Therefore, it is necessary that fast and accurate predictive models are developed that inherit the behaviour of a particle based model and even include the stochastic behaviour of the granular or bulk material. A potential technique to achieve this goal is by using metamodels. These are efficient models that relate design parameters to performance of equipment. Discovering how to identify and include the stochastic behaviour of granular materials and the translation of this information to a usable form in the design of bulk handling equipment is the aim of this research.

To reach this aim, the research is divided in four parts: The identification of stochastic behaviour of granular materials by means of experiments with a discharging hopper, investigate the potential use of metamodels in the design of bulk handling equipment by assessing the quality of different model types, the use of metamodels to include the stochastic behaviour of bulk materials in calibration of DEM models, and the application of metamodel-based robust design optimization to the design of bulk handling equipment. In all of these parts the results from experiments and numerical models are used to verify and validate the results.

In this thesis the essential questions regarding stochastic behaviour of bulk materials and the effects it has on design optimization procedures are discussed. First an experimental study to describe the behaviour of gravel in a hopper is presented aiming to understand the relationship between external and internal observed behaviour. This research shows that the behaviour of the granular material is related to the geometry of the hopper. Moreover, the stochastic behaviour of the granular material is not constant and changes with the geometry. Additionally, it was found that the type of measurement and wear in the setup, need to be considered when a reliable dataset is required.

Secondly, a study is presented in which the challenges related to the use and training of

metamodels are described. Here it becomes clear that the choice of a type of metamodel highly depends on the application and the dataset that is used for training. Furthermore, hyper-parameter optimization generally improves the quality of the metamodel and a validation strategy gives information on the robustness of the trained metamodel in between the data points used for training. The training procedure presented in this study can be used for the development of metamodels.

Thirdly, including the stochastic behaviour of the granular material in the calibration of DEM models leads to more accurate and robust performance of the DEM model in predicting key performance indicator values. Here, stochastic metamodels play an essential role as they improve the efficiency of the calibration and increase the reliability. Even though there is more effort required to perform a stochastic calibration it is a necessary step to improve accuracy of DEM models. The methodology presented in this study enables engineers and researchers to include stochastic behaviour of granular materials in their own discrete element models. Fourth and finally, combining stochastic metamodels that predict equipment performance and robust optimization techniques shows that more accurate design performance predictions can be made. The extensive experimental work, the comparison of the conventional design procedure and the proposed strategy support these findings. Including stochastics and metamodels shows that the reliability of DEM models and optimal designs is improved. The presented framework for the design of bulk handling equipment includes the procedure for training metamodels and the stochastic calibration methodology.

In the current procedure for design of bulk handling equipment, including stochastic behaviour of granular materials and detailed discrete element models effectively is difficult. The studies presented in this thesis lead to a design procedure that includes both these aspects and gives detailed information on how it can be applied. To improve the presented design procedure it is recommended that the procedure is applied to design problems at an industrial scale. Moreover, it is encouraged to study the dependency of stochastic behaviour on dynamic regimes and the effect of operation on the interaction properties between particles and equipment.

SAMENVATTING

Het begrijpen van het gedrag en het transport van bulkmaterialen is een essentieel onderdeel van veel industriële processen. Kleine veranderingen in het ontwerp van werktuigen of de eigenschappen van een bulkmateriaal kunnen leiden tot drastische prestatieveranderingen. Om deze processen te begrijpen, moet onderzoek naar het gedrag van granulaire materialen en hun interactie met werktuigen worden uitgevoerd. Onderzoek kan bestaan uit experimenteel of numeriek werk op verschillende schalen. Het gedrag tussen deeltjes, de interactie van kleine agglomeraten van deeltjes of het transport van miljoenen deeltjes. Om tot nauwkeurige modellen te komen is het essentieel dat de variëteit in vorm, grootte en andere eigenschappen van granulaire materialen wordt opgenomen. Door de variëteit in eigenschappen is het gedrag van korrelige materialen inherent stochastisch. Hoewel dit een belangrijk aspect is, wordt het niet vaak in onderzoek meegenomen. Naast het stochastische gedrag is het essentieel dat gedetailleerde modelleertechnieken zoals op deeltjes gebaseerde modellen worden gebruikt als hulpmiddel bij het ontwerpproces van bulkwerktuigen. Een belangrijke methode is de Discrete Elementen Methode (DEM), die de interactie tussen deeltjes en deeltjes en werktuigen tot in detail kan modelleren. Bij de optimalisatie van ontwerpen voor bulkwerktuigen is het echter moeilijk om deze modellen rechtstreeks op te nemen vanwege de daarmee gepaarde lange rekentijden. Daarom is het noodzakelijk dat er snelle en nauwkeurig voorspellende modellen worden ontwikkeld die het gedrag van een op deeltjes gebaseerd model overnemen en ook het stochastische gedrag van het granulaire of bulkmateriaal omvatten. Een mogelijke techniek om dit doel te bereiken is door metamodellen te gebruiken. Dit zijn efficiënte modellen waarmee ontwerpparameters direct gerelateerd kunnen worden aan de prestaties van het werktuig. Het doel van dit onderzoek is om te ontdekken hoe men het stochastische gedrag van granulaire materialen kan identificeren en deze informatie kan vertalen naar een bruikbare vorm bij het ontwerp van bulkwerktuigen.

Om dit doel te bereiken, is het onderzoek verdeeld in vier delen: De identificatie van stochastisch gedrag van korrelige materialen door middel van experimenten met een hopper, de mogelijkheden van het toepassen van metamodellen bij het ontwerp van bulkwerktuigen onderzoeken door de kwaliteit van verschillende modeltypen te beoordelen, het gebruik van metamodellen om het stochastische gedrag van bulkmaterialen bij de kalibratie van DEM-modellen op te nemen, en de toepassing van op meta-model gebaseerde robuuste ontwerpoptimalisatie op het ontwerp van bulkwerktuigen. In al deze onderdelen worden de resultaten van experimenten en numerieke modellen gebruikt om de resultaten te verifiëren en te valideren.

In dit proefschrift worden de essentiële vragen over stochastisch gedrag van bulkmaterialen en de effecten die het heeft op ontwerpoptimalisatieprocedures besproken. Eerst wordt een experimentele studie beschreven om het gedrag van grind in een hopper te bepalen en om de relatie tussen extern en intern waargenomen gedrag te begrijpen. Dit

onderzoek toont aan dat het gedrag van het korrelige materiaal verband houdt met de geometrie van de hopper. Bovendien is het stochastische gedrag van het korrelige materiaal niet constant en verandert het mee met aanpassingen in de geometrie. Daarnaast blijkt dat het type meting en slijtage in de opstelling in overweging moet worden genomen als men een betrouwbare experimentele dataset wil creëren.

Ten tweede wordt een studie gepresenteerd waarin de uitdagingen met betrekking tot het gebruik en de training van metamodellen wordt beschreven. Hier wordt duidelijk dat de keuze van een type meta-model sterk afhangt van de applicatie en de dataset die wordt gebruikt voor training. De optimalisatie van de meta-model hyperparameters verbetert over het algemeen de kwaliteit van het meta-model en een validatiestrategie geeft informatie over de robuustheid van het getrainde meta-model tussen de datapunten die worden gebruikt voor de training van het model. De trainingsprocedure die in dit onderzoek wordt gepresenteerd, kan worden gebruikt voor de ontwikkeling van metamodellen.

Ten derde leidt het opnemen van het stochastische gedrag van het granulaire materiaal bij de kalibratie van DEM-modellen tot nauwkeurigere en robuustere prestaties van het DEM-model bij het voorspellen van de belangrijkste prestatie-indicatoren. Hier spelen stochastische metamodellen een essentiële rol omdat ze de efficiëntie van de kalibratie verbeteren en de betrouwbaarheid vergroten. Ook al is er meer inspanning nodig om een stochastische kalibratie uit te voeren, het is een noodzakelijke stap om de nauwkeurigheid van DEM-modellen te verbeteren. De methodologie die in deze studie wordt gepresenteerd, stelt ingenieurs en onderzoekers in staat stochastisch gedrag van granulaire materialen op te nemen in discrete elementmodellen.

Ten vierde en tot slot, het combineren van stochastische metamodellen die de prestaties van werktuigen voorspellen en robuuste optimalisatietechnieken, toont aan dat er nauwkeurigere voorspellingen voor ontwerp prestaties kunnen worden gedaan. Het uitgebreide experimentele werk, de vergelijking van de conventionele ontwerp procedure en de voorgestelde strategie ondersteunen deze bevindingen. Het meenemen van stochastisch gedrag en het gebruik van metamodellen laat zien dat de betrouwbaarheid van DEM-modellen en geoptimaliseerde ontwerpen wordt verbeterd. Het gepresenteerde raamwerk voor het ontwerp van bulkwerktuigen bevat de procedure voor het trainen van metamodellen en de stochastische kalibratiemethodologie.

In de huidige procedure voor het ontwerp van bulkwerktuigen is het ingewikkeld om het stochastisch gedrag van granulaire materialen en het gebruik van discrete elementmodellen te implementeren. De studies die in dit proefschrift worden gepresenteerd, leiden tot een ontwerp procedure die deze implementatie mogelijk maakt en gedetailleerde informatie geeft over hoe deze kan worden toegepast. Om de gepresenteerde ontwerp procedure te verbeteren, wordt aanbevolen dat de procedure wordt toegepast op ontwerp problemen op industriële schaal. Bovendien wordt het aangemoedigd om de afhankelijkheid van stochastisch gedrag van dynamische regimes en het effect van het bulkproces op de interactie-eigenschappen tussen deeltjes en werktuig te bestuderen.

1

INTRODUCTION

1.1. RESEARCH AREA

In our daily life we encounter granular materials in many situations, whether it is the cereal you pour in your bowl for breakfast or a scoop of sand that is used to build a castle on the beach. In those cases you might wonder, why did the cereal get jammed in the box today whereas it poured constantly the day before, or why does the sand stick to your spade when it is wet but not when it is dry? Those questions are very logical and are also arise in heavy industries when new equipment to process raw materials is developed. In design of such bulk handling equipment (BHE) it is essential that the granular behavior of the bulk material and the interaction with the equipment is understood such that designs can be optimized and be used reliably and with high accuracy. Optimizing designs for performance and reliability is important considering the vast amount of raw materials that are being transported and processed yearly. Use of optimized equipment will eventually lead to a lower consumption of energy, lower costs, and lower environmental impact.

In Figure 1.1 several examples of bulk materials are shown. The term bulk material is used for all powder or granular materials consisting of a large amount of particles. They can be organic like corn or wood, raw earth materials like coal, iron ore, and gravel or preprocessed materials like iron ore pellets. It is clear to see that the shape of the particles is very different and that the size and shape is different even for the same material. This variability in the shape, size and surface properties of the particles make the behavior of a granular material inherently stochastic. Every time a granular material is handled, the orientation of the particles and their interaction changes which leads a variation in results. Therefore it is important to understand and characterize the stochastic behavior of a granular material and include this behavior in the design process. Figure 1.2 shows examples of bulk handling equipment and their interaction with a granular material. The shown equipment is capable of transporting several tons of material in each handling operation and generally has dimensions of multiple meters. Here the importance of understanding the interaction between materials and equipment becomes apparent. The

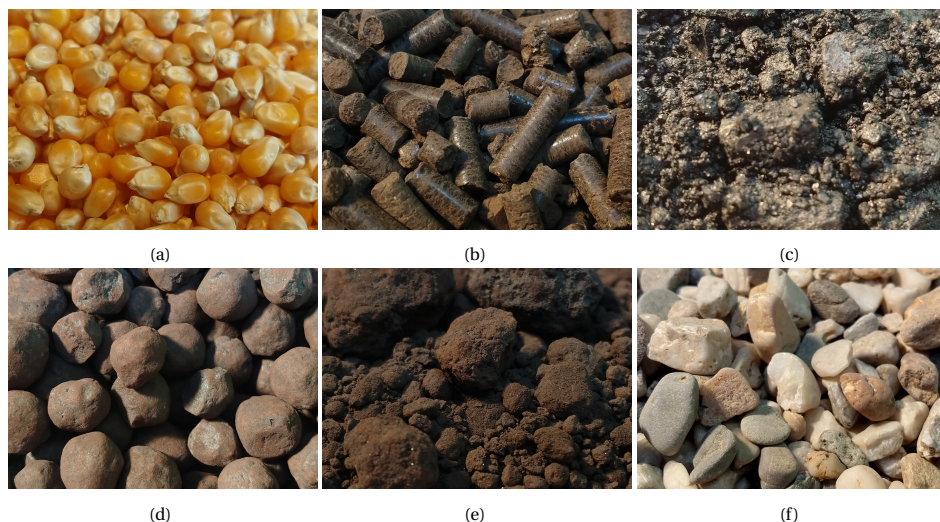


Figure 1.1: Examples of bulk materials (a) corn (b) wood pellets (c) coal (d) iron ore pellets (e) iron ore (f) gravel

bucket of an excavator is in contact with the bulk material and is subjected to wear which changes the way the material and equipment interact over time because of changing surface roughness or changes in the environment. The bulk material transported by a conveyor will travel differently through air depending on the velocity and size of the particles. Moreover, if there is no friction between particles and surface of conveyor belt the particles might not be transported at all. The grab is a complex mechanism where it's design may change for different categories of materials to reach the desired performance. The interaction is generally hard to describe by means of analytical functions. Therefore it is essential that the behavior and interaction with bulk materials of equipment is known for a large variety of designs and a large variety of materials such that these designs can be optimized.

1.2. THEORETICAL BACKGROUND

In Figure 1.3 the conventional and newly developed paths in the design process for bulk handling equipment are shown in more detail with time on the vertical axis and reliability on the horizontal axis. The design process can take different paths towards an equipment design. Here the left path is the current design procedure which starts with the analysis of the bulk handling equipment design problem. The general approach in this step is to identify the problem and understand the mean or average behavior of the equipment and granular material. Next, engineers come up with an initial idea for a design based on experience with the material or with the type of equipment that was used in the past. The initial design is then updated by trial and error until the design meets the requirements using the input from lab-scale experiments, prototypes, and evaluation of the structural integrity of the design. A relatively new method in design of bulk handling equipment



(a)



(b)



(c)

Figure 1.2: Examples of bulk handling equipment (a) excavator (b) conveyor belt (c) grab (courtesy of Nemag B.V.)

is the use of the Discrete Element Method (DEM) [1] in which the bulk material and its interaction with the material of the equipment can be modelled in detail. This is the path shown on the right. These models contain the mechanical interaction between the particles itself and the interaction with equipment through contact laws. These DEM models can be used to evaluate the performance of a new design without the need of expensive experiments. However, as easy as this sounds we have to be careful because these models are computationally expensive and the contact parameters need to be calibrated and validated if used to optimize designs [2, 3]. Next, the DEM model is ready to be used in the design process. Generally, this means that engineers come up with an initial design which is based on their experience apply a trial and error approach to improve the design by subsequent simulations. Even though this is a widespread approach, it poses a significant risk of tunnel vision because alternative designs are neglected. In addition, detailed DEM models for industrial-scale equipment design have to process millions of particles and is time consuming. The duration of a simulation can take a couple of hours but might also take days depending on the size and complexity of the system. For this reason, a trial-and-error based design process including DEM is generally concluded prematurely with a suboptimal result.

In describing the current design procedure and the recent developments with including DEM it becomes clear that each of the three steps have their limitations: Problem analysis, DEM model development, and design. In current analysis of bulk handling equipment problems the focus lies on the average or mean behavior of the equipment and does not include the stochastics of the granular materials that are processed even though this is an essential aspect of the behavior of the system. To gain insight on the behavior of bulk handling equipment it is essential to conduct experiments for different configurations. By repeating these experiments the degree of stochastic behavior of the equipment can be determined as well. The insights from these experiments improves the physical understanding of the system and is useful in the development of the DEM model.

In the development of a DEM model the insights on equipment and material behavior obtained in the analysis phase needs to be translated to the model. However, it is common to make simplifications and only incorporate the essential physical behavior in the DEM model. Exact modelling of granular materials is still difficult and a major focus point in literature. In order to obtain the most accurate DEM model it is necessary to calibrate the contact and material properties such that the overall behavior of the DEM model resembles the physical behavior of the granular system . The process of calibration of DEM models consists of matching measurable bulk parameters at laboratory scale and reproducing these with the DEM model by adjusting the calibration parameters [4–6]. Over the past two decades, research on the calibration of DEM models has been an important topic and lead to improvements in speed and accuracy [7–10]. However, these advances were generally focused on average behavior of a DEM model and neglect the stochastic behavior of the granular material. Currently there is no procedure to include the stochastic behavior in the calibration of DEM models.

The stochastic behavior of the granular material indirectly makes the performance of bulk handling equipment stochastic as well. In the current design procedure this is neglected

by focusing on the mean or average performance of the equipment [11–13]. However, in heavy industries, reliable equipment performance is important because entire processes can be shut down due to jamming of equipment or breaking down due to unexpected loading. Including the stochastic behavior of equipment is beneficial in the design process because it includes upper and lower performance limits.

To make the best choices in both the calibration of DEM models and design of bulk handling equipment, ideally, engineers would require an overview of the possible sets of calibration parameters or a set of designs. However, the use of time consuming DEM models makes it difficult to analyze all these paths and gather this information. A common approach to make the information from computationally expensive models more effective is the use of surrogate or metamodels [14–19]. A surrogate or metamodel is an inexpensive model which predicts the behavior of a numerically expensive model [20]. Metamodels are trained using a set of data from, for example, a DEM model and describe a relation between input and output parameters. In the case of calibration the metamodel can be used to predict the behavior of lab experiments based on a combination of contact parameters. For the design optimization of bulk handling equipment the metamodel can be constructed to predict the performance of the equipment based on the design parameters of the equipment. The main advantage of these models is their computational efficiency which is essential for design exploration and optimization where many iterations are used to find a solution to the optimization problem. Currently, the development of metamodels for bulk handling equipment which include the stochastic behavior is not covered frequently in literature.

1.3. RESEARCH AIM AND RESEARCH QUESTIONS

Based on the analysis of the design procedure for bulk handling equipment the aim of this thesis is,

To identify the effect of including the stochastic behavior of granular materials in the entire design procedure for bulk handling equipment

This includes the identification of the stochastic behavior of the granular material, the development and calibration of a DEM model and the design robust optimization of bulk handling equipment. In addition, the use of metamodels for fast and efficient progression through the steps in the design procedure is investigated. These aspects are covered by the following four research questions:

1. To what extent does the stochastic behavior of a granular material affect the performance of bulk handling equipment in the design space?
2. How can metamodels be used to describe the behavior of bulk handling equipment in a design space?
3. To what extent can the stochastic behavior of a granular material be captured in metamodel-based calibration of a discrete element model?
4. How does introducing metamodels and robust optimization to the design process of bulk handling equipment change the process and its outcome?

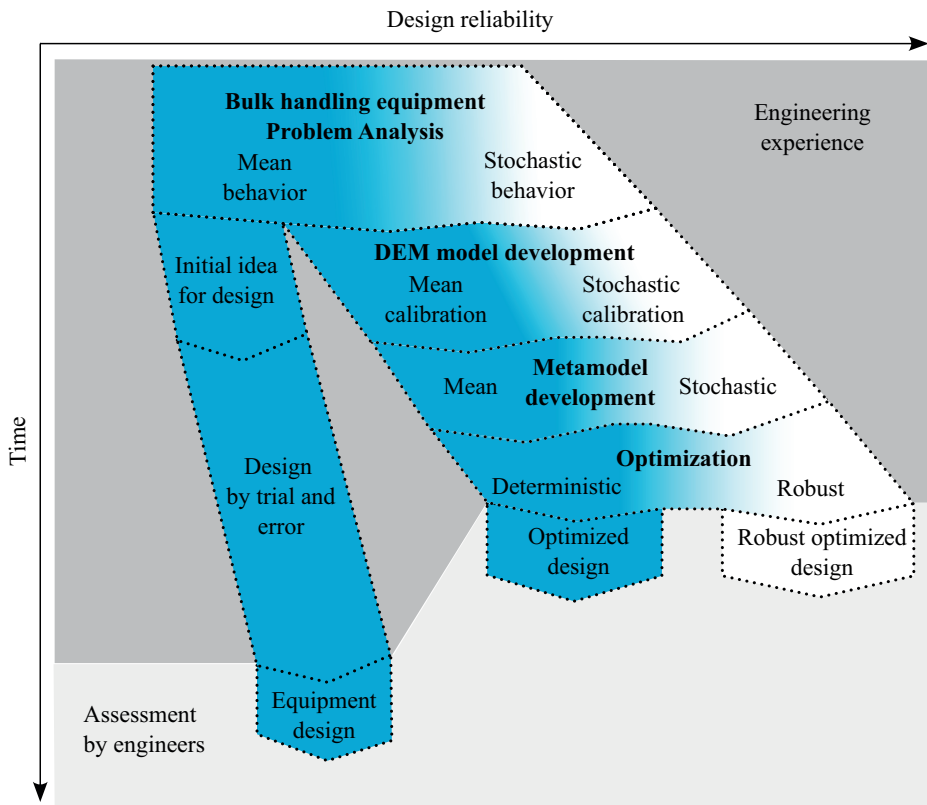


Figure 1.3: Flow chart for design procedure with and without metamodels, stochastic behaviour, and optimization

1.4. METHODOLOGY

To identify the stochastic behavior of material and equipment performance, an extensive experimental study is performed. The experimental setups consist of a geometrically adjustable hopper for which the effect of changing design parameters and repeatability can be investigated. Moreover, several calibration experiments to identify characteristics and stochastic behavior of the bulk material are used as well as tests to identify the interaction properties between particles and equipment. In total 456 tests have been performed for this research. The results of these experiments show that there is stochastic behavior of the material but also in equipment performance. It also appears that the stochastic behavior is dependent on how it is processed in equipment.

Secondly, to make wider use of DEM models in the design of bulk handling equipment, metamodelling is developed which relates the system performance to the design parameters of the system. The use of metamodelling and especially metamodelling that includes stochastic behavior has had little coverage in literature. However, before using a metamodel in both the calibration and design optimization, it is necessary to understand the limitations and possibilities of a metamodel. Metamodels are trained using a dataset but are also affected by the type of metamodel, hyper-parameter optimization, sample size, and validation strategy which influences the quality of a metamodel. These aspects are studied in Chapter 3 and give a basis for stochastic metamodelling and the insight needed to be able to build high quality metamodelling for calibration of DEM models and DEM-based design optimization.

Thirdly, DEM models are developed with a focus on including the stochastic behavior in the calibration of the DEM model by using metamodelling. To make a comparison, the metamodel-based calibration procedure is evaluated for a mean and mean-variance (stochastic) calibration in Chapter 4. The experimental results from the calibration experiments are used to validate the results of the calibration process. To make a full circle, the calibrated DEM model is validated with the results from the experimental study with the discharging hopper.

Finally, the last step in the design procedure is the design optimization using metamodelling. Here, both the deterministic and robust approach in design optimization are used to identify the effect of including the stochastics. By validating the optimization results, a comparison between the two approaches can be made.

All the steps lead to a comprehensive view on the effect of including stochastic behavior of bulk materials in modelling and designing bulk handling equipment. By combining experimental results, modelling, and optimization techniques, this research will aid engineers in rethinking their own approach with regard to design of bulk handling equipment and unravel some of the intricacies of granular behaviour.

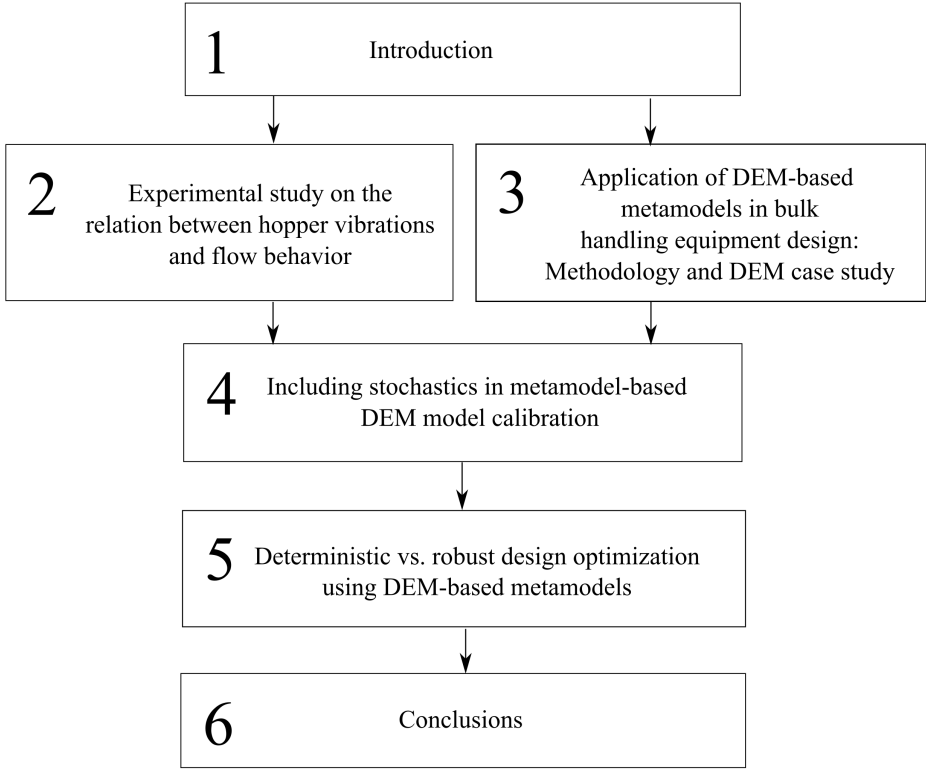


Figure 1.4: Outline of this dissertation

1.5. OUTLINE OF THIS THESIS

Chapter 2 includes an article on the identification of the flow mechanism in a semi 2D hopper discharging gravel where flow in the hopper is connected to the impact loads observed in loadcell data for a wide range of geometries.

Chapter 3 includes an article on the performance of several types of metamodels on a DEM data set of a discharging hopper related to a wide range of geometries.

Chapter 4 consists of an article in which the effectiveness of stochastic calibration is compared to deterministic calibration based on an experimental case study.

Chapter 5 consists of an article which investigates the effect of robust design optimization on the outcome of hopper designs compared to a deterministic optimization procedure.

Chapter 6 includes the conclusion of this thesis

2

EXPERIMENTAL STUDY ON FLOW INDUCED HOPPER VIBRATIONS AND THE RELATION TO GEOMETRY

The behaviour of granular materials in experiments and bulk handling equipment is stochastic by nature. The wide range of sizes, shapes and mechanical properties makes that particles are oriented differently each time the material is handled. Quantification of the stochasticity experimentally is complicated and requires thorough understanding of the governing physics and accurate measurements. In this chapter an experimental study on a discharging hopper is presented for which the relation between flow behaviour of the material and the impact on the bulk handling equipment is determined. Additionally, the stochastic relation between the geometrical properties of the hopper and two key performance indicators, the discharge rate and impact load are determined. The experimental data presented in this chapter is used to validate the models that are developed in the subsequent chapters.

2.1. INTRODUCTION

Hoppers are common equipment in a wide range of industrial processes and are used to store, feed and control the throughput of material. Depending on the process/application they are of different sizes, from large scale in concrete production to small-scale in pharmaceutical applications. In general, hoppers are designed for a process with a specific storage capacity and throughput where the design is based on the interaction between material and equipment and the behaviour of the bulk material. Even though the bulk behaviour is included, for many granular materials processed through a hopper, pulsating flow is a common phenomenon. This pulsating flow, in combination with the dynamic response of the hopper structure is the likely cause for silo quaking or music [21, 22]. Consequences of the pulsating flow in a hopper are the induced vibrations in the structure and additional wear of the material structure interface which may ultimately lead to failure of the hopper [23–26]. Additionally, the flow pulsations can be enhanced largely by the dynamic interaction between the bulk material and equipment structure. In design of silos the described phenomena and behaviour are essential to come to well performing designs. Design procedures for silos and hoppers have been thoroughly described by [27–29]. However, hopper vibrations or silo quaking as it is also called or impact during hopper filling is not included in four of the most common design codes [27]. To be able to update design codes for hoppers and silos with respect to quaking and vibrations more insight on the relation between flow behaviour and the induced vibrations needs to be obtained.

To gain insight on their behaviour hoppers are studied extensively for several decades, both numerically and experimentally [30–33]. Most recent experimental hopper studies for granular materials from a bulk handling perspective were focussed on the effect of particle shape on the discharge rate (e.g. [34–36]. Tangri et al. determined velocity profiles for discharging hoppers with different geometries and particle shapes based on discrete element simulations. A study by Slominski et al. focussed on the deformation and strain fields in the granular flow using particle image velocimetry (PIV) [37]. The study by Mehdizad et al. investigated the flow dynamics through MRI data and determined velocity fields based on phase differences between MRI images [38]. However, to the authors knowledge the relationship between flow behaviour and dynamic response of the hopper is not studied.

A technique to investigate flow behaviour of a moving medium based on image recordings is particle image velocimetry (PIV) or particle tracking velocimetry (PTV) which are methods mainly used for experimental fluid mechanics [39]. With PIV high speed images of a (granular) flow are converted to velocity and acceleration fields. PTV is used to track individual particles which seems to be most ideal but, for high velocity flows this method is not fully applicable [40]. More recently, PIV has been frequently used in research with respect to granular flows and referred to as g-PIV, geo-PIV [41], or granular PIV [42–48]. In this study we will use the general term PIV because the additions only refer to the specific application. Application of PIV to granular flows comes with several challenges which have to be addressed [48]. Specialized experimental setups need to be developed and reliable settings for the PIV analysis need to be determined. related to analytical

models. The flow behaviour can only be observed at the boundaries because granular materials are generally non-transparent. Average flow velocities for granular flows can be accurately obtained using PIV but fluctuations around the average flow called the granular temperature requires higher framerates and image quality. However, in this study we focus on the transient of the mean flow behaviour in a hopper which does not require a higher resolution.

Hopper vibrations are well known and the relation between the dynamic response of the hopper and solid pressures and flow patterns has been described thoroughly in literature. However, a relation between the vibration of the hopper and the optically visible changes in flow fields has not been provided in literature. To gain insight on the acceleration and deceleration of the granular material during discharge an experimental setup has been developed which can measure the pulsating behaviour through load cells and simultaneously record the flow of the material in the hopper through high speed image recording. The induced vibrations on the structure are generally measured with load cells [49, 50]. The high speed image recordings are analysed using PIV and used to determine the velocity and acceleration fields for the granular flow in the hopper. Based on the results of the PIV analysis, velocity and acceleration fields for the granular flow can be compared to the load cell data.

The aim of this study is to gain insight on the relation between dynamic loads on the hopper structure and the flow behaviour of the bulk material in the hopper. Exploring this relation is the primary aim of the present study. With this goal in mind, we focus on first-order effects and utilize a convenient small-scale setup that allows PIV measurements. We extensively investigate a wide range of geometries using loadcell data to obtain stochastic information on discharge rates and impact loads. On a selection of the dataset a PIV analysis is used to analyse flow behaviour and indirectly determine the discharge rate. In addition, we will show how well PIV can be used for the analysis of flow patterns by comparing PIV results to the loadcell measurements.

The full dataset resulting from this research has been made publicly available according to the FAIR principle (10.4121/fa7544d6-14fd-4372-a81f-e2e1b4a44832).

2.2. EXPERIMENTAL SETUP

To identify the hopper discharge behaviour the hopper setup described by Fransen et al. is used [51]. In this section the hopper setup with load cells, the discharging material, and the high speed camera setup are introduced.

2.2.1. HOPPER DISCHARGE SETUP

Figure 2.1 (a) shows the hopper setup filled with gravel. The hopper construction consists of an aluminium frame in which different wall materials can be placed for the inclined and vertical hopper sections. In these experiments the wall material is stainless steel which has worn through impact during earlier experiments. This leads to heavily indented walls with a higher surface roughness than the original material. The geometry is enclosed by

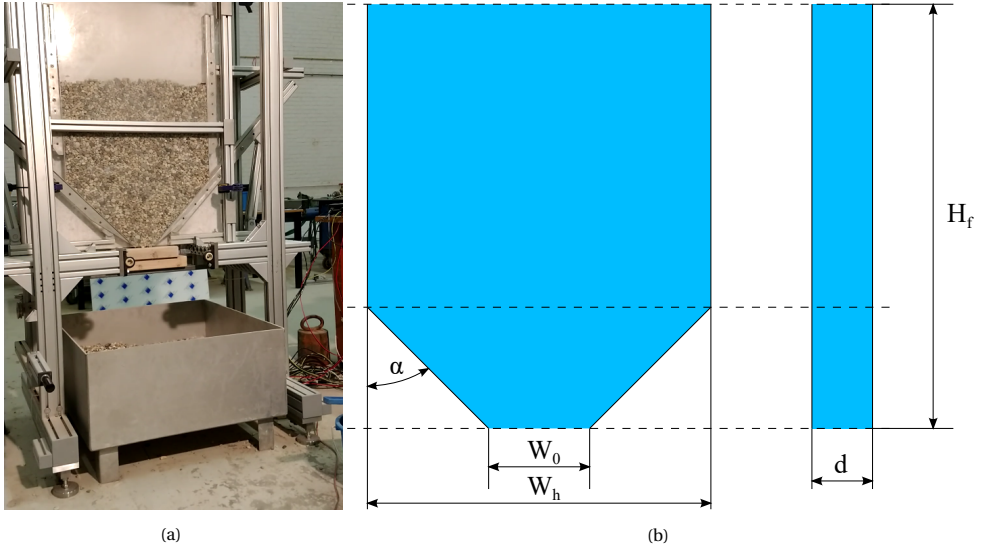


Figure 2.1: (a) Picture of the experimental setup (b) Dimensions of the hopper discharge experiment

Acrylic plates such that the flow of material during discharge can be recorded with a high speed camera. The hopper is filled with gravel by evenly cascading material through the top surface into the hopper.

The hopper angle α is adjusted in a range from 20 to 90 degrees and the discharge opening W_0 is adjusted from 50 to 200mm for these experiments. The depth of this setup d is 50mm and is fixed throughout the experiments. The total width of the hopper W_h is set to 600mm. The fill height H_f ranged from 600mm (in 50mm discharge opening cases) to 1000mm.

The experiments carried out with the setup are given in Table 2.1. For each hopper configuration, a different angle and size of the discharge opening, a new Acrylic front and back plate is used which is cleaned after each iteration of the experiment. In the table below it is already stated that some of the experiments were not successful because of errors in load cell measurements or high speed image recordings.

The entire setup is positioned on three load cells such that the vertical load exerted by the gravel material on the setup can be measured (AEB8D OIML R60 C3 Shear Beam Load cell from AE sensors). Three load cells are used such that offsets in the centre of mass changes during discharge are accounted for. The load cells measure the exerted forces at 50 Hz. The signals are processed through a Strain Gauge Amplifier (SGA) from Mantracourt and transferred to a computer through a NI-6001 DAC from Texas Instruments.

Compared to industrial sized hoppers this is a relatively small hopper. Therefore the results of experiments at this scale need to be put in the perspective of industrial applications. In this study the hopper designs used in the experiments cover alle hopper angles

Table 2.1: Experimental plan, including an indication of the experiments that were unsuccessful. These are indicated in between brackets.

	$\alpha = 20^\circ$	$\alpha = 30^\circ$	$\alpha = 45^\circ$	$\alpha = 60^\circ$	$\alpha = 75^\circ$	$\alpha = 82.5^\circ$	$\alpha = 90^\circ$
$W_o = 50mm$	10(2)	10	10	10	10	10	10
$W_o = 75mm$	5(1)	5	5	5	5	5	5
$W_o = 100mm$	5	5	5	5	5	5	5
$W_o = 150mm$	5	5	5	5	5(1)	5	5
$W_o = 200mm$	5	5	5	5	5	5	5

and push the size of the discharge opening to sizes for which flow is generally obstructed. This information can be used directly in large scale hoppers as guiding for stable discharge without the risk of arching. The transition from mass to core flow in the hopper is characteristic for this setup but can serve as an indication for large scale hoppers. Hopper design depends on the material behaviour and interaction properties with the structure. To make the effect of stochastic variability on the hopper performance into a general guideline for hopper design it is essential that experiments are conducted with large scale setups and that parametric studies with these setups include varying the filling procedure, initial density, grain diameter, wall friction angle, and other properties. In addition, limitations of this setup such as the small depth, accuracy of the measurement systems, and the absence of wall loadcell measurements should be considered in extension of the setup when future studies are conducted.

2.2.2. DISCHARGING MATERIAL: GRAVEL

The material used in the experiments is gravel which is a common material in heavy industries. The particle size distribution of the used bulk material has been determined by a sieve analysis with a HAVER&BOECKER HAVER EML 200 Premium sieve shaker. In total 10 sieves have been used with grid sizes of 1, 1.4, 2, 2.8, 4, 5.6, 8, 10, 12.5, and 16mm. In Figure 2.2 (b) the cumulative particle size distribution is shown. Based on the values for the cumulative particle size distribution we have determined the d_{10} , d_{50} , d_{60} through interpolation and based on the ratio d_{60} over d_{10} the uniformity coefficient C_u was determined. The gravel can be considered clean because the fines content is smaller than 5%. The $C_u = 1,7$ which defines the gravel as poorly graded (PG). These properties, among others, are presented in Table 2.2. In bulk material handling two types of density are considered, the particle and bulk density. For the gravel sample, both the particle and bulk density were determined. The particle density was determined by making use of Archimedes law where the displaced water volume is used to determine the volume of the particles and the weight difference measured by the scale to determine the weight of the volume leading to the particle density. We have repeated this experiment ten times to obtain an accurate average and these results are presented in Table 2.2. The bulk density of the material is determined by filling a bulk density tester ISO17828 (EN 15103) with bulk material and weighing the amount of material that is in the container. This tester meets the diameter and height requirements which should be at least 10 times the average particle diameter. The volume of the bulk density tester is 5 litres with an 0.2%

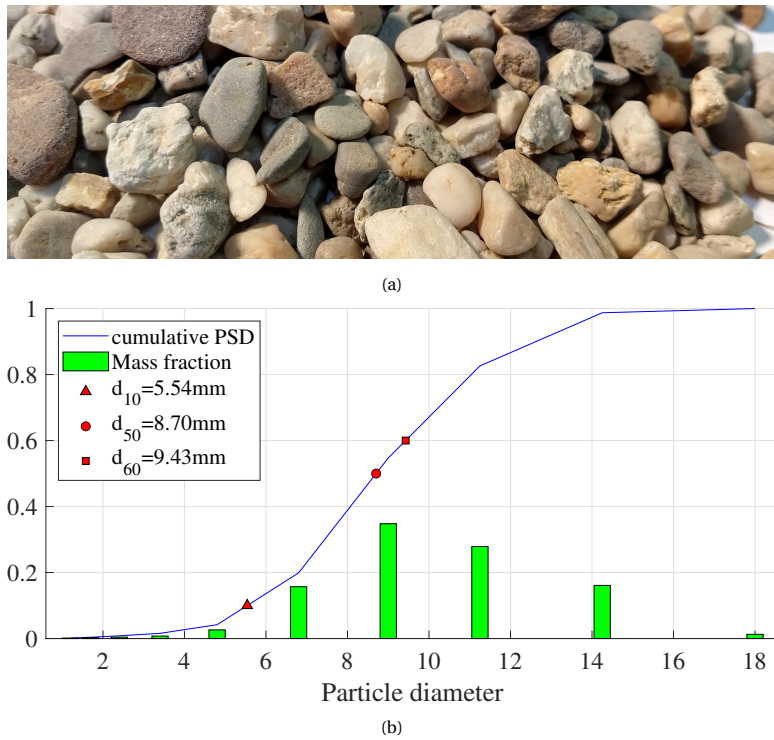


Figure 2.2: (a) Close-up picture of the gravel used in the experiment, (b) cumulative particle size distribution of gravel sample

Table 2.2: Gravel properties

Material properties		
Particle density	ρ_p	$2313,4 \pm 22,5 \text{ kg/m}^3$
Bulk density	ρ_b	$1473,06 \pm 15,4 \text{ kg/m}^3$
Angle of Repose	β	$41,40 \pm 0,36^\circ$
Void ratio	e	0,57
Fraction	d_{50}	17,41
	d_{60}	18,86
	d_{10}	11,08
	C_u	1,70
Roundness number	R_n	$0,48 \pm 0,12$
Sphericity	ψ	$0,70 \pm 0,17$

Table 2.3: Gravel properties

	mean μ_s	standard deviation σ_{mu_s}
Gravel-Stainless Steel (side walls)	$0,523(27,5^\circ)$	$0,05(2,86^\circ)$
Gravel-Acrylic (front and back plate)	$0,446(24,03^\circ)$	$0.096(5,5^\circ)$

tolerance. We have repeated this experiment 50 times which results in the same bulk density as found in [51]. From this test the average bulk density and the void ratio with a 95% confidence interval are obtained and presented in Table 2.2.

In addition, 100 particles have been closely examined to determine the sphericity and roundness of the particles. The sphericity ψ was obtained by measuring the particles with a caliper for the longest, smallest, and an intermediate cross-sectional length. The equation used to calculate the sphericity is $\psi = \sqrt[3]{(c^2/ab)}$ where a is the longest diameter, b an intermediate diameter, and c the smallest diameter. The roundness R_n was determined by comparing the shape of the particles to the Krumbains chart [52]. These values can be found in Table 2.2. The roundness of the particles shows a similar distribution where roundness can be both on the low and high side. The interaction between gravel and wall materials depends on the surface. In this case the surface of the side walls is worn out and pitted. With an inclined surface tester [53] we have tested for the angle of sliding friction of 25 individual gravel particles with impacted steel which corresponds to the walls of the hopper and acrylic material which corresponds to the front and back plate of the hopper. The inclined surface test was repeated 4 times with the same 25 particles. In Table 2.3 the average friction coefficient values have been presented.

2.2.3. HIGH SPEED IMAGING SETUP

The discharge of the hopper experiment is recorded using a FasTec IL5-H high speed camera with a manual 25mm Navitar Lens. The software used to control the camera and recording is FasMotion provided by FasTec. The distance from the lens to the front wall of

the hopper was 250cm and the height of the centre of the lens is 98,5 cm. The lighting conditions for the hopper were set with construction lights providing indirect light to the front of the hopper setup to avoid reflections on the acrylic plates. The experimental setup is shown in Figure 2.3 (a).

The recording area of the camera contains the width of the hopper, 10cm below the opening and 45 cm of the hopper height itself where the aluminium cross bar is located, see Figure 2.3 (a). In case of large angles such as the 20 and 30 degrees this means that the vertical sidewalls of the hopper are not visible in the recordings. At large discharge openings 150 and 200mm the recording frequency is 600Hz, for the 100mm cases the recording frequency is 400Hz, 300Hz for the 75mm cases, and 200 Hz for the cases with 50 mm discharge opening sizes. This ensures that all the experiments are fully recorded. The shutter speed was set to 650ms for all experiments.

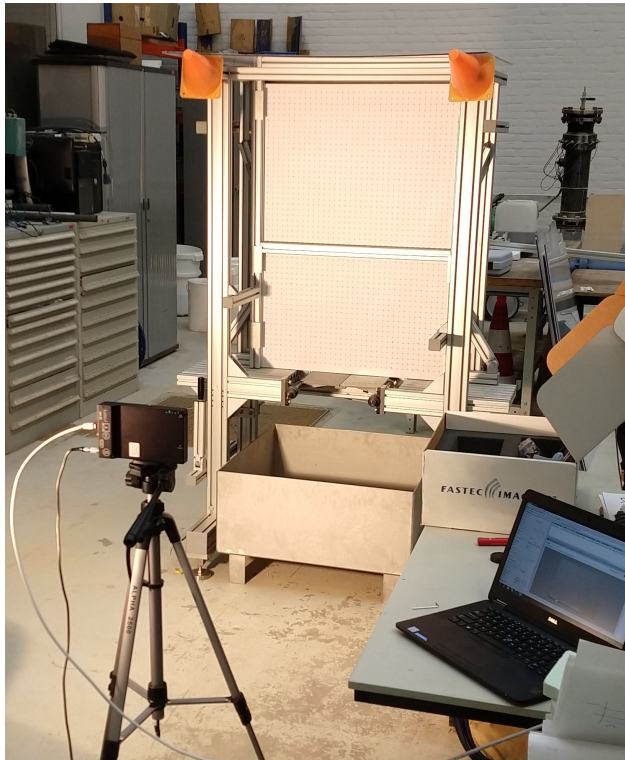
The lens of the camera was focussed manually using the following procedure. The first step was to put the lens at the focal point of the camera (0.95 in the case of the Navitar lens). In the live feed of the controller zoom in on the material in the centre of the hopper and start adjusting the focus of the lens. When a sharp image is obtained the lens is fastened. Next, the f-stop of the lens is used to adjust the back-focus. This is followed by zooming in on the edges of the setup and adjust the back-focus such that the contrast is optimal. To account for the image distortion by the lens in the PIV analysis a sheet of calibration markers was positioned in the flow region of the image and reference pictures were taken after setting up the camera, see Figure 2.3 (b).

2.3. DATA ANALYSIS METHODOLOGY

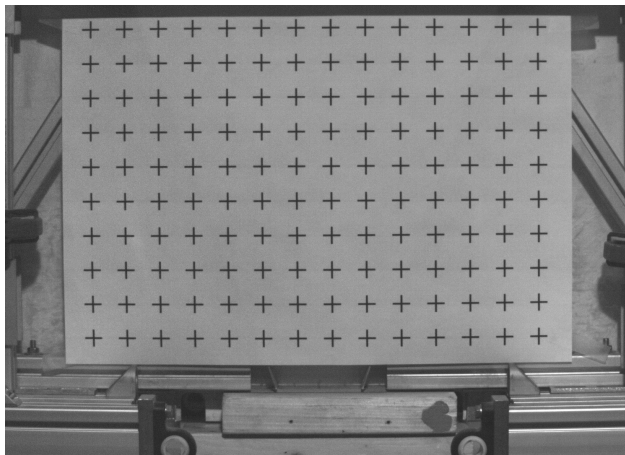
In Section 2.3.1 the analysis of the load cell data is discussed. Next, the processing of PIV data is discussed.

2.3.1. ANALYSIS OF LOAD CELL DATA

The load cell data consists of a force signal over time. By dividing the force with the gravity constant the mass in the hopper is determined which is shown in Figure 2.4 (a) for the first experiment with a 45 degree hopper angle and 100 mm discharge opening. From this force over mass signal the average discharge rate can be determined by linear interpolation of the signal in a steady flow region [51]. In Figure 2.2 (b) the force signal is shown for the first experiment with a 30 degree angle and a 150mm discharge opening. Here we identify the peaks and valleys in the fluctuation of the force signal from the load cells. The difference between a valley and peak defines the impact of the bulk material on the hopper setup. The black markers indicate the maximum difference between a peak and valley and the other peaks and valleys are indicated in red. This analysis is carried out on all experiments from the experimental plan shown in Table 2.1.

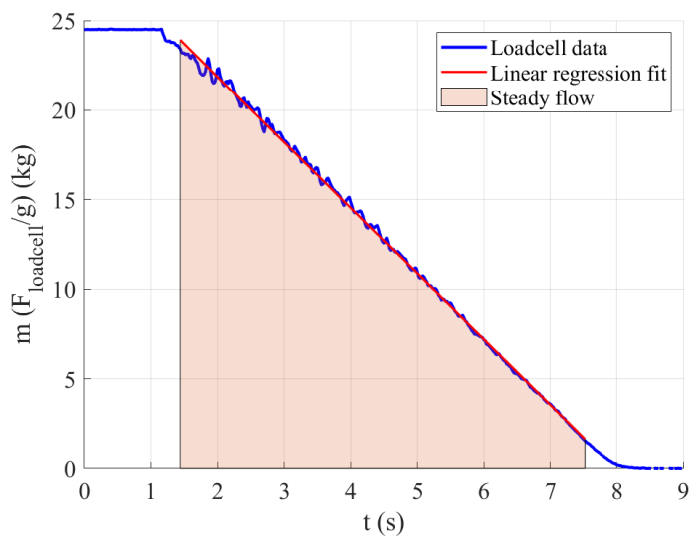


(a)

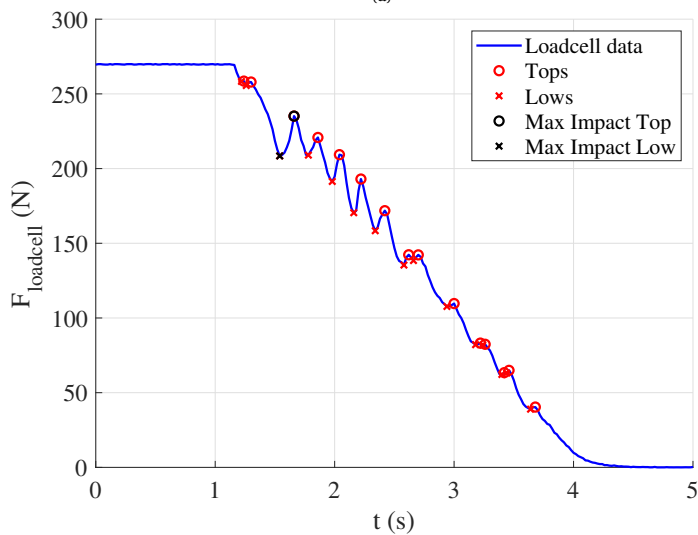


(b)

Figure 2.3: Experimental setup with camera position (a), Calibration grid before test with 40 by 40mm and 4mm thickness calibration marker(b)



(a)



(b)

Figure 2.4: Steady state discharge rate in steady discharge area (a) and peaks in the loading of the load cells due to acceleration and deceleration of granular material in the hopper (b).

2.3.2. IMAGE ANALYSIS USING PARTICLE IMAGE VELOCIMETRY (PIV)

The high speed images of the hopper discharge are processed with Particle Image Velocimetry (PIV) to obtain the velocity fields using PIVware software. In particle image velocimetry the changes in the characteristic pattern of an image are compared to the characteristic patterns in images from subsequent time steps [43]. The translation of the characteristic patterns between subsequent images determines the velocity of the material in the image. More details on the procedure can be found in Appendix A.1. To identify relation between velocities and hopper angles, the experiments with a 100mm discharge opening and a 20, 30, 45, 60, 75, and 90 degree hopper angle are chosen for analysis with PIV. For the PIV analysis of the images a patch size of 64 by 64 pixels was used which was able to give a good resolution at the inclined hopper walls and have limited oscillations in the obtained velocity data.

To analyse the flow patterns in the hopper the PIV data is plotted over the original image using a vector plot. For the analysis of the velocity profiles at 0, 10, 20, 30, and 35 centimetres above the outlet of the hopper the PIV data is filtered and linearly interpolated if not positioned exactly in a grid point of the PIV data. These velocity profiles are averaged over the stable flow region at the different heights where the stable flow region for the hopper outlet is the same as used for the discharge rate. With these velocity profiles the effect of hopper geometry on the velocity profile is determined. In addition, the stagnant zones during hopper discharge are determined based on the velocity profiles.

Next, the goal is to compare the load cell measurements with the PIV data. To do this it is necessary to obtain the acceleration fields in the hopper derived from the PIV data. From the velocity data the acceleration is determined by using the Euler Forward integration method with a time step size equal to $1/f_{rec}$.

$$a_i = \frac{v_{i+1} - v_i}{\Delta t} \quad (2.1)$$

The obtained acceleration fields are used for a comparison with the trajectory of the load cell signal by taking the average acceleration of the material in the hopper, a_y of the material in the hopper in vertical direction and scaling it to the loadcell signal leaving the transient behaviour unchanged. To improve the comparability of the acceleration and load cell signal the noise in the signal is reduced by passing both the PIV and load cell signal through a low-pass filter.

2.4. RESULTS

In total, 201 hopper discharge experiments were conducted. The dataset is sufficient for obtaining accurate averages and standard deviations for the discharge rate and impact load. In the following sections we will discuss the results and the trends that are observed.

In Section 2.4.1 we look at the discharge rates and impact loads for all geometrical setups of the hopper used during the experiments. These are hopper angles (α) of 20, 30, 45, 60, 75, 82.5, and 90 degrees with discharge openings (W_o) of 50, 75, 100, 150, and 200mm.

In Section 4.2 the results for the PIV analysis are discussed for all experiments with the hopper angles 20, 30, 45, 60, 75, and 90 degrees for a discharge opening of 100mm. This choice was made based on the computational cost of performing the PIV analysis for 30 experiments. In this Section the pulsating flow is visualised, the average velocity patterns, and the stagnant zones in the geometry are discussed. To answer the question on how the loads on the setup are related to the flow behaviour of the material we compare the loadcell data to the PIV data in Section 2.4.3 which consists of a comparison of the accelerations obtained from the loadcells and the PIV. In addition the discharge rates calculated based on the load-cell data are compared to the discharge rate from the PIV analysis. The arching phenomena observed during the experiments with a 50mm discharge opening have been added in Appendix A.2.

2.4.1. DISCHARGE RATES AND IMPACT LOADS

The performance of the hopper is assessed using the discharge rate (ϕ) and impact load F_{imp} which are key performance indicators (KPIs). The discharge rate is a KPI that is important in design of industrial process line whereas the impact load is important for the structural integrity of the hopper. To analyse the trend in the behaviour the data for the discharge is normalized with respect to the maximum key value as shown in Figure 2.5. In this figure the normalized value for the discharge rate is shown with black markers and the normalized 95% confidence interval (CI) are represented by the red markers. Along with the discharge rate and the impact load the initial void ratio of the particles in the hopper was determined for each experiment and was on average 0,527 with a standard deviation of 0,103. This is lower than observed with the density tests where it was 0,57. This difference can be attributed to the small depth of the hopper relative to the height. For reproducibility of results, the reference values for the average and standard deviation of the discharge rate and average impact load can be found in Appendix A.3. Here, it is seen that the normalized discharge rate, ϕ_{norm} , is equal to one at the 20-degree angle as the maximum discharge rates for each experiment were observed here and normalized with respect to the maximum value. The trend as a function of the hopper angle for each discharge opening size follow a similar path, especially the 100, 150, and 200 mm discharge openings. Over the range of angles the maximum relative difference in discharge rate is 24% of the normalized value for the 100, 150, and 200 mm discharge opening sizes. For the 50 and 75 mm discharge openings it is observed that this maximum relative difference is 42%. These results shows that there is a significant effect of the hopper angle and size of the discharge opening on the discharge rate for the same discharge material.

For the confidence intervals a clear transition is visible in the data at the transition point from 45 to 60 degree hopper angles. Here, the confidence intervals start to deviate with respect to the size of the discharge opening for the hopper angle that is used. A consistent trend in this behaviour as a function of the hopper angle or the size of the discharge opening is difficult to distinguish. However, it seems that for hopper angles below 60 degrees the confidence interval is smaller and therefore shows that the discharge rate is more stable. This transition might be related to the change from mass flow to core flow.

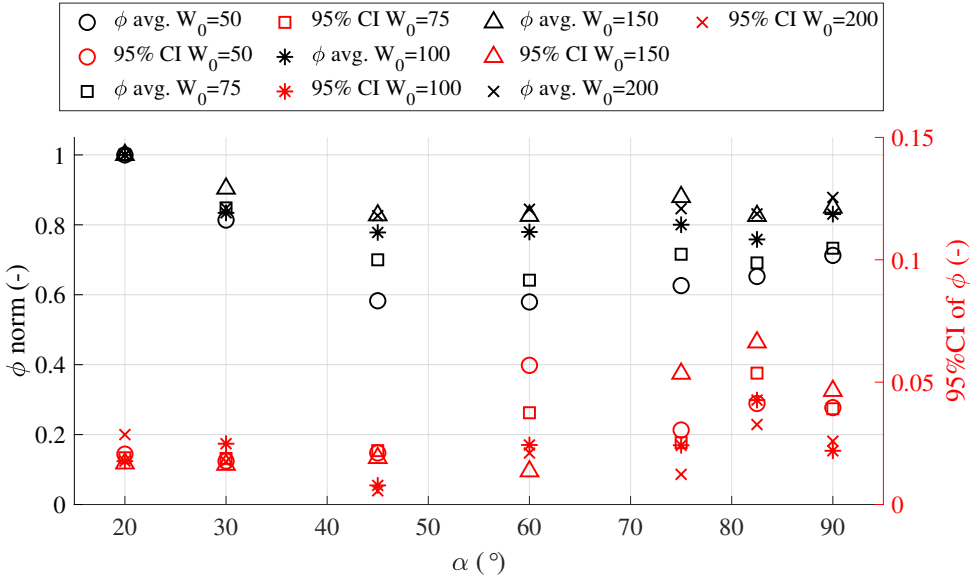


Figure 2.5: Normalized average discharge rate and the relative 95% CI for these discharge rates

In Figure 2.6 the normalized impact load, $F_{imp-norm}$, is shown with respect to the hopper angle represented by the black markers and the 95% CI of this impact load by the red markers. For the normalized impact load a clear decreasing trend is visible with an increasing hopper angle. A clear relation between the impact load at a specific hopper angle and all discharge opening sizes is not directly visible. The spread seems larger for the 30, 45, and 60-degree hopper angles than for the 75, 82.5, and 90-degree hopper angles.

To assess whether the average impact load is reliable the 95% CI of the normalized impact load is evaluated. The 95% CI of the normalized impact loads show a large variability with an irregular pattern over the different hopper angles with a rather low value at a 20 degree hopper angle as the exception. It could be distinguished that for 45, 60, and 75-degree hopper angle the confidence intervals are below 50% of the average impact load but can be as small as 10% depending on the size of the discharge opening.

2.4.2. PIV ANALYSIS: IDENTIFYING FLOW FIELDS IN DISCHARGING HOPPERS

The high speed image data obtained from the experiments is used to determine velocity fields by using PIV. In Section 2.4.2 stills from an experiment are shown where the acceleration and deceleration of the granular material is shown. Next, Section 2.4.2 discusses the dependency of average flow profiles on height and their reliability for the 20, 30, 45, 60, 75, and 90 degree hopper angles with a discharge opening of 100 mm. Based on this analysis we discuss the formation of stagnant zones in the hopper experiments, Section 2.4.2.

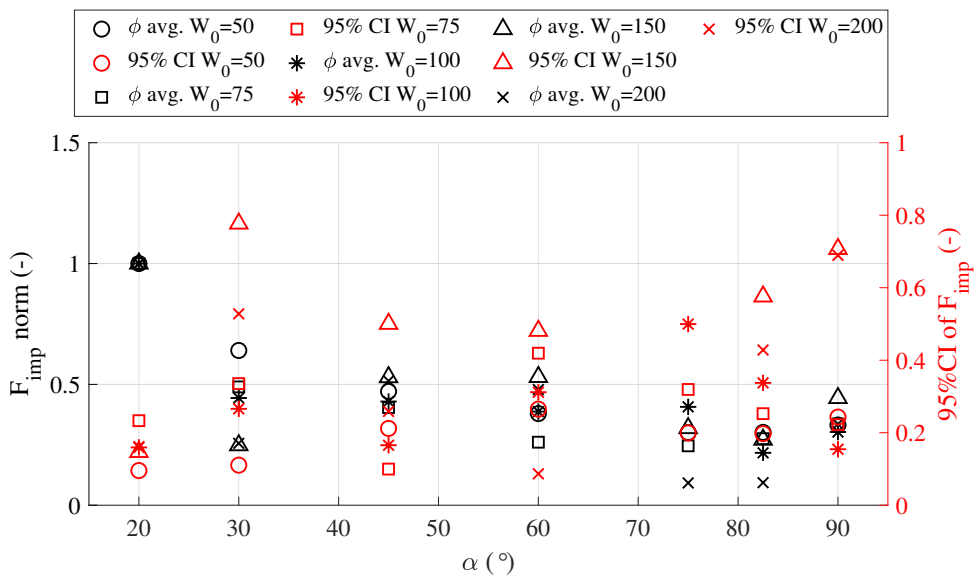


Figure 2.6: Normalized average of maximum impact load and the relative 95% CI for these impact loads

PULSATING FLOW DURING HOPPER DISCHARGE

During the discharge of a hopper pulsating behaviour can be observed which is related to the acceleration and deceleration of the material. In Figure 2.7 (a-f) 6 stills are shown from 0,54 till 0,78 seconds of the first experiment with a 20 degree hopper angle and 100 mm discharge opening. The tags t_i of the images can be found in Figure 8 where the load cell signal from the experiment is and where the average velocity in vertical direction from the PIV analysis is shown. In the load cell signal oscillations of 20N are visible and for the velocity signal a fluctuation of 0,5m/s within the signal is present. This indicates that the discharge rate fluctuating significantly compared to the maximum velocity in the hopper of 0,95m/s.

In the stills in Figure 2.7 the full velocity fields obtained with the PIV analysis are shown. In the first still the velocity field is shown for t_1 which is located at a valley in the load cell signal. Here the velocity field has a higher intensity over the hopper area and just passed a peak in the velocity signal calculated from the PIV results. In still 2 at t_2 it shows the velocity field over the entire hopper decreased in intensity. The material in the hopper is slowing down which corresponds to a deceleration and an increased load on the structure. This is seen in the load cell signal. At t_3 the material is still flowing in the bottom section but in the top part the material decreased in velocity compared to t_2 . In the load cell signal t_3 corresponds to the moment where the peak is reached. The still at t_4 shows that the velocity field has increased over the entire hopper area and corresponds to a stage where the velocity is still increasing and the loading of the load cell is decreasing. At t_5 the velocity field has fully developed again, corresponding to a peak in the velocity signal and a valley in the load cell signal. Finally, t_6 shows that the flow in the upper part of the

hopper has significantly decreased. Here it is still in the deceleration phase but already reached a valley in the velocity signal.

The figures shown above and the other images in the dataset show what occurs from a mechanical perspective. The material flows and accelerates into the funnel at t_1 . However, there is a limited area where the material can flow through causing the material to be compressed between the two walls leading to increased forces between the particles and walls. This leads to a lower flowability of the material and consequently a decrease in flow velocity but an increase in force on the hopper as shown in Figure 8. This is especially visible looking at the material in the hopper at the height of the first black spot in the structure of the hopper side walls. When the material keeps flowing from the orifice in the region below this line it ultimately frees up space for the material that has decelerated to start moving freely. Hence, all the above material will start to accelerate as well. This process has been thoroughly described for sand by Michalowski from both a theoretical and experimental point of view [32]. However, a difference that can be observed is that the irregularity in particle shape of gravel compared to sand causes irregularities in flow patterns whereas this is less pronounced with discharging sand. In Figure 2.8 the two signals are shown from the start of the experiments. Here, it can be seen that the flow is starting to develop and that the signals become nearly periodic after $t = 0.5$ seconds. As can be seen in the signal there is a slight phase change between the behaviour observed in the load cell and velocity signal. One of the reasons might be that the images were recorded at 400Hz whereas the load cell signal was recorded at 50Hz. In addition, the load cells are mounted beneath the hopper and there is a certain distance between the hopper walls and the load cells. This might lead to a delay in the measured signal by the loadcells and the image recording.

AVERAGE VELOCITY PATTERNS

From PIV analysis of the experiments with a 100mm discharge opening and 20, 30, 45, 60, 75, and 90 degree hopper angle the average velocity patterns at five heights in the hopper is determined. These heights are the outlet and 10, 20, 30, and 35 centimetres above the outlet as shown in Figure 2.9. Recalling the normalized discharge rates from Section 2.4.1 for the discharge opening of 100mm it is expected that the minimum flow velocity is approximately 22 percent lower than the velocity of the material in a 20 degree hopper. In Figure 2.9 (a) it can be seen that the velocity profiles at the outlet are self-similar for all angles as was also found by Mehdizad et al. in small scale MRI experiments [38]. Even though there is self-similarity in shape, the actual variation in the velocity profiles is large and about 33 percent. This indicates that if the discharge rate is to be determined based on the velocity profiles that errors are introduced.

In Figures 2.9 (b-d) flow heights above the outlet are shown which all show a transition in shape from an incomplete Gaussian profile at the 20-degree angle to a complete Gaussian profile for the 90-degree angle. The profiles for the 20 and 30-degree angle clearly show that there is velocity of the granular material at the wall. For the 20-degree angle there is flow along the wall for all flow heights and for the 30-degree angle this is present up to 20cm above the outlet. A closer look shows that the narrowest velocity profile is obtained at the 90 degree angle and shows the smoothest profile compared to the other angles.

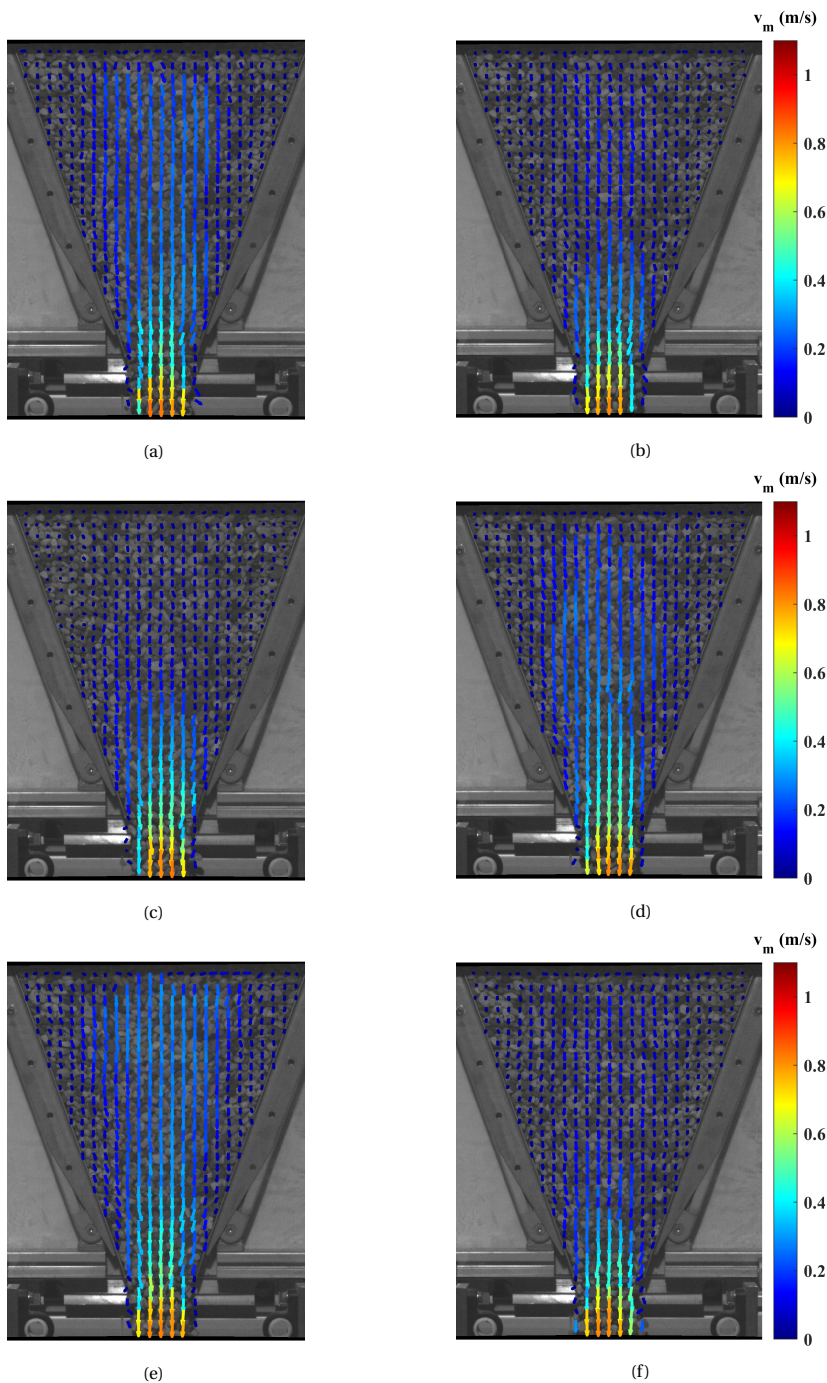


Figure 2.7: 6 instances during hopper discharge with magnitude and direction of velocity V_m , (a) $t_1 = 0,54s$ (b) $t_2 = 0,58s$ (c) $t_3 = 0,62s$ (d) $t_4 = 0,67s$ (e) $t_5 = 0,72s$ (f) $t_6 = 0,78s$

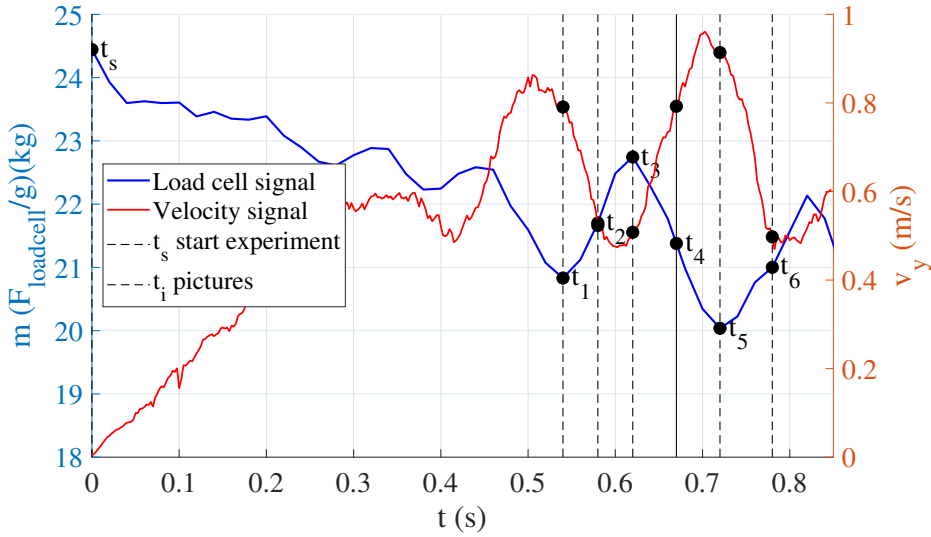


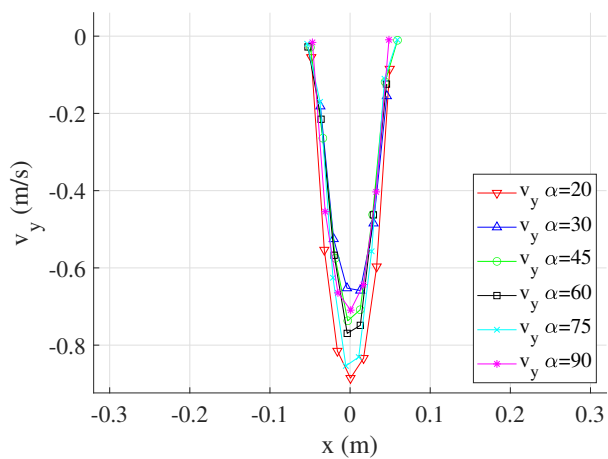
Figure 2.8: Acceleration and deceleration of granular material during discharge for hopper angle of 20 degrees and discharge opening of 100 mm.

At higher heights this profile becomes wider but less in magnitude, this is similar to the experimental results obtained by Steingart & Evans for zinc particles [47]. In the study by Gonzales et. al. a hopper with a hopper angle of 62,5 degrees was used for maize discharge which showed the same trend of velocity profiles at increasing height [54].

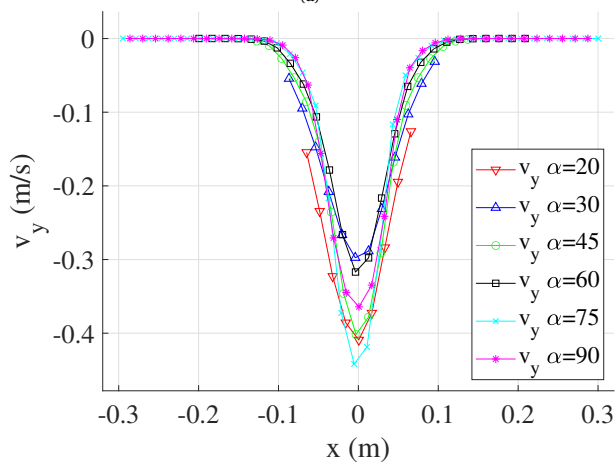
STAGNANT ZONES FOR DIFFERENT GEOMETRIES

The most common characterisation of a discharging hopper is whether there is mass or funnel flow. During mass flow all the material in the hopper is in motion whereas during funnel flow the material on the sides of the hopper forms stagnant zones and the material only flows in the centre. This behaviour highly depends on the hopper angle, bulk material, and wall properties. During the experiments and in the experimental results this behaviour was clearly visible. To determine where these stagnant zones start, the velocity profiles from the previous section were evaluated for velocities below $5 \times 10^{-4} (m/s)$. This corresponds to half a mm per second which is a fraction of the maximum velocity in the hopper which is between 0.8 and 1 m/s. Analysis of the velocity patterns leads to the stagnant and flow zones shown in Figure 2.10. The blue lines depict the hopper geometry, the red lines the edge where the material becomes stagnant, the stagnant zones are depicted by the red area, and the flow zones where the velocity is higher than the set threshold.

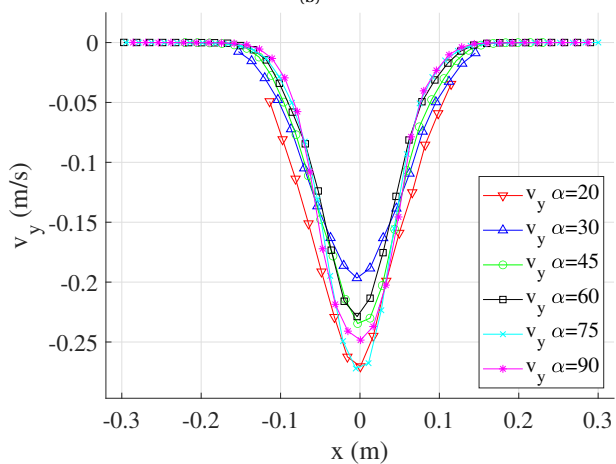
For the steepest angles at 20 and 30 degrees shown in Figure 2.10 (a) and (b) the flow velocities were higher than the threshold leading to no stagnant zones. This was also observed for the velocity patterns at the different heights in the hopper. At an angle of 45 degrees we see that a stagnant zone appears above the 0.1m line, below this line the velocity was higher than the threshold. It is expected that with decreasing hopper



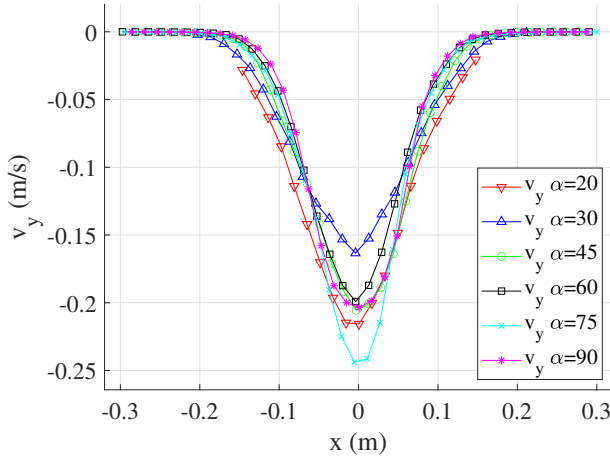
(a)



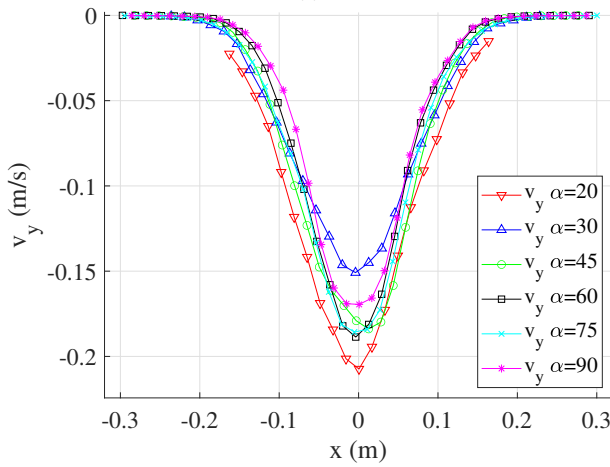
(b)



(c)



(d)



(e)

Figure 2.9: Average velocity patterns at different flow heights for all angles, (a) outlet (b) 10cm above outlet (c) 20cm above outlet, (d) 30 cm above outlet, (e) 35cm above outlet

angles the flow velocity alongside the walls decreases because the friction forces between particles and wall are less easily surpassed. For the 60 degree hopper angle in Figure 2.10 (d) we see that along the wall all the material is stagnant. In Figure 2.10 (e,f) the stagnant zones for the 75 and 90 degree hopper are shown respectively. As expected, stagnant zones are visible. In the figures for the 45 to 90 degree hopper angle a clear shape of the interface with the stagnant zones is visible. This is not a straight line but a curved line which curves towards the edges of the hopper outlet. This inline with the behaviour observed in other hopper studies [36, 37].

2.4.3. COMPARISON LOAD CELL TO PIV DATA

Individual analysis of the load cell and PIV analysis gave insight on the external behaviour of the hopper and the internal behaviour of the granular material. In this section these results are combined by first presenting a qualitative comparison of the force and acceleration signals obtained from the load-cell and PIV respectively. Secondly we present a comparison between the discharge rates obtained from the load-cell data and PIV.

FORCE AND ACCELERATION SIGNAL COMPARISON

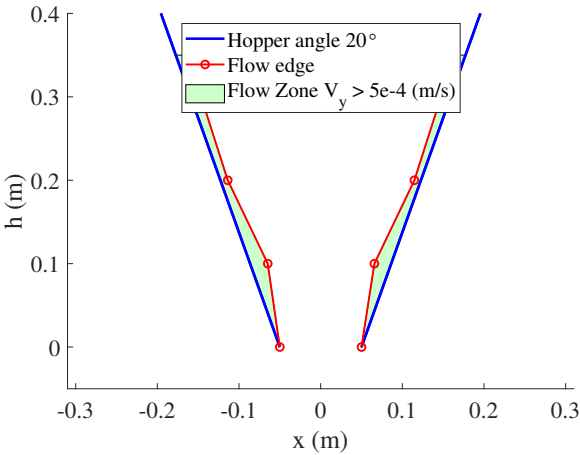
In Section 2.4.2 the flow fields in the hopper were compared to the moments where this occurs in the load cell and in the average velocity in the y-direction from the PIV analysis. Here, a clear phase difference was observed between the velocity signal and load cell signal which seems to be around 90 degrees. By integration of the velocity fields the acceleration and deceleration of the granular material is determined which has a phase change of 90 degrees and therefore should be in phase with the load cell signal. In Figure 2.11 (a) and (b) the fluctuation of the average acceleration in y-direction can be seen over time for a section of the first and second experiment of a hopper geometry with a 100mm discharge opening and a 20 and 30 degree angle respectively. In addition to the acceleration signal the filtered load cell signal LC is shown. These clearly show that the signals are nearly in phase. Based on these examinations it can be concluded that the pulsating force endured by the hopper is caused by the acceleration and deceleration of the granular material during discharge.

The fluctuations we see in the load cell data seem to be near harmonic but cannot be qualified as such. Each time a structure forms during discharge the composition is different and will lead to a different limit for failure of the structure. In the stochastic calibration study [51] we have seen that macro properties are stochastically distributed and tend to behave normally. This might also be the case for collapsing granular structures, however, this is a topic for further research.

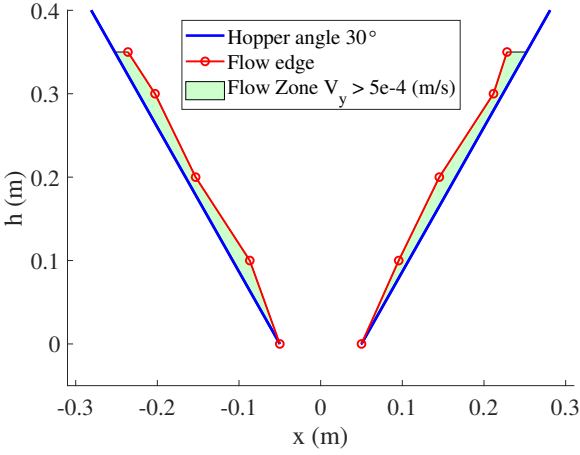
From the comparison of the processed data from the load cell analysis and the PIV analysis it is seen that the vibrations induced on the structure of the hopper are related to the flow behaviour of the granular material in the hopper.

COMPARISON OF DISCHARGE RATES FROM LOADCELL AND PIV MEASUREMENTS

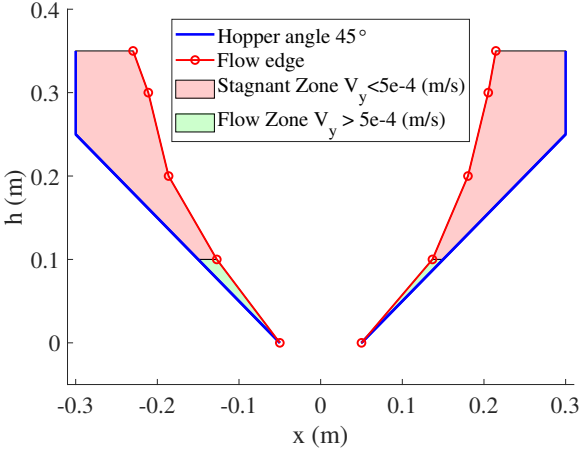
From both the load cell data and PIV analysis we have obtained discharge rates for angles 20, 30, 45, 60, 75, and 90 degrees and a discharge opening of 100 mm. In Figure 2.12 the



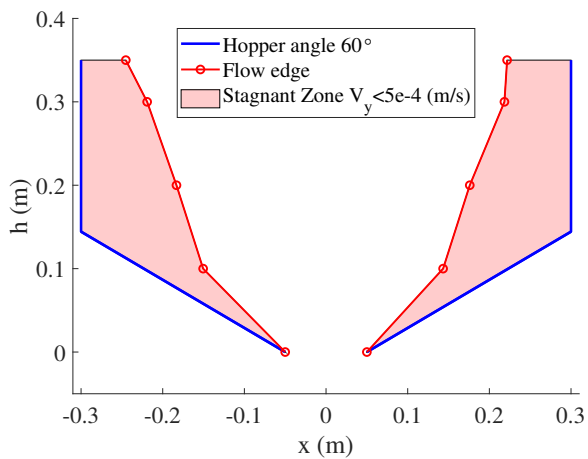
(a)



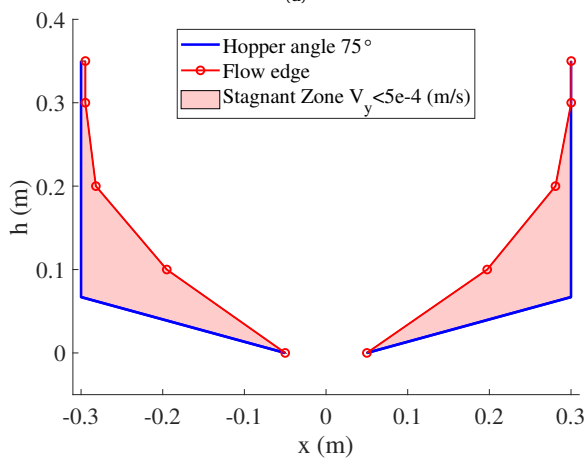
(b)



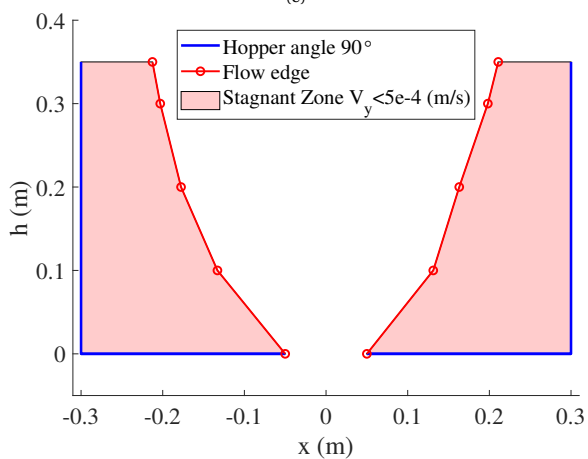
(c)



(d)



(e)



(f)

Figure 2.10: Stagnant zones (a) $\alpha = 20^\circ$ (b) $\alpha = 30^\circ$ (c) $\alpha = 45^\circ$ (d) $\alpha = 60^\circ$ (e) $\alpha = 75^\circ$ (f) $\alpha = 90^\circ$

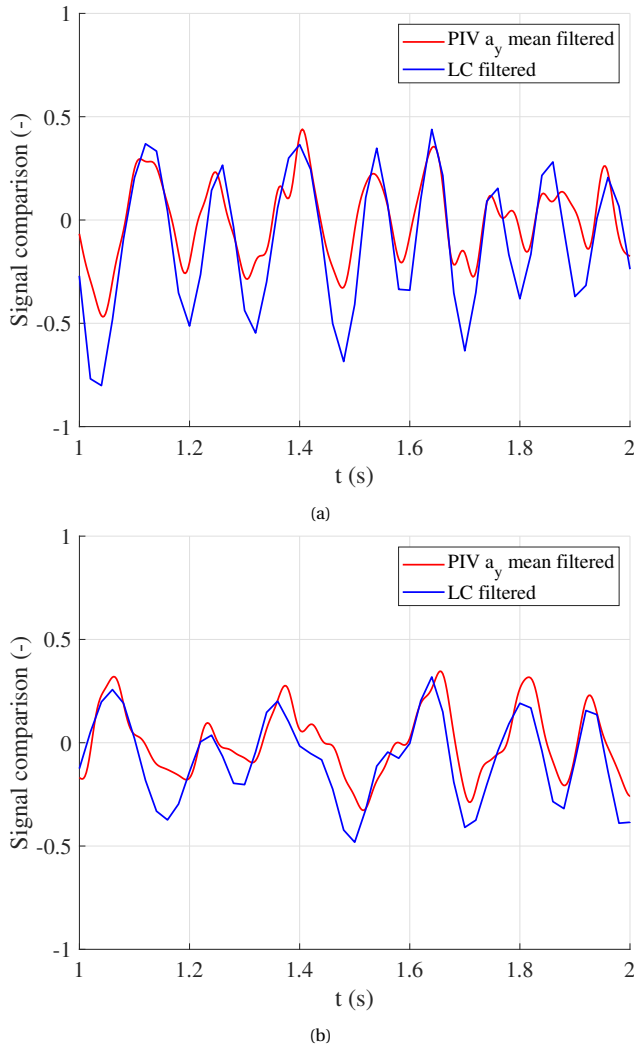


Figure 2.11: Comparison of the filtered acceleration signal in y-direction obtained from loadcell and PIV data (a) $\alpha = 20$, $d = 100$, run 1 (b) $\alpha = 30$, $d = 100$, run = 1

average discharge rate and the 95% confidence interval (CI) for the load-cell data in blue and derived from the PIV data in red are presented. The discharge rate is directly obtained from the load-cell data and only includes the error in fitting the discharge rate. For the discharge rate derived with PIV more steps are taken which are prone to error. First the accuracy of the PIV analysis itself, in this case it is likely to be 1 pixel relating to a 0.5 mm error. Secondly, in calculating the discharge rate additional errors can come up. The velocity profiles are based on the PIV analysis of the images in which only the particles in contact with the front wall are visible. The velocity at the wall is likely to be slightly lower than in the centre of the hopper. The bulk density used to calculate the discharge rate is the same as obtained in the bulk density test which might be slightly different from the bulk density in the experiment. For the velocity profile we have 8 to 6 points on the velocity curve which are used to approximate the total area under the velocity curve by means of the trapezium rule. With 6 to 8 the integration error might be significant.

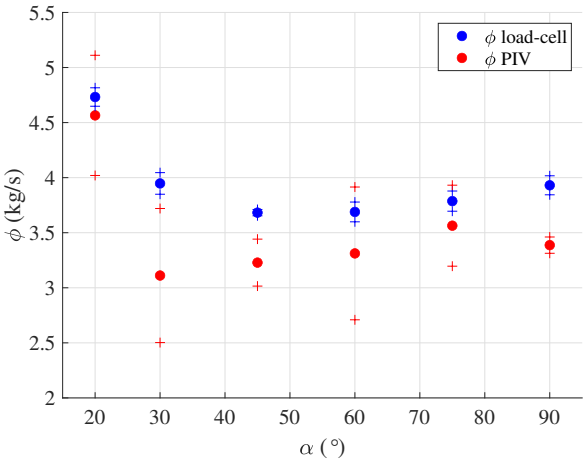
The results in Figure 2.12 (a) show that the mean discharge rate obtained from the PIV analysis is lower than the value obtained from the discharge rate. One of the reasons for this error might be that the PIV is based on the particle movement along the wall and not in the centre of the hopper. However, this effect is not likely to be big because of the shallow depth of the hopper. Regarding the trend in the data it seems that there is a point between the 45 and 60-degree hopper angle in which the trend goes from decreasing to increasing again. This might be related to the transition from mass to core flow. If we look at the percentage errors in Figure 2.12 (b) an average error of below 5 percent is achieved for the 20 and 75-degree hopper angles and between 5 and 20 percent for the other angles. In Figure 2.12 (c) and (d) the discharge rates calculated from the loadcell and PIV data for each individual experiment have been shown, respectively. Another reason for the error is found in the differences between subsequent runs of the experiment. It is observed that the discharge rates calculated from the loadcell data seems to be more or less stable around a mean. On the contrary, the discharge rates for the individual PIV data shows that there is a decreasing discharge rate with an increasing experiment number. This explains why the mean of the PIV based discharge rates is lower than for the loadcell based values. An explanation for the trend in the PIV discharge rates can be given based on the execution of the experiments. For each configuration of the hopper, size of the discharge opening and hopper angle, a new Perspex plate was used. During the first run of the experiment the Perspex plate is transparent and pristine which is likely to yield the highest detail in the high speed images. While carrying out more experiments the Perspex plate is cleaned but shows signs of wear. It is likely that the quality of the images decreases and that it becomes difficult for the PIV algorithm to keep track of the flow of particles due to the introduced noise by the wearing of the Perspex plate. To compare, Figure 2.12 (b) also shows the error of the mean discharge rate for the loadcell data with the discharge rate obtained from the first experiment for each hopper angle. These results indicate that the error between the first run of the PIV and the loadcell based discharge rate is positioned closer to the zero percent error except for the first experiment.

In Table 2.4 the numerical values for the average and standard deviation of the discharge rate are presented for each angle for both the load-cell and PIV data. Here, the standard deviation of the discharge rate is always higher for the results obtained with the PIV

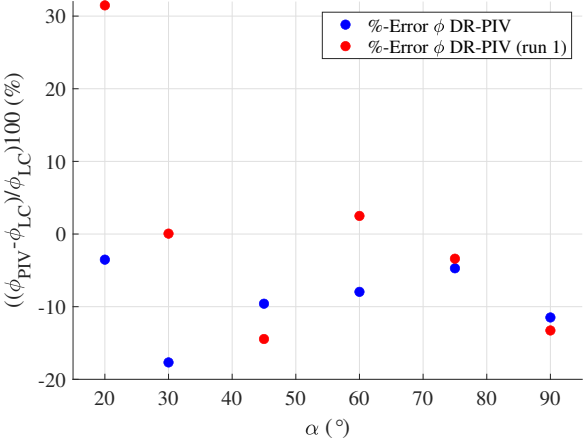
Table 2.4: Comparison of discharge rates from loadcells and PIV data

Hopper angle α	Loadcell (mean \pm std)	PIV (mean \pm std)	Error mean (%)
20	4.73 \pm 0.073	4.56 \pm 0.47	-3,53
30	3.95 \pm 0.085	3.11 \pm 0.53	-17,67
45	3.68 \pm 0.025	3.23 \pm 0.19	-9,59
60	3.69 \pm 0.078	3.31 \pm 0.52	-7,96
75	3.79 \pm 0.080	3.56 \pm 0.32	-4,71
90	3.93 \pm 0.075	3.39 \pm 0.06	-11,48

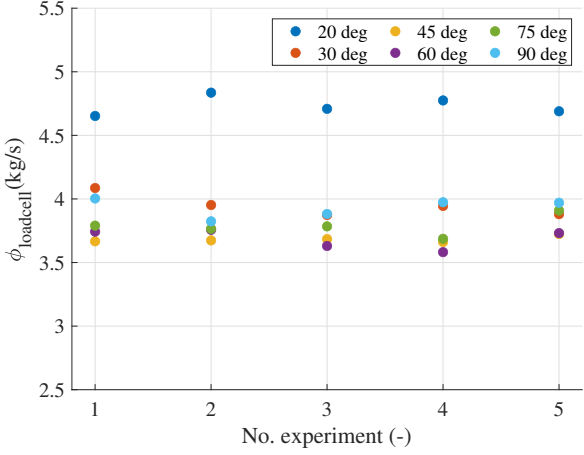
analysis than for the results directly obtained from the load-cell data. This clearly shows that the additional steps in determining the discharge rate leads to a higher uncertainty.



(a)



(b)



(c)

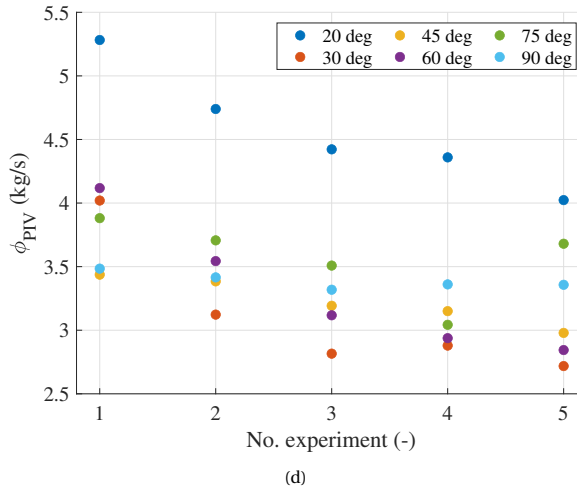


Figure 2.12: (a) Mean discharge rate obtained from load-cell data and PIV analysis with 95% confidence interval (b) Error in mean discharge rate in percentages, (c) Individual discharge rates per run from loadcell data (d) Individual discharge rates per run from PIV data

2.5. CONCLUSION

The aim of this study was to identify the relation between dynamic loads on the hopper structure and flow behaviour of the bulk material in the hopper. A wide range of geometries have been tested for hopper discharge with load cells and high speed imaging measurement techniques to get information on internal and external behaviour. The comparison of flow behaviour and load cell measurements showed that the flow behaviour of the granular material is related to the vibrations measured externally.

The discharge rates for the different geometries showed that increasing the hopper angle above the friction angle of the wall with the granular material leads to a roughly two times higher fluctuation in the discharge rate. This is related to the observation that this is also the transition point from mass to funnel flow. In addition, the high velocities and more prominent stick-slip behaviour in steep hopper angles (<30 degrees) also lead to wider confidence intervals for the discharge rate. Experimental observations showed that arching is likely to occur in hopper geometries where the hopper angle is in the range of the wall friction angle for the wall-granular material interaction and if discharge openings become too small.

The impact load decreases with an increasing hopper angle where it is likely that the impact of the granular flow on the structure dissipates in the stagnant zones. In terms of 95% confidence intervals the discharge rates are most stable from 20 to 45 degrees for all evaluated sizes of the discharge opening. For the impact load it shows that the 95% confidence intervals show a parabolic trend with the smallest interval at the 60-degree hopper angle.

The extensive experimental study shows that the variability in the performance of the hopper is not uniform over the range of discharge opening diameters and hopper angles for both the discharge rate and impact load. Even though the used experimental setup is limited, this variability should be an important consideration for designers of hoppers. Combining the information on the performance and variability of the discharge rate and the effect of impact load may be used to improve the design choice of hoppers.

The analysis of the flow profiles showed that these are influenced by the geometry of the hopper. In terms of reliability of flow profiles it can be seen that for average velocities the 95% confidence interval is in a range of 15 to 30% of the average velocity. This leaves room for optimizing the hopper geometry such that the fluctuation in the outflow is minimized to achieve a stable discharge.

Comparing the force signals from the load cells to the accelerations obtained with PIV lead to a clear correlation relating the granular behaviour in the hopper to the vibrations that can be measured externally. In the load cell signals the fluctuation of force with a periodic appearance was visible in hopper geometries with a steep hopper angle and large discharge opening. In the PIV results for these configurations the acceleration and deceleration of granular material was clearly visible and was in phase with the load cell signals. The accelerating behaviour can be explained by formation and breaking down of granular structures due to interlocking of the particles. By means of integration of the velocity profiles over the depth of the hopper we determined that PIV underestimated the hopper discharge measured with the load cells by 3,5 to 18%. The categoric underestimation is likely related to the wear of the field of view which increases with the number of experiments.

From the comparison of the processed data from the load cell analysis and the PIV analysis it is seen that the vibrations induced on the structure of the hopper are related to the flow behaviour of the granular material in the hopper. For further research the dataset is made available and can be used for validation (10.4121/fa7544d6-14fd-4372-a81f-e2e1b4a44832).

2.6. OUTLOOK

The experimental setup used in this study is an academic scale setup with its limitations. In further studies on this topic the setup should be extended with loadcell measurement capabilities for the side walls and hopper walls of the hopper. In addition, the width of the hopper should be increased to make comparison to Jenike diagrams for wedge-shaped hoppers possible. The data from the PIV measurements and load cell measurements contains information about the frequency of the pulsating behavior which requires further study. The detailed imaging of the experiments allows to evaluate the movement of particles and the intergranular structure. However, to do this accurately the experimental setup needs to be improved with additional loadcell measurement. To obtain a general formulation on the stochastic variability and its influence on design of hoppers it is essential that parametric studies are conducted considering changing grain diameters, wall friction angles, but also initial densities and different filling techniques.

2.7. ACKNOWLEDGEMENTS

We would like to thank Jerry Westerweel for providing us with the PIVware software package used to perform the particle image velocimetry analysis. In addition, we would like to thank Henry Wynaendts, Nienke Jorna, Roos Klaassen, and Thiadmar Visserman for their exploratory work with the experimental setup and Pieter van de Ven for the analysis of particle and wall friction properties.

3

APPLICATION OF DEM-BASED METAMODELS IN BULK HANDLING EQUIPMENT DESIGN: METHODOLOGY AND DEM CASE STUDY

Design of bulk handling equipment is an extensive process which involves the complex behaviour of systems and is usually based on empirical relations between design parameters and performance. This can be improved by using simulation based models. One of these methods is the discrete element method (DEM) which enables modelling of granular materials in equipment. However, these models are computationally expensive and therefore challenging to use in design optimization. To make discrete element modelling a common technique in equipment design it is essential that fast and inexpensive models are developed that can predict the outcome of DEM models. To unlock the advantages of DEM modelling, first different metamodelling techniques are investigated and validation strategies are discussed. Second, a proof of concept for the use of DEM-based metamodels with a hopper example demonstrates that even for small datasets metamodels can effectively capture the relation between design parameters and equipment performance.

Parts of this chapter have been published in the Journal of Powder Technology, M. P. Fransen, M. Langelaar, and D. Schott, Application of DEM-based metamodels in bulk handling equipment design : methodology and DEM case study, (2021) [55].

3.1. INTRODUCTION

Recent developments in modelling of large scale particle systems and an increase in computing power enable researchers and engineers to model behaviour of bulk and powder handling equipment in increasing detail. A powerful modelling technique for particulate systems is the discrete element method (DEM) [1]. While this method enables detailed modelling it still requires a large amount of computational resources, especially when the number of particles increases. Typically, DEM simulations can take hours or even days for large particle assemblies. Therefore, in modelling bulk handling equipment (BHE) these techniques are typically used to evaluate how small design changes affect the behaviour of the particles in the equipment. This is defined as local optimization and has proven to be a successful approach in development of equipment. However, local optimization is concerned with a specific design and only explores a small section of the design space. Therefore it is likely to miss superior designs that can be found if the entire design space was evaluated. To bridge the gap between local and global evaluation of behaviour of bulk handling equipment, metamodels are an excellent option. These data-driven models of a computationally expensive model such as DEM, which can be used as an inexpensive surrogate. Metamodels can be used at a global level for model approximation, design space exploration, problem formulation, and optimization support [19].

In the past decade the applicability of DEM increased significantly due to the introduction of GPU and parallel computing [7, 56]. Using a GPU results in a speed-up up to ten times [56], which makes it feasible to study large scale industrial systems and complex flows with DEM [9, 57, 58]. Strategies to further increase efficiency of DEM simulations include the use of hierarchical grid [59, 60], stiffness reduction [61] and coarse graining or particle upscaling [62, 63]. Still, there are limits to the speed-up that can be achieved. In design problems the amount of model evaluations is high which makes it computationally expensive despite speed-up measures. Moreover, bulk handling equipment (BHE) behaviour involves structural and kinematic responses for which coupling with numerical methods such as finite element (FE) and multibody dynamics (MBD) is required [64, 65], [66–72]. Such coupling leads to a further increase in computational costs. Therefore, metamodels show great potential in facilitating usage of DEM in bulk handling equipment design procedures.

There are two main types of metamodeling approaches. The first is model fitting (MF) where a mathematical relation between scalar design parameters and key performance indicators (KPIs) is defined. Well known methods for model fitting are response surface methodologies (RSM) [14, 19] and surrogate models [17]. The second approach is reduced order modelling (ROM) [15, 16, 18], where physical phenomena present in the system are modelled in a simplified manner while including spatial and transient information. Common methods in reduced order modelling are projection based reduced order models (PROM) [73], balanced truncation [16], and moment matching [18]. The computational effort required to construct ROM models varies significantly depending on the nature and complexity of the modelled system.

In contrast to their widespread use in other fields, in literature on design of bulk handling equipment with DEM, metamodeling techniques are rarely used. A few related studies for bulk handling can be found within the chemical engineering field. These are focussed on operational parameters rather than on design [74–76]. In this field an increase of the use of metamodels is observed because these models can be included in flow sheet descriptions of chemical processes [77, 78]. A combination of metamodeling techniques with computationally expensive particle based models such as DEM has been applied. Boukouvala [75] focussed on predicting the velocity profiles in a rotating drum by using a reduced order model. Rogers & Ierapetritou [78] suggest integration of reduced order and model fitting metamodels in flowsheets for unit processes in chemical engineering. Barrasso [74] studied the collision frequency in a continuously stirred reactor with a model fitted metamodel based on an artificial neural network (ANN). Furukawa et. al. [79] used response surfaces to map segregation of particles based on DEM data. However, the scale, material properties, and shape of the materials modelled in these studies is far different from the materials used in bulk material handling where irregular shapes and wide, gapped particle size distributions are common.

These studies show the potential of metamodeling in combination with particle based models to predict behaviour of bulk handling equipment designs. Given the high potential of these techniques and the presently limited use for BHE applications, there is need for a metamodel construction or training procedure that ensures that accurate metamodels are obtained for a design purpose. Model fitting and reduced order modelling are difficult to combine in one training procedure. In design of BHE scalar design parameters and KPIs are commonly used. To find a mathematical relation between those, model fitting is the most adequate approach. Therefore the focus of this study is on a training procedure for model fitted metamodels.

Figure 3.1 depicts the proposed framework for the use of DEM-based metamodels. First a DEM object model is developed after characterisation of the bulk handling problem. Instead of directly using this model in optimizing the equipment design, metamodels could be constructed after the DEM model development and before design optimization, as shown in Figure 3.1. Here the DEM model is used to generate training data for the metamodel. The metamodel training procedure is shown on the right of Figure 3.1. This starts with defining the design space and creating a sampling set for which the DEM model will generate the training data. Secondly, a suitable type of metamodel is chosen based on the distribution and expected trends in the data. Thirdly, hyper-parameters of the metamodel, i.e. additional parameters that affect the resulting shape, are optimized to obtain the most accurate metamodel for this data set. Finally, the model is validated using a validation strategy. Together, these steps form a systematic metamodel training methodology. After training of the metamodels is completed, they can be used in design space exploration, analysis, and optimization at low computational cost.

The aim of this study is to present, analyse and demonstrate the steps involved in methodically training DEM-based model fitting metamodels, with particular attention for intricacies related to the behaviour of bulk handling equipment. To illustrate the use of metamodels the training procedure is applied to a hopper design case. In this

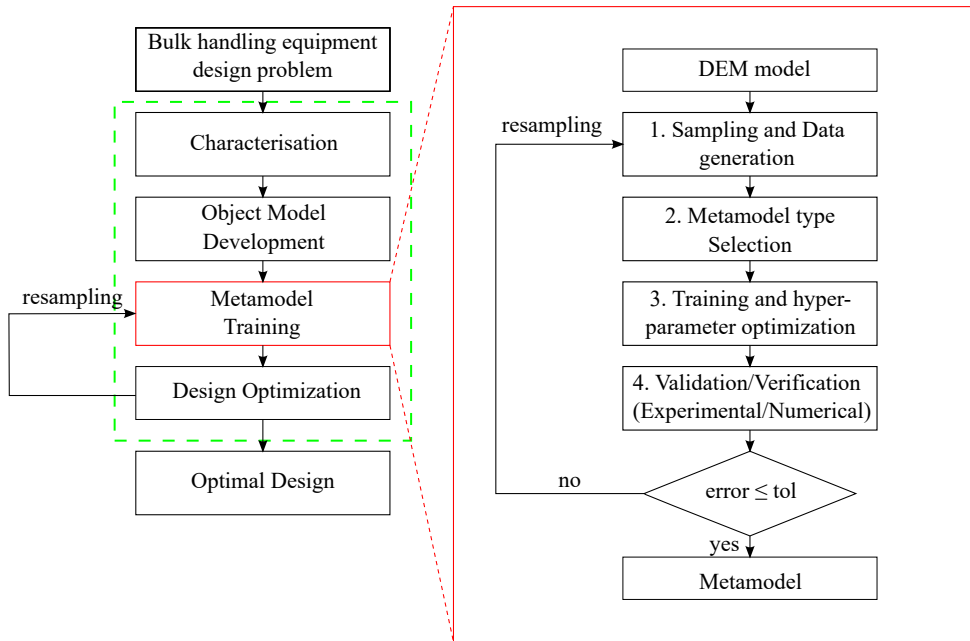


Figure 3.1: Framework for bulk handling equipment design based on metamodeling, with the various steps involved in methodical metamodel training outlined on the right.

case study three common metamodels are evaluated: Polynomial Regression (PR), Radial Basis Function Interpolation (RBF), and Kriging. Secondly, the design space is sampled, the effect of sample size is analysed and data is filtered. Next, the third step involves optimization of the hyper-parameters to obtain the most accurate metamodel. Lastly, in the fourth step the applied validation strategies are the validation set approach (VSA), k-fold cross-validation (K-fold CV) and leave one out cross-validation (LOOCV) with repetitions. Based on the results for these models recommendations for the use of metamodels in design with DEM models are given.

Following this introduction, Chapter 3.2 starts with a general introduction to metamodeling and a detailed description on building a model fitting based metamodel. Additionally, the theory for the three metamodels used in the test case is described. Chapter 3.3 introduces the DEM model of the hopper used in this study and presents the analysis of the generated data. After sampling, hyper-parameter optimization, and validation techniques for the hopper case are evaluated. Subsequently, in Chapter 3.4 the results obtained from the metamodels are discussed, after which Chapter 3.5 presents, the conclusions and recommendations for further research.

3.2. METAMODELLING

3.2.1. SAMPLING AND DATA GENERATION

Development of a MF metamodel starts by identifying the design space in which the metamodel must be valid. The size and bounds of the design space are defined by the limits of the design problem. After choosing a suitable design space the general procedure to obtain training data is to perform a design of experiments (DoE) or design of simulations (DoS) as it is called if one uses a numerical model for data generation. In these processes sampling locations are generated for the defined design space, using methods such as Sobol sampling, Latin Hypercube Sampling (LHS), Hammersley Sequence Sampling (HSS), Monte Carlo Sampling (MCS), or Direct Sampling (DS) [19]. There are many methods to sample design spaces which all have their own benefits and pitfalls. The reader is referred to Pardalos et. al. for further details [80].

The type of method that should be used depends on the desired sample size and properties. However, the sampling set does not have to be generated in one single step. To reduce the computational costs of generating data, the sample set can be gradually expanded by resampling or adaptive sampling [81]. These have become popular methods to find a sufficient sampling while minimizing training data generation costs [19, 82]. Especially in relation to DEM the use of adaptive and iterative sampling has been included in several studies [8, 83]. To sample the design space further, supervised or unsupervised techniques can be used. In supervised adaptive sampling, new points are added based on evaluating the performance of the metamodel for the previous sampling set. Unsupervised sampling is based on adding samples according to a method such as LHS or grid sampling to improve the model by simply increasing the size of the sampling set. However, in case of DEM data, resampling with many iterations might not be convenient. DEM simulations take a considerable amount of time, and multiple resampling steps would increase the duration of sample generation. Therefore, it should be considered how many resampling iterations are acceptable and how many sample points are added in each iteration. It can be more efficient and faster to have fewer iterations with more sample points than adding a single sample point each iteration.

Moreover, it needs to be considered that metamodels tend to behave poorly at the edges of the design space because most metamodeling techniques are not able to extrapolate well. To improve the metamodel at the boundaries, either sample points should be chosen slightly outside of the domain of interest, or one has to densify the training data on the boundaries of the design space such that they are better defined [19]. However, because DEM simulations are computationally intensive densification of the sampling set is inconvenient. Therefore, sampling a space bigger than the domain of interest is the recommended way to ensure sufficient accuracy in boundary regions.

After the data has been generated for the sample set, it must be processed and analysed before continuing with the second metamodel training step. To increase the quality of the sample set the results from the simulations might require an intermediate step where the data is filtered. Invalid and inaccurate simulation results must be identified and removed, so that the metamodel training is not adversely affected by this data. Of course

caution has to be taken when filtering data because there is a risk of leaving out data that is actually representative for the modelled system.

3.2.2. METAMODEL SELECTION

The second aspect of metamodel development is training of the metamodel. For the model fitting approach, this starts at constructing the function space or basis. The functions space contains basis functions such as polynomials, splines, or radial basis functions (RBF) [14, 19]. The chosen basis functions should together be able to represent the trends that are present in the data. Methods such as Kriging [84, 85], Gaussian process regression [86], artificial neural networks (ANN) [74] and radial basis function interpolation (RBFi) are suitable for capturing highly nonlinear trends and flexible in interpolation and filtering of data. A downside of polynomial regression (PR) is that these methods are based on less flexible polynomial basis functions [14]. On the other hand, this reduced flexibility of a polynomial basis can be exploited when dealing with irregular and noisy data, as it can provide a smoothing effect instead of exact interpolation. It must also be noted that compared to the computational expense of generating the DEM data the cost of training a metamodel is low. After defining the function space the task is to find the coefficients of these functions for which the metamodel fits the data best. Well known fitting methods are least squares regression, best linear predictor, log-likelihood, and multipoint approximation. The type of fitting method depends on how the optimal fit is defined and which technique is most suitable to find this fit.

In chapter 3.3 a numerical test case is presented involving two design parameters and two performance parameters. The three metamodels are built based on data obtained from a DEM simulation of a discharging hopper. Considered are a Polynomial Regression (PR), Radial Basis Function Interpolation (RBFi), and Kriging metamodel. These have been chosen because of their common use in engineering practice and because they are regression based, interpolation based, and a combination of interpolation and regression respectively. In the following subsections the foundation of these methods is discussed, including the basis-functions used to construct the models.

POLYNOMIAL REGRESSION

In Polynomial regression a polynomial function is fitted to a set of data points such that a response surface for the design domain is obtained. Even though this is a classical method it is still commonly used in developing response surfaces [87] because of its simplicity and smoothing capability. In this two-dimensional case study a response function f is represented as,

$$f(x_1, x_2) = \sum_{k=0}^m \sum_{l \leq k}^n a_{kl} x_1^k x_2^l \quad (3.1)$$

where x_1, x_2 are the polynomial dimensions and m and n are the order of the polynomial in dimensions x_1 and x_2 , respectively. The polynomial which is fitted to the data consists of multiple terms which each have a coefficient a_{kl} . In the regression process the values for these coefficients are determined by finding the least squares solution of the mean squared error between the reference value and the predicted value of the polynomial in these training points.

RADIAL BASIS FUNCTION INTERPOLATION

Radial basis function interpolation was first presented in [88] and was focussed on representing irregular surfaces with multi-variate functions. In RBF interpolation, a response function is represented by a summation of N radial basis functions $\phi(||x - d_i||)$ located at the training data points, d_i . We consider the commonly used inverse multi quadric radial basis function which is a full rank function which has a high information content,

$$\phi(||x - d_i||) = \frac{1}{\sqrt{1 + (\epsilon ||x - d_i||)^2}} \quad (3.2)$$

Here the $||x - d_i||$ term is the distance from a location x to a training point d_i . ϵ is the shape factor of the RBF and determines the width of the radial basis function. To make the RBFs represent the reference values u_i at the training points the correlation between each RBF must be calculated and the coefficients b_i need to be determined. This results in the following system,

$$\phi_{ij} b_j = u_i \quad \begin{bmatrix} \phi_{r_{11}} & \dots & \phi_{r_{1N}} \\ \vdots & \ddots & \vdots \\ \phi_{r_{N1}} & \dots & \phi_{r_{NN}} \end{bmatrix} \begin{bmatrix} b_1 \\ \vdots \\ b_N \end{bmatrix} = \begin{bmatrix} u_1 \\ \vdots \\ u_N \end{bmatrix} \quad (3.3)$$

which if solved, results in the coefficients b_i . With the coefficients the following interpolation function can be formulated,

$$f(x) = \sum_{i=1}^N b_i \phi(||x - d_i||) \quad (3.4)$$

The predictor function $f(x)$ calculates the correlation between the points x and the training points and by multiplying with the coefficients b_i and summation of all contributions, the function value at locations x is predicted. The resulting function exactly reproduces the reference values at the training points, and smoothly interpolates between those.

KRIGING

A Kriging model is a model based on both regression and interpolation. The concept of kriging has been developed by Krige [89, 90] and finds its origins in geotechnical sciences. Currently there exist many variants and Kriging is a common technique to construct predictive models. A well-known Kriging toolbox is the DACE toolbox [91], which is also used in this study. Kriging is very flexible in fitting nonlinear data trends because the covariances can be tuned by the sample data [14]. The Kriging predictor can be defined as follows

$$f(x) = \sum_{i=1}^k c_i g_i(x) + Z(x) \quad (3.5)$$

and consists of a sum of regression components which are second order polynomials in the first term and a realization of a random stochastic process $Z(x)$ in the second term.

$$Z(x) = \sigma_l^2 \phi(||x - d_i||) \quad (3.6)$$

Here $\phi(||x - d_i||)$ gives the covariances between the training points based on their Euclidian distance and σ_l is the process variance. Similar to RBF, various choices for ϕ

are possible. In the Kriging model in this study the squared exponential Gaussian is used for calculating the covariance between the data points and the points that need to be predicted, given by:

$$\phi(||x - d_i||) = e^{-\theta_i ||x - d_i||} \quad (3.7)$$

Kriging is more computationally expensive than the RBF and PR method because it needs to find a fit for the regression and the interpolation components of the model. Finding a good fit is generally achieved by maximizing the likelihood of the fit which is a hyper-parameter optimization technique that is discussed in the next section.

3

3.2.3. HYPER-PARAMETER OPTIMIZATION

To improve the fit of a metamodel the parameters of the used basis functions can be optimized, commonly called hyper-parameter optimization. For the three models described in this section three different approaches are taken to optimize the parameters. For the polynomial regression model the parameter that needs to be optimized is the order of the polynomial in x and y direction, N_x, N_y respectively. It can be argued that this order should be as high as possible such that the more detail can be captured by the model. However, beside the possibility of overfitting, adding higher orders might result in oscillations in the response surface which decreases the accuracy of the metamodel, also known as the Runge phenomenon. Therefore it is recommended that metamodels based on polynomial regression are checked for these artefacts and base the order of the polynomial on the accuracy of the resulting metamodels. In this case the metamodels are built for zeroth to fifth order polynomials for both design parameters and the optimal coefficients correspond to the combination with the lowest root mean squared error.

In the RBF model the optimization parameter is the support radius c of the RBF. Because the RBFs are located at the training points there will be exact interpolation. The only error at these points is the machine precision error of the system. Therefore the parameters need to be optimized using a different strategy. To identify the error of the metamodel, the RSME is determined by Leave One Out Cross Validation as used by Urquhart et. al. [92]. The support radius c is optimized such that the RMSE is minimized. With this method it must be noted that it is computationally expensive.

The Kriging model which is based on the DACE toolbox [91] uses log-likelihood maximization of the metamodel to determine the optimal shape factor values. In the case of this Kriging model there is a shape parameter for each dimension, θ_1 and θ_2 . The optimization of these parameters is implemented in the toolbox. This approach minimizes the process variance which ensures that the reliability of the metamodel in between the training points is maximized.

3.2.4. METAMODEL VALIDATION

A next essential step is validation of the metamodel. The goal of metamodel validation is to verify their ability to predict values in the design domain. There are three frequently used methods for validation: the validation set approach (VSA), k-fold cross validation

(k-CV), and leave-one-out cross validation (LOOCV) [93]. In each method, the sampling set is divided into a training and validation subset, and metamodel predictions at the validation points based on the training set are compared against the validation values. The three approaches mainly differ in the way the samples are divided. In the VSA the sampling set is divided into a training and validation set according to a user-defined ratio. The k-CV divides the samples into k subsets of equal size which are combined to form k different cross validation sets. Finally, in LOOCV, a validation set consists of one sample point and all the remaining data points are put in the training set. This is repeated for the total number of data points. All three validation methods will be considered in the case study presented in the next section.

The random division of the sampling set in VSA and k-CV introduces some variability in the results, and additional methods exist to improve consistency. One method to mention is stratification, which ensures that the validation and training sets contain data points from every section of the domain. However, use of stratification requires heuristic information on the model. Another method to obtain consistent results from the validation strategies is to repeat the procedure with new randomized divisions. This gives an insight into the stability of the validation error prediction. In both the VSA and k-CV approach common validation set sizes are 10 and 20% of the entire data.

3.3. DEM-BASED METAMODEL TEST CASE: DISCHARGING HOPPER

3.3.1. DEM (OBJECT) MODEL

In this case study the object model used is a semi-two-dimensional silo, shown in Figure 3.2. This model has been built in MercuryDPM, an open source discrete element software package [94]. The material properties that will be used for this study are fictive and only valid for this numerical example. In reality, every bulk material has to be characterized experimentally to find the correct values for its properties. Bulk properties are heavily affected by environmental conditions such as the humidity and temperature. Additionally, the particle size distributions and surface properties can differ between batches of material. As the focus of this case study is on demonstrating the process of constructing a DEM-based metamodel, these complications are not taken into account. The metamodeling techniques described in Section 3.2.2 are applied to the data generated with the object model. For the hopper example the angle α and the discharge opening W_o are the design parameters. The KPIs are the discharge rate and coefficient of variation [50].

MODEL GEOMETRY DESCRIPTION

The geometry of the silo is fixed except for the hopper angle α and discharge opening W_o , which are chosen as the design parameters. A cross section of the silo and its dimensions are shown in Figure 3.2. In order for the silo model to have a feasible geometry the range for the hopper angle α is 10 to 100°. The size of the discharge opening ranges from 15 to 210mm for a fixed silo width W_h of 0.6m as denoted in Table 3.1. The ratio of hopper width

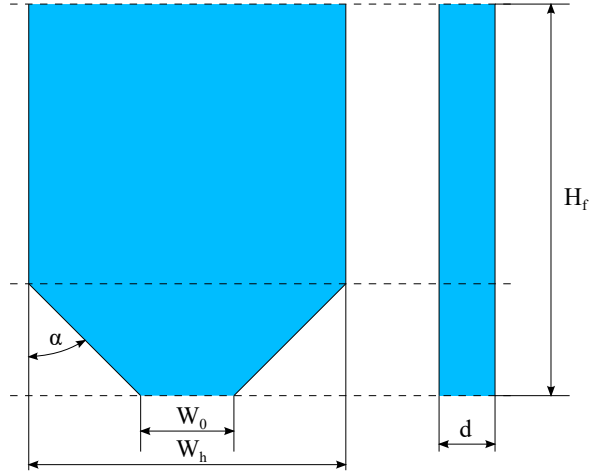


Figure 3.2: The silo geometry used in the DEM model. α represents the angle of the hopper and W_o describes the width of the outlet opening. The silo width is described by W_h , silo depth by d , and the fill height of the silo by H_f .

to discharge opening approximately equals 3 which meets the condition $W_h > 2.5W_o$ set for having constant discharge rate during hopper discharge [95].

MATERIAL DESCRIPTION

The bulk material is modelled by spherical particles for which the particle size is described by a normal distribution with an average diameter of 8 mm and a standard deviation of 2.0mm. Particle sizes in this range are common in bulk handling applications. However, because the time-step size depends on the smallest particle size, the particle size distribution is truncated to the range of 5 to 14mm to limit computation time. The density of the particles is set to 2500 kg/m^3 which is similar to the density of gravels and sands. The bulk stiffness E_b of the material is set at 70MPa and is used to calculate the contact stiffness k following this relation [96],

$$k = \frac{E_b V}{C_n r_{avg}^2} \quad (3.8)$$

where V is the average particle volume, C_n the contact number, for loose packing equal to 4 [97], and the average particle radius r_{avg} of the particle size distribution. The time step Δt is based on the response time t_c of the contact between two particles which is calculated as,

$$t_c = \frac{\pi}{\sqrt{\frac{k}{m_{eff}} - \left(\frac{\gamma}{2m_{eff}}\right)^2}} \quad (3.9)$$

here k is the contact stiffness, m_{eff} is the effective mass of the two copies of the smallest particle, and γ is the damping of the contact. To ensure a stable simulation the time step for integration should be far smaller than the response time, $\Delta t \ll t_c$ [98]. A safe ratio that is commonly used in MercuryDPM for large scale simulations is $\Delta t = \frac{t_c}{10}$ [94].

Table 3.1: Geometric properties silo

Property	Value
α	$10 - 100^\circ$
W_o	$15 - 210mm$
W_h	$600mm$
H_f	$800mm$
d	$5,3 \times 10^{-2}mm$

Table 3.2: Properties of the contact between particle-particle, particle-wall 1, and particle-wall 2.

Property	P-P	P-W1	P-W2
μ_s	0,2	0,5	0,3
μ_r	0,2	—	—
$k_n(N/m)$	$2,93 \times 10^5$	$5,86 \times 10^5$	$5,86 \times 10^5$
$k_t(N/m)$	$\frac{2}{7}k_n$	$\frac{2}{7}k_n$	$\frac{2}{7}k_n$
$\gamma_n(Ns/m)$	0,3	0,3	0,3
$\gamma_t(Ns/m)$	$\frac{2}{7}\gamma_n$	$\frac{2}{7}\gamma_n$	$\frac{2}{7}\gamma_n$

CONTACT MODEL DESCRIPTION

In this study a linear visco-elastic friction contact model has been used to model particle-particle and particle-wall contact [96]. The particle-particle contact is shown in Figure 3.3 and consists of two spring-damper combinations and a figure to represent the friction between the particles. The contact stiffness k has a component k_n in normal and k_t in tangential direction. For the damping of the contact normal and tangential components γ_n and γ_t apply. Friction between the particles is represented by sliding and rolling friction coefficients, μ_s and μ_r . The torsion in this model has been turned off to reduce the complexity of the contact model. The property values for each contact model can be found in Table 3.2. These settings will ensure that in the simulated hopper designs the dominant flow mode is core flow. The contact stiffness of the walls is, P-W1 and P-W2 are set to two times the contact stiffness of the particle-particle (P-P) interaction [3]. Where the side walls (P-W1) have a high friction coefficient of 0,5 and the front and back wall of the hopper (P-W2) have a lower friction coefficient of 0,3. The friction coefficient for the side wall is in the same range found for bonded iron particles on steel [53]. The friction value for the front and back walls is set to a lower value because we assume less friction on this wall. The damping in the entire system is the same for particles and walls and is equal to 0,3 (Ns/m). In this case study we have assumed values for the contact properties. However, these properties can be determined with experiments on a micro scale directly and inversely through macro scale experiments. Examples are the wall friction coefficients by using a shear cell [31] or an inclined surface tester [53] and the bulk modulus and internal shear angle by means of a compression test.

SIMULATION SETTINGS

Before the start of the simulation the silo is filled by a randomized particle generator while the outlet remains closed. After starting the simulation the particles are allowed to settle

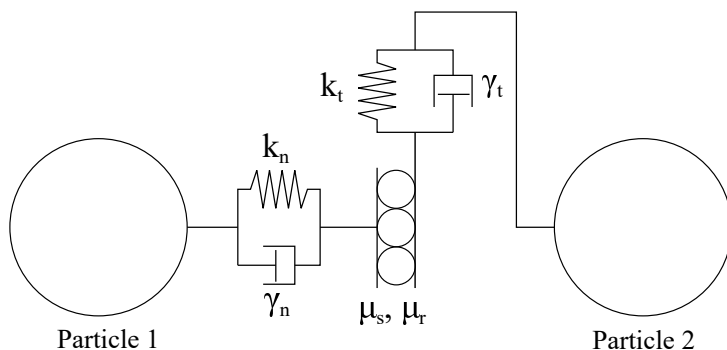


Figure 3.3: Description of the normal, tangential, rolling, and sliding contact between the particles which is also used to model particle-wall contact

and at $t = 1,5s$ all particles above the fill height are removed. The fill height is $0,8m$ which ensures that the discharging time of the silo is sufficient for analysis of the granular flow. At $t = 1,6s$ the outlet opens and allows particles to discharge from the hopper. The total simulation time is set to 25 seconds to ensure that for all configurations emptying of the silo is achieved. A stopping criterion has been added to the model which stops when the ratio between the kinetic and elastic energy becomes smaller than 10^{-6} . This stopping criterion ensures that simulations are stopped when the flow of material stopped or the hopper is empty. Therefore unnecessary simulation steps are prevented. For stability of the simulation the time step is set to $8,7 \times 10^{-6}s$ which is equal to the contact time divided by ten, $t_c/10$.

3.3.2. DEM DATA ANALYSIS

The DEM simulations provide particle location and velocity information which are used to identify material flow characteristics in the hopper. In this case study the mean discharge rate ϕ and the coefficient of variation ψ of the discharge rate are used as the KPIs of the hopper. These values are calculated by using the method described by [50]. The average discharge rate coefficient of variation is determined in the steady flow region of the discharge as shown in Figure 3.4. The data obtained from the simulations is filtered after determining the KPIs where the training points which have no flow are removed from the dataset.

3.3.3. SAMPLING

We assume that there is no prior knowledge on the behaviour of the DEM model. Therefore, it is desired to get a uniformly distributed sampling set which covers the design space equally. To obtain this set, the Sobol sampling technique is used because one of its properties is that it produces a highly uniform sampling of the domain. The design space which ranges from 20 to 90° hopper angles and 25 to $200mm$ discharge opening sizes is the desired domain. In order to obtain sufficient samples near the boundaries, the design space ranging from 10 to 100° hopper angles and discharge opening sizes of 15

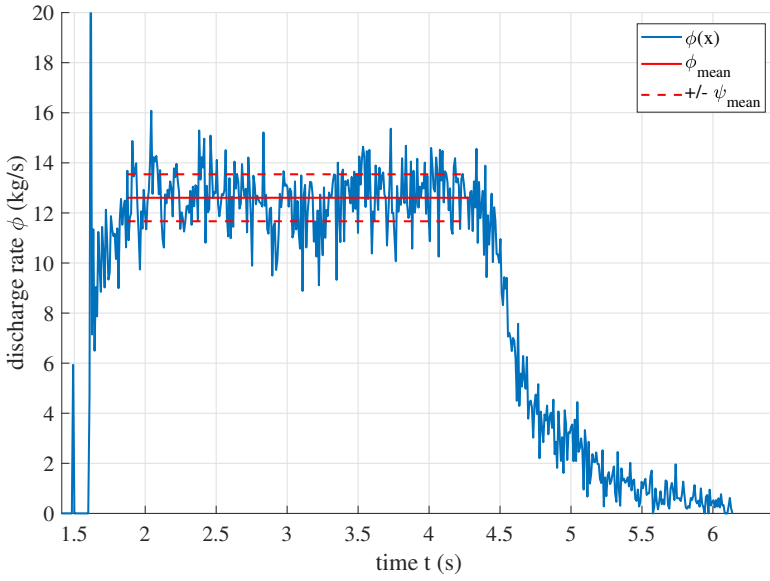


Figure 3.4: Discharge rate versus time obtained from simulations data, red line is the average discharge rate and the red dotted lines represent the CoV

to 210mm. Covering this with 100 samples results in 72 interior points and 28 exterior points, as shown in Figure 3.5.

3.3.4. HYPER-PARAMETER OPTIMIZATION

In general it is difficult to manually determine the appropriate values of the hyper-parameters of the basis-functions which will result in an accurate metamodel. Therefore optimization of these hyper-parameters as described in 3.2.3 is an important step in metamodel construction. To demonstrate the effect these hyper-parameters have on the resulting metamodels a set of metamodels with predefined hyper-parameter values and a set with optimization hyper-parameter values are compared. Our aim is to highlight, by means of this example, that hyper-parameter optimization is important to construct high quality metamodels. In the case study initial models have been built with the set of hyper-parameter values shown in Table 3.3. Here, N_1 and N_2 are the order of the polynomials, c is the value for the shape factor of the multi-quadric radial basis function, and θ_1 and θ_2 are the shape factors of the basis functions of the Kriging model for the two design parameters.

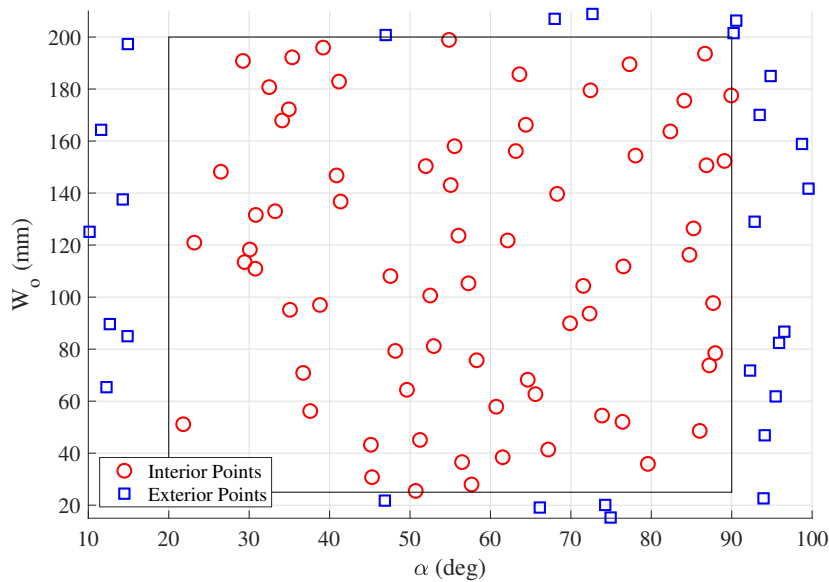


Figure 3.5: Distribution as a result of Sobol sequence sampling.

Table 3.3: Initial parameter values used without hyper-parameter optimization

	Optimized pa- rameter	Discharge rate ϕ	Coefficient of variation ψ
PR (polynomial order)	N_1, N_2	2, 2	2, 2
RBF1 (Inverse multi-quadric)	c	1	1
Kriging (Hyper-parameter correlation function)	θ_1, θ_2	1, 1	1, 1

Table 3.4: Validation strategies and applied settings

	Training set	Validation set ϕ	Number of iterations
VSA 10%	90%	10%	1
VSA 20%	80%	20%	1
k-CV 10	90%	10%	10
k-CV 5	80%	20%	5
LOOCV%	N-1 data points	1 data point%	N

3.3.5. VERIFICATION

For the metamodels in this paper the VSA, k-CV, and LOOCV validation strategies are performed where the root mean squared error (RMSE), given as

$$RMSE = \sqrt{\frac{\sum_{i=1}^N (f - f^*)^2}{N}} \quad (3.10)$$

between the metamodel predictions and validation values is used as the error measure. For the VSA a 20 and 10% validation set size of all data points is evaluated. For k-CV the values $k = 5$ and $k = 10$ are used which means an equal subset size of 20 and 10% respectively. Both the approaches are repeated ten times to take the effect of random subset generation into account. The LOOCV method has to be run only one single time because it is deterministic, but consists of $N = 80$ individual validations. In Table 3.4 the sizes of the training and validation sets are shown for each method and the number of iterations that are included in the validation strategy.

3.4. RESULTS

3.4.1. DEM SIMULATION RESULTS

The data for training the metamodels has been obtained by running simulations with the model described in Section 3.3.1. The system used to execute the simulation sample is a DELL Precision 5820 with an Intel Xeon W-2223 CPU @ 3.60 GHz x 8 cores. The whole set of simulations took around 28 days in serial mode using all 8 cores. The average simulation time was 53,8 hours. However, the simulation time is geometry dependent. A simulation with a large discharge opening and low hopper angle is faster than one with a small discharge opening and high hopper angle. In Figure 3.6 (a) a screenshot of a discharging hopper with an angle $\alpha = 47,6^\circ$ and a discharge opening $W_o = 108,1 \text{ mm}$ is shown. With the current wall friction settings and this specific combination of angle and discharge opening core flow is observed in the hopper. Moreover, on the left and right side of the hopper stagnant zones are visible where the particle velocity stays zero during discharge. Figure 3.6 (b) shows the hopper with an angle $\alpha = 45,3^\circ$ and a discharge opening of 30,8 mm which results in arching of the material in the hopper and consequently no flow. The total number of simulations is 100 corresponding to the Sobol sampling of the design space shown in Figure 3.5. With the simulation data, the discharge rate and coefficient

of variation (CoV) have been calculated and are used for all the models in this section. The simulation results are shown as data points and contour plots in Figure 3.7 with the discharge rate in (a,b) and the coefficient of variation in (c,d). These performance parameters are essential in hopper design, because in general the aim is to achieve continuous flow with low CoV [29]. In the figures the data points are denoted by dots. The black dots (80 data points) represent silo designs where there was flow in the silo, whereas the red dots (20 data points) represent the designs which have no flow. In this case study the aim is to develop metamodels that can predict flow conditions of hopper designs with a discharge rate of 2 kg/s and up. To avoid the steep transition from no-flow to flow regime, based on this analysis the model is trained only for the data points having flow and is only valid for discharge rates higher than 2 kg/s .

As seen in Figure 3.7 (a), the discharge rate increases monotonically with the discharge opening W_o . Along the α -axis the hopper angle is shown where the data seems to follow a more constant level. This indicates that the discharge rate mainly depends on the size of the discharge opening and that the hopper angle has a limited effect. This is in line with the theory on hopper flow by Schulze [29]. In Figure 3.7 (b) the data in (a) is represented by a contour plot where the isolines show the same trend. Moreover, in the 25 to 60mm zone for all angles the transition from flow to no-flow is visible by the change from black to red dots. Decreasing the size of the discharge opening causes the formation of arches in the hopper. These arches continuously collapse until they become stable at the transition from no-flow to flow. This can also be seen in the CoV which increases when the discharge opening becomes smaller. To prevent arch formation in designs a minimum discharge opening is used which is equal to 8-10 times the average particle size [29]. We use a truncated particle size distribution with an average particle diameter $r_{avg} = 10,2 \text{ mm}$. Using the lower bound of 8 times, would result in a discharge opening of $81,6 \text{ mm}$ which safely ensures flow of the material even above the 2 kg/s threshold as can be seen in Figure 3.7 (b).

In Figure 3.7 (b) a dependency of the discharge rate on the hopper angle is visible by a curve shape in all isolines. In the transition area between 50 and 70° hopper angles and above the 150 mm discharge opening a shift in discharge behaviour is observed where discharge rate for 9, 11, and 13 kg/s isolines show a move in the upward direction which is different from the smoother curves at lower discharge rates. This behaviour can be explained by the behaviour at the walls for the lower hopper angles. In the hopper model a wall friction coefficient, $\mu_{p,w_1} = 0,5$, between particles and wall is defined which corresponds to a wall friction angle of $26,6^\circ$. We would expect that sliding of the material along the wall will stop or decrease at hopper angles $63,4^\circ$ and higher. When the angle stays below $63,4^\circ$ the wall friction force is likely to be lower than the force exerted by the particles on the wall, which enables flow along the walls. If the hopper angle becomes higher than $63,4^\circ$, stagnant zones will form which shifts the sliding interface from particle-wall to particle-particle and therefore changing the flow behaviour.

Figure 3.7 (c) shows the data points for the second KPI, the coefficient of variation ψ for the discharge rates in Figure 3.7 (a). The fluctuations in the discharge rate show a different dependency on the design parameters than the discharge rate. However, the

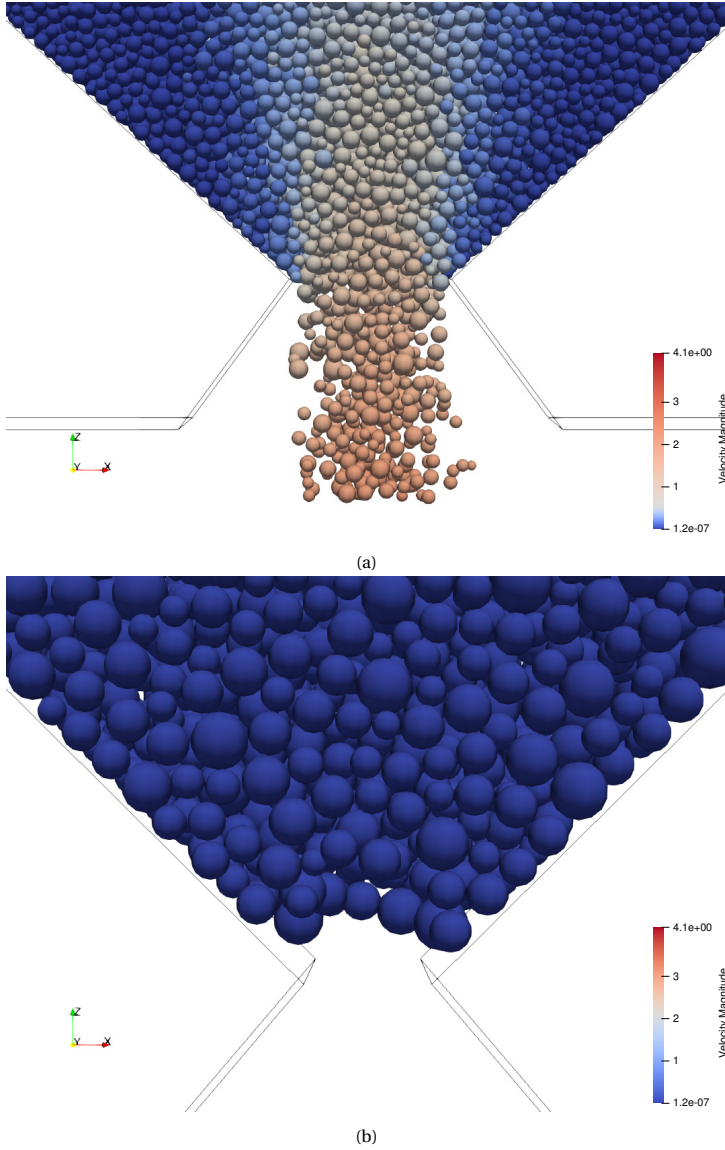


Figure 3.6: DEM simulation stills (a) Core flow hopper discharge ($\alpha = 47,6^\circ$, $W_o = 108,1mm$) and (b) an example of no flow due to arching ($\alpha = 45,3^\circ$, $W_o = 30,8mm$)

Table 3.5: Optimized Hyper-parameters

	Optimized pa- rameter	Discharge rate ϕ	Coefficient of Variation ψ
PR (polynomial order)	N_1, N_2	5, 5	5, 5
RBF (Inverse multi-quadric)	c	2, 05	4, 09
Kriging (Hyper-parameter correlation function)	θ_1, θ_2	(7, 98), (10, 16)	(4, 19), 19, 04

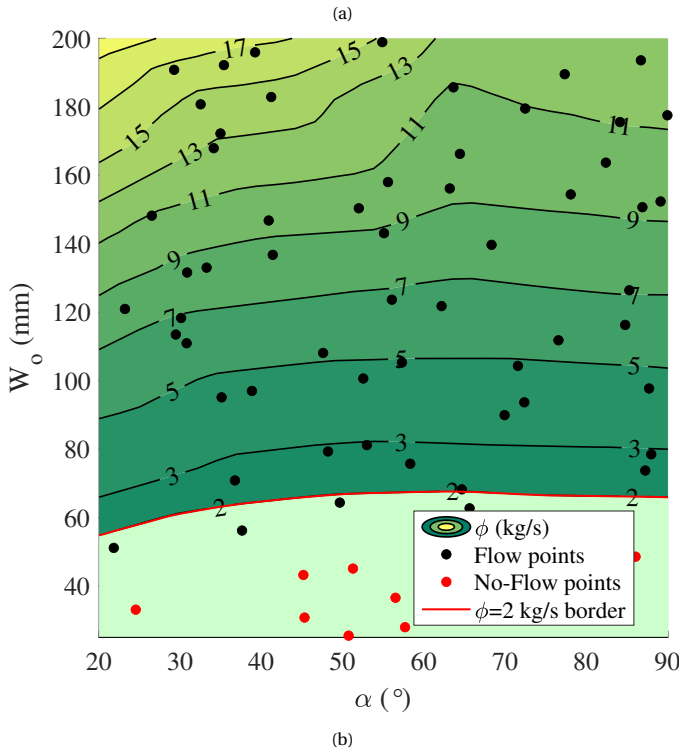
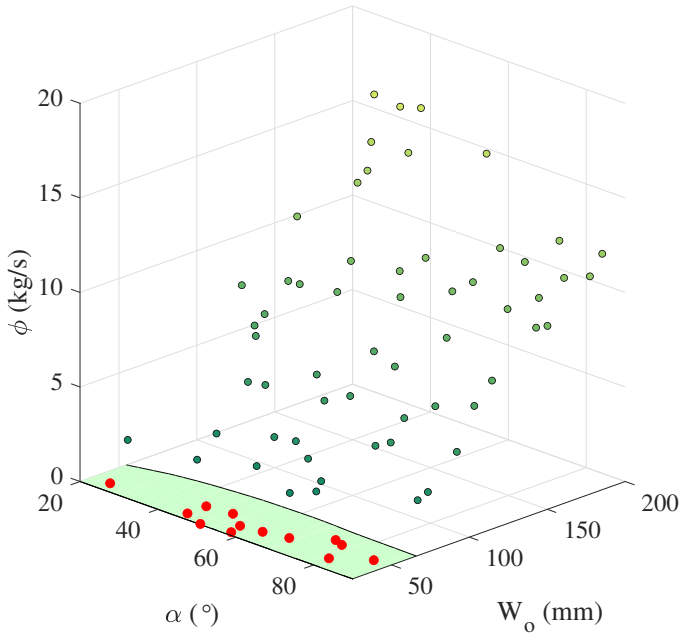
area in Figure 3.7 (b) depicting the change in flow behaviour also shows changes in the CoV because of the accumulation of isolines in that area. As with the discharge rate this can be attributed to the change from particle-wall to particle-particle interface. Based on the CoV data it can be seen that for angles below the transition area the CoV becomes lower and therefore the discharge rate becomes more stable. In the transition area the CoV starts to increase for increasing hopper angles which results in unstable discharge. In the 60 to 150mm region we can see a valley in which the CoV increases when the discharge opening becomes smaller for all angles although at a different rate. With smaller discharge openings and at higher hopper angles the flow becomes less stable.

3.4.2. EFFECT OF HYPER-PARAMETER OPTIMIZATION

In Figure 3.8 the three metamodels for the discharge rate without hyper-parameter optimization are shown. The PR metamodel in Figure 3.8 (a) has been built with a second order polynomial for the two design parameters. This figure shows a curved surface fitted through the data, which is below the data points for a hopper angle between 45° and 90° and lies above the data points for lower angles. The ability of a PR model to fit to the data highly depends on the trends in the data, distribution of samples over the design space and the order of the polynomial [19]. In Figure 3.8 (b) and (c) the RBF and Kriging metamodels are shown where irregularities in the surface are present between 150 and 200 mm and hopper angles between 50° and 70° and for the Kriging model we see fluctuations at the 50 mm and 20° point. These undulations present in the RBF and Kriging metamodel might be caused by the inappropriate values for the shape parameters of the basis-functions. Concluding, with polynomial regression a smooth surface is obtained. The RBF and Kriging models in (b,c) show more local fluctuations when the distance between data points increases but are capable of capturing both the nonlinear behaviour at smaller discharge openings and the global trend of the dataset.

The metamodels based on the CoV data are shown in Figure 3.9. In Figure 3.9(a) the PR metamodel shows that the fit of the polynomial surface is able to capture the trend of the data on a global level but the regression function is not able to capture local detail in the data set. The RBF and Kriging models show the same behaviour as with the discharge rate. Several fluctuations are visible along the 200 mm line for all angles as well as for the 20° line, which indicate that the shape parameter is too small to capture the actual curve.

To obtain the best possible metamodels, hyper-parameter optimization was carried out



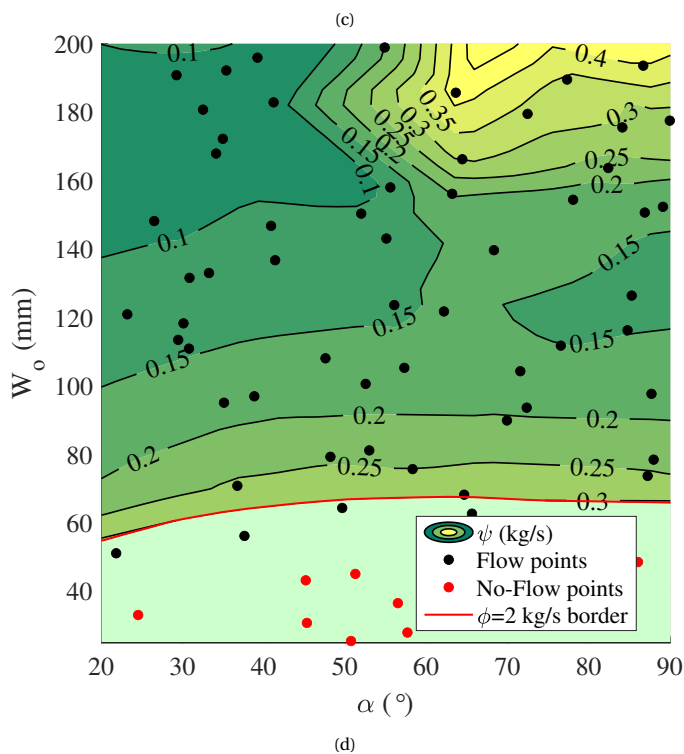
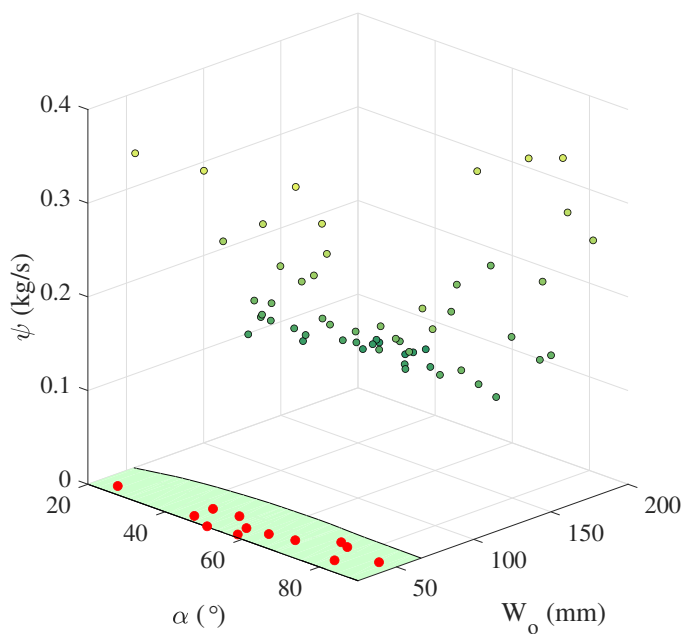


Figure 3.7: Results of discharge rates ϕ with (a) the data points and (b) a contour plot, coefficient of variation ψ results in (c) 3D plot of data points, (d) contour plot.

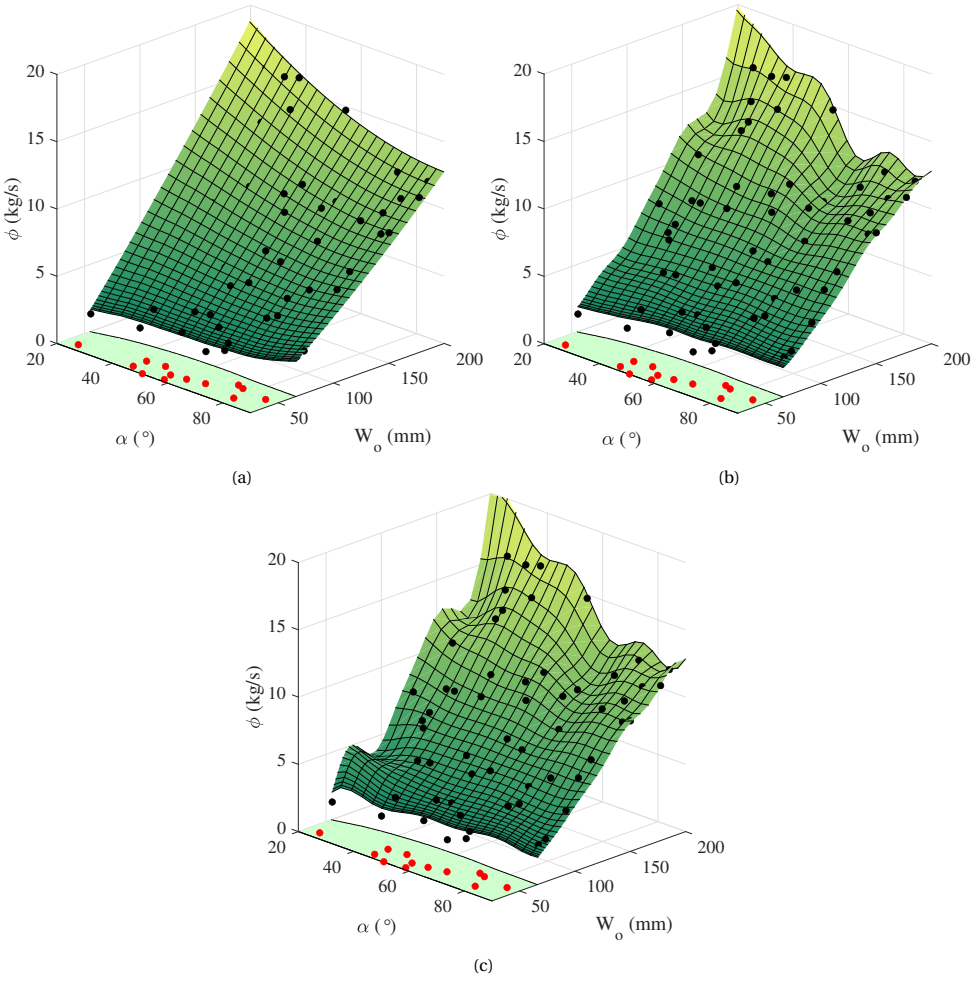


Figure 3.8: Metamodels without hyper-parameter optimization for the average discharge rate (a) Polynomial Regression (b) Radial Basis Function Interpolation (c) Kriging

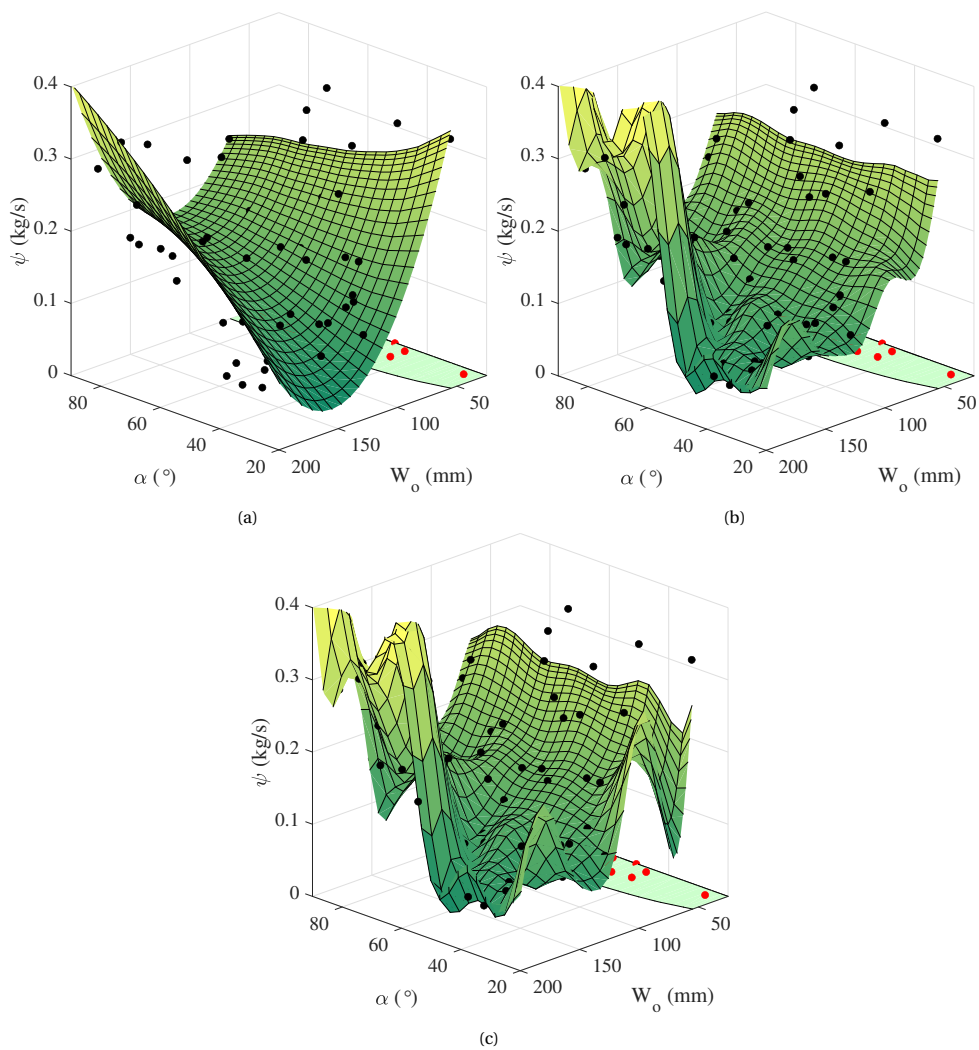


Figure 3.9: Metamodels without hyper-parameter optimization for the coefficient of variation (a) Polynomial Regression (b) Radial Basis Function Interpolation (c) Kriging

for 50 random initial guesses where the best performing parameter values were chosen as the optimal hyper-parameter values Table 3.5. For the PR metamodel it was found that the fifth order polynomial should be used for both design parameters and the KPIs. The optimal RBF shape parameter of the CoV is larger than the one for the discharge rate, because of the presence of flat areas in the CoV surface, which requires an RBF with a larger radius. For the Kriging model we can see the same behaviour as for the RBFs, where a smaller value for theta results in a narrow Gaussian whereas a larger value gives a wider Gaussian. Unlike the RBF, the Gaussian has two shape parameter values for each performance parameter, one in the direction of each design parameter.

Using the results of the hyper-parameter optimization, new metamodels have been trained for the hopper data set. Figure 3.10 shows the results for the discharge rate, together with the data points. While based on the same data, the three models are different compared to the default metamodel results. The higher order polynomial enables the PR metamodel to fit better to the trend in the data. With the RBF and Kriging metamodels, the fluctuations in the surface are reduced or absent. All three models show a transition zone for large discharge openings ($>150\text{mm}$) and angles between 50° and 70° . However, the PR model is less able to describe this transition zone compared to RBF and Kriging models because it is less capable to capture local changes in the trend.

The dataset containing the CoV at the data points and the corresponding metamodels are shown in Figure 3.11. All metamodels are able to capture the global trend. However, the PR model is not able to capture the local changes in the data set but produces a smooth trend surface. In addition, at the 20° and 200mm point the PR model will predict negative CoV values which are infeasible. The RBF and Kriging models do show a more irregular surface but are able to capture the local behaviour better. The effect of hyper-parameter optimization on the resulting metamodels can also be achieved by adjusting the hyper-parameters through trial and error until the quality of the model is maximised. However, hyper-parameter optimization with the described methods is far more efficient and will become even more convenient when the number of design and performance parameters increases.

To a certain extent, metamodels are able to predict the behaviour of the discharge rate and CoV within the bounds of the design space. It needs to be realized that all models developed on a data set need to be evaluated on their ability to predict the actual behaviour. In the case of low dimensional problems it is possible to visualize the data but when the dimensionality increases this becomes more difficult. Therefore, quantitative measures are required, which will be discussed in the following section.

3.4.3. METAMODEL VALIDATION

The validation strategies introduced in Section 3.2.4 have been evaluated to determine the accuracy of the PR, RBF, and Kriging metamodel in predicting values at unknown design points. The three models used to evaluate the validation strategies are trained with the optimized parameters presented in Table 3.5 using the percentages of the 80 sample dataset denoted in Table 3.4. All the strategies have been repeated 10 times to get

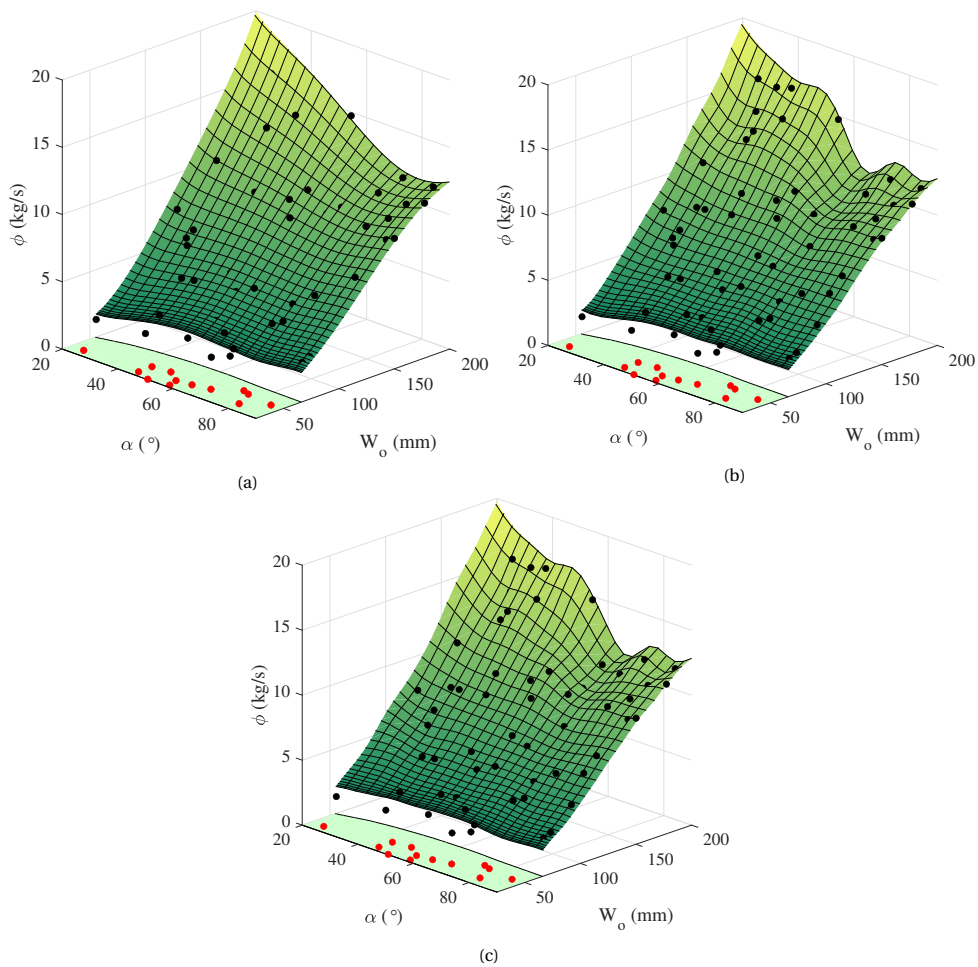


Figure 3.10: Metamodels for average discharge rate (a) Polynomial Regression (b) Radial Basis Function Interpolation (c) Kriging

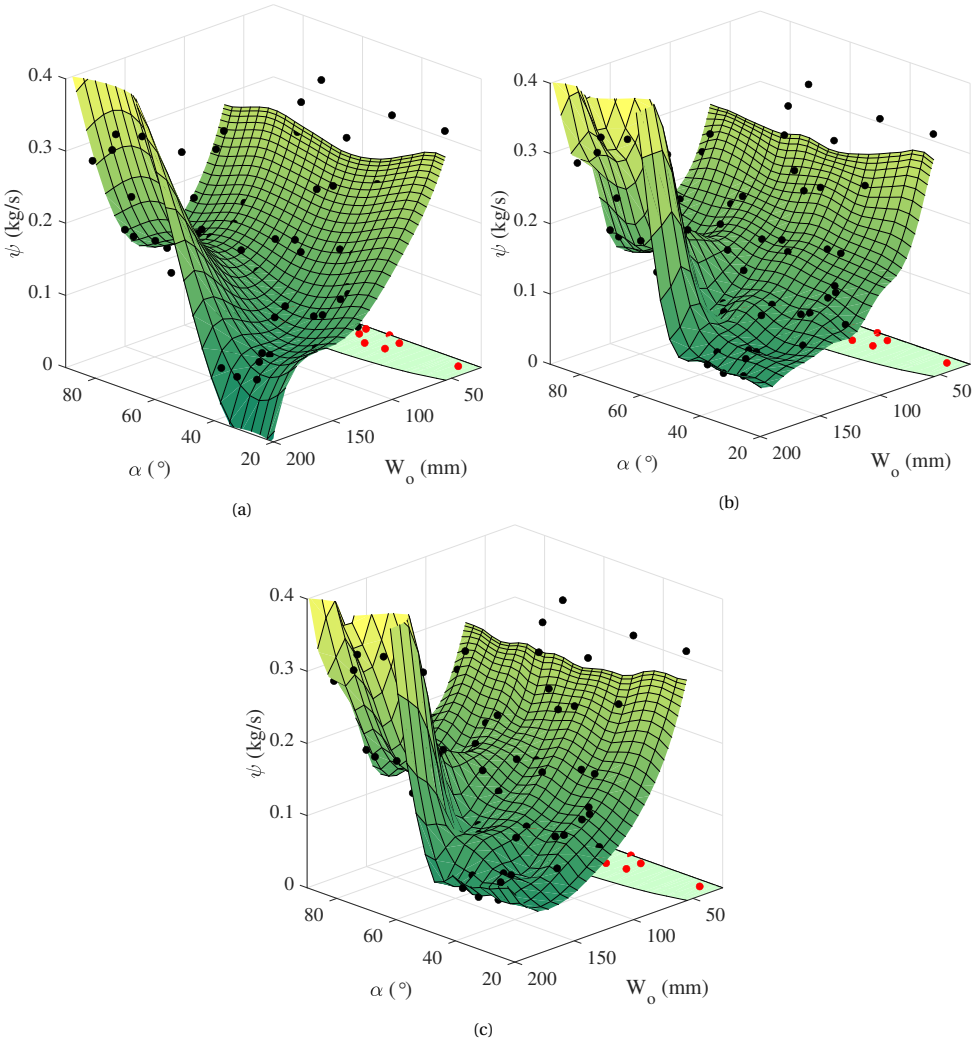


Figure 3.11: Metamodels for the coefficient of variation (a) Polynomial Regression (b) Radial Basis Function Interpolation (c) Kriging

a measure on the reliability of the measured errors. All of these strategies give insight on how well the metamodels performs at predicting KPI values at new design points.

The bar charts in Figure 3.12 and Figure 3.13 show the average RMSE between the validation set values and the metamodel predictions for the discharge rate and coefficient of variance, respectively. As a results of the 10 repetitions the variance of the average RMSE can be shown. For the discharge rate results in Figure 3.2 it can be seen that for the VSA and kCV approaches the prediction error is in the order of 4 to 7,5% and for the LOOCV is below 0,2%. In terms of the variance it can be seen that it is nearly absent for the LOOCV approach but that it is larger for the VSA approach then for the kCV approach. For the CoV results in Figure 3.13 we see that the average error is much higher and ranges from 15 to 20% which can be explained because the trends in the CoV data are more complex than those in the discharge rate data. If data near the validation points is not included in the training set it becomes more difficult to predict, especially when the behaviour is non-linear. For the LOOCV approach we see a small error of at most 1,5%. In terms of variance the same effect can be observed as with the discharge rate where the variance of the VSA approach is higher than the kCV variance. Results for both KPIs show that prediction errors are large if a data set of 72 (90%) or 64 (80%) points are used. This suggests that additional data points should be generated.

As mentioned, the major difference that can be observed for both results is that the variance of the kCV approach is smaller than of the VSA approach. This indicates that the kCV approach is more reliable in giving insight on the validity of a metamodel than the VSA approach. Compared to the kCV and VSA approach the LOOCV shows that the errors given by the metamodels is very small. Here it is important to consider that with the LOOCV approach more data points are used for training a metamodel compared to the kCV and VSA approach. As a consequence, if the ratio between number of validation points and training points becomes too small the effect of leaving one data point out will reduce and therefore lead to low validation errors.

To evaluate the validation error the LOOCV method can be used if the training data set is small, in the order of 50 data points. For larger data sets one should use the VSA or kCV approach where the kCV approach gives the most reliable validation error. In terms of time consumption the LOOCV approach is the most expensive looping through all the data points. Next is the kCV approach which uses k iterations in determining the validation error, therefore computational expenses increase with k . Followed by the VSA approach which only evaluates the validation error of a single division of the data into a training and validation set. With respect to DEM-based metamodels the computing time of these validation errors is irrelevant due to the cost of DEM-data generation. Evaluating metamodels by multiple validation strategies leads to a more complete insight on their accuracy and allows a designer to make a better choice for the type of metamodel that is going to be used.

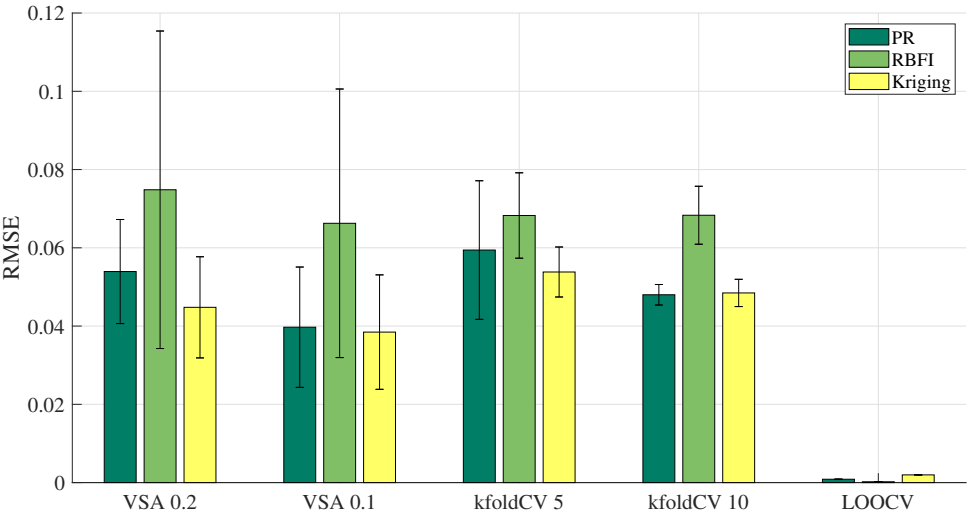


Figure 3.12: Validation strategy errors for the discharge rate ϕ

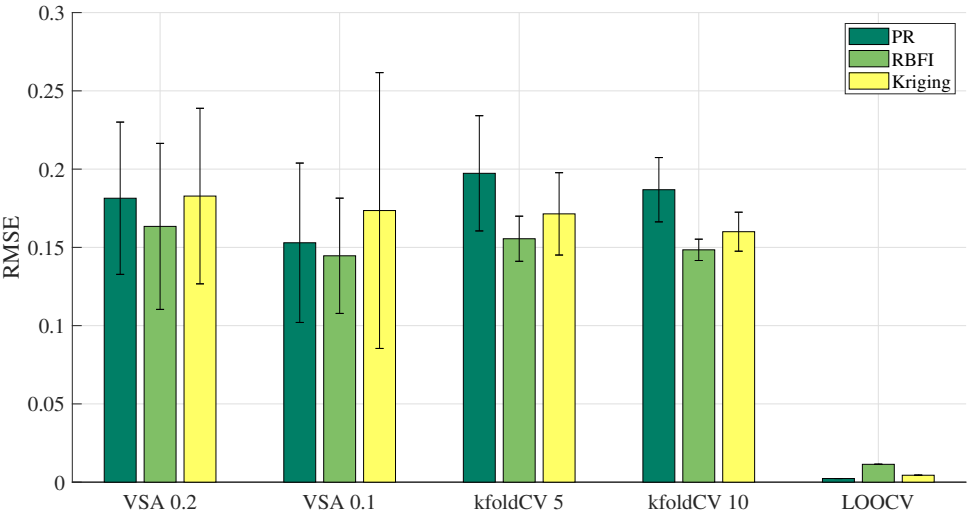


Figure 3.13: Validation strategy errors for the coefficient of variation ψ

3.4.4. EFFECT OF SAMPLE SIZE ON ACCURACY

Generating DEM data is computationally expensive, therefore insight on the effect of sample size on the quality of the metamodel is required. To study the effect of sample size on the RMSE of the metamodel we gradually build the three models by increasing the sample size from 1 to 80 by 1. These 80 samples are the points in the data set representing material flow. After each increase in sample size a training set is drawn from the full dataset to train the three models, using the metamodel training procedures discussed in 3.2.2. To avoid any bias of the order of the subset, this process has been repeated 1000 times where for each repetition the order of the subsets is changed randomly. Finally, the average RMSE is calculated. In Figure 3.14 the development of the averaged RMSE is shown for the Polynomial Regression, RBF, and Kriging metamodels of both the discharge rate and CoV.

Note that some models cannot be built beneath a certain sample size. The PR metamodel uses a 5th order polynomial fit, which can only be determined when more than 21 data points for a two-variable problem are available because that equals the amount of coefficients. However, [14] suggests that the amount of samples should be at least twice or three times the amount of coefficients of the polynomial to obtain accurate metamodels. Building an RBF model is already possible from a single sample. However, low sample numbers will not lead to representative metamodels. The Kriging model built with the DACE toolbox requires a minimum of 5 data points for training based on the number of undetermined coefficients for the second order regression part of the model. For the RBF and Kriging models it can also be seen that the error goes to zero at a sample size of 80. This occurs because both RBF and Kriging have almost exact interpolation at the data points, therefore the error in the data points is at machine precision.

Figure 3.14 (a) and (b) show that in all models the error reduces for increasing sample sizes. For the discharge rate, the Kriging model performs better over the entire range compared to the PR and RBF models. It can be observed that the RBF model outperforms the PR model over the entire range but performs similarly at a sample size of 50 data points. The results for the coefficient of variation data show that the PR model is not able to get an accurate prediction of the CoV while, both the RBF and Kriging model show a large increase in quality when the sample size increases. Note also that the PR fit quality with lower sample numbers shows a larger standard deviation, indicating a stronger dependence on the selected design points.

For DEM-based metamodels it is essential to know the amount of samples required to reach a certain quality level of a metamodel. This depends on the accuracy that is required for the prediction of mean performance parameters. Table 3.6 shows the number of points required to reach a 2 and 5% error of the model. The PR model only reaches the 5% error limit for the discharge rate but is not able to get to 2%. The RBF and Kriging model perform similar and are able to reach the thresholds with this dataset. However, the Kriging model requires less data points to reach the 5% and 2% threshold than the RBF model for the discharge rate. For the CoV they require the same amount of data points. The better performance of the Kriging metamodel can be related to the basis of training the model which is minimizing the global process variance of the Kriging model

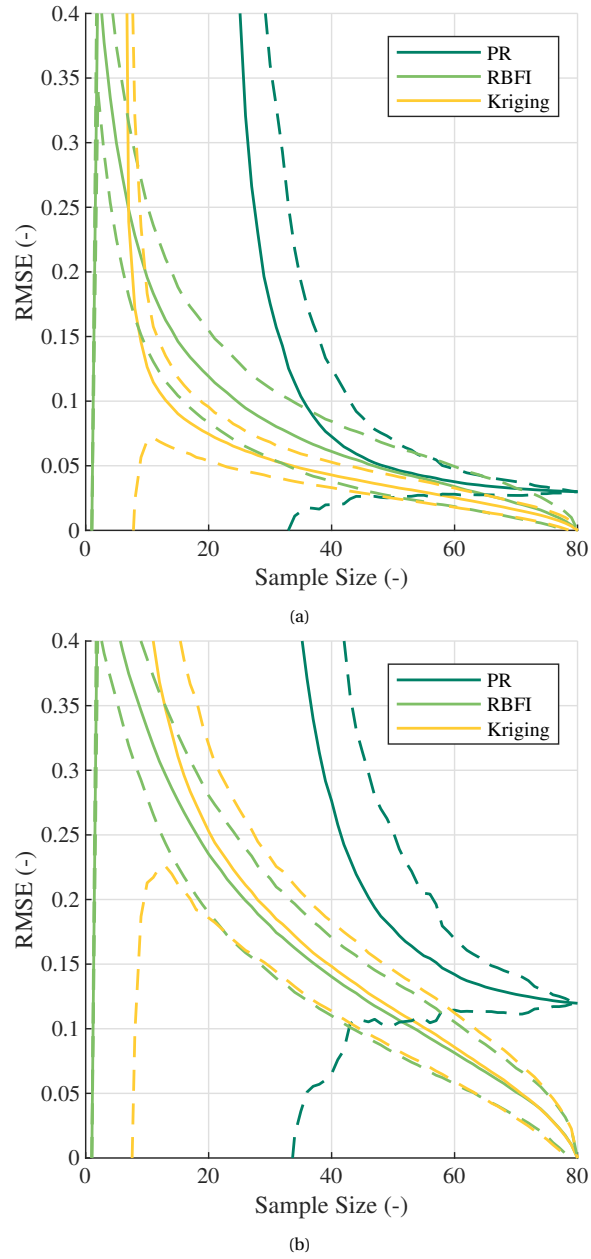


Figure 3.14: The effect of sample size on the RMSE of the metamodel (a) averaged RMSE vs. sample size for the discharge rate (b) averaged RMSE vs. sample size for the coefficient of variation where in both figures the dashed lines represent the standard deviation

whereas for the RBF model the error in the data points is used which does not imply global optimality.

Based on the results of this test case it is advised to start with a sufficient sample size of 50 data points and gradually expand the amount of data points until the desired quality is reached. However, this number changes when the number of design parameters and KPIs changes. If the dimensionality (number of variables) increases the sample size should be increased accordingly to maintain a sufficient sampling density. To determine if more points need to be added the effect of sample size should be used. The process of expanding the sample set is referred to as adaptive or sequential sampling in literature [19, 81]. In the case of DEM-based metamodels the time required for generating data is much higher compared to training, validating, and updating of the metamodel itself. Therefore an approach where some time is invested in determining the quality of the metamodel based on the sample size before additional simulations are started is most efficient.

3.4.5. SUMMARY OF FINDINGS

The three metamodels used in this study showed that hyper-parameter optimization is an essential step for obtaining accurate metamodels, regardless of the metamodel type. Hyper-parameter optimization can be performed on a trial and error basis but automatic hyper-parameter optimization is preferred.

The results in this section show that it is necessary to determine which data is useful and relevant before building a metamodel. Filtering or excluding specific data might lead to more accurate metamodels but caution has to be taken because the data set may become less representative for the process.

In order to acquire accurate metamodels a representative error measure should be used to assess the quality. The results show that the use of k-fold CV gives reliable information on the validity of the metamodels. A single metamodel type that fits all datasets is not found which makes it worthwhile to test several metamodels and even have a different type for each performance parameter. Although this is time consuming the time spent is small compared to the time spent on developing the DEM model and generating the data through simulations.

To determine if the size of the sampling set is sufficient the effect of sample size and the validation error should be evaluated. Based on these errors the need for more data can be determined. To start metamodel construction, a sufficiently large data set should be trained to have a basis, in this hopper case study with two design parameters this is 50 data points. In additional resampling steps the size of the sampling set can be expanded.

The results for the three metamodels used in this case study showed that the Polynomial Regression model was the least accurate model and could not reach validation errors less than 3% for the discharge rate and 12% for the CoV. The Kriging model performed better for the discharge rate than the RBF model while both models performed nearly identical for the CoV. Therefore, unless a particular polynomial trend is expected, RBF

Table 3.6: Minimum amount of data points required for 2 and 5% accuracy levels

Discharge rate ϕ	PR	RBF	Kriging
2%	-	75	70
5%	45	45	32
Coefficient of variation ψ	PR	RBF	Kriging
2%	-	78	78
5%	-	70	70

and in particular Kriging should be preferred for their efficiency and generality. A 5% error for the discharge rate was reached with a small amount of data points whereas the models for the CoV required at least 70 points. Based on the results it can be seen that increasing complexity of the trends in the data requires larger data sets if accurate metamodels are desired.

3.5. CONCLUSIONS

In this study a methodology for constructing DEM-based metamodels has been presented and demonstrated on a case study. Different metamodels were trained and the effect of hyper-parameter optimization, sample size, and validation strategy was analysed for the first time in context of DEM. From this study it can be concluded that DEM-based metamodels can aid in revealing and understanding trends in the performance of bulk handling equipment in relation to selected design parameters, at acceptable computational cost. In using metamodels combined with DEM it is not advised to universally apply one single type of metamodel. The behaviour of performance parameters might match certain metamodel types better than others. Moreover, metamodel training is far less computationally demanding compared to the DEM data generation phase. Therefore it is advised to evaluate several types of metamodels and use the most adequate type for each performance parameter. To further increase the quality of metamodels hyper-parameter optimization should be applied to obtain the best possible metamodel for a given data set.

As a proof of concept, we analysed and validated the application of three model fitting metamodeling techniques using a representative BHE example: polynomial regression, radial basis function interpolation, and Kriging, and showed the ability of these methods to capture the discharge behaviour and the coefficient of variation of a silo in a wide design space. In this study the Kriging model performed best in predicting the discharge rate whereas the Kriging and RBF models were better in predicting the coefficient of variance. Polynomial regression showed the strongest smoothing behaviour, which may be desired in case of noisy datasets. The overall results show that metamodels based on these techniques provide an sufficiently accurate representation of the bulk handling equipment behaviour for use in the equipment design process.

In relation to the design of BHE it is essential that metamodels with high accuracy can be trained for small or limited data sets because of the computational burden of DEM simulations. In this study the focus was on obtaining accurate predictions for average performance values. However, in bulk handling processes the behaviour of bulk material is stochastic by nature. Therefore, further research is required in training of metamodels including stochastic data such that this information can be included in exploring design options.

4

INCLUDING STOCHASTICS IN METAMODEL-BASED DEM MODEL CALIBRATION

In the design process for bulk handling equipment it is essential that the models used are accurate and reliable. For discrete element models this means that they need to be calibrated. The common method of calibration focusses on the mean behaviour of the material or equipment. Although this is practical the behaviour of granular materials is inherently stochastic and should be included. In this chapter a study is presented that includes stochastic behaviour of granular materials in the calibration process. Building on the findings in Chapter 3 [55], the stochastic behaviour of the bulk material is included in the metamodels used in calibration. The presented calibration procedure is validated experimentally and shows that including the stochastics improves the accuracy of the DEM model. These results show that there is a large potential for including the stochastic behaviour in other steps of the design process for bulk handling equipment such as robust design optimization.

Parts of this chapter have been published in the Journal of Powder Technology, M.P Fransen, M. Langelaar, D.L. Schott, Including stochastics in metamodel-based DEM model calibration, (2022) [51].

4.1. INTRODUCTION

To design reliable bulk handling equipment (BHE) engineers and researchers rely on particle-based models to predict the performance of a new design [99]. The discrete element method (DEM) is used to model granular materials and analyse a wide range of related applications. Accurate predictions can only be made if the input parameter values such as friction coefficients and material properties are chosen adequately. To this end, calibration with experimental findings is typically used. However, granular processes are stochastic by nature leading to random results if repeated. This stochastic behaviour is caused by the large variety of particle shapes, sizes, and particle packing compositions in granular systems.

4

In current calibration approaches the DEM parameters are optimized to ensure that the mean values for the performance parameters are matched to the calibration targets [2, 100–102]. However, the mean calibration approach accounts only marginally for the stochastic nature of granular processes originating from distributions of particle shape, size, and microstructural composition. Alternatively, an iterative Bayesian filtering framework in combination with analysis of stress dependency paths can be used to minimize the variance of the solution and obtain more accurate calibration results [8, 83]. In this study the initial packing of the bulk material was known through X-ray tomography and exactly represented in the DEM model. In practice, this information is usually available which means that we generally assume random initial packings and repeat experiments to obtain mean and standard deviation values. Experiments for calibration and validation are commonly repeated 3–5 times. This number seems arbitrary because the mean and standard deviations of key performance indicators (KPI) may not have converged to a stable value with this number of repetitions. Additionally, if mean and standard deviations are used in developing BHE designs the common approach is to work with confidence intervals based on standard deviations. For reference, in case of three repetitions the 95% confidence interval with a t-distribution is equal to 1,837 times the standard deviation which approximately induces a 6,5 times wider confidence interval compared to a factor 0,284 when experiments are repeated 50 times. Even though this number of repetitions is not feasible in practice, this study can be used as a reference for a suitable number of repetitions.

Moreover, with increasing irregularity of particle shapes and sizes the variance in experiments increases. Therefore, in experiments with granular materials it is not uncommon to have relatively high standard deviations when material becomes more heterogeneous. For the quartz sand calibration experiments, Derakshani reports standard deviations of 2,64% for the sandglass test with three repetitions [103]. For the gravel calibration experiments with three repetitions, standard deviations between 0,5 and 4% of the mean KPI values for the lifting cylinder, shear box, and drop down test were reported [102]. For wood chips reported standard deviations range from 3,44% to 6,45% for the Angle of Repose and 3,85% to 7,41% for the Angle of Slip [104]. The subsequently tested wood chip feeding system resulted in a standard deviation of 4,5% for eight repetitions. In large scale applications like the grab validation study on spherical iron ore pellets by Lommen resulted in a 2% error for the payload with three repetitions [11]. Another grab validation

study for cohesive iron ore reported a standard deviation of the average payload of 5,74% for three repetitions [105]. Combined with the confidence intervals this leads to 95% confidence intervals of up to $\pm 10,5\%$ around the mean in the discussed cases. In design of bulk handling equipment, these confidence intervals are generally too high to obtain reliable designs. Therefore, the effect of repetitions on the reliability of experiments with bulk materials is investigated in this study.

Ideally, the DEM model should exhibit the same stochastic behaviour as observed in reality. This requires that the stochastics are included throughout the development of the DEM model. To the author's knowledge, stochastic behaviour of granular processes is rarely included in calibration except for a recent study using random initial packing [10]. Therefore, we propose including the stochastic behaviour in a metamodel which is subsequently used to predict mean and variance in the calibration. To include the stochastics in a metamodel there are two options. Firstly, two individual metamodels are trained for the mean and variance as was demonstrated by [14], here we use a noiseless Gaussian Process Regression (GPR) metamodel which results in a metamodel based on exact interpolation. Secondly, a noise included Gaussian Process Regression metamodel which includes the KPI variance in the noise term [86]. The GPR model has been previously used in a DEM calibration context of bulk material [106]. Furthermore, a mean-variance calibration approach is proposed which includes the variance of the calibration experiments in the objectives of calibration procedure. In mean-variance optimization of DEM parameters, the focus of the optimization algorithm is to find parameter values for which both mean and variance match those of the experimentally obtained targets. In contrast, mean calibration only focusses on finding parameter values for the mean of the targets. In this paper, the noiseless GPR is referred to as the interpolation-based metamodel (IBM) and the noisy GPR is referred to as the Regression-based metamodel (RBM). Both these metamodeling approaches are used and compared for mean and mean-variance calibration of DEM parameters. In addition, we study the influence of the number of repetitions on the obtained calibration results.

We apply the aforementioned approach to a gravel case study where three material parameters are calibrated using a pile forming test, ledge test, and bulk density test. The parameters that are calibrated are the sliding and rolling coefficient, and the particle density. The calibration results are applied to a DEM model of a hopper and the resulting discharge rate is compared to the experimental equivalent. This case study is chosen because of the good measurability of the KPIs and their frequent use for calibration in this field.

The experimental setups in the case study and analysis are described in Section 4.2. The experiments are followed by the development of the DEM models of the experimental setups in Section 4.3. Next, Section 4.4 introduces the metamodeling approaches and the mean and mean-variance calibration, which are demonstrated with the previously described experiments. The results of the calibration and a comparison between the interpolation-based and regression-based metamodel calibration and the proposed mean-variance calibration and mean calibration is given in Section 4.5. Lastly, this work ends with conclusions and an outline for further work on this topic.

Table 4.1: Wall-Gravel interaction properties

	mean μ_s	var $\sigma(\mu_s)$
Gravel-Stainless steel (impact)	0,523	0,05
Gravel-Stainless steel (sliding)	0,456	0,044
Gravel-Acrylic (sliding)	0,446	0,0965

4.2. EXPERIMENTAL METHODS AND MATERIALS

The goal of DEM calibration is to obtain a set of DEM parameters such as friction coefficients and material properties for which the KPI obtained from an experiment is matched to the KPI from a DEM model of the same experiment. In this study, we use the bulk calibration approach (BCA) in which small scale calibration experiments are used to determine the DEM parameters. These calibration experiments provide well-isolated macro properties of the granular material, the KPIs. Ideally, for each DEM parameter an calibration experiment with a specific macro property is desired [4–6]. In general, the behaviour of granular material in calibration experiments is assumed representative for the behaviour of the material in large-scale bulk handling applications. In this study three calibration experiments, a pile forming test, ledge test, and bulk density test are used which are discussed in Section 4.2.1. After finding the DEM parameter set these values are applied to a DEM model of a large-scale hopper model for which the numerical results are compared to the experimental results of the hopper setup described in Section 4.2.2. Analysis of the experimental results to obtain the calibration (pile forming, ledge, and bulk density test) and validation (hopper) KPIs can be found in Section 4.2.3. The results for these experiments are presented in Section 4.2.4.

In this case study gravel is used which is categorised as dry cohesionless bulk material similar to the gravel used in previous studies [102, 106]. The particle size distribution (PSD) of this material was found using a Haver and Boecker sieve shaker tester which resulted in a normally distributed PSD with an average radius of 5,02mm and a standard deviation of 1,39mm. The particle density was measured with a submerged mass density test and averages on 2313,4 kg/m^3 for ten repetitions.

The experimental setups consist of a combination of stainless steel or acrylic plate material which can have three types of wear. The wall-particle interaction properties have been measured with an inclined surface tester for 25 particles on the wall material and their wear state. These wear states are stainless steel with wear due to sliding, stainless steel and impact wear, and acrylic with sliding wear. The stainless steel with sliding wear is the state of the wall of the bulk density tester. The stainless steel with impact wear is present in the hopper due to the pounding of the particles on the walls during filling. The acrylic with sliding wear is present in the shear box test, pile-forming test, and in the front and back walls of the hopper. The sliding friction properties have been shown in Table 1 and shows the mean and variance values for the experiment. In the DEM models of the experiments the mean value of the friction coefficient is used.



Figure 4.1: Laboratory scale tests (a) Pile forming test (b) Ledge test (c) Bulk density test

4.2.1. LABORATORY SCALE EXPERIMENTS

The calibration experiments are a pile test, ledge test, and bulk density test as shown in Figure 4.1 (a,b,c). The KPIs are the Angle of Repose (AoR) β , Angle of Movement (AoM) θ , and the bulk density ρ_b obtained from the pile, ledge, and bulk density test respectively. These experiments have been selected because they are representative for different aspects of the final application. The pile-forming test resembles the kinetic behaviour of the material exiting the silo and the formation of the pile beneath the silo. The ledge test is representative for the movement of the material along stagnant zones when the hopper is discharging. The bulk density test is a representative test for the filling of the hopper. The pile forming test consists of an elevated structure from which gravel is dropped in a container enclosed consisting of acrylic plates, Figure 4.1 (a) and Figure 4.2 (a). The acrylic plates have a wear profile corresponding Gravel-Acrylic (sliding). The

top container is filled up to 110 mm with gravel after which the bottom plate is removed. This starts the flow of material through the orifice of the top container. Consequently, the material fall on the bottom plate of the lower container and a pile starts forming. After the formation of the pile, a camera is used to photograph the sidewall of the container. This photograph is later used to determine the angle of repose, β .

The ledge test is a container with a retractable sidewall, Figure 4.1 (b) and Figure 4.2 (b). The container has acrylic walls which have the wear properties of Gravel-Acrylic (sliding). At the edge, the container has a ridge of 2x20 mm covering the entire trailing edge of the container. This ensures that when the sidewall is retracted that there is a stable base of gravel. The container is filled up to 214 mm with gravel after which the sidewall is retracted. After retracting the wall, the material starts to flow which continuous until a stable slope is left in the container. Of this pile a photograph is taken which is analysed to obtain the angle of movement, θ .

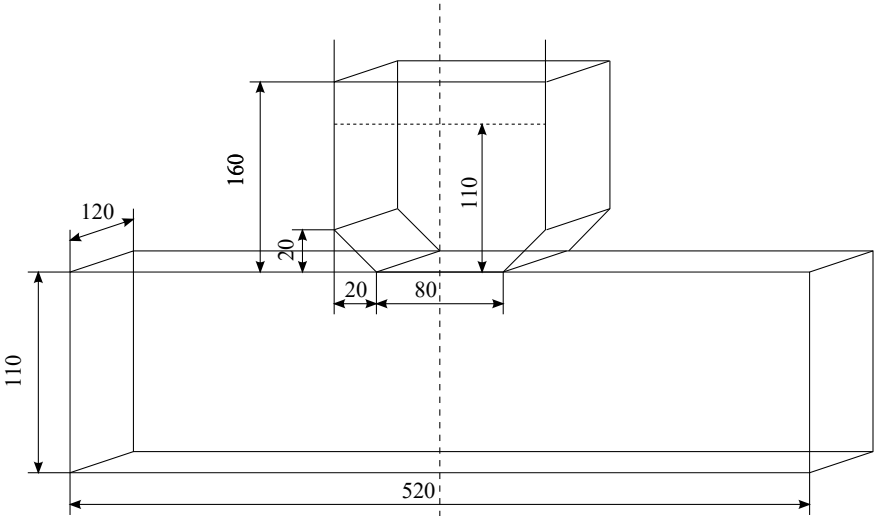
The bulk density test involves a cylindrical container with a radius of 82 mm and a height of 237 mm, the bulk density cylinder ISO 17828 (EN 15103), Figure 4.1 (c) and Figure 4.2 (c). It has a volume of 5 litres with a 0,2% error. Due to the repetitive use of the container the material has wear properties corresponding to Gravel-Stainless steel (sliding). First the empty cylinder's weight is measured with a scale (Kern EMS 12K.01). Next, it is filled with gravel until the upper edge of the tester is reached and weighed again to obtain the mass of the bulk.

4.2.2. LARGE SCALE HOPPER EXPERIMENT

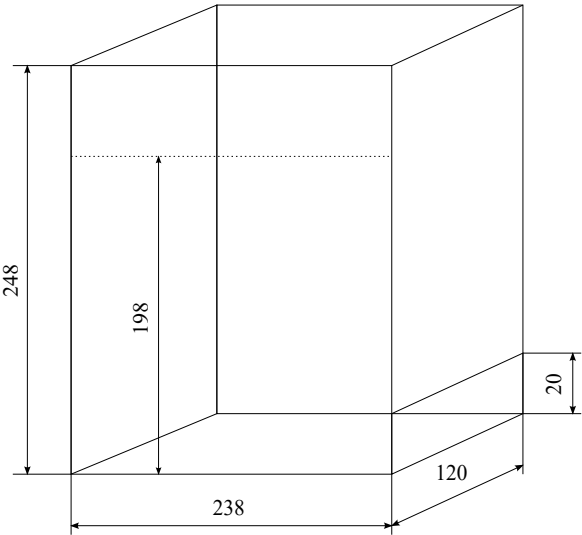
The semi-two dimensional hopper setup is shown in Figure 4.3. The hopper walls are connected to an aluminium frame. The sidewalls of the hopper have worn due to impact which lead to a pitted surface (Gravel-Stainless steel (impact)). These sidewalls are enclosed in the front and back by 5 mm acrylic transparent plates which have been subjected to sliding wear. The angle of the hopper walls is 45° and the size of the discharge opening is 100 mm. The width of the silo is 602 mm and the depth is 50 mm. At the bottom of the hopper a steel bar held by electromagnets closes the orifice of the hopper. To commence discharge of the hopper the steel bar is released by turning off the magnets using a switch. To measure the weight of the bulk material in the hopper the entire structure is positioned on load cells (AEB8D Shear Beam Load cell from AE sensors). The signal of the load cells is sent to a data acquisition box (Texas Instruments) and processed using Labview to a data file. The weight data is measured and stored at a frequency of 50 Hz during the discharge of the hopper. Due to the scale of this setup the number of repetitions is set to five, this number is sufficient because discharge rates are time averaged values which lead to more stable results in the case of a steady-state flow.

4.2.3. ANALYSIS EXPERIMENTAL RESULTS

The KPIs of the pile forming and ledge test are determined by analysis of the pictures of the experiments. This analysis follows the same procedure in both experiments, therefore the analysis is only discussed for the ledge test. First, the distortion of the pictures is



(a)



(b)

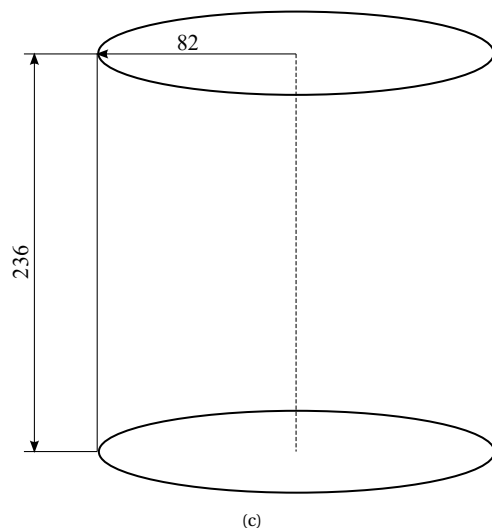


Figure 4.2: Dimensions of the experimental setups (a) pile forming test, (b) ledge test, (c) bulk density test, with dimensions in millimetres

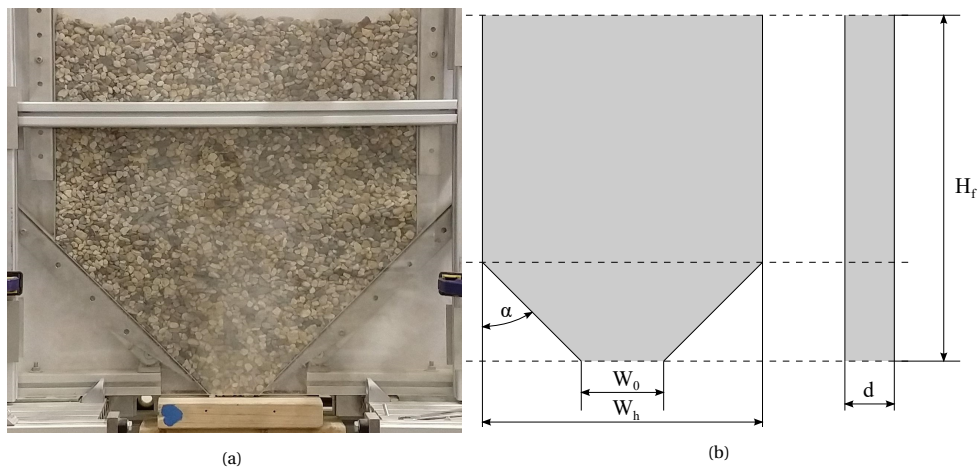


Figure 4.3: Experimental setup for the large scale hopper

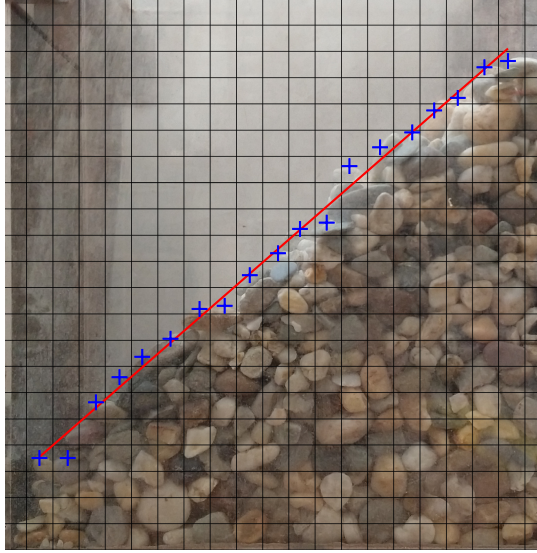


Figure 4.4: Image of a ledge test result where the blue crosses are placed on the edge of the pile and a linear regression (red line) is applied to find the angle of movement. This procedure is the same for the pile-forming test to determine the angle of repose.

corrected after which a square grid is layered over the pictures as shown in Figure 4.4. This grid has equal spacing in both directions and is equal to two times the average particle radius obtained from the PSD. In the squares along the material edge the particle with the highest location is identified. This is a manual process which comes with errors because of the analyst determining the points, by using squares this error is minimized and the relative distance between points is kept similar. The highest locations are denoted by the blue crosses in Figure 4.4 and are used as the input for a linear regression analysis to find the angle of movement. Based on the angles from all experiments the mean and variance of the Angle of Movement are determined.

The bulk density is determined by dividing the bulk mass in the container measured with the scale by the volume of the container. As we have repeated all the laboratory scale experiments 50 times the distribution of the data can be analysed, especially if the data is normally distributed. Therefore, the Lilliefors test is used to determine if the data from the experiments is normally distributed. These tests turned out to be positive for a 5% significance level which means that the data from the experiments is normally distributed. Based on these observations we can proceed with mean and mean-variance based calibration. The data obtained from the large-scale hopper experiment is the evolution of the force exerted on the hopper by the material sampled at a frequency of 50 Hz. From this data the discharge rate as a function of time can be determined using linear regression as illustrated in Figure 4.4. Assuming that the constant force fit divided

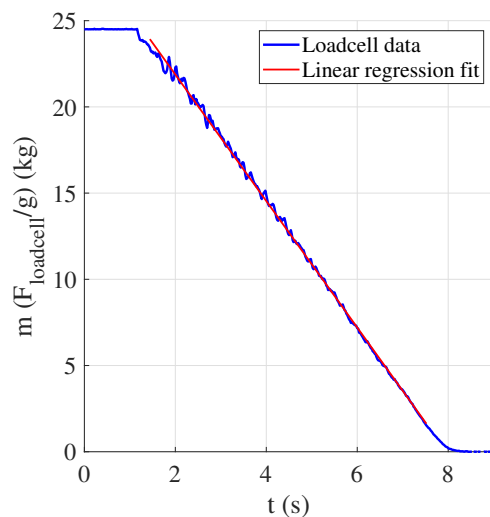


Figure 4.5: Linear regression fit to the load cell data, the slope of the fit is the discharge rate of the mass flow in the hopper.

by the gravity constant leads to an average discharge rate in kg/s . For each large scale hopper experiment the steady state discharge rate ϕ is calculated. The mean discharge rate and its variance are calculated for the five repetitions of the experiment.

4.2.4. EXPERIMENTAL RESULTS

The experiments for the Angle of Repose, Angle of Movement, and bulk density have been repeated 50 times. On these datasets, a Lilliefors test has been applied to determine if these datasets are likely to be normal with 95% confidence. For all three sets it was found that the data is normally distributed which justifies including the confidence intervals in the analysis of the experimental results. In Figure 4.6 (a,c,e) we can see the way the mean value and 95% confidence interval (CI) of the angle of repose, angle of movement, and the bulk density of the material develops when the number of repetitions increases. In addition, the $\pm 1\%$ boundaries are given which indicate the relative size of the error in the mean value. As we can see, the mean stays within the 1% boundaries after the number of repetitions increases over 29 for the angle of repose. The angle of movement reaches a stable bandwidth of $\pm 1\%$ around the 41.5 degree angle after nine repetitions where it leaves this bandwidth once at 30 repetitions. For the bulk density we see that the mean is in the 1% bandwidth after three repetitions. However, the mean stabilises when 20 repetitions are reached. The 95% CI of the mean is determined using the t-distribution for a number of repetitions lower than 30 and using the z-distribution for numbers higher or equal to 30 assuming that the central limit theorem holds. Based on the confidence intervals we can say that at 50 repetitions the true mean of the AoR is within 2,2% of the mean with 95% certainty. For the AoM this is equal to within 1% and for the bulk density

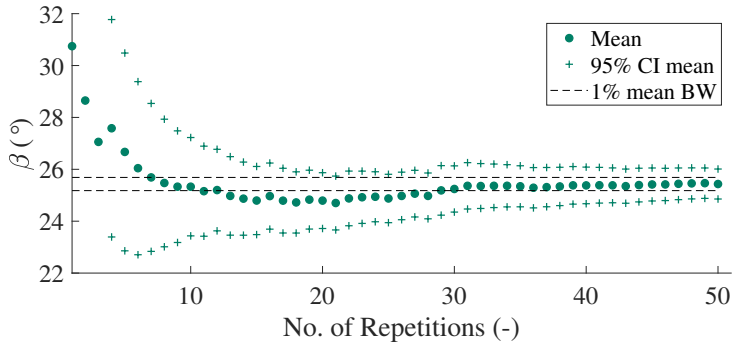
Table 4.2: Calibration targets for the Angle of Repose, Angle of Movement, and bulk density for 50 repetitions and the validation target for the discharge rate for 5 repetitions.

Calibration Targets	KPI	No. of experiments	Mean \pm CI 95%	Standard Deviation \pm CI 95%
Pile test	β_e ($^\circ$)	50	25,43 \pm 0,58	2,09 \pm (-0,24;+0,48)
Ledge test	θ_e (deg)	50	41,40 \pm 0,36	1,38 \pm (-0,36;+0,31)
Bulk density test	ρ_{be} (kg/m^3)	50	1473,1 \pm 3,0	10,94 \pm (-1,88;+2,52)
Validation Target				
Hopper test	ϕ_e (kg/s)	5	3,68 \pm 0,029	0,025 \pm (-0,011;+0,030)

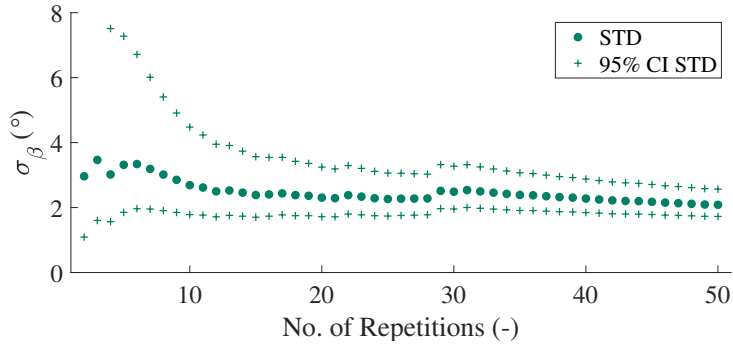
within 0,2%. In the calibration procedure described in Section 4 we assume that both the calculated mean and standard deviation are the true values. Therefore, we use these values as the calibration targets. The CIs are only used to indicate the reliability of the experimental results.

In Figure 4.6 (b, d, f) the standard deviations and their 95% CI are shown. For the AoR and AoM stabilisation of the standard deviation can be observed after 15 repetitions but for the bulk density it keeps declining with the number of repetitions. For the CI of the standard deviation the chi-distribution is used to account for the sample size. Observing the confidence intervals, it is visible that for low numbers of repetitions the confidence intervals for the angle of repose and bulk density are much wider than for a high number of repetitions. These observations indicate the necessity of having sufficient repetitions in calibration experiments for irregular shaped and randomly packed bulk materials.

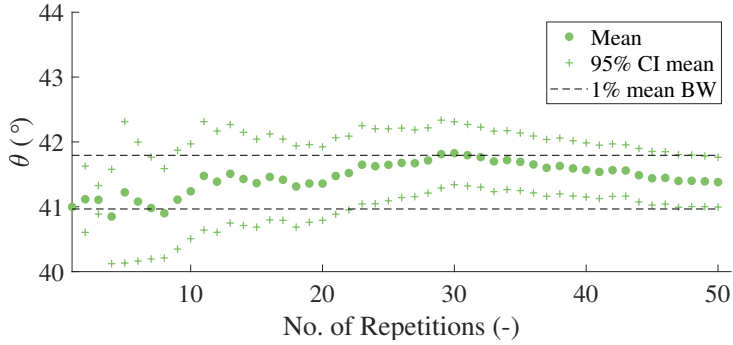
In this case study the effect of increasing the number of repetitions in a dataset on the calibration and validation result are evaluated. However, for conclusions regarding the most accurate calibration approach the entire dataset of 50 repetitions will be used. In these cases, it is also important to notice that one can consider the standard deviation relative to the mean. These calibration targets are shown in Table 4.2. It is found the standard deviation is 8,2% for the Angle of Repose, 3,3% for the Angle of Movement, 0,74% for the bulk density. These percentages show that the variability of each calibration differs significantly. This can be explained by the nature of the calibration experiments. In the bulk density test a container is filled with material which is very confined and restricts high velocity movement of the particles. Hence an experiment that will have less variability. In the ledge test a container is filled as well but when the sidewall is removed the material starts moving. Moreover, the sliding interface in the ledge test causes higher variability of the angle due to the changing orientation of the particles in each repetition of the experiment. In the pile-forming test the material falls from the container on a free surface where the orientation and high velocity of the particles results in a higher variability of the experimental result.



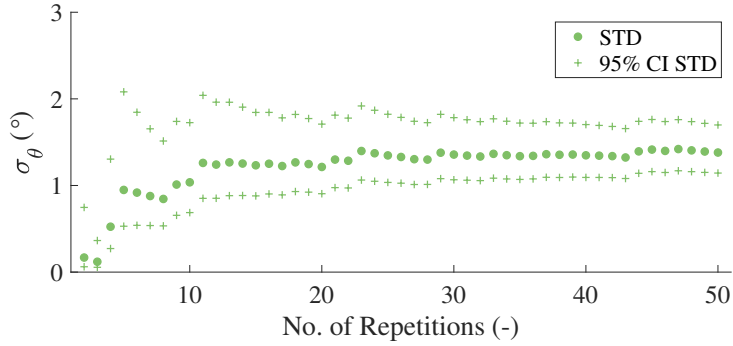
(a)



(b)



(c)



(d)

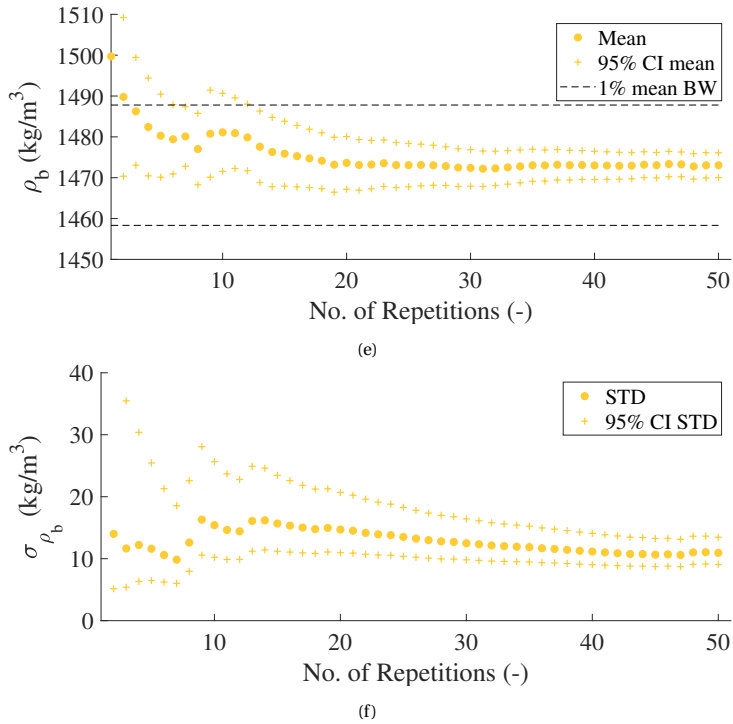


Figure 4.6: In figures (a, c, e) the development of the mean value and 95% CI related to the number of repetitions of the calibration experiment is shown for the Angle of Repose, Angle of Movement, and Bulk density, respectively. Additionally a bandwidth of 1% shown around the mean value for 50 repetitions. Figures (b, d, f) show the development of the standard deviation and its 95% CI.

4.3. DEM MODELS

The DEM models of the hopper and calibration experiments are built based on the schematics shown in Figure 4.2. The model assumptions for the granular material and material structure interaction are described in Section 4.3.1. Next, the procedure for initialisation of the models is described in Section 4.3.2. Finally, the analysis of the simulation results is discussed in Section 4.3.3.

4.3.1. DEM MODEL ASSUMPTIONS AND MATERIAL PROPERTIES

In general, DEM models of a granular process are simplifications of the actual process. For reproducibility, the procedures followed and assumptions made in creating the model are as follows. In this study we use Mercury DPM, an open source discrete element package [94] to build the three-dimensional DEM models. Although the particle shapes are irregular they are modelled as spheres. As suggested by Wensrich & Katterfeld, the irregular shapes of the particles and its behaviour is assumed to be described by the rolling friction coefficient in the contact model [107]. The size of the spheres follows the experimentally determined PSD but is truncated between -1.5 STD and +5 STD around the particle size mean. Ideally, the particle size distribution in DEM is identical to the experimentally obtained distribution. However, for reasonable simulation times truncation of the PSD is justified [12].

The contact model used to describe normal, tangential, sliding, and rolling interaction for particle-particle and particle-wall contact is the model developed by Luding [96]. This model is suitable for modelling dry cohesionless granular solids. The contact stiffness k for particle-particle interaction is determined by using the micro-macro relation given in the following equation,

$$k = \frac{KV_p}{C_n r^2} \quad (4.1)$$

where K is the bulk modulus of the granular material, V_p is the particle volume of a sphere with the average particle radius from the PSD, C_n is the coordination number, and r is the average particle radius [96, 108]. The bulk modulus K of the material is set to 70MPa. The particle contact number, or coordination number, is assumed to be equal to 4 which corresponds to loose material [97]. The damping coefficient of the material is assumed to be equal to 0,3 [49]. The material properties have been tabulated in Table 4.3 and the contact properties for the particle-particle contact can be found in column two of Table 4.4. Based on these properties the size of the time-step can be determined. For the time-step size we assume that $\Delta t = t_c/10$ where t_c is the collision time between the particles for the smallest particle size and was used in previous work as presented in Chapter 3.

For the interaction between particles and three types of walls sliding and rolling friction coefficients are defined. The mean values of the measured sliding friction properties declared in Table 4.1 are directly included in the DEM model and are assumed uniform over the wall surface. Here it is assumed that the walls have uniform properties and are therefore not spatially dependent. The rolling friction coefficient could not be measured

Table 4.3: Material properties gravel.

Bulk modulus	$E_b = 70 \text{ MPa}$
Particle density	Calibration parameter
Contact number	$C_n = 4$ [97]
Particle size distribution (PSD)	5.02 (mm) +/- 1.39 (mm) sieve test results, in simulation the particle size is limited to -1,5 and +5 sigma.
Time step	$\Delta t = \frac{t_c}{10}$

Table 4.4: Material properties gravel.

Stiffness	Particle-particle	Particle-wall
Contact stiffness k	$k_p = 3,67743 \times 10^5 \text{ (N/m)}$	$k_w = 2k_p$
k_r	$\frac{2}{3} k_p$	$\frac{2}{3} k_w$
k_s	$\frac{2}{7} k_p$	$\frac{2}{7} k_w$
Damping		
γ	0,3	0,3
γ_s	0,3	0,3
γ_r	0,3	0,3
Friction		
μ_s	Calibration parameter	Experimental sliding friction values (Tabel 4.2)
μ_r	Calibration parameter	$\mu_r = 2\mu_s$

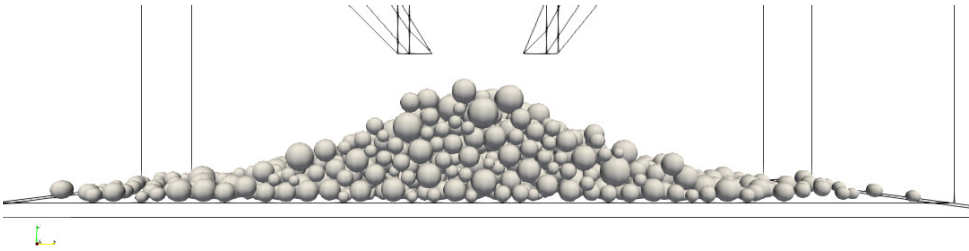
directly. Therefore the relation $\mu_r = 2\mu_s$ is adopted which is common in DEM models for calibration [3, 109] to ensure sliding is the dominant mode of motion in the simulation. The contact stiffness of the walls is also assumed to be twice the size of the contact stiffness of the particles, $k_w = 2k_p$ [3]. The properties can be found in the third column of 4.4.

The particle density has been identified experimentally but because of the assumption of spherical particles adjustments to the particle density might be needed. Therefore it is decided to use the particle density as a calibration parameter. In the particle-particle contact, the sliding and rolling friction coefficients are parameters that are subject of the calibration because both these properties cannot be measured directly.

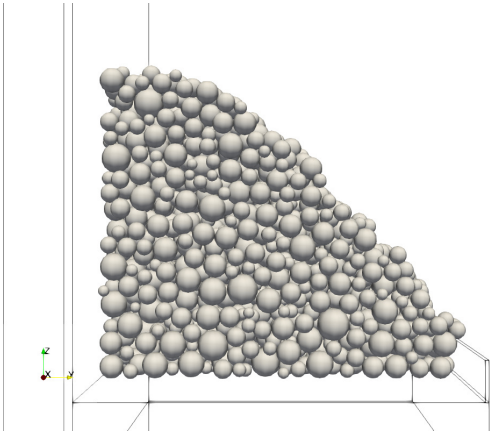
4.3.2. INITIALISATION OF DEM MODELS AND SIMULATIONS

In Figure 4.7 examples of the simulation results for the DEM models of the calibration experiments for $\mu_s, \mu_r = 0.5$ and $\rho_p = 2750 \text{ kg/m}^3$ are shown. Here it can be seen that pile formation occurs in the pile test shown in Figure 4.7 (a), a slope in the ledge test result (b), and a filled bulk density container in (c).

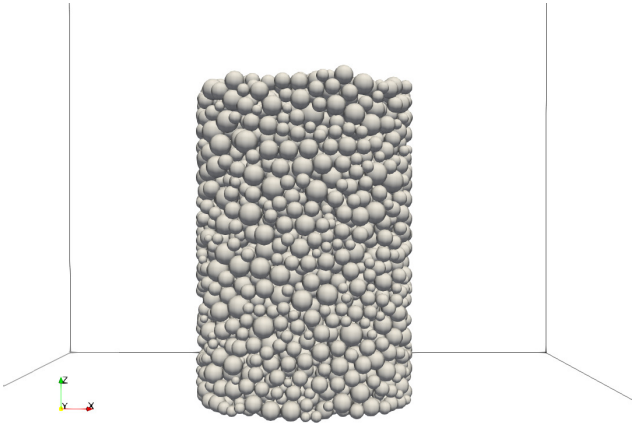
To resemble the filling process in the experiments random filling is used. The procedure is illustrated by the filling procedure for the bulk density container. For each DEM model a volume is defined in which the particles will be generated. In the case of the bulk density



(a)



(b)



(c)

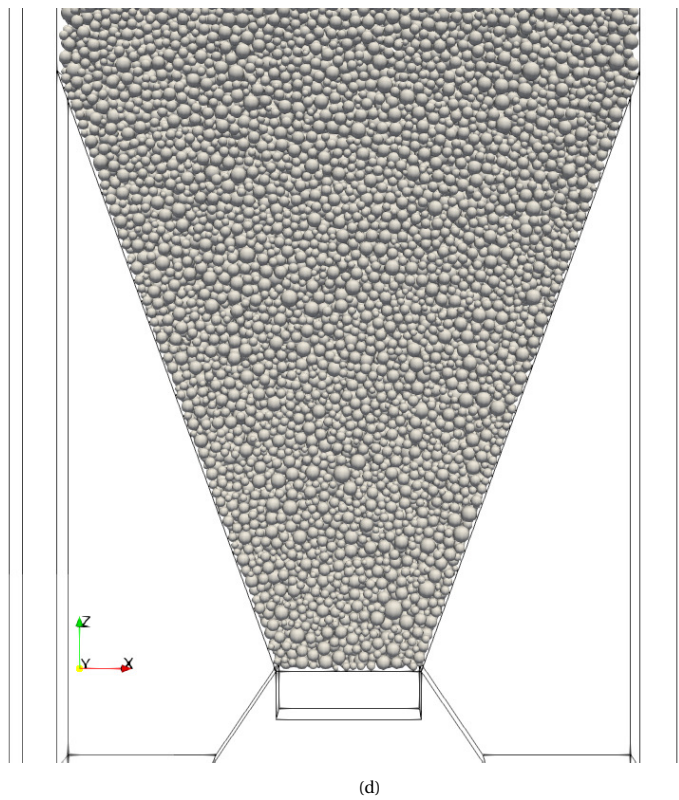


Figure 4.7: Simulation results for the pile (a), ledge (b), and bulk density test (c) for sliding and rolling friction coefficient of 0,5 and a particle density of 2750 kg/m^3 and a visualisation of a filled DEM model of the hopper (d).

Table 4.5: Simulation settings

DEM models	Filling height H_f	Activate deletion boundary
Hopper test	0,66m	1,5s
Pile test	0,11m	1,55s
Ledge test	0,218m	1,55s
Bulk density test	0,236m	1,5s

tester it is the volume of the test apparatus. A circular generation plane is defined at the bottom of the tester and moves up to fill the tester with a predefined volume. The first loop is to generate particles in the circular plane of the bulk density tester. In this loop a random location in the plane is chosen by randomly generation of an angle for the angular location 0 to 360 degrees on the circle and a radius from 0 to the outer radius of the tester. At this location, a particle is generated with a radius drawn from the particle size distribution obtained from the experiments. Before generating it is checked whether the particle is in contact, if so, it is not placed, else, it is placed and the next particle can be placed. With each step in generating a particle, the height of the horizontal generation plane is increased with a step size of $r = 1 \times 10^{-4}$ to ensure proper filling of the volume where the average particle radius is r . After adding a particle its volume is subtracted from the total volume that needs to be added. When this added volume reaches zero or less the particle generation stops. With this procedure a volume is filled with particles without contact. After initialization of the particles, the simulation is started and particles settle under the influence of gravity.

The procedure for all simulation setups is similar while the shape of the generation plane is adjusted to the setup. In the DEM models, the mass of material added to the setup is larger than the amount needed to fill the setup. Therefore, when the particles have settled, the deletion boundary that removes excess material above the filling height H_f for each setup is activated. This activation time is different for each model but equilibrium is reached before the deletion boundary is activated (Table 4.5).

For the hopper simulation material flow starts upon removal of the bottom of the hopper at $t=1,6s$. In the ledge and pile forming test the sidewall and bottom are removed at 1,65s, respectively. The stopping criterion for all simulations is when ratio between the elastic and kinetic energy of the particles in the system becomes lower than 10^{-6} [55]. The hopper simulation has an additional stopping criterion that ensures that the simulation stops when the mass in the hopper is equal to zero.

The DEM models of the calibration experiments are run on a cluster which uses 2x Xeon E5-2680 v4, 28 core CPU's. The average CPU time for the DEM models of the laboratory scale tests is 5h for the bulk density test, 7,5h for the pile forming test, and 12h for the ledge test. The simulation time is denoted as an average because the packing, value of the friction coefficient, and density influences the behaviour of the model and the simulation time.

4.3.3. ANALYSIS SIMULATION RESULTS

The DEM simulations provide data files containing the locations and velocities of the particles. This data is used to determine the KPI values for each DEM model. In contrast to the experimental analysis the analysis of simulation results is automated. Therefore this method is not prone to any error from the analyst whereas the experimental analysis relies on picking data points by hand which can induce errors. For each repetition and sample point this value is calculated which in turn is used to determine the mean and variance values. These values are used as training data for the metamodels used in the calibration procedure (Section 4.4.3).

To obtain the angle of repose from the pile test simulations a grid search is performed to find the locations of the largest combination of particle z-value and its radius in bins. In this search, only the particles located at front are considered analogous to the analysis of the experimental results where only the visible particles are analyzed. The pile has two slopes as shown in Figure 4.8 (a) for which the approach is to determine the angles at both sides of the pile. The left edge of the search area is d_{s1} which is located 0,1m left of the center of the setup along the x-axis. The right edge of the search area for the left angle is located at d_{e1} which is located 0,01m to the left of the setup center on the x-axis. This search area is divided into a number of bins based on the length of the search area divided by the average particle diameter rounded up to an integer. In this case study 9 bins are used. For the right angle the same procedure is followed. After finding the highest particles in each bin, this data is used to determine the angle of repose by linear regression for both the left and right side which are averaged.

After the ledge test simulation finished, the bulk material has formed a stable slope as shown in Figure 4.8 (b) for which the angle can be determined. However, the calibration parameter values in the sample do affect the shape of the slope. Increasing the friction values increases the slope of the heap but also forms a horizontal plane at the back of the shear box after which the slope starts. To obtain the accurate angle of movement the particles lying in this plane should not be considered. To obtain the angle of movement, the first task is to find the particles which have the highest z-values at the front of the simulation. Note that this z-value is the sum of the z-value of the center of the particle and the radius of the particle. As with the Angle of Repose, we do this by looking for the largest combination of z-value of the particle and its radius in bins. The left edge of the search area is defined by the adopted friction relation, $d_s = (\max(\mu_s, \mu_r)/0.9) \times 0.06$ and the right side of the bin is located at $d_e = 0,228m$ which is 0,01m from the leading edge of the shear box. The area between d_s and d_e is divided into a number of bins. The number of bins is determined by dividing the distance between d_s and d_e by the average particle diameter and rounding up. In this way we ensure that the particle in each bin is the highest. After a particle is found in each bin, linear regression is applied to find the angle of movement θ . This method is identical to the experimental analysis.

The result of the bulk density simulation is a volume filled with particles as shown in Figure 4.7 (c). From the data file the volume of each particle in the container can be calculated, and by multiplying with the particle density and dividing the total mass by the volume of the container the bulk density is obtained.

For the analysis of the hopper results the same procedure is followed as with the experimental hopper results but using the numerical data instead of the experimental (Section 4.2.4).

4.4. METAMODEL AND CALIBRATION METHODS

Our calibration, verification, and validation procedure is shown in Figure 4.9. It starts with the calibration experiments shown on the left side of the figure. We use the Pile Test, Ledge Test, and the Bulk density test with the mean and variance of the Angle of Repose, Angle of Movement, and bulk density as output which is discussed in Section 4.2. For each of those experiments a DEM model has been developed as discussed in Section 4.3.

4

The first step in the calibration procedure is to define the bounds and sample the calibration space, described in Section 4.4.1 and 4.4.2. The results of the DEM simulations for the sample will be used in the metamodel training step and are subsequently used for DEM parameter calibration. We use two types of metamodels to describe the relation between calibration parameters and KPIs. The first type is an interpolation-based metamodel that describes the mean and variance of the KPIs by two separate metamodels. The second type is a regression-based metamodel, which is a metamodel that incorporates both mean and variance of the KPIs. Details on the models and training procedure are discussed in Section 4.4.3. For the calibration step, we use both the commonly used mean calibration approach and our newly introduced mean-variance calibration approach. The main difference between these methods is that the latter includes the variance of the KPI in the calibration in addition to the mean. In both approaches, using the DEM-based metamodel the DEM parameter values are determined that provide the best agreement with the experimental KPI data. The calibration is further discussed in Section 4.4.4. After this calibration step, the found optima need to be verified in the verification step as discussed in Section 4.4.5. Here the found DEM parameter sets are reintroduced to the DEM models of the calibration experiments and the simulation results are compared to the results predicted by the metamodels. If the verification results are not satisfactory, the sample of the calibration space can be enriched by adding samples or the optimization settings in the calibration can be adjusted. In this study resampling based on the calibration and verification results is not considered. After successful verification, the DEM parameter set is used as input to the validation step by executing simulations with the DEM hopper model which is described in Section 4.4.6. The results of these simulations are compared to the experimental results from the Hopper discharge experiment. If the error between the experiments and simulations is acceptable, a validated DEM model of the equipment has been obtained. If the error is too large revisiting the calibration or sampling step is required.

In this study we show the effect of the mean and mean-variance calibration strategy in combination with the interpolation-based and regression-based metamodels on the evolution of the found DEM parameter optima when the number of repetitions of the calibration sample simulations increases. In addition, the quality of these found optima are evaluated for the calibration and equipment experiments.

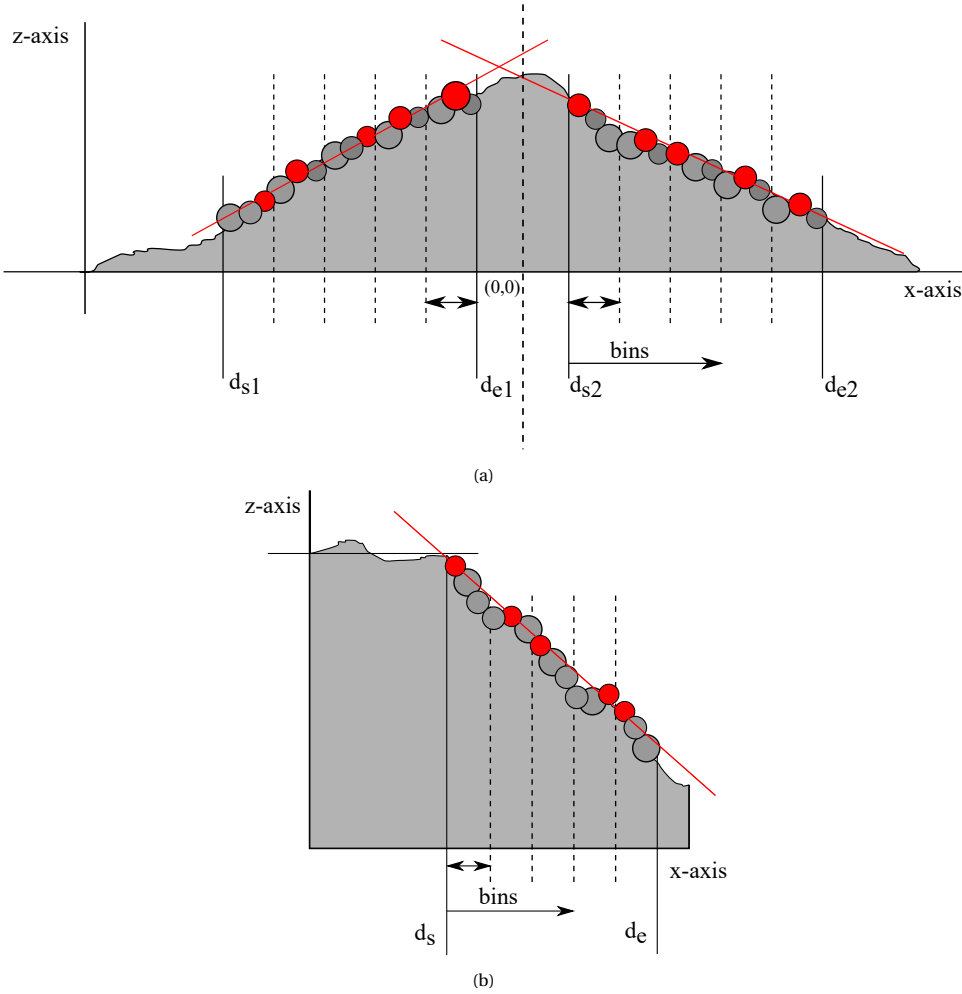


Figure 4.8: Visualisation of the analysis of the simulation results where a linear regression is applied to the highest located particles in each bin (a) determination of angle of repose (b) determination of the angle of movement

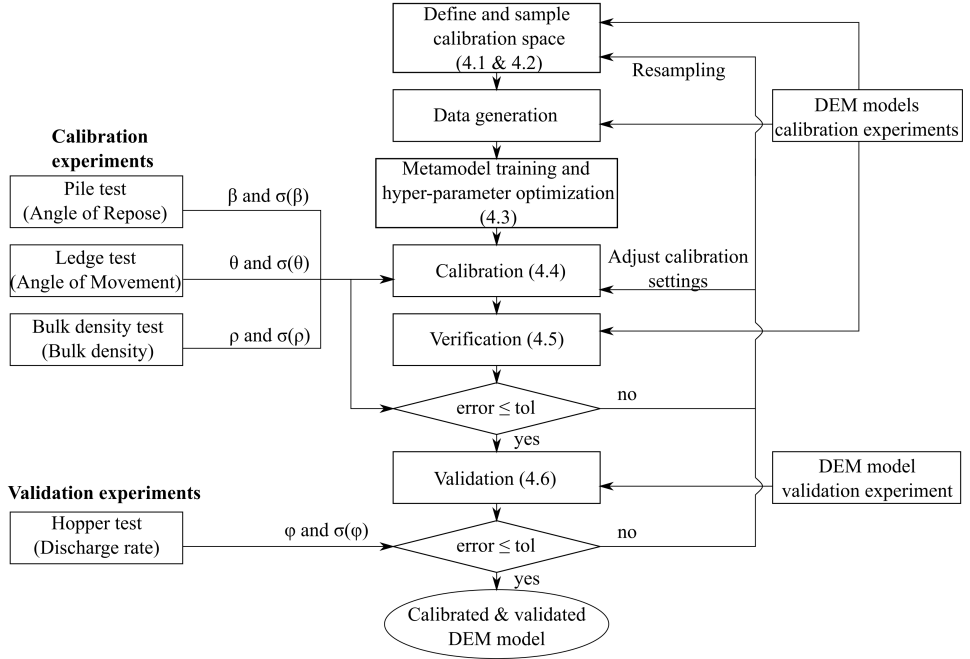


Figure 4.9: Overview of steps taken in the calibration approach and the validation.

4.4.1. BOUNDS OF THE CALIBRATION SPACE

Ensuring that there is a solution present in the calibration space that is used is an essential step in the calibration procedure. In this approach we define lower and upper bounds for the calibration parameters which are the sliding friction coefficient, rolling friction coefficient, and particle density. The lower and upper bound of the friction coefficients has been set to 0,1 and 0,9 based on common values in literature involving gravel experiments as well [12, 110]. In combination with the measured particle density $\rho(p_e)$, the bulk density can be determined by running the bulk density simulation. To determine the bulk density bounds, this is done for two situations, the experimental particle density with the highest friction coefficients and the lowest friction coefficients. Moreover, to ensure stability of the outcome these two situations have been repeated 50 times with random material packing to get an accurate estimate of the average bulk density and its standard deviation. Based on the results from these simulations, the experimental particle density, and the experimental bulk density the lower and upper bound for the particle density can be found by using the following two equations,

$$\overline{\rho_{p_{s-lb}}} = \frac{\overline{\rho_{b_e}}}{\rho_{b_s}(\mu_{s-lb}, \mu_{r-lb}, \rho_{p_e})} \overline{\rho_{p_e}} \quad (4.2)$$

$$\overline{\rho_{p_{(s-ub)}}} = \frac{\overline{\rho_{b_e}}}{\rho_{b_s}(\mu_{s-ub}, \mu_{r-ub}, \rho_{p_e})} \overline{\rho_{p_e}} \quad (4.3)$$

Table 4.6: Bounds of the calibration space

Calibration parameter	Lower bound	Upper bound
μ_s (-)	0,1	0,9
μ_r (-)	0,1	0,9
ρ_p (kg/m ³)	2542,9	2834,7

where (ρ_{b_e}) is the average experimental bulk density, (ρ_{b_s}) is the average simulated bulk density which depends on the friction coefficients and experimental particle density. The average experimental particle density is denoted by the term (ρ_{p_e}). The lower and upper bound are denoted by lb and ub. With these lower and upper bounds of the particle density determined, they can be used in combination with the sliding and rolling friction coefficient limits to check if the lower and upper limits of the KPIs of the other calibration models, the shear box and pile test, stay in their respective bounds. After verification of these results the next step is to define the boundary sample. In this case study we have three parameters which results in a three-dimensional calibration space with the following bounds denoted in Table 4.6. For these lower and upper bound values we have confirmed that the lower and upper bounds result in values for the angle of repose β , angle of movement θ , and bulk density ρ_b which contain the experimentally found calibration targets. In Section 4.3 the model assumptions have been declared where it is assumed that the material has a contact number of 4. After the simulations described here the contact number was found to be $\approx 4,36$ with lower limit of 3,6 and an upper limit of 5 depending on high or low friction, respectively. This makes 4 a reasonable assumption for the contact number.

4.4.2. SAMPLING THE CALIBRATION SPACE

After the feasibility check of the calibration space bounds it can be sampled. The sample consists of two parts, a sample covering the edges of the calibration space and a sample covering the internal volume of the calibration space. Sampling of the edges is essential if metamodels are used for the calibration because these have poor extrapolation abilities beyond the space covered by the data points. In this case the boundary sample consists of 27 sample points located at the corners of the calibration space, at the halfway points between the corner points, and the center points in the plane and cube as shown as purple squares in Figure 4.10. To cover the internal space of the calibration space an internal sample of 100 points based on Latin Hypercube Sampling (LHS) with the maximin criterion is applied to obtain a sample that covers the calibration space. These sample points are denoted by blue circles in Figure 4.10. The total number of sample points is 127 which leads to a sampling density of $\eta = 127^{\frac{1}{3}}$ which is equal to 5,02 samples per unit step in the normalised three dimensional calibration space.

To obtain accurate predictions of the mean and variance of the KPIs the simulations for the sample points are repeated 50 times where in each repetition the packing of the particles is randomly generated. The total number of simulations is equal to 4050 for the boundary sample for the DEM models of the calibration experiments. For the internal

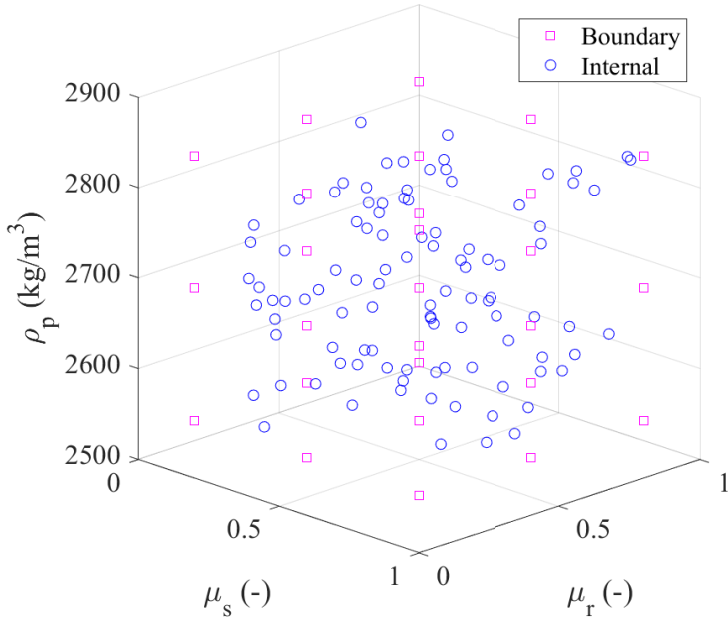


Figure 4.10: Three dimensional representation of non-normalized sample space.

sample, the number of simulations is 15000 which totals 19050 simulations training the calibration metamodels. In this study a high number of repetitions is used to find an accurate reference value. Based on the results, recommendations can be given on the amount of repetitions that are needed to reach an accurate calibration result.

4.4.3. METAMODEL TRAINING

The results from the simulations for the calibration sample are used to train a Gaussian Process Regression metamodel which will be denoted by $f_i(x)$ where i is the index of the KPI and $x = [\mu_s, \mu_r, \rho_p]$ is a vector containing the calibration parameters as variables for which the GPR metamodel gives a prediction of the KPI. The mean and standard deviation values obtained from the DEM simulation results are normalized such that a normalized mean and coefficient of variation can be used in training the metamodels. As mentioned in the introduction, two types of metamodels are trained

1. Separate noiseless GPR models based on interpolation for normalized mean and coefficient of variation of the KPI [14]
2. Single noisy GPR model based on regression including both normalized mean and coefficient of variation of the KPI [86]

A Gaussian process is a collection of random variables, any finite number of which have a joint Gaussian distribution [86]. The Gaussian process GP is an approximation of the real

process $f_i(x)$ that it intends to model. The GP consists of a mean function $m(x)$ and a covariance function $k(x, x')$.

$$f_i(x) \approx GP(m(x), k(x, x')) \quad (4.4)$$

In building a metamodel with Gaussian Processes the correlation function between the training points needs to be chosen which forms the basis of the model. In this case, the correlation function (Equation 4.5) is chosen as a squared exponential Gaussian in R^3 with a shape factor l^2 and an amplitude factor σ_f which in this case are both set equal to 1. To add more flexibility to the correlation function, the contribution of each design parameter is determined based on the Euclidean distance and is weighted with a coefficient a_i for each calibration parameter (Equation 4.6). This makes the shape factor l^2 obsolete and would interfere in the hyper-parameter optimization process. The factor σ_f is set equal to 1 because in the noiseless GPR there is no influence on the solution and in the noise included GPR a value of 1 is suitable because it preserves the ratio between the normalized mean values and coefficient of variation. These coefficients are called hyper-parameters which can be user-defined or optimized. In Gaussian Process Regression it is common to optimize these hyper-parameters by using type II log-likelihood maximization [86]. In this method the negative marginal log-likelihood function (Equation 4.7) is minimized to find the hyper-parameter values. Where K is the covariance matrix, σ_n^2 is the coefficient of variation in the training points, and N is the total number of training points. In the noiseless GPR the coefficient of variation in the training points is equal to zero whereas it contains the coefficients of variation in each datapoint in the noisy GPR.

$$\phi(x) = \sigma_f e^{\frac{-1}{2l^2} r^2} \quad (4.5)$$

$$r = \sqrt{(a_1(x_1 - x_{1,c})^2 + a_2(x_2 - x_{2,c})^2 + a_3(x_3 - x_{3,c})^2)} \quad (4.6)$$

$$\log(P(y|X)) = -0.5y^T(K + \sigma_n^2 I)^{-1}y - \frac{1}{2}\log K + \sigma_n^2 I - \frac{N}{2}\log 2\pi \quad (4.7)$$

The maximization problem is solved using a constrained optimization solver in $[-1, 1] R^3$ using the interior point method on which theory can be found here [111]. To ensure that the initial guess for this gradient-based solver does not miss the global optimum we have used 100 random initial guesses to rule out this effect. After solving the maximization problem, the found optimum for the hyper-parameters of each KPI is fixed input in training the calibration metamodels used for optimization of DEM-parameters.

The metamodel prediction (Equation 4.8) for the mean value consists of the correlation between the training points and predicted point, $k(x, x^*)$. This is multiplied with the inverse of the summation of the Gram matrix $K(x, x)$ and the variances σ_n^2 and with the reference values y from the DEM simulation results for the training points in the calibration space to obtain a prediction of the mean at x^* . The variance predictor (Equation 4.9) is a correction based on the prior covariance of the predicted points $k(x^*, x^*)$ minus the information the training points give about the function [86].

$$f(x^*) = k(x, x^*)^T (K(x, x) + \sigma_n^2 I)^{-1} y \quad (4.8)$$

$$V(f^*) = k(x^*, x^*) - k(x, x^*)^T (K + \sigma_n^2 I)^{-1} k(x, x^*)^T \quad (4.9)$$

In this case study we defined three KPIs, the angle of repose β , angle of movement θ , and the bulk density ρ_b for each of which we have developed the interpolation-based and regression-based metamodels. All these calibration metamodels have DEM parameters as their variables, the sliding friction μ_s , rolling friction μ_r , and the particle density ρ_p . For the interpolation-based metamodels this results in six metamodels. A separate mean and variance predictor for each KPI. In the regression-based metamodel the mean and variance predictor are included in a single model which results in three metamodels. Notation: Interpolation-based metamodels are denoted by IBM, regression-based metamodels by RBM, followed by the abbreviation of the calibration method. M for the mean calibration and MV for the mean-variance calibration.

4

4.4.4. CALIBRATION OF DEM PARAMETERS

In the previous section we have described the two types of calibration metamodels that are developed for the calibration procedure. Both these models can predict mean and variance values for the KPIs of the laboratory scale experiments. Next to these two metamodeling approaches, in the calibration of the design parameters we can choose between using a mean (M) or mean-variance (MV) calibration approach. Here, the mean calibration approach focusses on matching the mean values of the experimental and numerical KPI values. The mean-variance approach matches both mean and variance values of the experimental and numerical KPI values. As discussed in Section 4.2, the calibration targets are the experimentally obtained mean and variance for which we assume that the found values are the true mean and variance. This means that in the calibration we do not include the confidence intervals around the found mean and variance values. In this section these two approaches and the used solver for the optimization problem are described. The following calibration approaches will be evaluated.

1. Mean calibration with interpolation-based GP model (IBM-M)
2. Mean-Variance calibration with interpolation-based GP model (IBM-MV)
3. Mean calibration with regression-based GP model (RBM-M)
4. Mean-Variance calibration with regression-based GP model (RBM-MV)

The two calibration approaches are applied to each of the two calibration metamodels for an increasing number of repetitions. This means that calibration metamodels are trained with data for all number of repetitions individually to see how the optimal solution changes with increase of the number of repetitions.

To calibrate the DEM-parameters a multi-objective optimization problem is formulated which is solved using constrained optimization with the interior-point-method [111]. In order to find a global optimum, the optimization is run 100 times with different initial guesses in the calibration space to find the optimum DEM-parameter set.

MEAN MULTI-OBJECTIVE OPTIMIZATION PROBLEM

For the mean calibration problem the goal is to match the mean KPI values from the experiments to those of the simulations. To calibrate the DEM-parameters the following multi-objective optimization problem is defined.

$$\min c(x) \quad (4.10)$$

Where $c(x)$ is a summation of the objectives for the optimization problem. The goal of calibration is to find DEM parameter values for the sliding and rolling friction coefficient for the interaction between gravel particles and the particle density. For each KPI (Angle of Repose, Angle of Movement, bulk density) an objective is defined according to the following equation,

$$c_i(x) = w_i \frac{K_{i-e} - K_{i-s}(x)^2}{K_{i-e}} \quad (4.11)$$

Where K_i represents the KPI, w_i the weight of the objective, and x is a vector containing the DEM parameter values. The subscript e for the KPI denotes that it is the experimental value and the subscript s of the KPI denotes that it is the numerical or simulation value. The term $K_{i-s}(x)$ provides a prediction of the mean and variance of the KPI by the metamodel described in Section 4.4.3. The objective is normalized by the simulation value of the KPI and squared such that the objective returns a positive value.

For this case study there are three KPIs resulting in three objectives which are summed in $c(x)$. Each objective is normalized and is therefore equally important if the weights are equal to one. For the clarity of this study we have decided to keep the weights equal to 1, $w = [111]$. However, in practical applications these weights can be adjusted if the engineer or researcher decides that some KPIs are more important than others.

MEAN-VARIANCE MULTI-OBJECTIVE OPTIMIZATION PROBLEM

For the mean-variance calibration problem the definition of the optimization problem is the same as in Equation 4.11. However, in addition to the mean objectives the relation between the mean and variance is utilized to define six additional objectives. These objectives are the mean plus and minus the standard deviation, which is the square root of the variance, of the KPI. The standard deviation of the KPI is used because it has the same unit as the mean. The upper bound is defined as the error between the sum of the experimental mean K_{i-e} and standard deviation value $\sigma(K_{i-e})$ and the sum of the numerical prediction for the mean K_{i-s} and standard deviation $\sigma(K_{i-s})$ as described in Equation 4.12. The lower bound is defined as the error between the experimental mean minus the standard deviation value and the numerical prediction for the mean minus the standard deviation as described in Equation 4.13.

$$c_i(x) = w_i \left(\frac{(K_{i-e} + \sigma_{K_{i-e}}) - (K_{i-s}(x) + \sigma_{K_{i-s}(x)})}{K_{i-e} + \sigma_{K_{i-e}}} \right)^2 \quad (4.12)$$

$$c_i(x) = w_i \left(\frac{(K_{i-e} - \sigma_{K_{i-e}}) - (K_{i-s}(x) - \sigma_{K_{i-s}(x)})}{K_{i-e} - \sigma_{K_{i-e}}} \right)^2 \quad (4.13)$$

In the mean-variance calibration problem each objective has a weight. Here, the weights indicate the importance of each part of the objective function. For the objective of the

mean value the same weights are used as in the mean calibration case. The weights for the mean \pm standard deviation objectives is defined by a factor C which scales the influence of these objectives. The value chosen for $C = 0,5$ and kept constant in this case study which result in the weight vector $w = [1 \ C \ C \ 1 \ C \ C \ 1 \ C \ C]$. We assume that the lower and upper bound are equally important and that the sum of these should be equally as important as the mean objective of the specific KPI.

4.4.5. VERIFICATION OF DEM PARAMETER SETS

For each of the four calibration approaches described in the previous section, 50 sets of DEM-parameters for metamodels trained with mean and variance data are obtained. These optimal DEM-parameter sets are applied to the DEM models of the laboratory scale experiments. The results are verified by comparing KPIs from the simulation results to the calibration targets. To reduce the number of simulations, a selection of obtained DEM-parameter sets will be evaluated. This selection is defined by the DEM-parameter sets corresponding to 1, 2, ..., 10, 15, 20, 30, 40, 50 repetitions. Simulations for these 15 sets are repeated with the same number of repetitions as the number of repetitions used to train the metamodels. From these simulations the mean and standard deviation values for the KPIs are determined. These values are used to verify the accuracy of the metamodel prediction of the optima of the KPIs mean and mean \pm standard deviation. Furthermore, the verification results are evaluated with respect to the calibration targets to get insight on the quality of the calibration results.

4.4.6. VALIDATION OF OPTIMAL DEM PARAMETER SETS FOR LARGE SCALE HOPPER MODEL

In addition to the verification, the DEM parameter sets need to be applied to the DEM model of the hopper and simulated. The hopper discharge experiments described in Section 2.2 were repeated 5 times so for the validation the DEM parameter sets from the mean and mean-variance calibration were repeated 5 times as well. This procedure as applied to the same solutions as described in the previous section to reduce the number of computations. The results from these simulations are used to determine the error between the experimental results and numerical results by using the following equation.

$$\epsilon_{\phi} = \frac{\phi_s - \phi_e}{\phi_e} \times 100\% \quad (4.14)$$

To determine if the interpolation-based or regression-based metamodel with the mean or mean-variance calibration results in the best performing DEM model the results for 50 repetitions are compared in more detail.

4.5. RESULTS

In this section the results of this study are presented. Section 4.5.1 starts with an evaluation of the quality of the interpolation-based and regression-based metamodels. Next, the

calibration results are evaluated in Section 4.5.2 followed by the verification of these results in Section 4.5.3. In this section the quality of metamodel prediction of the KPIs is verified first followed by a comparison between the predicted KPIs and the calibration targets. In Section 4.5.4 the validation results are presented for the large-scale hopper application.

4.5.1. METAMODELS FOR CALIBRATION

The quality of the metamodel determines the quality of the DEM parameter set found through optimization. To gain insight on the quality of the metamodel the training error of the model can be assessed. Because training error does not give insight in the quality of the predictions in between training points the predictions by the metamodel are compared to a validation set.

4.5.1.1. TRAINING ERROR

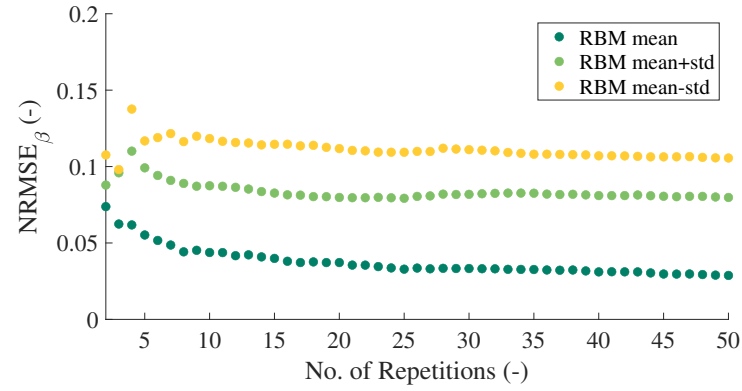
The calibration models have been trained according to the method described in Section 4.4.3. For these models, the normalised root mean squared error (NRMSE) is calculated such that the accuracy in training of the model can be evaluated and compared for the different KPIs, (Equation 4.15).

$$NRMSE = \frac{\sqrt{\sum_{i=1}^N \frac{f_i^*(x) - f_i(x)^2}{N}}}{\bar{f}} \quad (4.15)$$

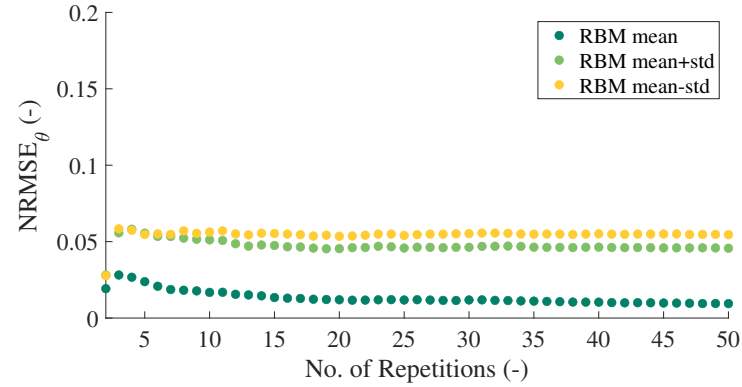
In Figure 4.11 the NRMSE for the mean, mean \pm standard deviation for the interpolation-based and regression-based metamodels are shown. In Figure 4.11 (a) to (c) it can be seen that the error of the interpolation-based metamodel is close to machine precision which can be regarded as numerical noise. This can be explained by the fact that the interpolation-based models are exact in the data-points. In Figure 4.11 (d) to (f) the RSE for the stochastic models is shown where errors in the mean prediction are small but errors in the mean \pm standard deviation are significant. The trend of the RSE of the Angle of Repose and Movement indicates that increasing the number of repetitions leads to a decreasing error up to 20 repetitions after which stabilisation occurs. The NRMSE for the bulk density is below 0,0005 which indicates an accurate metamodel. The majority of the improvement of the regression-based metamodel accuracy for the Angle of Repose and Movement occurs up to the first 20 repetitions, which is an indication of the importance of repeating simulations to obtain accurate metamodels. Based on the training error the RBM of the bulk density is best, followed by the RBM of the AoM, and lastly the AoR.

4.5.1.2. VALIDATION ERROR

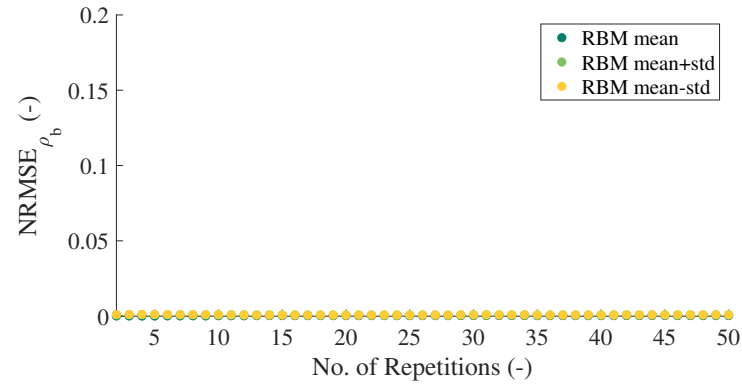
The results in Figure 4.11 show that the interpolation-based metamodels (IBM) are more accurate in the data-points than the regression-based metamodels (RBM). However, the accuracy of a metamodel is mainly determined by its ability to predict KPI values at locations in between the used training set. To verify this ability a validation strategy



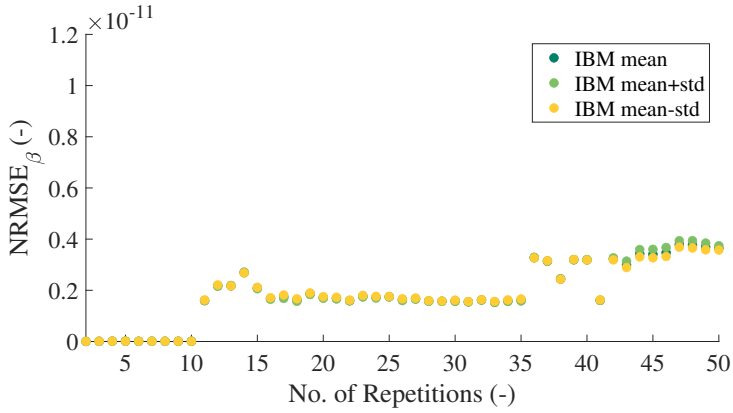
(a)



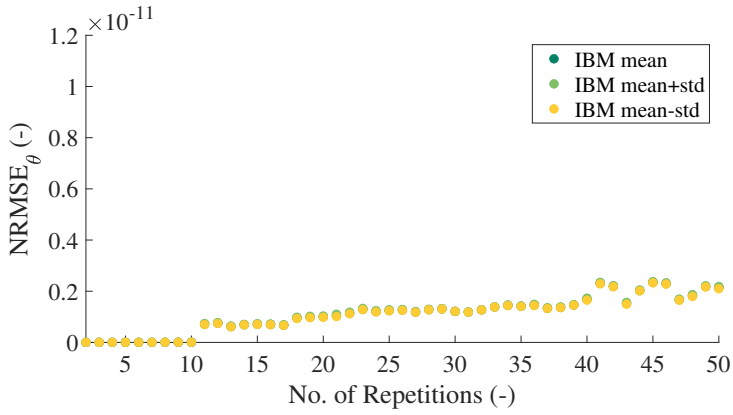
(b)



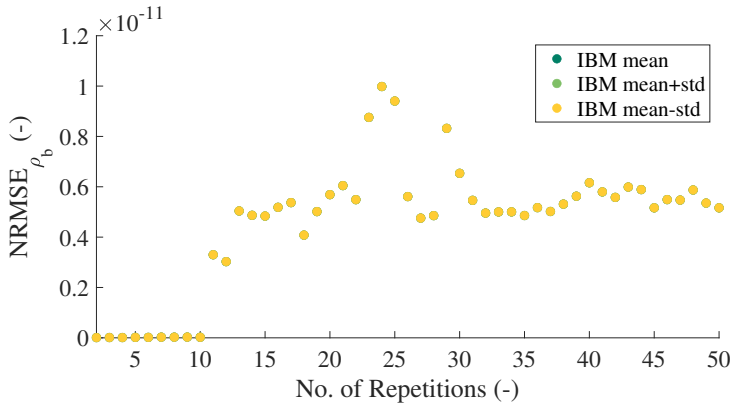
(c)



(d)



(e)



(f)

Figure 4.11: Normalized Root Mean Squared Error (NRMSE) in the training points for interpolation-based metamodels (a,b,c) and regression-based metamodels (d,e,f) for the Angle of Repose β , Angle of Movement θ , and Bulk Density ρ_b data

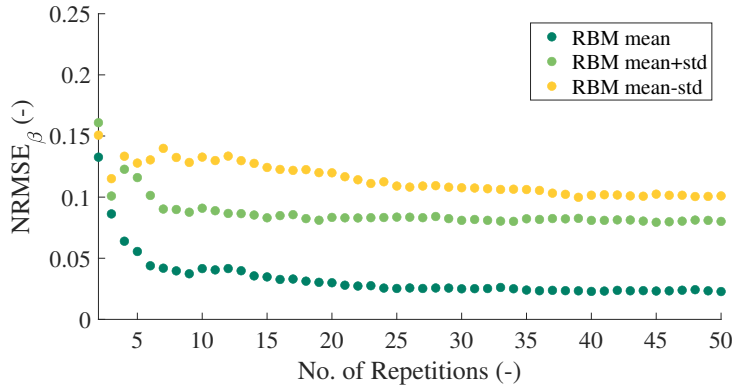
such as validation set approach (VSA), Cross-validation, or leave one out cross validation (LOOCV) should be used [55]. Therefore, an additional 32 data point sampling set has been simulated for 50 repetitions such that the 20% validation set approach can be applied. The results in Figure 4.12 show the NRMSE error for the interpolation-based metamodel in (a-c) and for the regression-based metamodel in (d-f).

For all KPIs and both the IBM and RBM approach it shows that the addition of repetitions to the dataset leads to a decrease in NRMSE. The difference between the IBM and RBM approach is that the NRMSE of the IBM develops less consistent than the error of the RBM. Considering the mean prediction of the AoR and AoM the NRMSE is 1,5 to 2,5 times lower for the RBM models than for the IBM models. This means that the RBM models are more reliable in predicting the mean. For the mean prediction of the bulk density we see that both the IBM and RBM metamodels lead to similar levels of accuracy. With respect to the bandwidth of the standard deviation around the mean it is observed that for the IBM the error is in the same range as the mean error. This indicates that these models have a small prediction error in the magnitude of the standard deviation but that the error of the mean causes a large shift of the bandwidth. For the RBM of the AoR we see different behaviour. In addition to a shift of the bandwidth due to the mean error it is observed that the mean \pm standard deviation has a larger error for the lower limit than for the upper limit. This indicates an additional error introduced by the RBM in the prediction of the variance. This same behaviour is also visible for the AoM but has a smaller magnitude compared to the AoR results. In contrast to the mean \pm standard deviation of the bulk density for the IBM the bandwidth error of the RBM decreases fast in the first 20 repetitions.

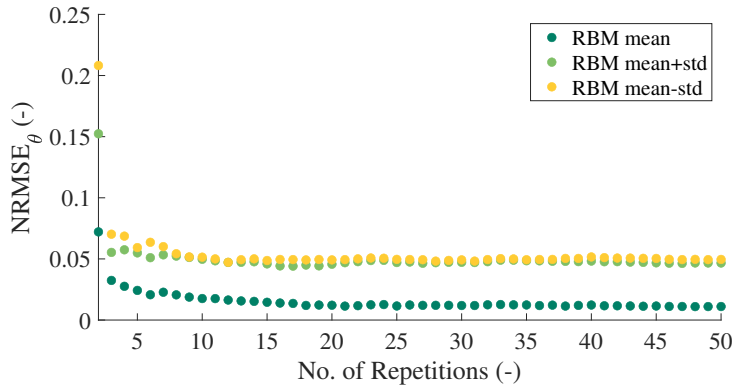
Overall, the regression-based metamodel is more reliable in predicting the mean value which results in smaller offsets in the location of the bandwidth of the standard deviation around the mean. Due to the error in mean prediction by both metamodel types the standard deviation bandwidth has an offset. For the IBM the prediction of the standard deviation is accurate in magnitude but has an offset in location due to the error of the mean. The RBM has an inaccurate prediction of the standard deviation magnitude and an induced offset due to the error in the mean prediction leading to an asymmetric bandwidth of the standard deviation.

4.5.2. CALIBRATION RESULTS

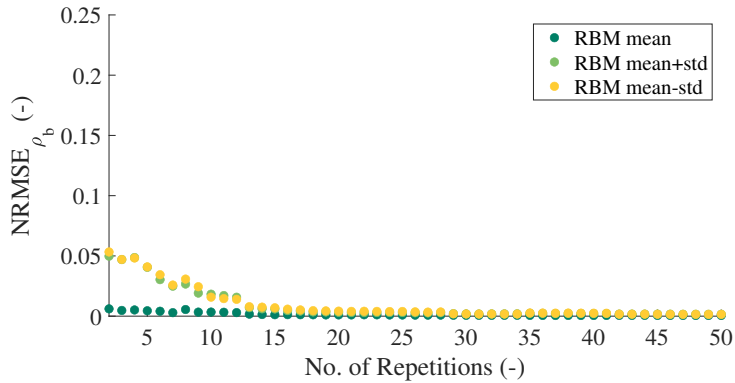
The resulting DEM parameter values of the mean (M) and mean- variance (MV) calibration with the interpolation- and regression-based metamodels (IBM & RBM) are shown in Figure 4.13. For all three calibration parameters it is observed that the calibration with interpolation-based metamodels results in irregular development of the parameter values μ_s , μ_r , and ρ_p with the increase of the number of repetitions. On the contrary, the regression-based metamodel calibration presents a relatively smooth and steady parameter evolution for an increasing number of repetitions. This indicates that the optimal DEM parameter set is approximately reached at 20 repetitions, which is useful information if this method is applied in engineering practice. Note also that at a more conventional amount of 3-5 repetitions, the parameter values have not stabilized for either method. In Figure 4.14 (a-f) the mean and mean \pm standard deviation of the KPI



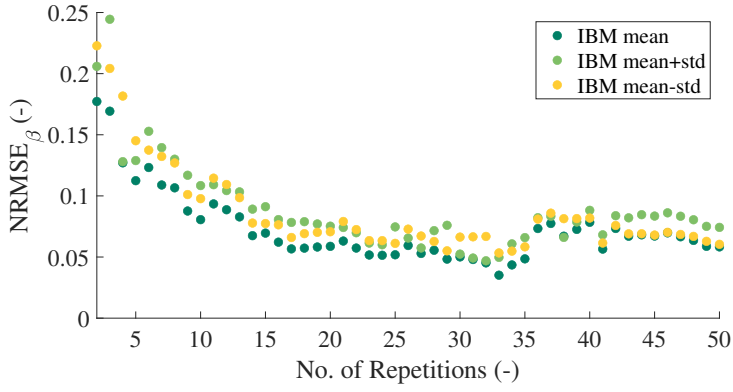
(a)



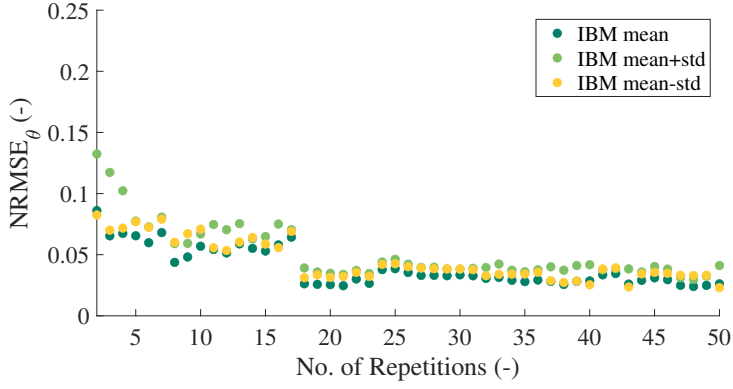
(b)



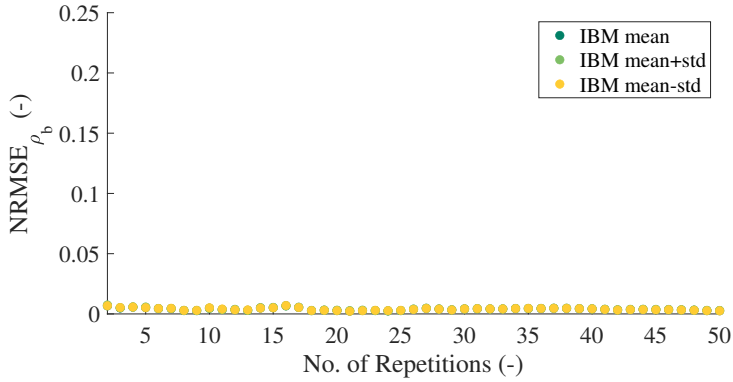
(c)



(d)



(e)



(f)

Figure 4.12: Normalized Root Mean Squared Error (NRMSE) in the validation points for interpolation-based metamodels (a,b,c) and regression-based metamodels (d,e,f) for the Angle of Repose β , Angle of Movement θ , and Bulk Density ρ_b data

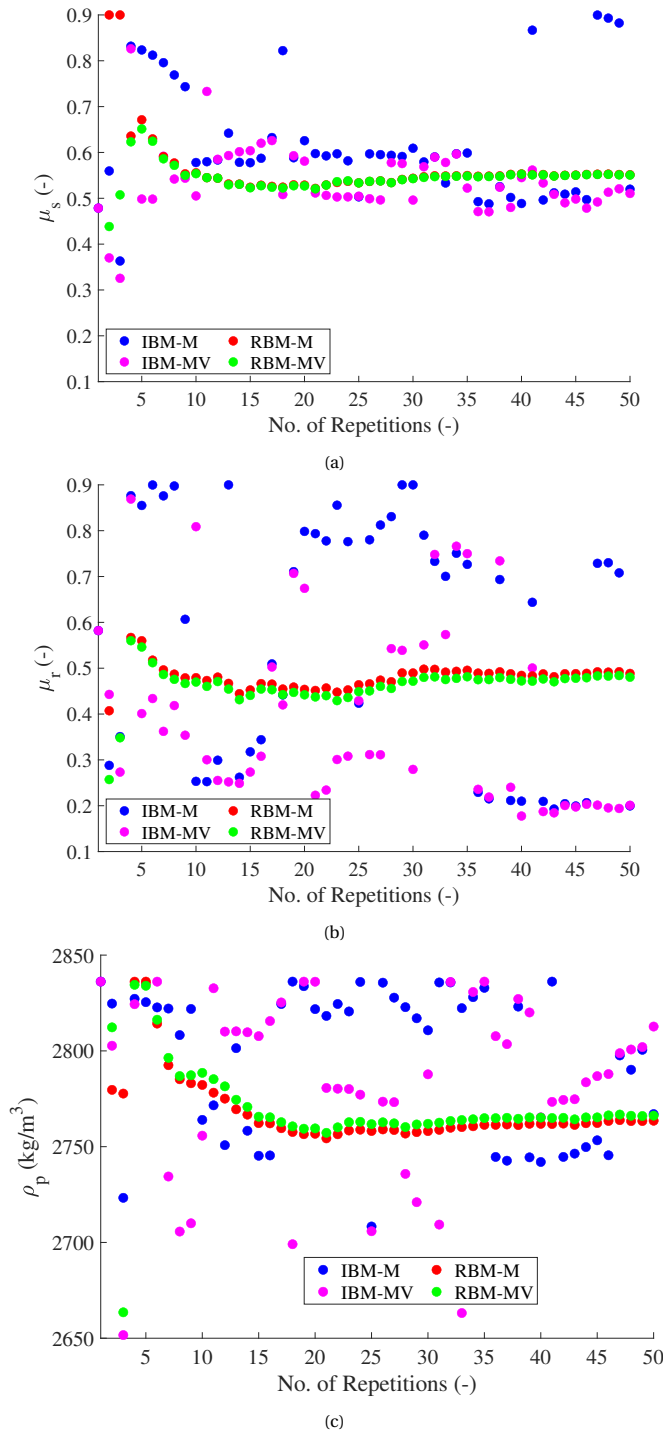


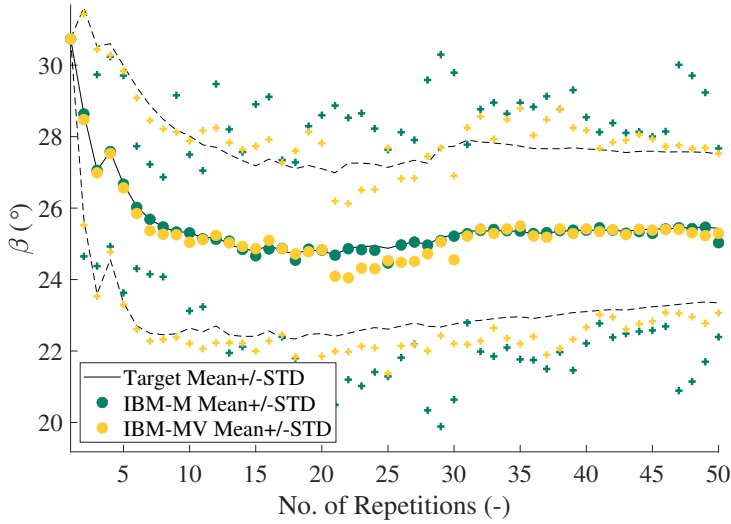
Figure 4.13: Development of the DEM parameter values μ_s , μ_r , and ρ_p resulting from mean (M) and mean-variance (MV) calibration with interpolation- and regression-based metamodels (IBM & RBM) with increasing number of repetitions.

values are presented corresponding to the optimal DEM parameter values in Figure 4.13. For all four calibration approaches, Figure 4.14 (a) and (b) shows the Angle of Repose as a function of the number of repetitions. Figure 4.14 (c) and (d) show the Angle of Movement and (e) and (f) show the bulk density. Figures (a,c,e) show the results obtained with the mean and mean-variance calibration approach with the interpolation-based metamodells, and Figures (b, d, f) show the results obtained with the regression-based metamodells. With respect to the IBM and RBM calibration the clear difference is the consistency of the calibration results obtained with the RBM compared to the IBM calibration results. As was observed with the validation of the metamodel in Section 4.5.1 the IBM models are more sensitive to changes in the dataset than RBM models.

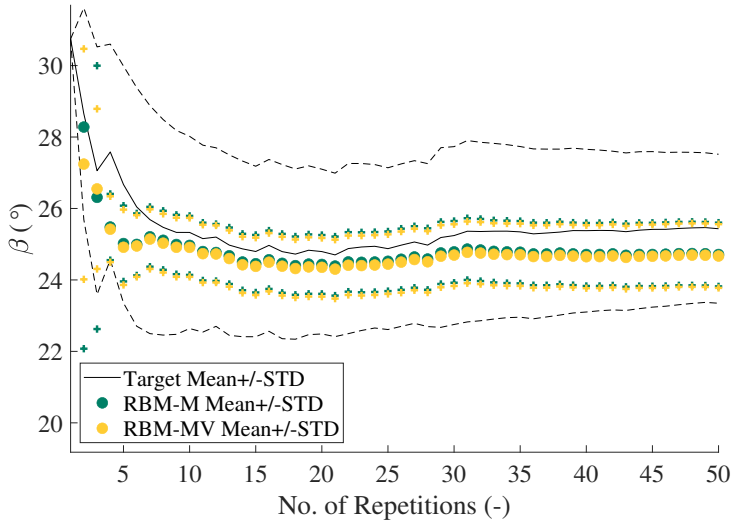
4

Even though IBM is more sensitive to changes in the dataset, the performance for both mean and mean-variance calibration with the IBM is good. For the mean calibration, the match of the AoR and AoM is good over the entire range and the bulk density has a good match after 36 repetitions. The match for mean \pm standard deviation is close for the AoR, twice the target for the AoM and half of the target for the bulk density. This is reasonable because the mean \pm standard deviation is not included in mean calibration. For the mean-variance calibration the match of the mean value of the AoR is good. The match to the mean of the AoM is quite good but less than for the mean calibration. The mean of the bulk density fluctuates considerably before converging to a relatively good match. The mean \pm standard deviation is included in the mean-variance calibration approach and shows a slightly better match to the targets compared to the mean calibration approach.

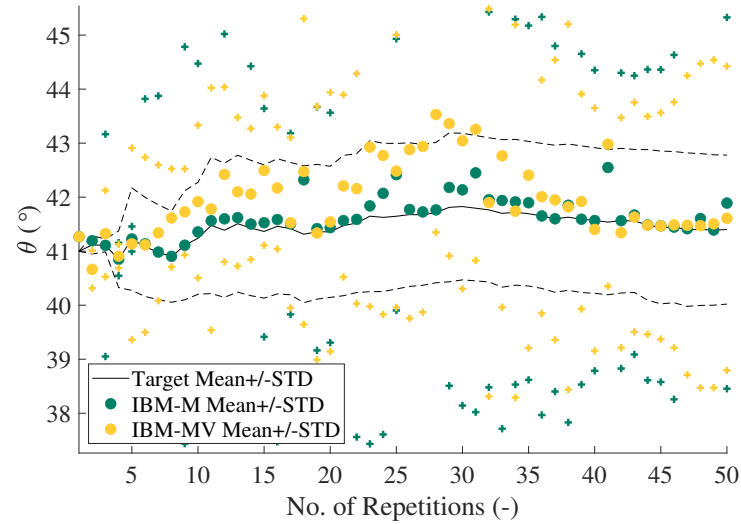
The performance of the calibration approaches with the RBM models gives consistent results. However, the error between the calibration results and the target is significant and is around -5% for the AoR and +5% for the AoM over the entire range of repetitions. For the bulk density a good fit to the calibration target was found after 10 repetitions. With respect to the mean \pm standard deviation values the AoR shows that the bandwidth is half of the calibration target. For the AoM the bandwidth is similar to the target in magnitude and half of the target for the bulk density. Comparing the mean and mean-variance calibration approach with the RBM it is observed that there is no significant difference between the calibration results apart from a small shift. This means that in this case there is no added benefit by adding the variance to the calibration. At 50 repetitions, the dataset for training the metamodells has the highest reliability and therefore we assume that the results of the calibration is the most accurate. In Table 4.7 the DEM parameter values for calibration with 50 repetitions are shown. For the IBM calibration it can be seen that the DEM parameter values are close. The largest difference can be observed for the particle density. For the RBM calibration we can see that the DEM parameters are more or less similar for the mean and mean-variance calibration. Between the interpolation-based and regression-based metamodel calibration it can be seen that the sliding friction is slightly higher, the rolling friction is almost 2,5 times higher, and the particle density is in the same range.



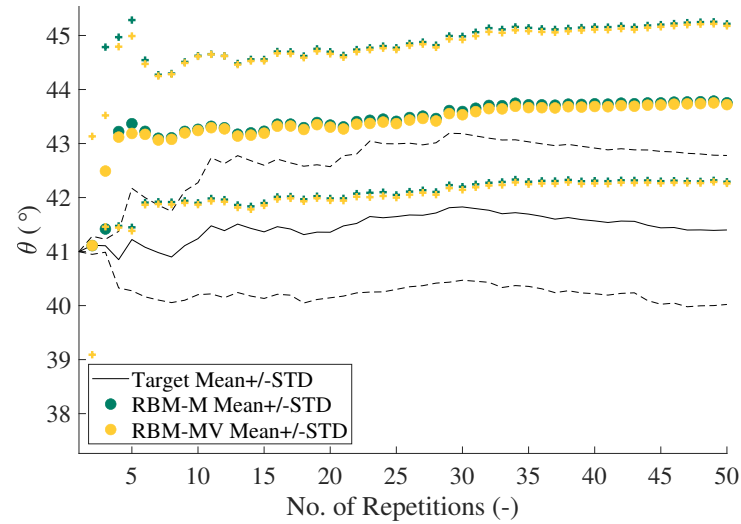
(a)



(b)



(c)



(d)

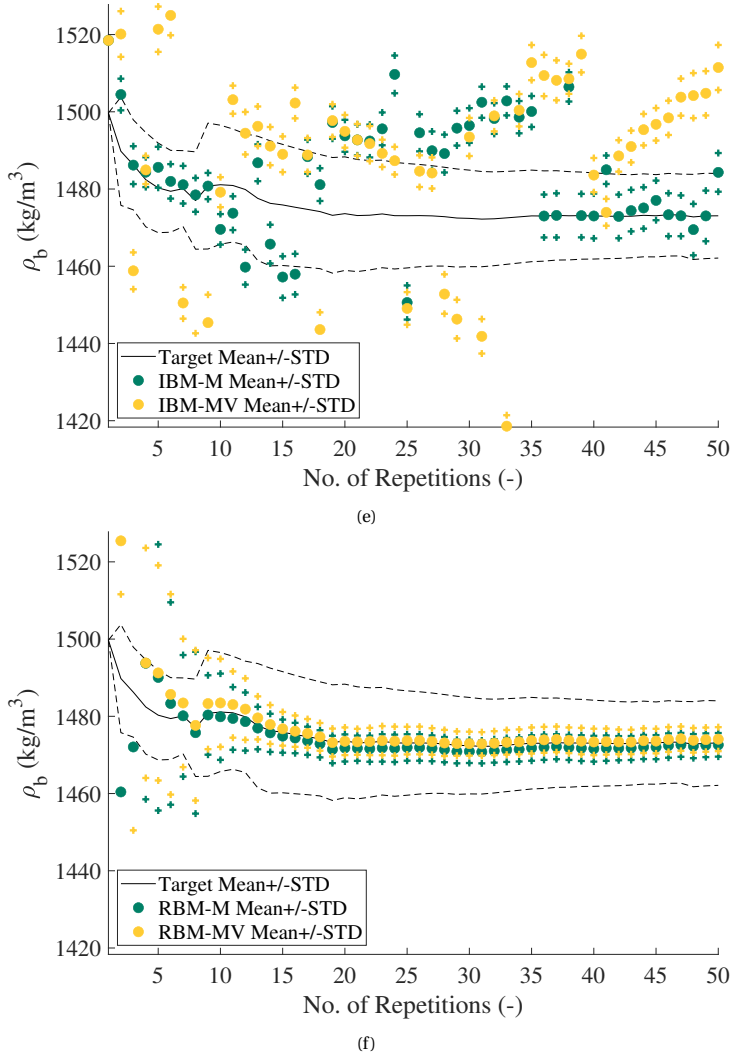


Figure 4.14: Mean and mean-variance calibration results for the Angle of Repose, Angle of Movement, and Bulk Density for the interpolation-based metamodel (a,c,e) and regression-based metamodel (b,d, f) respectively.

Table 4.7: DEM parameters after calibration for mean and mean-variance calibration with interpolation-based and regression-based metamodels at 50 repetitions of the sample

	IBM-M	IBM-MV	RBM-M	RBM-MV
μ_s	0.5198	0.5106	0.5513	0.5506
μ_r	0.1996	0.2010	0.4885	0.4804
$\rho_p(kg/m^3)$	2767.0	2812.7	2763.5	2766.2

4.5.3. VERIFICATION OF LABORATORY SCALE SIMULATIONS AND VALIDATION WITH EXPERIMENTAL RESULTS

In this section the verification results from the mean (M) and mean-variance (MV) calibration for the interpolation- and regression-based metamodels (IBM & RBM) are presented. In Section 4.5.3.1 the results from the verification simulations are compared to the KPI values corresponding to the calibration results. This comparison gives an indication of the quality of the metamodel predictions in the calibration procedure. In Section 4.5.3.2 the results from the verification simulations are compared to the calibration targets which gives insight on the quality of calibration results. For the DEM parameter sets of the cases where [1,...,10, 15, 20, 30, 40, 50] repetitions were used the simulations of the laboratory scale experiments are verified.

5.4.3.1. COMPARISON KPI VERIFICATION SIMULATIONS AND CALIBRATION RESULTS

The calibration results are a prediction by the metamodel which can include errors as shown with the training and validation error evaluation in Section 4.5.1. In Figure 4.15 (a-d) the error percentage between the calibration and verification results for the mean of each KPI and mean \pm standard deviation of each KPI are shown to indicate the magnitude of this metamodel prediction error. For the IBM-M and IBM-MV results in Figure 4.15 (a) and (b) large errors with respect to the calibration results is seen for the Angle of Repose β and the Angle of Movement θ when the number of repetitions is below 10. For the IBM-M calibration results the error in the Angle of Movement stays large until 30 repetitions and reduces for a higher number of repetitions. On the contrary, the Angle of Repose becomes more accurate after 10 repetitions but becomes inaccurate after 30 repetitions. This might be caused by overfitting which is a known risk of interpolation-based metamodels. Figure 4.15 (b) shows similar behaviour for the IBM-M and IBM-MV calibration results, however the point of change is located at 20 repetitions instead of 30. Overall, the verification results show that for mean and mean-variance calibration with interpolation-based metamodels large errors can occur even at higher numbers of repetitions. For the error in the mean \pm standard deviation bandwidth asymmetry can be observed which is caused by the inaccurate prediction of the mean. The Angle of Repose exhibits an error of -10% for the upper limit and -20% for the lower limit. The error is within 5% for the Angle of Movement and is below 1% for the Bulk Density.

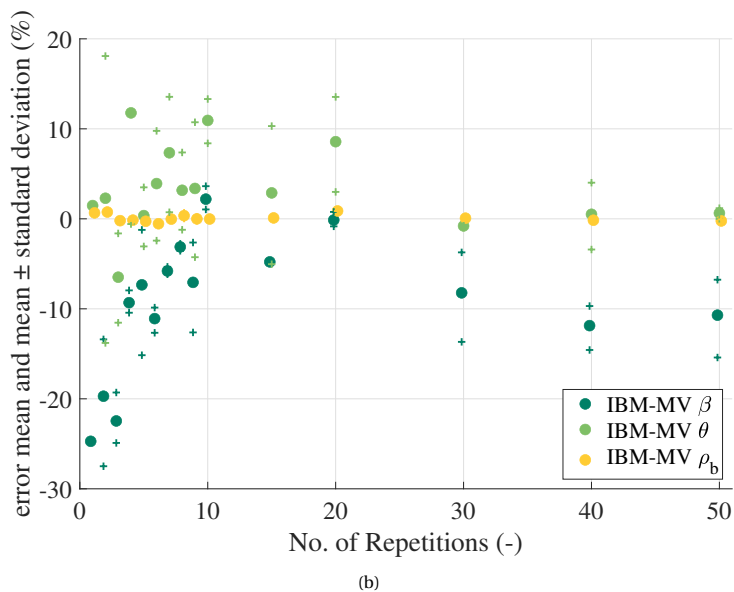
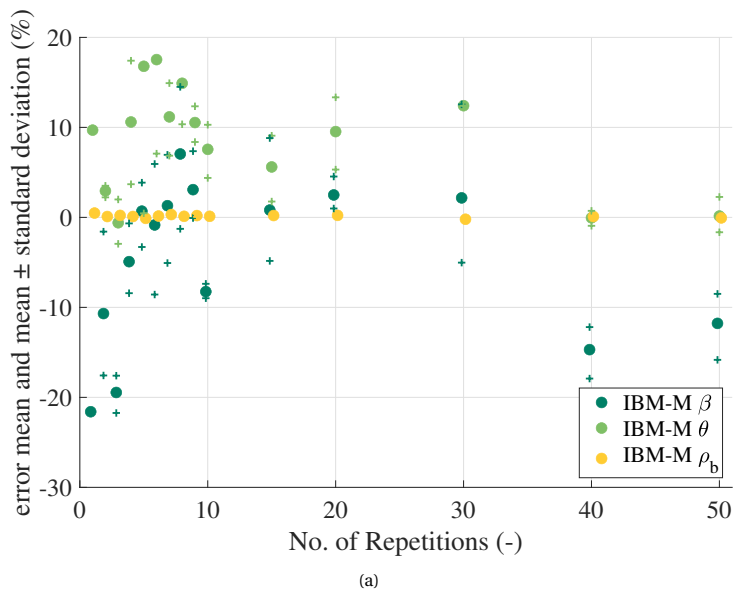
In Figure 4.15 (c) and (d) the verification error of the regression-based metamodel calibration results are shown. For the mean prediction by both mean and mean-variance calibration results large errors are observed up to ten repetitions but the magnitude is

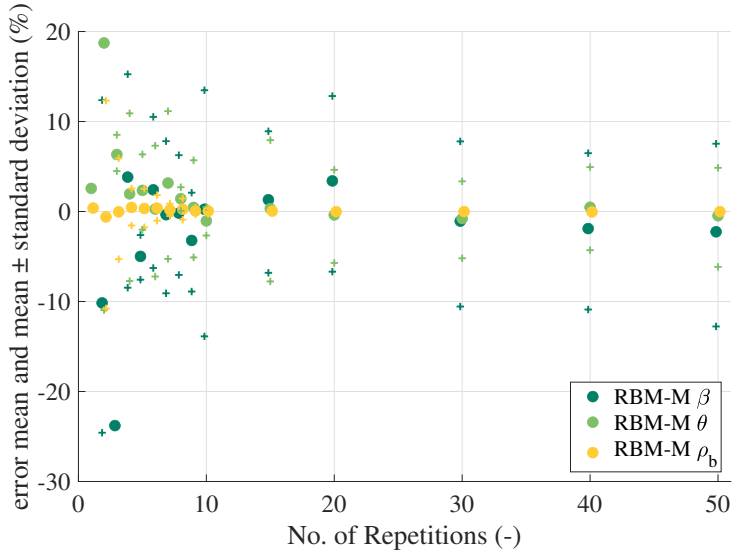
smaller than for the IBM calibration results. The errors for the mean \pm standard deviation are significant. After 10 repetitions, the verification error is close to zero for the Angle of Movement and bulk density for both the mean and mean-variance calibration. For the Angle of Repose the error stays within a 5% bandwidth when the number of repetitions is increased. The error in the mean \pm standard deviation bandwidth is quite symmetric because of the accurate prediction of the mean value. However, the magnitude shows an error of 15% for the Angle of Repose, 7% for the Angle of movement and below 1% for the Bulk Density. As expected for both IBM and RBM the error in the Bulk density prediction is small because the error in the validation of both metamodels was small.

4.5.3.2. COMPARISON KPI VERIFICATION SIMULATIONS AND CALIBRATION TARGETS

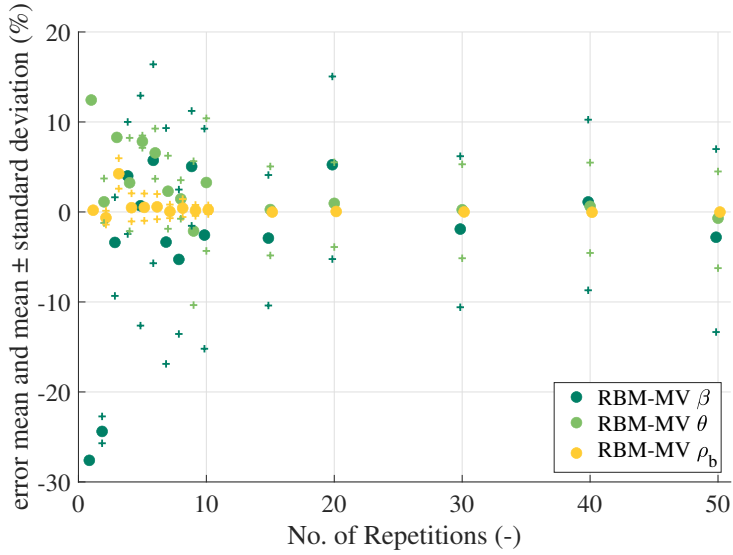
The verification simulations show that RBM metamodels give more reliable calibration results. However, the next step is to look at the quality of the calibration results compared to the calibration targets. In Figure 4.16 the percentage error between the calibration results and calibration targets are shown for the mean and mean-variance calibration with the IBM and RBM metamodels. While the calibration results for the interpolation-based metamodels showed a good fit to the calibration results in Figure 4.14, it can be seen in Figure 4.16 (a) and (b) that the error observed with the verification leads to errors with the calibration target. This is especially visible for the Angle of Repose up to 30 repetitions and Angle of Movement after 30 repetitions. For the IBM calibration it is observed that the calibration results are inconsistent with the increase of the number of repetitions. The RBM calibration results in Figure 4.16 (c) and (d) show more consistency. Especially after 30 repetitions a balance can be found between the error for the Angle of Repose and Movement where the percentage error stays the same. The stability and consistency in these results make the regression-based metamodel calibration more reliable. There are no significant differences observed between the mean and mean-variance calibration.

To determine which calibration method performs best the results for 50 repetitions are compared to the experimental results for the calibration targets. In Table 4.8 the percentage error between the verification result and calibration target is shown for 50 repetitions. At 50 repetitions, the percentage error for the calibration with interpolation-based metamodels is between 11 and 14% for the Angle of Repose, 1 and 1,5% for the Angle of Movement, and 0,5 to 2,5% for the Bulk Density. The results for the calibration with regression-based metamodels shows errors between 5 and 6% for the Angle of Repose, 4,5 and 5,5% for the Angle of Movement and 0,1% for the Bulk Density. Here it is clearly visible that even though the errors in matching the calibration targets is quite large the calibration results with regression-based metamodels are more balanced than those of the interpolation-based metamodels. Due to the errors in the mean value of the KPIs the bandwidth of the standard deviation will exhibit an asymmetric error as presented in the bottom section of Table 4.8. On average, the mean-calibration with the regression-based metamodels presents the best match to the experimental calibration targets and gives the most reliable DEM parameter set for this case. Based on these results it can be seen that the predictions by regression-based metamodels are more reliable which makes these a better choice for the calibration of the DEM parameters even though in the final results the predictability of the mean \pm standard deviation is poor. The discrepancy in the mean \pm standard deviation might also be a result of the modelling assumptions for the DEM models of the laboratory experiments themselves, where the stochastic behaviour as



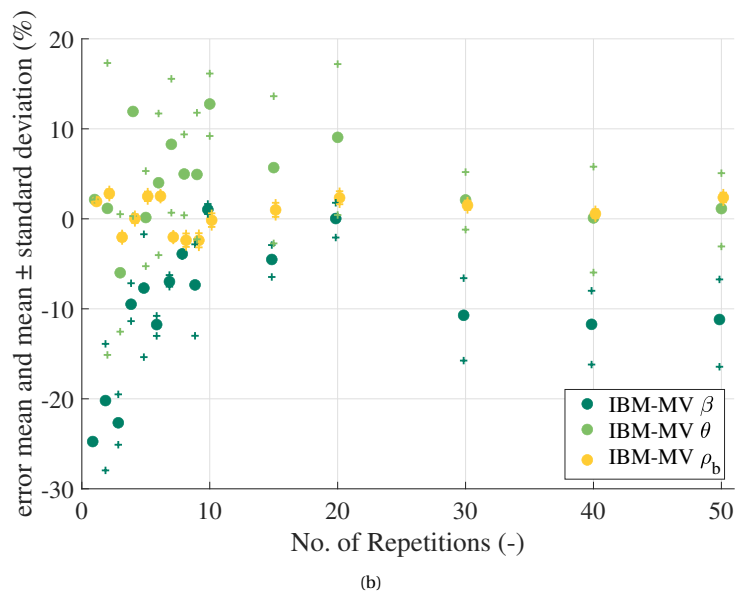
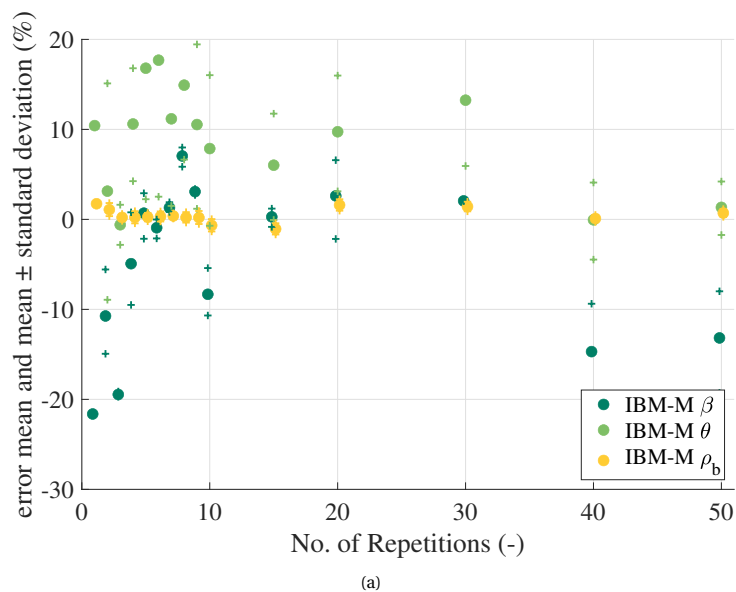


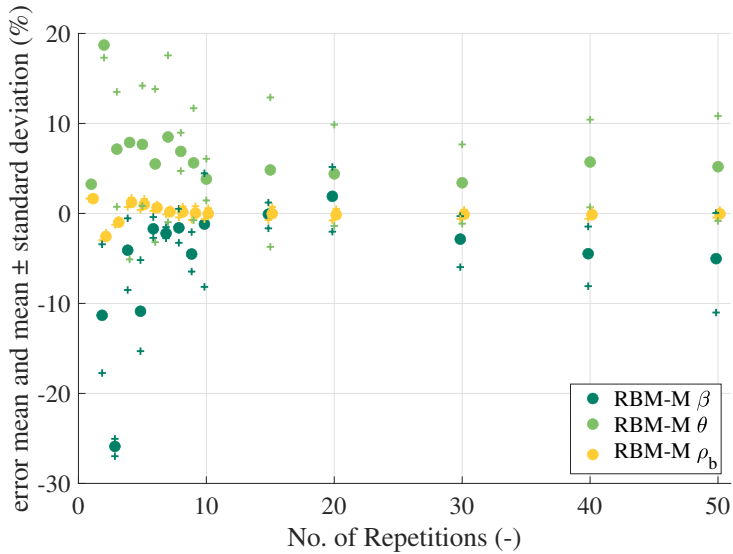
(c)



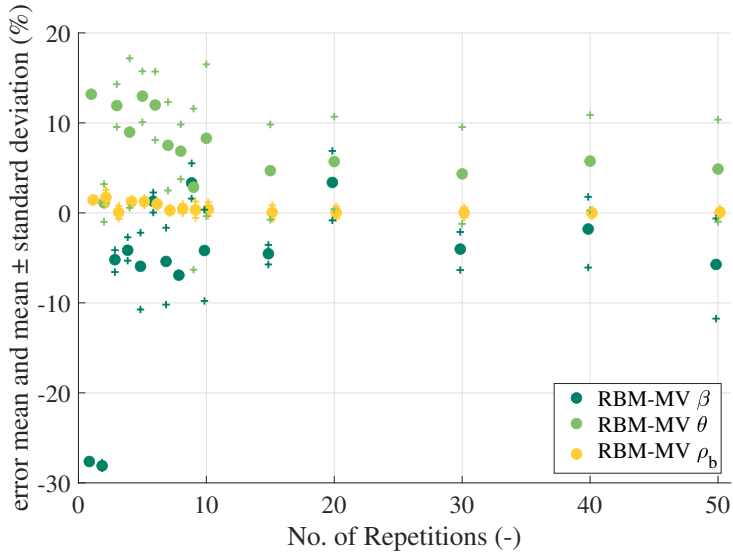
(d)

Figure 4.15: Percentage error for the mean (·) and mean \pm standard deviation (+, Δ) for the Angle of Repose β (blue), Angle of Movement θ (red), Bulk Density ρ_b (magenta) for (a) interpolation-based metamodel mean calibration (b) interpolation-based metamodel mean-variance calibration (c) regression-based metamodel mean calibration (d) regression-based mean-variance calibration.





(c)



(d)

Figure 4.16: Error verification results to calibration targets

Table 4.8: Percentage error between verification results and experimental calibration target values where the underlined results show the most accurate result

	IBM mean	IBM mean-variance	RBM mean	RBM mean-variance
Mean KPI % error				
AoR	-13.17	-11.19	-5.02	-5.73
AoM	1.34	1.14	5.19	4.87
BD	0.71	2.37	-0.04	0.06
Mean \pm standard deviation KPI % error				
AoR	-8.00 / -19.28	-6.73 / -16.44	0.05 / -11.01	-0.62 / -11.75
AoM	4.21 / -1.73	5.07 / -3.07	10.83 / -0.83	10.36 / -0.99
BD	0.28 / 1.14	1.84 / 2.91	-0.47 / 0.38	-0.39 / 0.52

seen in experiments is captured to a lesser extent. As shown in the results, there is no significant difference in the outcome of the mean vs. mean-variance calibration using the regression-based metamodels. In addition, the calibration procedure using multiple laboratory setups leads to a multi-objective problem for which it is not certain that there is an optimal solution matching all the targets perfectly. As decided in Section 4.4.3 the weight of each objective was kept to one for the mean and 0.5 for the variance interval. By changing these values objective weights can be changed, ultimately affecting the outcome of the calibration. An in-depth investigation of this influence is however outside of the scope of this study.

4.5.4. VALIDATION OF HOPPER MODEL

In this section we present the validation of the DEM model of the hopper described in Section 4.3 with the experimental results described in Section 4.2. For this model the discharge rate of the hopper during steady flow is compared for the DEM model of the hopper and the experiments. The calibration of the DEM parameters lead to 4 sets (IBM-M, IBM-MV, RBM-M, RBM-MV) of DEM parameters for each number of repetitions that was used in training the metamodels for the calibration. For the DEM parameter sets of the cases where [1,...,10, 15, 20, 30, 40, 50] repetitions were used the hopper simulations have been carried out five times, the same as the number of experiments. In Figure 4.17 the obtained mean and standard deviations for the discharge rate are shown for each of the cases. In these results a large difference between the results obtained with the interpolation-based and regression-based metamodels can be observed. The interpolation-based metamodel calibration results show for both the mean and mean-variance calibration that there is much fluctuation in the results. The mean-calibration mean error follows an irregular path which is close at 30 repetitions but far from the validation target for the other points. In the mean-variance case the mean error tends to decrease up to 15 repetitions after which the error starts increasing continuously. In terms of the bandwidth of the mean \pm standard deviation large fluctuations are present for the mean calibration but less for the mean-variance calibration. Indicating that including

the variance in the calibration has a certain effect. Compared to the bandwidth of the validation target the bandwidth in the simulation results is larger. For the regression-based metamodel calibration the results are closer to the experimental results for the entire range of repetitions. Both mean and variance calibration cases show a stable offset which starts decreasing after 15 repetitions. For the mean \pm standard deviation it is observed that after 10 repetitions the bandwidth stabilises at a bandwidth that is around two times the bandwidth of the validation target. From these results it can be seen that the calibration with the regression-based metamodels leads to more stable output compared to the calibration with the interpolation-based metamodels. Mean-variance calibration shows slightly better performance than the mean calibration but in terms of confidence intervals with five repetitions this observation is not significant. Table 4.9 shows the mean and the standard deviation of the discharge rate for the calibration results with 50 repetitions. For both these results the 95% confidence intervals are also shown based on a t-distribution where $n=5$. For these intervals we applied the same method as described in Section 4.2. In the third column the relative errors to the mean and the mean plus minus the standard deviation are shown.

The results show that for the discharge rate the mean-variance calibration with the stochastic model gives the most accurate prediction of the discharge rate (RBM-MV). This model is followed by the mean calibration with the stochastic model (RBM-M), the mean calibration with the deterministic model (IBM-M), and lastly the mean-variance calibration with the deterministic model (IBM-MV). Differences of up to a factor 6 are found in the mean error percentage, while all methods use the same dataset. This illustrates the importance of using the correct calibration procedure. Overall, it is observed that the variance prediction shows large errors with respect to values found in the experiments. This indicates that the results from the DEM model of the hopper with the optimal DEM parameter sets have a higher variability than those from the experiments. Reasons for this observation might be the simplification of particle shape from irregular to spherical and uniformity assumption of material properties and contact parameters in the DEM model.

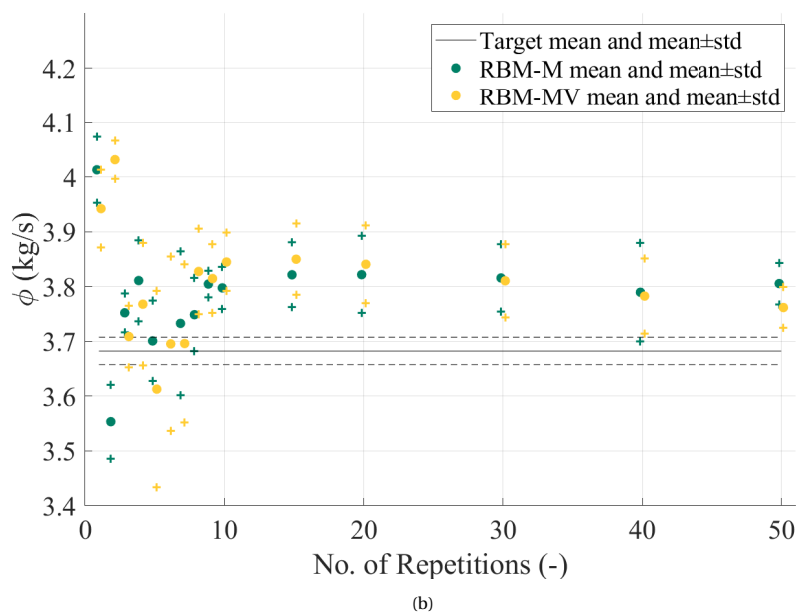
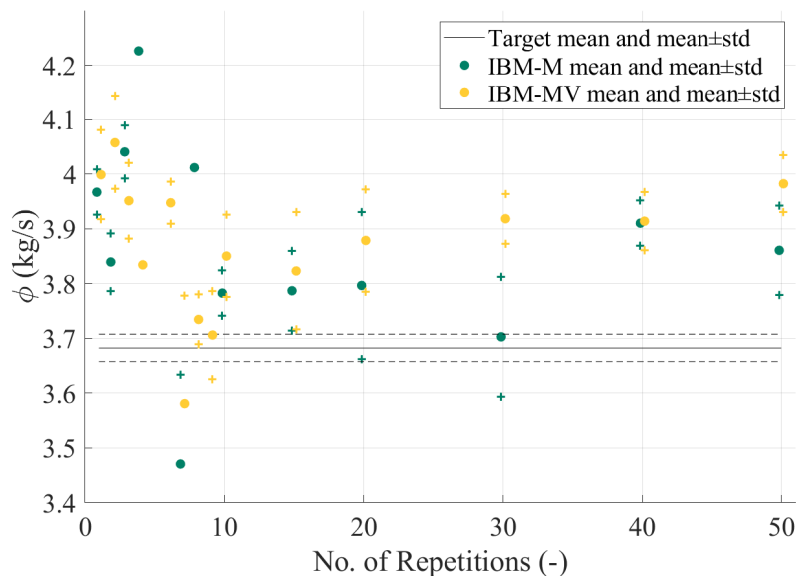


Figure 4.17: Results for the validation simulations of the hopper with respect to the number of repetitions

Table 4.9: Percentage error between verification results and experimental calibration target values where the underlined results show the most accurate result

Model	Discharge rate $\phi(kg/s)$	Percentage error with respect to the experimental results
	mean (95% CI [LL;UL]) \pm sigma (95% CI [LL ;UL])	
Experimental results	3,70 (95% CI [3,67 ;3,73]) \pm 0,026 (95% CI [0,014 ; 0,056])	Reference
IBM-M	3,86 (95% CI [3,77 ;3,95]) \pm 0,081 (95% CI [0,036 ; 0,260])	mean error 4,84% (mean \pm std) error (3,33% ,6,33%)
IBM-MV	3,98 (95% CI [3,92 ;4,04]) \pm 0,052 (95% CI [0,023 ; 0,167])	mean error 8,15% (mean \pm std) error (7,46% ,8,83%)
RBM-M	3,81 (95% CI [3,76 ;3,85]) \pm 0,038 (95% CI [0,017 ; 0,121])	mean error 3,34%(mean \pm std) error (3,01% ,3,67%)
RBM-MV	3,76 (95% CI [3,62 ;3,80]) \pm 0,037 (95% CI [0,016 ; 0,118])	mean error 2,15% (mean \pm std) error (1,84% ,2,46%)

4.6. CONCLUSION

Experiments with granular materials often exhibit significant variation, which have to the best of the authors' knowledge not been included in calibration approaches. In this paper we investigated the inclusion of stochastics throughout the development of the DEM model, in the calibration, verification with lab experiments, and validation with a hopper application. We used metamodels to predict KPI values and proposed a mean-variance calibration approach that includes the variance of the calibration experiments in the objectives of the calibration procedure. The conclusions of this study are as follows.

- The calibration experiments showed stability for the KPI mean after 5 repetitions for the bulk density, 10 for the Angle of Movement, and 30 for the Angle of Repose. However, in practice 3-5 repetitions is common which means that increasing the number of repetitions should be considered for obtaining reliable calibration targets.
- Stabilization of experimentally obtained variances occurs at a higher number of repetitions than stabilization of the mean, which is an additional motivation to consider the required number of repetitions.
- Based on the verification results in this study, regression-based metamodels prove to be better at predicting mean KPI values than interpolation-based metamodels, both in terms of accuracy and number of required repetitions, and are therefore recommended in metamodel or surrogate model based calibration.
- Both regression-based and interpolation-based metamodels give inaccurate predictions of the variance for the DEM models of both the calibration and the validation experiment. The cause of these inaccuracies might be related to the modelling assumptions in the DEM model or to the used number of repetitions in training the metamodel.

- Accurate prediction of KPI variances by metamodels proves to be harder than predicting KPI means. Therefore, further research is needed on accurately including the variance in DEM model calibration.

Although this study focused on a particular granular material, DEM model and application example, it is expected that the observed trends and the associated conclusions extend to a wide range of use cases, due to the inherent stochastic nature of granular processes. Therefore, it is recommended to conduct further research on including and identification of stochastic behavior in granular processes and their implications on DEM modeling of particulate systems.

5

DETERMINISTIC VS. ROBUST DESIGN OPTIMIZATION OF A DISCHARGING HOPPER: A VALIDATED CASE STUDY

In design of bulk handling equipment optimization techniques are not commonly applied because of the high computational costs of detailed models such as DEM. As shown in the previous chapters, metamodels are a technique which makes capturing global behaviour and calibration more effective. These metamodels make design optimization of bulk handling equipment possible. In this chapter the numerical data obtained with the hopper DEM model is used to train a stochastic metamodel. This stochastic metamodel is used to investigate deterministic and robust design optimization strategies for hopper design. The results from the optimization are validated through a series of additional hopper discharge experiments. These results show that reliable designs can be obtained through the presented design process and that including metamodels makes the entire process more efficient.

Parts of this chapter have been published in the Journal of Powder Technology, M.P. Fransen, M. Langelaar, D.L. Schott, Deterministic vs. robust design optimization using DEM-based metamodels (2023) [112].

5.1. INTRODUCTION

In design of Bulk Handling Equipment (BHE) the use of Discrete Element Method (DEM) models to predict and evaluate performance in equipment design is increasing. The major advantage of this approach is the ability to evaluate a wide range of equipment designs without the need of conducting expensive experiments. The major downside is that if the number of particles [113], complexity of the equipment kinematics [13, 105], and interaction complexity [100, 114] increases, the computation time of simulations is increases as well. In addition, DEM models require calibration which also becomes a computationally intensive process if the number of calibration parameters is increased [8, 51, 115].

To counteract these high computational costs, metamodels are used in both calibration of and design of bulk handling equipment. Richter & Will introduced a metamodel-based global calibration (MBGC) framework and showed how metamodels can be effectively used in calibration [116]. Most DEM calibration optimization problems are multi-objective optimization problems (MOOP) with multiple calibration parameters [115]. Furthermore, a number of metamodeling approaches were successfully used in calibration of DEM models. Artificial neural networking (ANN), Gaussian process regression (GPR), multi-adaptive regression splines (MARS), and universal kriging (UK) were applied by Richter et. al. [106]. An iterative Bayesian framework including a Gaussian mixture model (GMM) is used by Cheng et. al. [8]. Based on the findings by Fransen et. al. (2022) it is recommended to use regression-based metamodels for the mean prediction to obtain accurate calibration results at low costs. Similar benefits are expected in using metamodels for design optimization where typically a large number of performance evaluations is required. However, it is important to note the limitations of the use of metamodels as they are approximations of the DEM model and therefore inherit a model error. Overall, metamodels perform well when used to interpolate but poor in extrapolation. Therefore, quality of the data and the sampling are important for the performance of a metamodel. Metamodel-based design optimization (MBDO) is referred to by Wang & Shan [19] but in design of bulk handling equipment metamodels have not been used extensively [55]. In design, we generally have to deal with similar problems as in DEM model calibration: multiple design parameters and performance characteristics, which requires similar solving techniques.

Currently, the focus of optimization of BHE designs is on the mean performance of the equipment [11, 13], i.e. the deterministic approach. However, granular systems are stochastic in nature resulting in uncertainty of design performance. To achieve an optimal design which has a good match to the mean performance and a minimized variance robust optimization strategies can be applied [117, 118]. As indicated for the calibration of DEM models it is an effective approach to use DEM-based metamodels in MBDO instead of DEM simulations in the loop for calibration parameter estimation. In the case of robust design optimization, metamodels can be used in a similar fashion because they can predict both mean and variance. To the authors' knowledge, robust MBDO has not been investigated in relation to bulk handling equipment design.

The aim of this study is to show how robust metamodel-based design optimization can be applied to bulk handling equipment design with DEM-based metamodels and, to show how this method compares to a conventional deterministic approach and to identify application challenges. In this study, we present a methodology/framework for robust Metamodel-based Design Optimization (MBDO) for design of bulk handling equipment in Section 5.2. Next, Section 5.3 describes the design problem for a discharging hopper starting with a description of the experimental setup and DEM model, followed by the analysis of experimental and DEM results and sampling of the design space. It continues with a description of training the DEM-based metamodel and a formulation of the optimization problem. Lastly, the two design case studies are described to which the robust MBDO approach and deterministic MBDO are applied. In Section 5.4, the resulting DEM training set is evaluated as well as the resulting metamodel. This is followed by the results of the two design case studies where deterministic and robust optimization are compared. This section ends with a discussion on the obtained results related to the quality of the DEM data compared to experiments, mismatch between DEM metamodel predictions and the verification results, and the discrepancies observed between DEM metamodel predictions and experimental results.

5.2. METHODOLOGY

Bulk handling equipment is used to transport or process wide varieties of granular material. However, the behaviour of a granular material in general is stochastically distributed. This stochastic behaviour is caused by differences in particle packing's, sizes and in variations of material properties. Additionally, properties of the bulk material such as consolidation, moisture content, and temperature might affect the inter-particle physics leading to variable bulk strength and cohesion. This leads to distributed performance of the BHE around a certain mean performance. Even though this is known, the stochastic behaviour of the granular material and its effect on the equipment performance is not considered in the design process. Therefore, we introduce a methodology that includes the stochastic behaviour of granular materials in the bulk handling equipment design process.

In this section the global implementation of robust metamodel-based design optimization (MBDO) including verification and validation to design of bulk handling equipment is explained. The scheme in Figure 5.1 shows the steps taken in the design process of BHE if MBDO, verification, and validation are included. A bulk handling equipment design problem starts with describing the system or problem where design and key performance indicators (KPIs) are defined. The next step in the approach is to create a numerical model of the equipment and the material that needs to be handled. For this purpose the Discrete Element Method (DEM) is used which can simulate behaviour of the bulk and interaction with the equipment. However, DEM models are generally a simplification of the physical system and are therefore reliant on calibration of material and contact parameters of the DEM model. After the calibration of the DEM model, this model needs to be validated to demonstrate that the model possesses a satisfactory range of accuracy consistent with the intended application of the model within its domain of applicability [119]. The calibrated

and validated DEM model of a hopper used in this study is adopted from Fransen et. al. [51]. DEM simulations take a considerable amount of time, which makes direct use of DEM models in optimization inconvenient. To overcome this, a metamodel-based design optimization (MBDO) procedure can be used. This procedure uses a DEM data set to train a metamodel which gives predictions on BHE performance at low cost.

The first block in MBDO is design space sampling and DEM data generation shown in Figure 5.1. After sampling the data, the DEM model can be used to generate the data. As the DEM model is stochastic due to the random initial packing of material this means that the simulations need to be repeated for each sampling point. This gives information about the average performance and the standard deviation of the design performance prediction. For a metamodel to be able to predict both mean and variance, it is essential that both are included in training the metamodel.

The second step in MBDO is metamodel training, which has been thoroughly described by Fransen et. al. for a DEM case study [55]. For the proposed robust optimization it is required that information on the standard deviation of a KPI is supplied during training of the metamodel such that the metamodel can be trained to give predictions of both mean and variance of the KPI. In training the metamodel, hyper-parameter optimization is included such that the best fit of the metamodel to the data is obtained [86]. Moreover, a common step is to use resampling to improve the quality of the metamodel. However, when the set verification and validation tolerances are not violated by the initial sample resampling is not required. In Section 5.3.4 the metamodel training procedure and the relation to the case study is discussed in more detail.

After training the metamodel, the next step is design optimization which can be further divided in two types, deterministic and robust optimization. In deterministic optimization, only the mean performance of the BHE is used to find the optimal design whereas in robust optimization the standard deviation of the BHE performance is also included. These differences are further discussed in Section 5.3.5, which also elaborates, on solving the optimization problem leading to the optimal design(s). Next, the found optima need to be verified by carrying out DEM simulations of the found designs. For the verification of the results, a tolerance is set for the maximum error of the designs' performance relative to the optimization target. If the tolerances are not met, resampling of the design space can be carried out or the weights in the optimization problem can be adjusted. When the results have reached the desired accuracy, the next step is to validate the optimal designs using an experimental setup. For the validation, an additional tolerance is set which should be higher than the verification tolerance because there is a probability of error propagation through the subsequent steps. If the design reaches the criteria, a design with the desired performance is obtained and the design procedure is successful. Verification, validation, and the case studies are further discussed in Section 5.3.6.

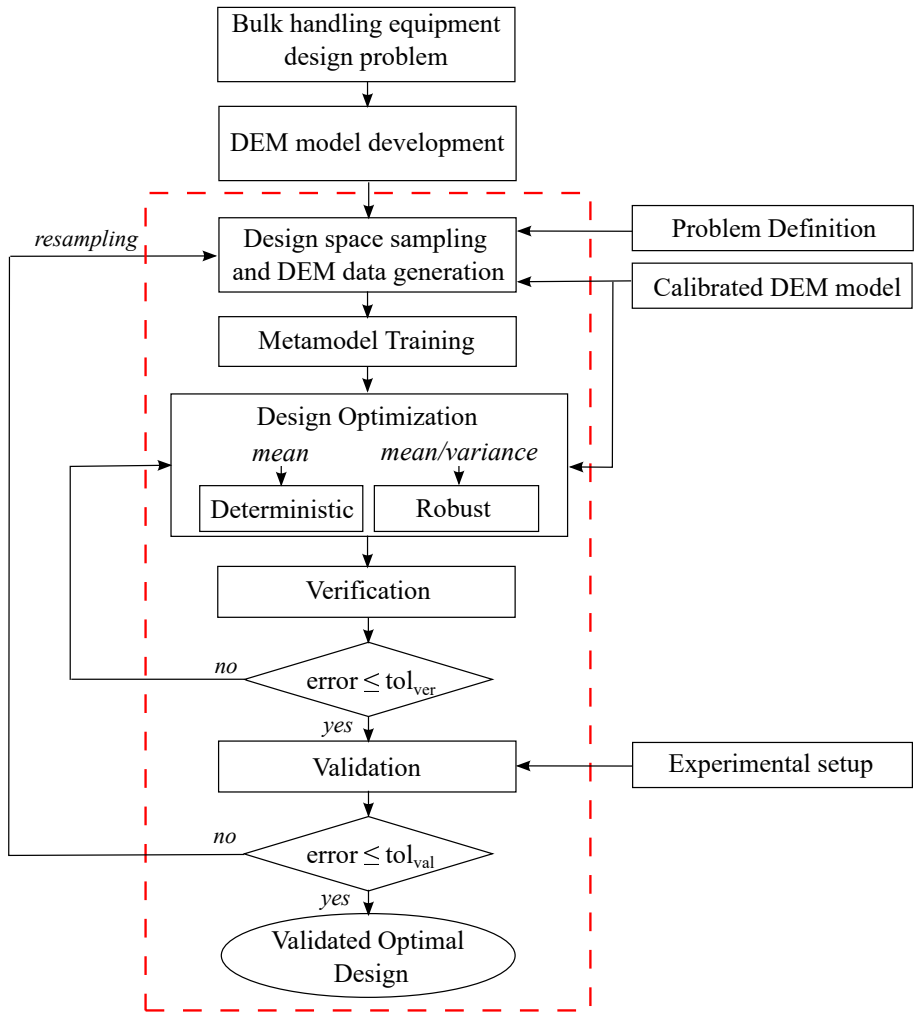


Figure 5.1: Framework for Metamodel-based Design Optimization (MBDO) (red area) included in the process for bulk handling equipment design

5.3. DEM-BASED METAMODEL DESIGN OPTIMIZATION FOR A DISCHARGING HOPPER

The metamodel-based design optimization (MBDO) method described in Section 5.2 is applied to a hopper case study that will be described in this section in more detail. Specific choices made for the various steps are also detailed here. Hoppers are pieces of bulk handling equipment that are frequently used in processing plants to regulate flows of material. In the design of a hopper there are many restrictions such as occupied space and which construction materials can be used in combination with the bulk being processed. However, the key performance indicator (KPI) that is most frequently used to assess the effectiveness of a hopper is the discharge rate.

5.3.1. EXPERIMENTAL SETUP AND DEM MODEL OF HOPPER

In this study, an experimental setup of a semi two-dimensional hopper is considered which has been shown in Figure 5.2. This setup consists of four adjustable stainless steel wall sections which can be used to change the geometry of the hopper. These four adjustable walls are clamped between two 5 mm Perspex plates. The setup is positioned on load cells such that the force exerted by the bulk can be measured. For further information on the experimental setup the reader is referred to Fransen et. al. [51]. The load cell data from the experiments is used to determine the discharge rate. In addition, the setup is used to validate the results from the deterministic and robust MBDO. Gravel is used as a bulk material in this experimental setup and was modelled in DEM using spherical particles. The gravel has been stored in a dry environment with a low humidity, therefore we assume the material can be regarded as dry and has no cohesion. In addition, the material falls under the well-graded gravel category for which it is common to take zero cohesion into account (Swiss Standard SN 670 010b, Characteristic Coefficients of soils, Association of Swiss Road and Traffic Engineers). After calibration of the DEM model, the hopper discharge was validated for a hopper configuration with a hopper angle α of 45° and a discharge opening W_o of 100mm. The model from this study showed an overestimation for the mean of 2,15% and 42% higher standard deviation. Even though the error in standard deviation is large it is only 1% of the mean. We assume that this level of error is in the same range in the selected design space. The DEM model is used to replicate the experimental setup and to generate a DEM data set for the metamodel. In Figure 5.3 (a) an image of the experimental setup of the hopper is shown and a still from the initial configuration of the DEM simulation in (b).

5.3.2. ANALYSIS OF EXPERIMENTAL AND DEM SIMULATION RESULTS

The KPI of the case study is the steady-state discharge rate ϕ for which both the mean and standard deviation are used. From the hopper discharge experiment the force ($F_{loadcell}$) exerted by the bulk material on the load cell over time is obtained which can be used to determine the steady-state discharge rate. In Figure 5.4 (a,b) the process of determining the discharge rate is illustrated for the experimental and DEM data respectively. A difference between the experimental and DEM data is the presence of spikes in the force

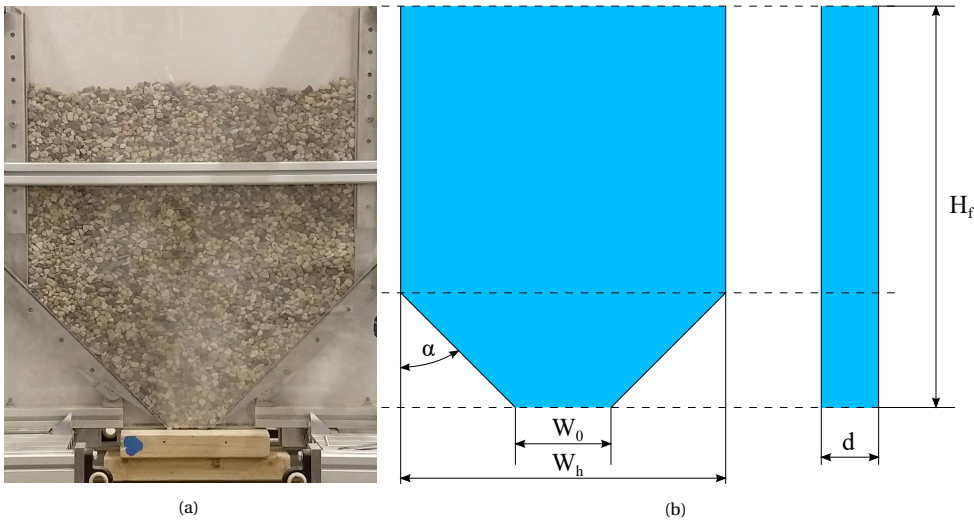


Figure 5.2: Experimental hopper setup (a) and dimensions (b) $W_h = 602\text{mm}$, $d=5\text{mm}$. The fill height depends on the mass inserted.

data. This is explained by the difference in measurement location. The force measurement in the experiment is not located on the walls as is the case for the simulation result but under the base of the setup. The structure between the walls and the load cells has a dampening effect on the forces on the wall and therefore the measurement.

To obtain the average discharge rate in kg/s the average force exerted per second needs to be determined. Assuming this value is stable we can divide this force by the gravity constant (g) to obtain the average mass discharged per second. This value approximates the discharged mass that cannot be measured exactly in the experiment. Even though it is possible to determine the exact mass discharged in a DEM simulation we use the force-based approach because this gives results for experiments and simulations that can be compared. The fitted data between the force based and mass based discharge rate in the DEM simulation showed small deviations and are therefore representative for the performance.

5.3.3. SAMPLING OF DESIGN SPACE AND NUMBER OF REPETITIONS

The design space in this case study is sampled in an irregular spaced rectangular grid for discharge openings of 50, 75, 100, 150, and 200 mm and angles 20, 30, 45, 60, 75, 82.5, and 90 degrees as shown in Figure 5.5. For the hopper angles, a minimum of 20 degrees was chosen because of the limits of the experimental setup. At the high end of the angles, an additional sample was added at 82.5 degrees to have a higher information density in this location. The used sample consists of 35 points which means that this sample has a sampling density of $35^{1/2} = 5.92$ per unit length in the normalized design space. This is approximately in the same range as the sampling density used in previous work for a

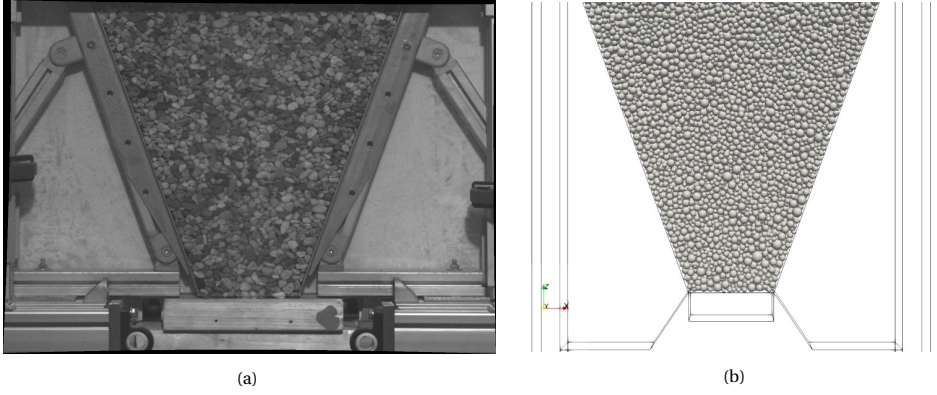


Figure 5.3: (a) Picture of experiment where the block at the bottom prevents the discharge of material (b) Picture of simulation where only the walls and bottom of the experimental setup are modelled.

5

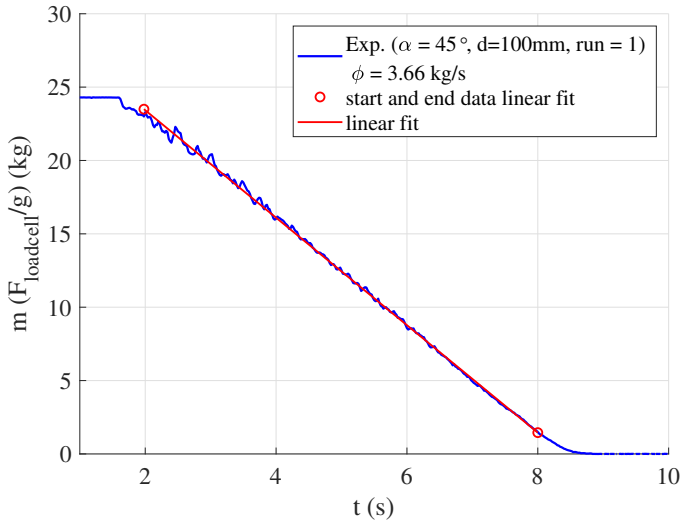
three-dimensional calibration case [51]. For each design point in the sampling we carry out five repetitions to get an average and a standard deviation. This number is enough considering that the discharge rate is already a steady-state value averaged from time dependent discharge data. The results of these simulations are discussed in Section 5.4.1.

The sample shown in Figure 5.5 has also been carried out using the experimental setup. To be consistent with the experiments the number of repetitions is kept the same as with the experiments. At a 150 mm discharge opening and 75 degree angle the number of repetitions is equal to four because of a failed experiment. The same holds for one of 20-degree angle and 75 mm discharge opening experiment. For the 50 mm experiments it was decided to use five repetitions as a basis and extend to ten if arching occurred. In the 60-degree case, arching occurred five times and therefore the additional 5 repetitions were not conducted. The 20-degree case was repeated 10 times but two of those experiments failed. To be consistent with the experiments that have been carried out we used the same initial mass of bulk material contained in the experiment in the simulations and used the same number of repetitions for each design in the sample. In calculating the mean, standard deviation, and confidence intervals the different number of repetitions accounted for.

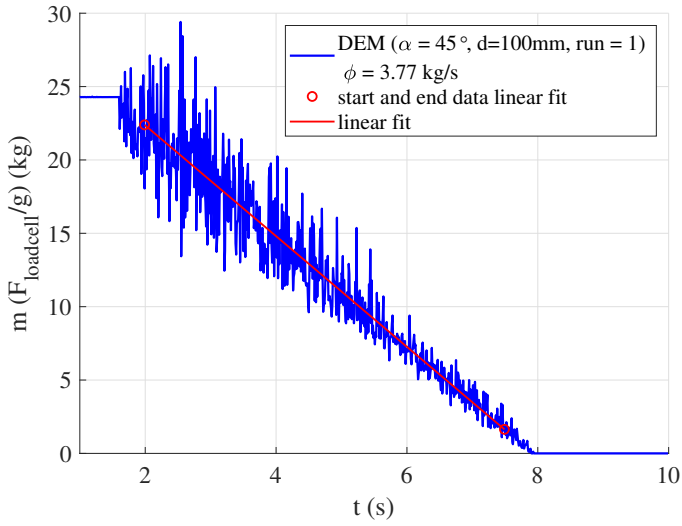
5.3.4. METAMODEL TRAINING

The generated DEM data for the sample of the design space is used to train a Gaussian Process Regression (GPR) type stochastic metamodel [86]. Before the data is used, feature scaling based normalization is used which shifts the data to a $[-1,1]$ range. The standard deviation corresponding to the mean values is converted to the coefficient of variation σ/μ which is input for the σ_n component in the training procedure.

The metamodel is denoted by $G_{KPI}(x^*)$ for any given KPI where x^* is a vector containing the design variables for which a prediction of the mean and variance of the KPI is desired.



(a)



(b)

Figure 5.4: Determining discharge rate from load cell data (a) and from the simulation of the same experiment (b)

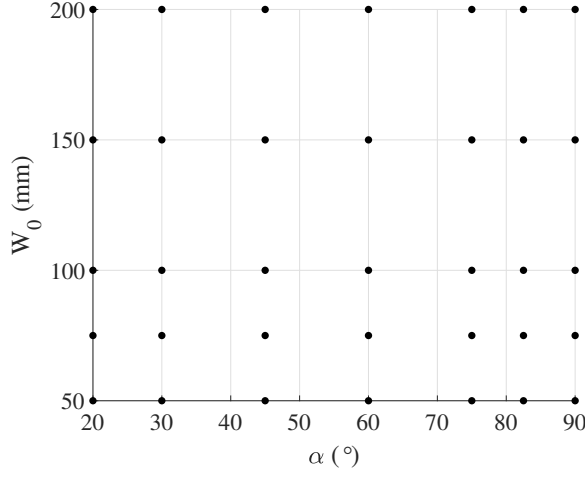


Figure 5.5: Determining discharge rate from load cell data (a) and from the simulation of the same experiment (b)

5

In the case study, the KPI is the discharge rate and the design variables are the hopper angle α and the size of the discharge opening W_o , $x^* = [\alpha^* W_o^*]$. The metamodel is trained with the DEM data generated for the sample presented in Section 3.3 which consist of a mean and variance value of the KPI at the data points in the sample. By including both mean and variance in training the metamodel we allow the metamodel to predict the mean and variance. In training the metamodel we assume that the variance obtained in the data points from the training set is the true variance [51]. Thus, the trained DEM-based metamodel gives a prediction of the mean and the variance in the design space.

The GPR metamodel uses a basis function to obtain the correlation between two points x_1 and x_2 . Here x_1 and x_2 can both be training points, two prediction points, or a training and a prediction point. In this case the basis function is a squared exponential Gaussian ψ in R^2 ,

$$\psi = \sigma_f e^{-\frac{1}{2l^2} r(x_1, x_2)^2} \quad (5.1)$$

where σ_f and l^2 represent the first two hyper parameters and $r(x_1, x_2)$,

$$r(x_1 = [\alpha_1, W_{o,1}], x_2 = [\alpha_2, W_{o,2}]) = \sqrt{c_1(\alpha_1 - \alpha_2)^2 + c_2(W_{o,1} - W_{o,2})^2} \quad (5.2)$$

is a function which determines the Euclidian distance between two points, x_1 and x_2 . This distance is determined based on the two design variable values in the two points which are adjusted by the second two hyperparameter values c_1 and c_2 . Here c_1 and c_2 function as a shape parameter for the basis function on the design variables α and W_o .

The metamodel $G_{KPI}(x^*)$ is used for mean and variance prediction of the KPI. The mean prediction function,

$$\begin{aligned}
G_{KPI}(x^*) &= k_{KPI}(x, x^*)^T (K_{KPI}(x, x) + \sigma_{KPI,n}^2 I)^{-1} y_{KPI} \\
&= \begin{bmatrix} \psi(x_1, x^*) \\ \vdots \\ \psi(x_n, x^*) \end{bmatrix}^T \left(\begin{bmatrix} \psi(x_1, x_1) & \dots & \psi(x_1, x_n) \\ \vdots & \ddots & \vdots \\ \psi(x_n, x_1) & \dots & \psi(x_n, x_n) \end{bmatrix} + \begin{bmatrix} \sigma_{KPI,1}^2 & \dots & 0 \\ \vdots & \ddots & \vdots \\ 0 & \dots & \sigma_{KPI,n}^2 \end{bmatrix} \right)^{-1} \begin{bmatrix} y_1 \\ \vdots \\ y_n \end{bmatrix}
\end{aligned} \tag{5.3}$$

consists of the correlation between the training points x_1 to x_n and the predicted point x^* , $k_{KPI}(x, x^*)$. Based on the summation of the Gram matrix $K_{KPI}(x, x)$ and the variances $\sigma_{(KPI,n)}^2$ of the system and the reference values y_{KPI} in the training points a prediction is made for the mean value. The variance predictor,

$$\begin{aligned}
V_{KPI}(x^*) &= k_{KPI}(x^*, x^*) - k_{KPI}(x, x^*)^T (K_{KPI}(x, x) + \sigma_{KPI,n}^2 I)^{-1} k_{KPI}(x, x^*)^T \\
&= k_{KPI}(x^*, x^*) - \begin{bmatrix} \psi(x_1, x^*) \\ \vdots \\ \psi(x_n, x^*) \end{bmatrix}^T \left(\begin{bmatrix} \psi(x_1, x_1) & \dots & \psi(x_1, x_n) \\ \vdots & \ddots & \vdots \\ \psi(x_n, x_1) & \dots & \psi(x_n, x_n) \end{bmatrix} \right. \\
&\quad \left. + \begin{bmatrix} \sigma_{KPI,1}^2 & \dots & 0 \\ \vdots & \ddots & \vdots \\ 0 & \dots & \sigma_{KPI,n}^2 \end{bmatrix} \right)^{-1} \begin{bmatrix} \psi(x_1, x^*) \\ \vdots \\ \psi(x_n, x^*) \end{bmatrix}
\end{aligned} \tag{5.4}$$

is a correction based on the prior covariance of the predicted point $k_{KPI}(x^*, x^*)$ minus the information the training points give about the function [86].

As shown in Equation 5.1 and Equation 5.2, the metamodel has tunable parameters that can be used to improve the quality of the model. The parameters σ_f , l^2 , c_1 , and c_2 are the hyper-parameters of the basis function and need to be optimized for a good fit of the metamodel to the training data. The σ_f parameter balances the effect of the added noise and l^2 controls the shape of the function. However, the l^2 term is kept constant because the hyper-parameters c_1 and c_2 in the basis function have the same function of controlling the shape of the basis function. Therefore optimizing these three would lead to an undetermined problem. To optimize the hyper-parameters the marginal log-likelihood function,

$$\log p(y_i | X) = -0.5 y_i^T (K_{KPI} + \sigma_{KPI,n}^2 I)^{-1} y_i - \frac{1}{2} \log(|K_{KPI} + \sigma_{KPI,n}^2 I|) - \frac{N}{2} \log(2\pi) \tag{5.5}$$

of the metamodel is maximized. Here 100 random initial guesses in a range from 0 to 100 are used to find the optimal set of hyper-parameter values because the log-likelihood function is expected to be nonconvex. To find this set the interior point method is used [111]. The resulting metamodels are discussed in Section 5.4.2.

5.3.5. FORMULIZATION OPTIMIZATION PROBLEM

In essence, the optimization problem for the design of the hopper is similar to the calibration problems described in previous studies [115]. Therefore, most solving methods used in these studies can also be applied in the optimization of design. However, there are distinct differences in the type of solutions that are obtained. When genetic algorithms or other types of swarm methods are used, the design domain is populated with samples which generally evolve over time to a set of solutions. These solutions can form a Pareto-front on which a designer can pick a design which gives the best-balanced solution. A different approach is to let the optimizer find single or several local optimal designs and converge to a set limit as used by [51] with the interior-point method. This is the method that is used in solving this optimization problem. This optimization is repeated with 100 random initial guesses spread around the design space using Latin Hypercube Sampling (LHS). Using a 100 random initial points ensures that the majority of the local optima is found.

To define the optimization problem we define objective function f for the described optimization problem. This objective function is formulated using the weighted-sum method [118] which is used in robust optimization because of its ease and simplicity. In this case study the multi-objective problem consists of two objectives. The first part of the objective function describes the discharge rate constraint which needs to reach a specified value. The second part of the objective function is the variance objective. The relative importance of these two parts is controlled by the factor κ . The solution will focus more on an exact match to the mean if κ moves to one whereas a higher focus on the variance is achieved with a small κ . This formulation has been chosen because it shows a clear relation between the importance of the mean and its variance. The objective function,

$$f = \kappa \left[\frac{\mu_1}{\mu_1^*} \right]^2 + (1 - \kappa) \left[\frac{\sigma_1}{\sigma_1^*} \right]^2 \quad (5.6)$$

consists of two components, a mean and standard deviation objective for each KPI. The first component,

$$\left[\frac{\mu_1}{\mu_1^*} \right]^2 = \left(\frac{\phi(x) - \phi_t}{\phi_t} \right)^2 \quad (5.7)$$

is the square of the relative error between the mean prediction of the discharge rate by the metamodel and the discharge rate target $\phi(x) - \phi_t$ which is divided by the discharge rate target ϕ_t . The second component,

$$\left[\frac{\sigma_1}{\sigma_1^*} \right]^2 = \left(\frac{\sigma(\phi(x))}{\max(\sigma(\phi(x)))} \right)^2 \quad (5.8)$$

is the square of the ratio between the predicted standard deviation of the discharge rate and the maximum standard deviation of the discharge rate present in the model. This ensures that the standard deviation is minimized in a range from zero to one.

5.3.6. CASE STUDIES INCLUDING VERIFICATION AND VALIDATION

In this paper we will look at two case studies which are representative of a hopper design case. The optimization problem described in the previous section will be solved for these two cases. For both cases we will use a threshold in the verification error of 5% and for the validation the results should remain within a 10% threshold to cover error propagation between the verification and validation step. These cases will be a discharge rate target of 4 kg/s (Case 1) and 8 kg/s (Case 2). For the deterministic optimization, the coefficient κ is equal to one and for the robust optimization case the coefficient $\kappa = 5/6$ which corresponds to a 5:1 ratio between the mean and variance. This ratio has been chosen because the actual discharge rate of the hopper is the essential performance indicator. The variance is an additional measure that focusses the optimization into the direction of a reliable design and therefore has a smaller coefficient. Using a ratio of 1:1 would likely result in a design optimum with a large mismatch to the targeted discharge rate. The two discharge rate cases are used to show difference between deterministic and robust optimization by only considering the discharge rate KPI. These results will be discussed in Section 5.4.2.

To put the case studies into context with an industrial setting we have to address the following. Relative to industrial scale hoppers, the size of the hopper used in this case study is small. However, results from this study serve as a proof of concept and might lead to opportunities for research focussed on scaling and validation on a pilot-scale, and later on to the industrial scale. In addition, more complex bulk materials including cohesion and other inter-particle behaviour are interesting topics.

5.4. RESULTS

In this chapter the results from the metamodel training and optimization studies described in Section 5.3 are presented. First we analyse the DEM simulation data and evaluate the trained DEM-based metamodel. Next, the results of deterministic and robust design optimization approaches for the discharge rate and its standard deviation as the objectives are discussed. This section also includes the verification and validation of the optimization results.

5.4.1. DEM DATA AND DEM-BASED METAMODEL

The training data for the DEM-based metamodel consists of DEM data for the discharge of a hopper. In 5.6(a) the discharge rates obtained from the DEM data set used for metamodel training is shown combined with a surface plot of the trained metamodel. For the discharge rate in 5.6 (a) we can observe an approximately linear relation between the hopper angle and the size of the discharge opening but with different gradients. 5.6 (b) depicts the standard deviation of the average discharge rate from the simulations and the predictions by the metamodel. This clearly shows that the standard deviation is high for the 50mm discharge openings. This is most likely related to the slow and irregular discharge process and the possibility of arch formation as is discussed in more detail in Appendix B.1. For the 75 and 100 mm discharge openings we see similar levels of variation,

Table 5.1: Coefficients of Gaussian Process Regression Metamodel

Metamodel	σ_f	l^2	$c_1(\alpha dir.)$	$c_2(W_o dir.)$
G_{DR}	1.797	1	1.201	0.166

up to 0,1 kg/s, which starts to increase again with increasing discharge openings. At the 60- and 75-degree hopper angles we see low variation in the discharge rate for the higher discharge openings.

Based on the mean and standard deviation of the discharge rate the Gaussian Process Regression (GPR) metamodel is trained as described in Section 5.3.1. This leads to the coefficients for the GPR for the discharge rate listed in Table 5.1. Together with the provided dataset, these values allow the GPR metamodel, G_{DR} , to be reconstructed. Based on the large difference between c_1 and c_2 the included flexibility for different parameters is justified.

5

In Figure 5.6 (c,d) the contour plots of the mean and standard deviation predictions by the DEM-based metamodel are shown. Figure 5.6 (c) shows isolines of constant discharge rate and exhibiting a near linear relation with the discharge openings based on the distance between the isolines as was also visible in the DEM data. The dependency on the hopper angle shows a slightly curved relation. Figure 5.6 (d) shows the standard deviation where regions of low standard deviations are visible indicating areas containing reliable designs.

Visually it is difficult to assess the errors made in predicting mean and standard deviation of the discharge rate in the design space. Therefore the percentage error in prediction is depicted in Figure 5.6 (e,f) for the mean and standard deviation respectively. Here the error percentages for the 50 mm discharge opening are left out because these percentages are very high for both mean and standard deviation. This can be explained because all simulations at the 50mm discharge opening encountered arching at one point during the simulation leading to high errors. This is highly undesirable in a hopper design and therefore it is not likely that design solutions for the prescribed cases will be found in this region. In the remainder of the design space, the variance prediction is reasonably accurate and follows the trend in the data and therefore deemed good enough to be included in the optimization. For further information on the arching phenomena in the simulations we refer to Appendix B.1. In Figure 5.6 (e) it is seen that the error for the 75mm discharge opening varies greatly with the hopper angles. An over or under estimation of at most 6% of the discharge rate is expected for most angles except for the 30, 75, and 82.5 degree angles. As is the case with the 50mm opening, the 75mm opening DEM simulations encountered arching as well but not for all simulations. For the 100 mm discharge opening we see that the fit is accurate within 1.5%. At 150mm the metamodel is accurate except for the 60 and 75-degree hopper angles which look at errors of at most 6%. For the 200mm discharge opening the error is within 1.5% except for the 90-degree angle.

In Figure 5.6 (f) the error in standard deviation prediction shows significantly higher values than for the mean prediction. This was already clearly visible in Figure 5.6 (a)

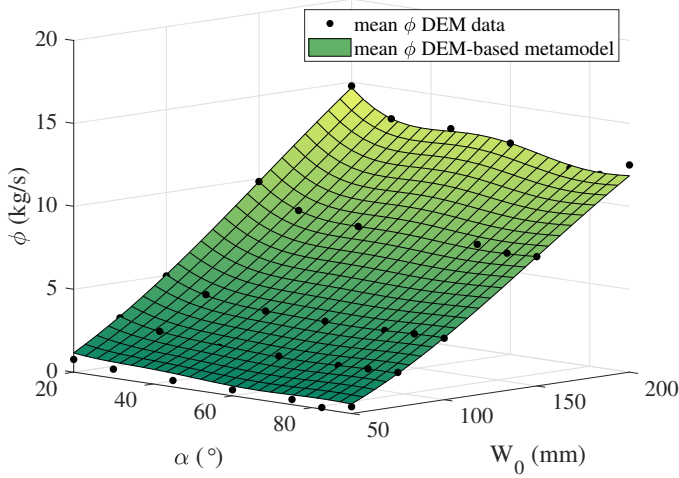
where large differences between the training data and the metamodel surface were seen. As a results the error fluctuates quite severely between -40 and +40% throughout the design space. Even with these high fluctuations, Figure 5.6 (a) shows that the metamodel is able to follow the trend in the data which is essential for robust optimization. However, for the application it is important that the prediction of the standard deviation is also accurate. Even though it can be used, the analysis of the metamodel and DEM-data clearly indicates that for quantitative prediction, the reliability of the standard deviation should be increased by increasing the number of repetitions of the DEM simulations in each data point.

Overall, in most regions of the design space the mean prediction error is well below 3% with some exceptions reaching 6%. Based on these errors in mean prediction and the trend presented by the metamodel for the standard deviation, we proceed with using the metamodel in deterministic and robust optimization.

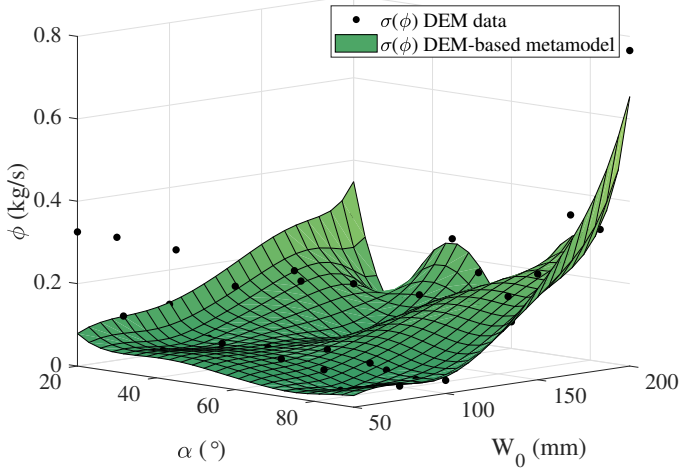
5.4.2. DETERMINISTIC VS ROBUST DESIGN OPTIMIZATION

To identify the effect of using deterministic and robust design optimization (DO) two case studies are investigated. In these case studies we optimised a hopper design using deterministic and robust optimization for a discharge rate of 4 kg/s (Case 1) and 8 kg/s (Case 2). In Figure 5.7 the contours of the discharge rate (a) and standard deviation (b) are visualized in the design space. The magenta and red coloured dots are the results from the deterministic optimization for Case 1 and 2. The yellow and blue dots represent the solutions for the robust optimization for Case 1 and 2. The deterministic optimization results clearly show that solutions are not unique and present a wide variety of design options with the same performance. Based on the single objective for the discharge rate in both cases the solver will return solutions on the isoline for the corresponding discharge rate, which represents designs of equal performance. However, the solutions for both cases are all located in the middle of the isolines and not at the outer hopper angles even though the solutions would give the same result. This can be explained by the interior point method which uses a barrier function that initially promotes searching the interior of the domain.

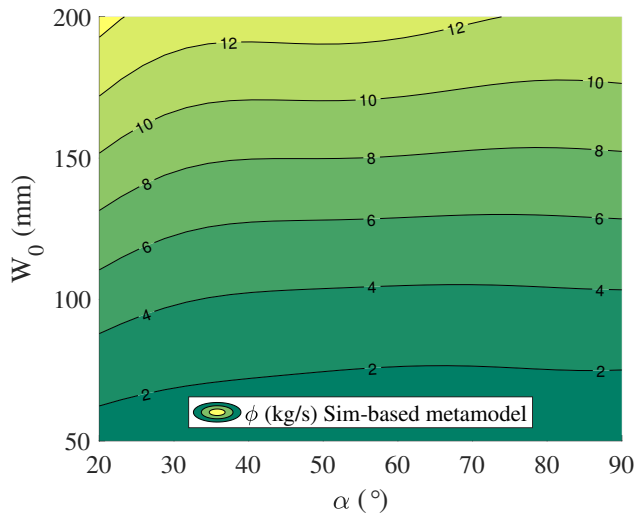
The robust optimization results for cases 1 and 2 including the variance as a second objective clearly show more distinct solutions compared to the deterministic results. The robust optimization results for case 1 show three distinct optima of which the 81 degree and 104mm design has the lowest variance followed by the 44-degree and 103mm and 31-degree and 98 mm design. The location of the robust designs in Figure 5.7 (b) shows a clear minimum in variance for the 45-degree solution in Case 2 and shows that the other solutions are located at points where there is large curvature in the isoline of the standard deviation. The exact designs and performance of the robust optima are shown in Table 5.2. Comparing the two cases shows that there are two solutions with a similar angle in both cases: the 45- and 81-degree hopper angle where only the size of the discharge opening is different. The 31-degree angle present in case 1 is not present in Case 2. Additionally, it is



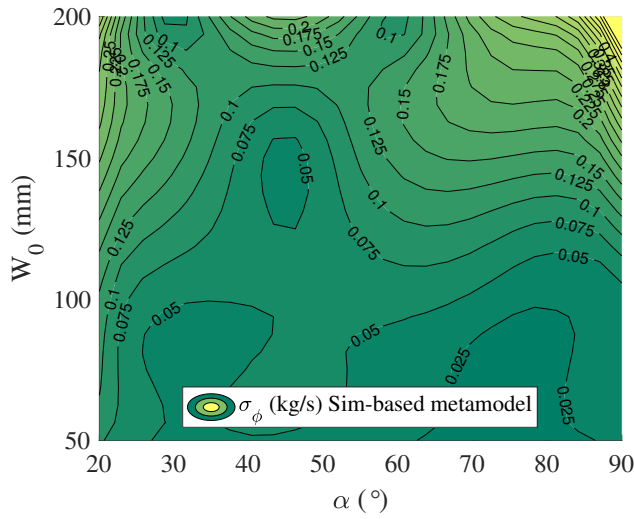
(a)



(b)



(c)



(d)

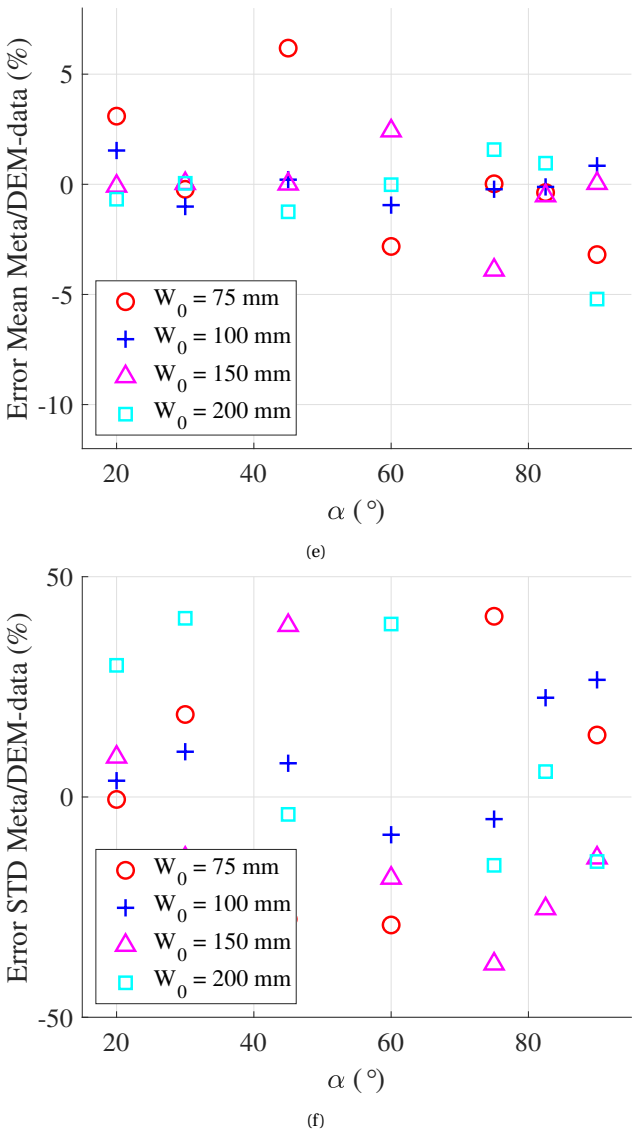


Figure 5.6: Figure 6 Surface plots of the mean and standard deviation predictions by the metamodel (a,b) contour plots of the mean and standard deviation (c,d) and the percentage error between the DEM-based metamodel predictions and DEM data for mean and standard deviation (e,f)

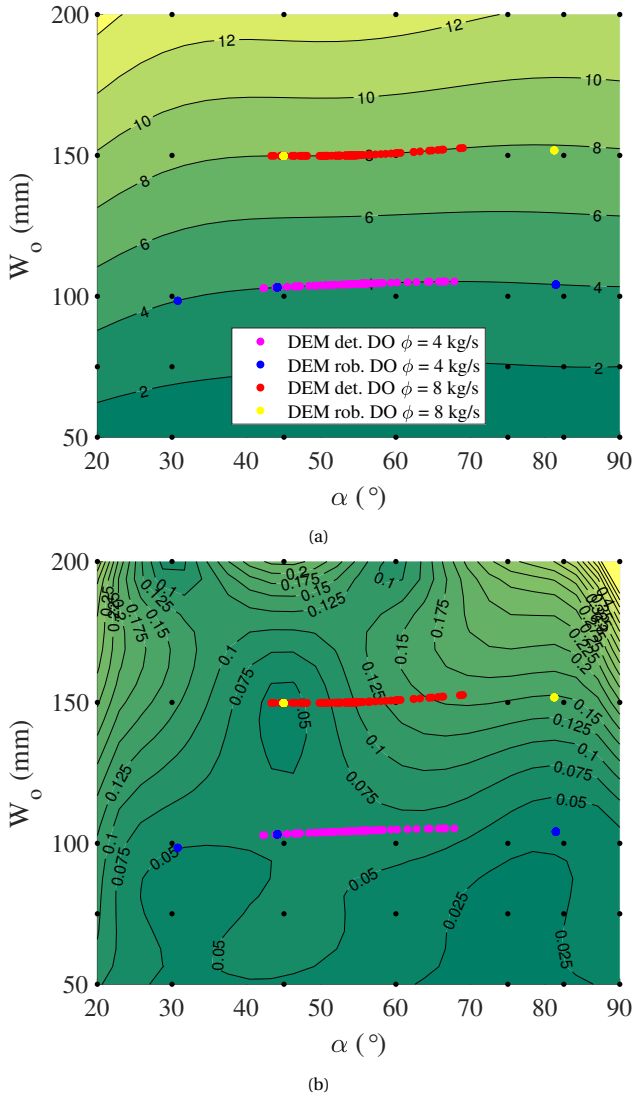


Figure 5.7: Deterministic and robust optimization results for both the 4 kg/s and 8 kg/s discharge rate target

Table 5.2: Local optima for robust optimization results with the corresponding average and standard deviation of the discharge rate

	Hopper angle	Discharge opening	Average discharge	Standard deviation	
	$\alpha(^{\circ})$	$W_o(mm)$	rate $\phi(kg/s)$	discharge $\sigma(\phi)(kg/s)$	rate
Case 1: $4\left(\frac{kg}{s}\right)$	30.77	98.42	3.994	0.05	
	44.11	103.2	3.999	0.051	
	81.45	104.1	3.997	0.032	
Case 2: $8\left(\frac{kg}{s}\right)$	44.96	149.8	7.993	0.039	
	81.23	151.8	7.84	0.147	

visible that there is a small difference between the target discharge rate compared to the deterministic results. This is caused by the additional objective for which the optimizer has to start making a trade-off. The 81-degree solution for Case 2 shows a discharge rate difference of about 2% and also the largest standard deviation, which indicates this is a poor local minimum.

Comparing the deterministic and robust optimization results, we see that only the 45-degree solutions in the robust optimization are present in the deterministic results. The solution at 31 and around 80 degrees are not present when using the interior-point-method but might become visible when different search algorithms are used. In the deterministic case, the standard deviation information from Figure 5.7 (b) is not used but by projecting the solutions it can be seen that using the standard deviation by means of robust optimization could be used to make design decisions from the deterministic optimization results.

Based on the deterministic optimization results a design between 42- and 69-degree hopper angles with their corresponding widths would result in a hopper with the right performance for both Case 1 and 2. For the robust optimization, we would have three hopper designs for Case 1 and two solutions for Case 2. For both Cases there are solutions around a 44- and 81-degree hopper angle that would be suitable where the 44-degree design is equally reliable for Case 1 and 2 but the 81-degree design only for Case 1. However, these designs are only based on the performance of the design and do neglect other aspects which would be encountered in engineering and operation of the equipment. For example, with an 81-degree angle stagnant zones would form on the slopes of the hopper walls because friction with the wall keeps the material in place. This would lead to a core flow dominated hopper which decreases wear of the equipment but might increase material wear. On the contrary, a 44- or 31-degree angle would lead to flow along the walls and a mass flow dominated hopper performance with increased equipment wear for abrasive materials but less material wear. Numerically, it would be clear that the 44/45 degree angle would lead to the most reliable performance for Case 2 but if engineering and operational aspects are considered one of the other designs might

Table 5.3: Verification design points along the 4 and 8 kg/s discharge rate isoline predicted by the metamodel

$\alpha(^{\circ})$	20	30	40	50
Case 1 $W_o(mm)$	87.9	97.9	102.4	103.9
Case 2 $W_o(mm)$	131.5	145.1	149.6	149.8
$\alpha(^{\circ})$	60	70	80	90
Case 1 $W_o(mm)$	104.9	105.2	104.4	103.4
Case 2 $W_o(mm)$	150.8	152.8	153.7	152.4

be chosen. In Appendix B.2, an elaboration can be found on design considerations in hopper design.

VERIFICATION OF DETERMINISTIC AND ROBUST OPTIMA

As part of the method described in Section 5.2 the results from the deterministic and robust optimization are verified. The metamodel predicted a discharge rate isoline for both cases in the design space of the hopper. This resulted in the deterministic optimization procedure to find a distribution of points on this isoline. Instead of verification of all these points on the isoline we decided to verify the metamodel prediction at 8 points along the isoline distributed from 20 to 90 degrees with a 10-degree interval with their corresponding discharge openings as found in Table 5.3. For each of these points the DEM simulation is repeated 5 times with an initial random packing of particles. In Figure 5.8 (a) and (b) the mean (blue dots) and 95% confidence interval (CI) of the mean (blue envelope) are shown as predicted on the isoline by the DEM-based metamodel for both cases. In addition, the verification results of the mean and 95% CI of the mean are shown. Overall, it can be seen that the verification results show good resemblance with the predicted results by the DEM-based metamodel for the isolines of 4 and 8 kg/s. Most of the designs on this isoline will be within 2,5% of the prediction which is acceptable looking at the set tolerance of 5%. The 95% CI from the verification results shifts with the location of the mean but overall the behaviour in variance is similar to the predictions by the DEM-based metamodel. Some exceptions in the behaviour are discussed below. Considering the limited number of repetitions, these results are promising for use of DEM-based metamodels in design optimization for bulk handling equipment.

In Case 1 it is clearly visible that at the 90-degree hopper angle the mean has an error of 5% as well as a wide 95% CI. The second simulation for the 20-degree point encountered arching directly at the start of the simulation, therefore it is not included in calculating the discharge rate in this point. For the third simulation the same occurred but when the half of the hopper had already discharged. This was long enough for calculating the discharge rate and is therefore included. However, it must be noted that with the 20-degree case there is a high likelihood of arching so it is not a reliable design point. Another simulation that shows a large error with the predicted discharge rate is the second simulation for the 90-degree angle case. During the discharge of the hopper the mass flow slows down halfway during the discharge but comes up to speed again, leading to a lower average discharge rate. This slight plateau forming also occurred with the second and third simulation for the 30-degree angle. The likelihood of arching increases with

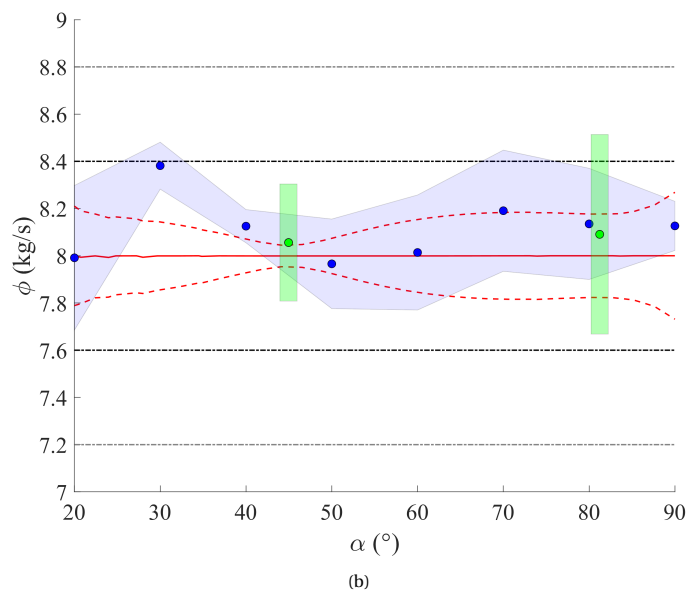
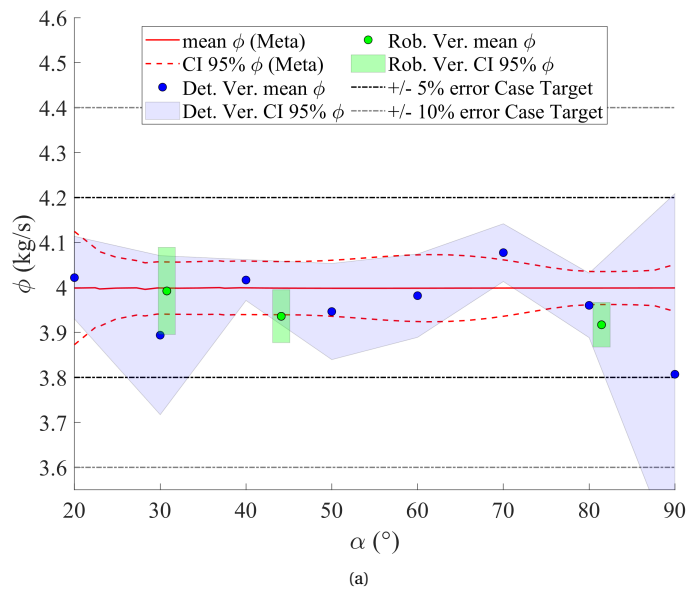


Figure 5.8: Verification results of isoline verification points for 4 kg/s (a) and 8 kg/s discharge rate (b)

decreasing discharge opening sizes which is clearly the case for the 20-degree hopper angle. Plateau forming or stalling during discharge is a phenomenon that can ultimately lead to arching so it is not strange that this occurs at the 30-degree angle and is likely to become more severe with a decreasing discharge opening size. In the 8 kg/s case we do not observe arching which can be explained by the fact that the discharge openings never reach the sizes in which arching starts to occur. This case shows that at 20-, 50- and 60-degree angles the verification results are matching the DEM-metamodel prediction. For the 40-, and 70- to 90-degree angles we see an overestimation of approximately 2.5% for the mean discharge rate. One exemption is the 30-degree angle, which shows a 5% overestimation. The confidence interval shows approximately the same behaviour as predicted but is on average wider than predicted.

In addition to the verification of the deterministic results the robust optima are also verified. Therefore 5 repetitions of the DEM model simulation for each local optimal design have been carried out as was the case for the generation of the DEM data for the metamodel. The error percentages for the verification of the robust optima are shown in Table 5.4. For visualisation, these results are combined with the deterministic results in Figure 5.8 where in (a) the verification results for Case 1 are shown and (b) shows Case 2. The green dot represents the predicted mean for each optimum and the green rectangle represents the 95% CI of the mean in this location. The Case 1 discharge rate verification results show that the mean for the 31 degree hopper angle is a closely matches the predicted optimal mean. However, the 95% CI is 1.7 times wider than for the predicted mean. For the other two optima it can be observed that the metamodel predicts a higher mean than the verification results. The difference between prediction and verification is 1.6% and 2% for the 45- and 81-degree case, respectively. The CI of the 44-degree case is the same in magnitude but shifted due to the error in the mean. For the 81-degree case the CI is 35% wider than predicted and shifted due to the large error in the mean.

For Case 2 we see that at the 45-degree hopper angle the verified mean is 0,8% higher than predicted. In the 81-degree case this is 3,2% but here it should be observed that the found optima was already slightly off from the target and that the verification results are closer to the initial optimization target. In terms of the CI it can be seen that it is wider in both cases up to 4.5 times for the 45-degree angle. Considering the mean prediction we would accept these optima because they are within the 5% tolerance that we have set even though the confidence intervals show significant errors. However, for a full evaluation it is important to study how the optima of both cases behave when these are experimentally validated.

VALIDATION OF DETERMINISTIC AND ROBUST OPTIMA

We performed validation of the deterministic and robust optimization results by means of experiments using the setup introduced in Section 5.3.1. For the validation of the DEM-based metamodel prediction the same designs as for the verification simulations are used. Here it is important to notice that the hopper angle and size of the discharge opening in the points presented in Table 5.4 cannot be set exactly because of the measurement error

Table 5.4: Local optima for verification of the robust optimization results with the corresponding average and standard deviation of the discharge rate

		Avg. discharge rate $\phi(kg/s)$	Std. dev. discharge rate $\sigma(\phi)(kg/s)$	% error with mean robust optima	% error with stan- dard deviation in robust optima
Case 1: 4(kg/s)		3.992	0.084	-0.044	70
		3.936	0.051	-1.575	4
		3.917	0.043	-1.999	35
Case 2: 8(kg/s)		8.056	0.216	0.786	453
		8.091	0.368	3.199	150

5

of the angle ($\pm 0,1$ degree) and discharge opening (± 1 mm) of the physical setup. In Figure 5.9 (a) and (b) the DEM-based metamodel prediction for the discharge rate for Cases 1 and 2 are shown combined with the verification results. These are the same as shown in Figure 5.8 but the validation results for the deterministic and robust optimization are added. The validation results for the deterministic optimization are represented by the red triangles for the mean and the red shaded area for its 95% confidence interval. For the robust optimization results yellow triangles are used and the yellow shaded area represents its 95% confidence interval. In addition to these visual results the percentage errors with the optimization target are presented in Table 5.5.

Overall we can see that the DEM-based metamodel and the DEM model itself underestimate the actual discharge rate of a design in both the deterministic and robust cases. However, in the preceding verification it was found that the DEM-based metamodel is relatively accurate in predicting the outcome of a DEM simulation for both the mean and its confidence interval. The validation results indicate that the DEM-based metamodel predictions are closer to experimental results in the region of Case 2 of the design space than for Case 1.

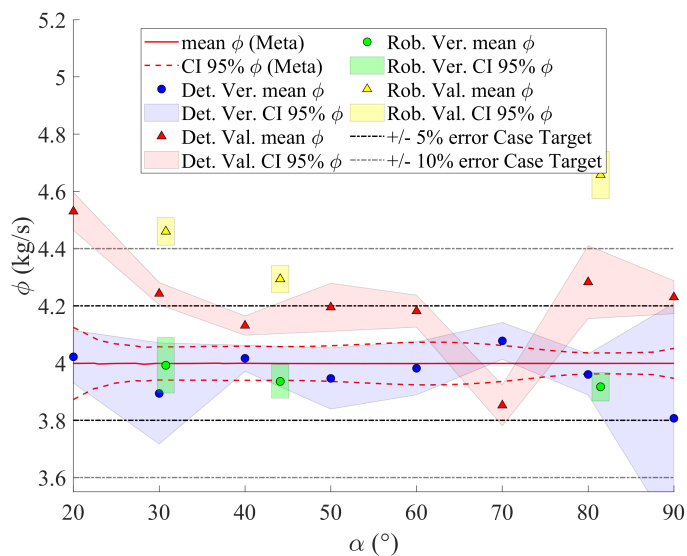
For deterministic Case 1 the largest mean error between the DEM-based metamodel prediction and the experimental results is present at a 20-degree angle and is about 13%. In the 30- to 60-degree angle range the error fluctuates between 3.5 and 6.5%. At 70 degrees it is observed that the error in mean prediction is around 4%. Remarkably, this is the only design for which an underestimation of the discharge rate is observed in the validation even though the load cell data is consistent. For the 80- and 90-degree angles we see 6 to 7.5% errors. The robust Case 1 validation results show an error of 12% for the 31,8-degree hopper angle, 7,5% for the 45-degree angle and 16,5% for the 81-degree angle. All of these results show that the found robust optima underestimate the actual discharge rate. Relative to the deterministic validation results the robust validation result shows an higher error. In terms of the 95% confidence interval it can be seen that this is similar for the predicted 95% CI by the DEM-based metamodel and even slightly smaller.

The validation results of deterministic Case 2 shown in Figure 5.9 (b) show a maximum error at the 90-degree hopper angle of around 9%. At the 40-degree hopper angle the error in mean prediction is around -8%. All the other errors are within the 5% error margin. In terms of the 95% confidence interval we see that it is twice as small as the predicted width of the confidence intervals by the DEM-based metamodel. For Case 2 the DEM-based metamodel predicts local optima at the 45 and 80-degree hopper angles. The validation results seem to show the same behaviour which reinforces the idea of quantitatively using the variance in robust optimization. For the robust optima it can be seen that the 45-degree optimum has an error of around 4% and the 81-degree angle a 9% error. The 95% CI of the first optima is 230% as wide as the prediction by the DEM-based metamodel whereas for the second optimum the error is only 33% wider than predicted. This indicates that predicting confidence intervals is difficult, especially with a low number of repetitions.

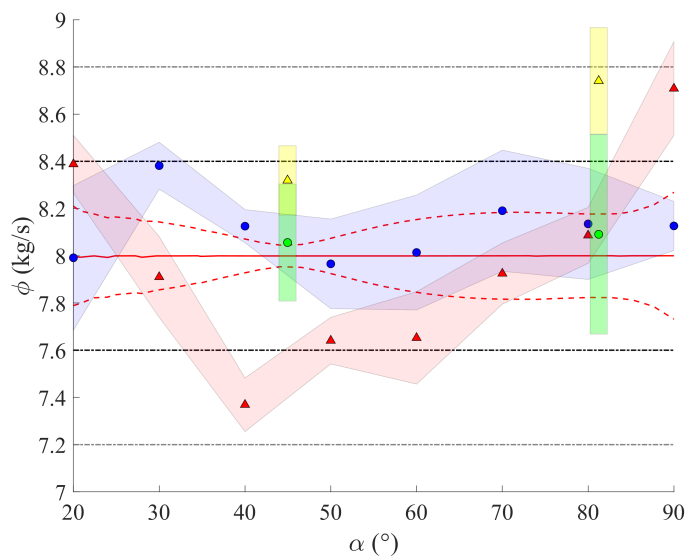
In both cases relatively large errors are observed in the validation results whereas the verification results did not show these to the same extent. The source of this difference can be explained by comparing the DEM data to experimental results in the same data points. This shows that the 2% error obtained from the calibrated DEM model at a 45-degree hopper angle and 100 mm discharge opening is not consistent throughout the design space. In Appendix B.3 these results are compared in more detail. These results showed that the error between DEM and experimental data is not consistent throughout the design space. When the DEM model cannot produce accurate predictions in the entire design space, increased errors in the performance of optimized designs can be expected.

Comparing the validation results from both cases it is observed that the validation error of the mean prediction by the DEM-based metamodel stays within the 10% error threshold for Case 2. For Case 1 we see that in most locations the error stays within 10% of the DEM-based metamodel prediction except for the 20-degree hopper angle and the first and third robust optima. In terms of acceptance of the solutions on the isolines we would accept most solutions if the 10% error threshold for the validation was considered. However, the results clearly show that the error at the 20-degree angle is significantly larger than for the other solutions. These results indicate that there is a significant error between the experiment and the DEM-model even though it has a 2% error based on the calibration [51]. Based on the trajectory of the isoline results it is clear that the error is not consistent throughout the design space. This means that the assumption of uniform errors throughout the design space cannot be made. Explanations for this inconsistency are the different flow velocity regimes in the different designs which are not considered in the calibration.

Based on the validation results we can assume that the DEM-based metamodel optimization results for Case 2 can all be used and for Case 1 only in the range from 30 degrees and higher even though the robust optima showed errors higher than 10%. From a deterministic optimization perspective all designs in these regions would be acceptable. For the robust optimization results only the 45-degree design for Case 1 would be acceptable as are both solutions for Case 2. A question that should be asked is whether the optimization is actually robust if errors seep in the method by means of



(a)



(b)

Figure 5.9: Mean and 95% CI predicted by DEM-based metamodel, verification and validation from the deterministic and robust optimization with 5 and 10% error margins with respect to the mean target for Case 1 and 2 in (a) and (b) respectively.

Table 5.5: Local optima for validation of the robust optimization results with the corresponding average and standard deviation of the discharge rate

		Avg. discharge rate $\phi\left(\frac{kg}{s}\right)$	Std. dev. discharge rate $\sigma(\phi)\left(\frac{kg}{s}\right)$	% error with mean robust optima		% error with standard deviation in robust optima
				metamodel prediction	DEM-based prediction	DEM-based meta-model prediction
Case 4 $\left(\frac{kg}{s}\right)$	1:	4.46	0.042	11.67		-16.75
		4.29	0.042	7.36		-18.35
		4.66	0.072	16.52		124.11
Case 8 $\left(\frac{kg}{s}\right)$	2:	8.32	0.127	4.08		226.45
		8.74	0.196	11.49		33.35

the quality of the data, DEM-model, and metamodel. However, the small errors between DEM-based metamodel predictions and the verification results for a small number of repetitions shows that MBDO using a DEM-based metamodel has potential.

5.5. CONCLUSIONS

In design of bulk handling equipment the stochastic nature of granular material behaviour is rarely included as is the use of metamodel-based design optimization (MBDO). Therefore this study investigates the effect metamodel-based deterministic and robust optimization strategies have on hopper design optimization. Both strategies use DEM-based metamodels for the prediction of mean and variance and are verified and validated by the DEM equipment model and experiments, respectively. The goal of this study is to introduce a robust MBDO, identify the differences between deterministic and robust optimization strategies and the challenges that might be encountered.

The deterministic and robust design optimization case studies show that for deterministic optimization a multitude of local optima are distributed over the isoline of the desired discharge rate whereas the robust optimization zones produces more specific solutions by using the variance. The verification of the deterministic optimization results showed an error in mean prediction within a 5% bandwidth, whereas the errors found in robust optimization results did not exceed 2,5%. The confidence intervals showed more fluctuation and are therefore less reliable. However, based on the mean prediction it seems that robust optimization leads to better performing optima.

One common issue in the use of metamodels in a design process is the effect of error propagation due to a mismatch between the metamodel and the data it is trained on. This is true for metamodels that predict a mean or both mean and variance and is directly affected by the reliability of the used mean and variance training data. In addition, the optimization results are affected by a mismatch between DEM model and experiments. These errors became clearly visible in the verification and validation stage of the deterministic and robust optimization results.

Overall, the use of DEM-based metamodels gives insight on the behaviour of bulk handling equipment which can be used for finding suitable designs in the design space. For bulk handling systems with multiple design and performance parameters and similar problems in other domains, design optimization strategies such as the deterministic and robust approach are good options to find a range of optimal designs. The robust optimization finds designs which in addition to optimized mean performance also exhibit low variance. However, the quality of the optimization relies highly on the quality of the mean and variance data that is available for the metamodel. This is one of the biggest challenges in applying robust MBDO in design of bulk handling equipment.

6

CONCLUSIONS AND RECOMMENDATIONS

6.1. CONCLUSIONS

The current procedure for design of bulk handling equipment does not include the stochastic behaviour of granular materials. However, the results from the experimental studies for the design space of bulk handling equipment and for the calibration experiments show that it is essential to include the stochastic behaviour of the bulk material in the design procedure. Even though it is necessary to include the stochastic behaviour there are implications to the implementation such as increased computational effort and the need to repeat experiments. In this thesis it is systematically shown how the stochastic behaviour of equipment and material can be obtained through experiments, how it can be included in modelling the bulk material using DEM, and how stochastic metamodels can aid in the robust optimization of bulk handling equipment design. This systematic approach leads to a new design procedure which can greatly improve the accuracy and reliability of modelling and design of bulk handling equipment. The aim of this thesis is:

To identify the effect of including the stochastic behaviour of granular materials in the design procedure for bulk handling equipment.

To achieve this aim, an extensive experimental and numerical study has been performed which incorporates the stochastic behaviour in the analysis of the bulk handling equipment design problem, the development and calibration of a DEM model, and the design optimization of bulk handling equipment. The conclusions are organized according to the research questions stated in Chapter 1.

Research Question 1: To what extent does the stochastic behavior of a granular material affect the performance of bulk handling equipment in the design space?

The experimental studies in this thesis show that the stochastic behaviour depends on the type of experiment that is conducted. Moreover, the stochastic behaviour of the discharge rate of the hopper experiment depends on the geometry of the hopper. The variance of the discharge rate is up to 7% of the mean discharge rate after 5 to 10 repetitions for many design configurations. Additionally, a clear transition from mass to core flow was observed where the physical behaviour of the granular material in the hopper changes. The impact loads inflicted on a hopper are relevant for the life expectancy of the structure. The variance of the maximum impact load is in a range of up to 70% which has significant effects on the design reliability. The analysis of the experimental data in the design space shows that the variance of the hopper performance is geometry dependent. In the calibration experiments which were conducted for 50 repetitions it showed a variance of 0,74% to 8.2% of the mean value of the calibration parameters. Noteworthy is that this variance seemed to increase with increasing dynamic behaviour due to the type of experiment. In addition, the interaction between the bulk material and equipment is related to the overall behaviour of the system. These results indicate that the stochastic behaviour is not a characteristic property of the bulk material alone as it is affected by geometric boundary conditions, changes in flow regimes and flow density. Moreover, for stable performance and calibration targets it is essential that experiments are repeated until the mean reaches a stable value. If not, unstable mean values will lead to badly calibrated DEM models and give unreliable performance predictions for equipment design.

6

Research Question 2: How can metamodels be used to describe the behaviour of bulk handling equipment in a design space?

Metamodels are a common technique to relate input and output of a system in a computationally efficient way. However, in relation to DEM models metamodels are rarely applied. In this thesis the application of metamodels to DEM model data is studied by introducing a methodology for training and validation of a DEM-based metamodel supported by a proof of concept. In the proof of concept different metamodels were trained which showed that they can capture the behavioural trends in the design space of the bulk handling equipment. The study showed that hyper-parameter optimization is essential for obtaining accurate metamodels. In the case study it was found that the required sample size is not consistent for each key performance indicator of the model. In addition, it is essential that boundary sampling techniques are applied because data-driven models are based on interpolation or regression and generally perform poorly in extrapolation. Moreover, in assessing the quality of the metamodel it is essential to select a proper validation strategy. Concluding, the study showed that DEM-metamodels can be applied in the design of bulk handling equipment even for small datasets but different metamodels should be tried before selecting the most suitable metamodel.

Research Question 3: To what extent can the stochastic behaviour of a granular material be captured in metamodel-based calibration of a discrete element model?

In conventional calibration the parameters of DEM models are only calibrated for the mean performance of the model. However, the calibration experiments for this study

showed that achieving stable results in a lab setting already requires up to 30 repetitions which is more than the common value of five repetitions usually used in calibration studies. This means that even for conventional mean calibration the number of repetitions of experiments should be increased.

In this study it is shown that including the stochastic behaviour of the material in the calibration leads to different sets of calibration parameter values. To include stochastic behaviour, a methodology for stochastic calibration is introduced which can be used in engineering practice. Moreover, the DEM models calibrated by including the stochastic behaviour showed that more accurate predictions of mean behaviour are obtained. Accurate prediction of the variance proved to be difficult and remains a topic for further research. In the calibration procedure, DEM-based metamodels relating calibration targets to calibration parameters were used to find the parameter values. These metamodels were able to capture the mean relation and the stochastic trend of the relation between calibration targets and parameters. The validation of the equipment with the found calibration parameter values from the calibration procedure showed that including the stochastic behaviour leads to more accurate DEM models (2,15%) compared to conventional mean calibration (3,34%).

Research Question 4: How does introducing metamodels and robust optimization to the design process of bulk handling equipment change the process and its outcome?

The final part of the design procedure is design of bulk handling equipment. For bulk handling systems with multiple design and performance parameters and similar problems in other domains, design optimization strategies such as the deterministic and robust approach are good options to find a range of optimal designs. Metamodel-based robust optimization finds designs which in addition to optimized mean performance also exhibit low variance and are therefore more robust. However, the quality of the optimization result relies highly on the quality of the mean and variance data that is available for the metamodel.

This dissertation presents a validated framework for deterministic and robust design optimization which incorporates the methodology for metamodel training and procedure for stochastic calibration. The metamodels based on DEM data can describe the behaviour of the equipment in the design space where the mean behaviour was accurate but the variance was only accurate in trend. However, in robust optimization also accurate trend information can be useful to steer designs in the right direction. The verification of the deterministic and robust optimization showed that the mean prediction for the deterministic case stays within a 5% bandwidth around the target whereas the robust optimization stays within a 2.5% bandwidth. The validation of the deterministic and robust optima in the case study showed that most optima stayed within the 10% error margin. These results indicate that robust optimization theoretically leads to more robust performing optima.

6.2. RECOMMENDATIONS

The research presented in this thesis shows that it is essential to include stochastic behaviour of bulk handling equipment in the design procedure. However, the case studies and proof of concept presented in this work have a relative low complexity compared to other bulk handling equipment. It is suggested to investigate if the introduced methodologies can be applied to more complex systems and be validated at an industrial scale. Here it is important that scale effects are identified which can aid in translating granular behaviour at a laboratory scale to industrial systems.

On a more detailed level, there are many aspects that require further inquiries. First of all, identification of the stochastic behaviour of granular materials is essential if it is to be used in design of bulk handling equipment. Here it is important that the stochastic behaviour across different dynamical regimes is better understood and that guidelines are set for the number of repetitions required to get an accurate representation. This will ensure that calibration of DEM models can be made more efficient and that the accuracy of DEM models can be increased.

Secondly, DEM-based design in general is an approach that should be used more frequently in design of bulk handling equipment. DEM models provide a better understanding of the behaviour of a bulk material that is handled. Metamodels based on data provided by DEM models help in finding design solutions that have the desired performance. Here it is important that techniques and methodologies are developed that are able to build accurate metamodels based on size limited data-sets. In this light, research is required on the possibility of using AI or machine learning techniques to improve the reliability of these models. For the increase of accuracy of these metamodels it is essential that the stochastics are included. To achieve this, small scale experiments that can be repeated with little effort need to be included in the calibration and design procedure. In addition, detailed representation of granular shapes and properties in DEM models will help capture the stochastics of the granular behaviour. The increase in accuracy of DEM models and understanding of the material improves the quality of DEM models and makes the use of metamodels for design optimization a logical step. By taking these steps the design procedure for bulk handling equipment can be gradually improved towards the basis that is presented in this dissertation.

Nowadays, there is a trend in moving to open science and data. In order to make steps in the field of modelling granular materials this is an essential development. Therefore, all the experimental data (10.4121/fa7544d6-14fd-4372-a81f-e2e1b4a44832) and sources of the numerical data related to this thesis are made publicly available according to the FAIR principle.

A

APPENDICES TO CHAPTER 2

A.1. PIV PROCEDURE

In this appendix the procedure for the particle image velocimetry is described. The images recorded by the high speed camera inherit a distortion caused by the deformation of the image by the lens. To account for this distortion a picture is taken of a calibration grid which is used to correct for the distortion. Using an object detection algorithm the locations of the crosses are found. Subsequently, applying polynomial regression to the centres of the crosses and using the fact that the calibration sheet is straight the corrections needed for the picture distortion are found. These corrections are stored and are used to correct the images recorded for each experiment. These calibrated (undistorted) images are used for the PIV analysis.

The first step in the PIV analysis is to define a grid spaced with 64 by 64 pixels for the entire image. In each grid cell the interrogation area is moved in an area 32 pixels (half the grid size) around the grid cell for a subsequent image as shown in Figure A.1. In this scanning operation the cross-correlation between the interrogation area and original grid cell is calculated by using FFT. Based on the cross-correlation in which correlation peaks are found the displacements in x and y direction are estimated by a Gaussian Peak Fit. Based on preliminary research on a small set of images the ratio between the largest peak in the image and the second largest an average ratio of 8 is obtained which means that the largest peaks are well detectable for this grid size.

In the PIV analysis the found velocity vectors might show unrealistic values between a row of well predicted points. Therefore a median filter with 5 neighbouring interrogation squares is used to filter the outliers. The PIV result is a velocity field in pixels per time step, to obtain the actual velocities we have to scale with the pixel to m number $C_P x 2m$ and the time correction coefficient C_t which is based on the used framerate for the recordings.

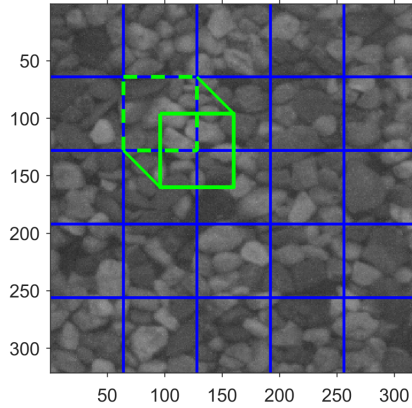


Figure A.1: Interrogation area movement

A.2. ARCHING

During the experiments we observed both phenomena described in the introduction, arching, and pulsating flow. The formation of arches is a common phenomenon in hoppers and silos. In this case arching was observed in the experiments with a 50mm discharge opening which is equal to 5,75 times the average particle diameter. As generally accepted, decreasing the size of the discharge opening of the hopper below 8-12 average particle diameters leads to an increasing risk of arching and therefore stopping the flow of the hopper (Schulze, 2008). In Figure A.2 the percentage of experiments that contained arching compared to the total number of experiments is shown. Here it is observed that for a hopper angle of 60 degrees arches always form. The probability of arching decreases when the angle is increased or decreased where at both ends the probability of arch forming becomes roughly 50%.

We observe that the probability of arching decreases with increasing and decreasing hopper angles from the 60 degree angle. The friction angle between the wall and the granular material is equal to 27,5 degrees which corresponds to a 62,5 degree hopper angle due to its definition. For hopper angles higher than this threshold we would expect that the probability of arching decreases because with increasing steepness of the hopper overcoming the frictional forces becomes easier. When the hopper angle decreases the granular material will not initiate movement itself leading to stagnant zones where material is at rest. Here it is likely that a shear zone will form where the granular material shifts from stagnant to full motion. If the hopper angle decreases it is probable that the stagnant zones will stabilize further as will the transition zone. This might lead to increasing consistency of the granular flow and a decrease of the probability of arching. However, these are explanations that require validation through additional research.

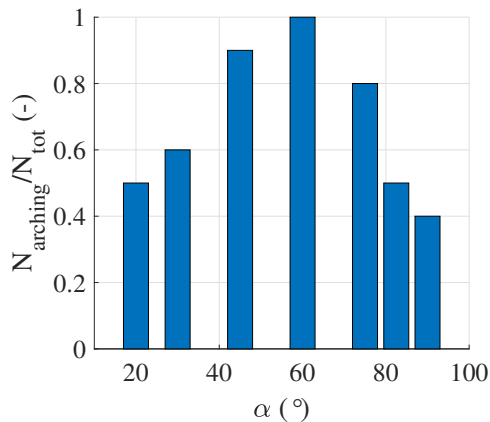


Figure A.2: Interrogation area movement

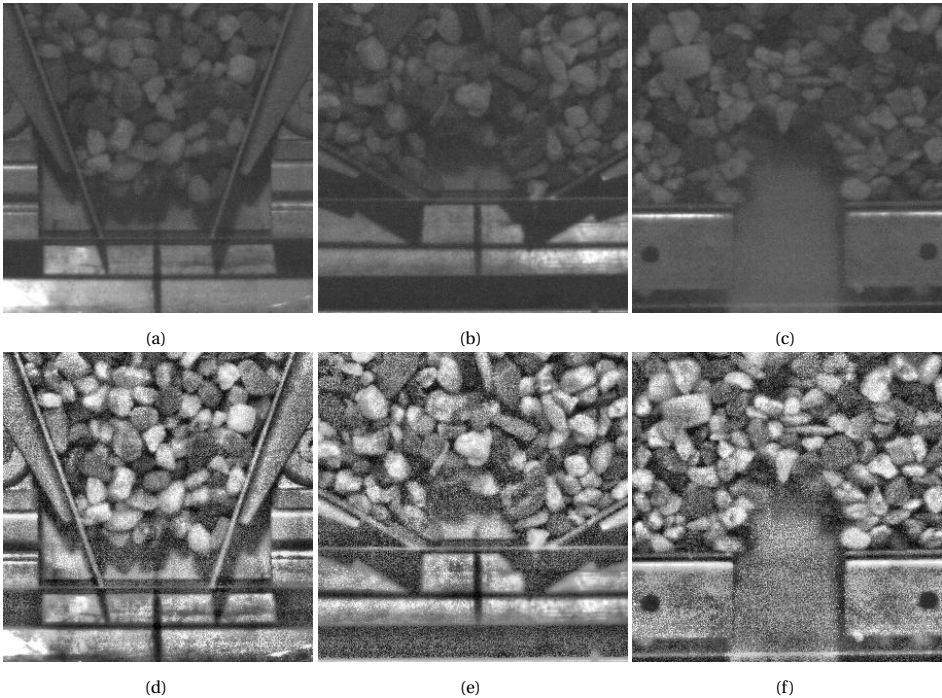


Figure A.3: Examples of arching during the experiment with $W_0 = 50\text{mm}$, arch at 20 degree angle (a,d), at 60 degree angle (b,e), at 90 degree angle (c,f)

A.3. REFERENCE VALUES DISCHARGE RATE AND IMPACT LOAD

In this appendix the reference values for the discharge rate and impact load can be found.

Table A.1: Average discharge rates with standard deviation in (kg/s)

$d \alpha$	$\alpha = 20^\circ$ (used for normal- ization)	$\alpha = 30^\circ$	$\alpha = 45^\circ$	$\alpha = 60^\circ$	$\alpha = 75^\circ$	$\alpha = 82.5^\circ$	$\alpha = 90^\circ$
$50mm$	9,46 ± 1,11	6,06 ± 0,95	4,45 ± 1,34	3,59 ± 0,83	2,84 ± 0,81	2,85 ± 0,8	3,14 ± 1,08
$75mm$	16,10 ± 2,71	7,88 ± 2,30	6,50 ± 0,56	4,20 ± 1,53	3,96 ± 1,10	4,44 ± 0,97	5,41 ± 1,05
$100mm$	20,54 ± 2,85	9,11 ± 2,11	8,81 ± 1,27	7,95 ± 2,16	8,36 ± 3,63	4,45 ± 1,31	6,22 ± 0,84
$150mm$	26,41 ± 3,38	6,55 ± 4,43	13,99 ± 6,09	14,01 ± 5,86	8,43 ± 6,72	7,16 ± 3,59	11,71 ± 7,20
$200mm$	47,28 ± 6,65	12,10 ± 5,56	24,32 ± 5,48	22,63 ± 1,71	4,36 ± 4,04	4,41 ± 1,64	15,88 ± 9,53

Table A.2: Average impact loads with standard deviation in (N)

$d \alpha$	$\alpha = 20^\circ$ (used for normal- ization)	$\alpha = 30^\circ$	$\alpha = 45^\circ$	$\alpha = 60^\circ$	$\alpha = 75^\circ$	$\alpha = 82.5^\circ$	$\alpha = 90^\circ$
$50mm$	1.44 ± 0.068	1.17 ± 0.054	0.84 ± 0.046	0.83 ± 0.083	0.90 ± 0.071	0.94 ± 0.1	1.03 ± 0.105
$75mm$	2.99 ± 0.088	2.54 ± 0.084	2.09 ± 0.081	1.92 ± 0.126	2.14 ± 0.095	2.07 ± 0.195	2.19 ± 0.150
$100mm$	4.73 ± 0.073	3.95 ± 0.085	3.68 ± 0.025	3.69 ± 0.078	3.79 ± 0.080	3.60 ± 0.266	3.93 ± 0.075
$150mm$	9.25 ± 0.273	8.21 ± 0.173	7.65 ± 0.255	7.64 ± 0.182	8.14 ± 0.668	7.68 ± 0.896	7.86 ± 0.640
$200mm$	14.85 ± 0.744	12.42 ± 0.227	12.27 ± 0.120	12.54 ± 0.463	12.56 ± 0.272	12.51 ± 0.669	13.04 ± 0.59

B

APPENDICES TO CHAPTER 5

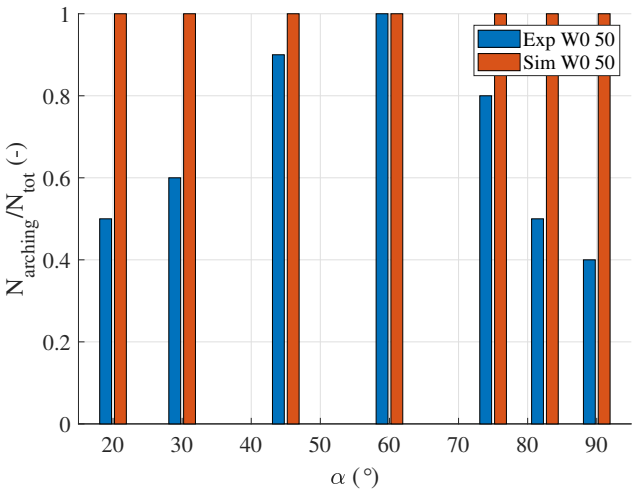
B.1. ARCHING

As mentioned at the beginning of this section arching may occur at small discharge openings if the discharge opening is smaller than ten times the average particle diameter (Schulze, 2008). For the case study this means that the minimum size of the discharge opening should be 100,4mm. However, in the design space also 50 a 75mm size samples are included. In Figure 10 the occurrence of arching in both experiments and simulations is shown for each hopper angle for the 50mm discharge opening in (a) and 75mm discharge opening in (b). In the experiments it was observed that at a 60-degree angle and 50mm discharge opening arching occurs at each instance. For an increasing and decreasing angle we see that the probability of forming of arches reduces. In contrast, in the DEM simulations arches form for each simulation at 50mm discharge openings. Looking at the 75mm discharge opening results it can be seen that the simulations show arching at small and large angles but no arching at a 75-degree angle. This behaviour is exactly opposite to the experimental results with a 50mm discharge opening. These results indicate that the DEM model is not able to reproduce a phenomenon such as arching accurately. Moreover, these results show that validation of calibration results is important and that multiple KPIs should be verified and validated.

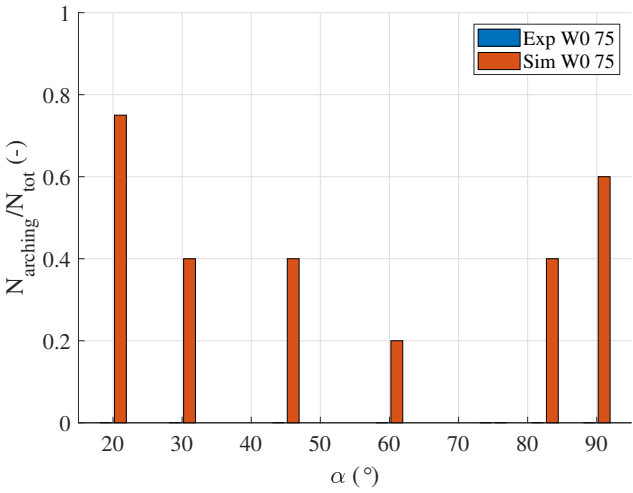
B.2. DESIGN CONSIDERATIONS

In design optimization of bulk handling equipment it is important to consider additional behaviour of material and equipment in assessing the found optima. One of these phenomena was arching which was described in A.1. In bulk handling equipment the interaction between material and structure is not only determined by the geometry but also by the condition of the structure. The stainless steel wall in the hopper geometry is impact loaded and has a friction coefficient of 0,52 which results in a friction angle of 27,5-degrees. In Figure B.1 showing the contour plots, this means that all points around the 62,5-degree angle are likely to show stick slip behaviour. For angles below 62,5-degrees

B



(a)



(b)

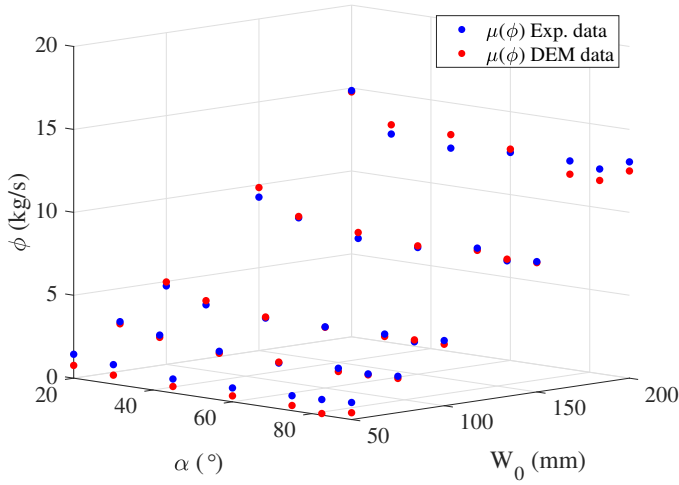
Figure B.1: Arching in the hopper for experiments and simulations for 50mm discharge opening (a) and 75 mm discharge opening (b)

there is continuous movement of particles and possibility of mass flow. Whereas, above 62,5-degrees, stable stagnation zones and core flow will occur. In Figure B.1 showing the optimization results for Case 1 we see that the 30 and 45-degree solutions for the DEM data will likely be mass flow. However, the third solution for the DEM data is at an 80-degree angle which is likely in the core flow regime. With respect to the design choice in the DEM solution of Case 1 the choice is not limited to the discharge rate and its variance but also to the type of system that is desired. If the material that is put through the hopper has an abrasive nature, the mass flow designs are not convenient because they would increase equipment wear. This means that the core flow design would be the correct choice. However, it can be argued that friction between particles is not desired because of material wear making the mass flow designs the better option despite the lower variance in the core flow design. It is important that when the design is chosen the optimization result is not blindly accepted because other aspects of the design in operation should be considered.

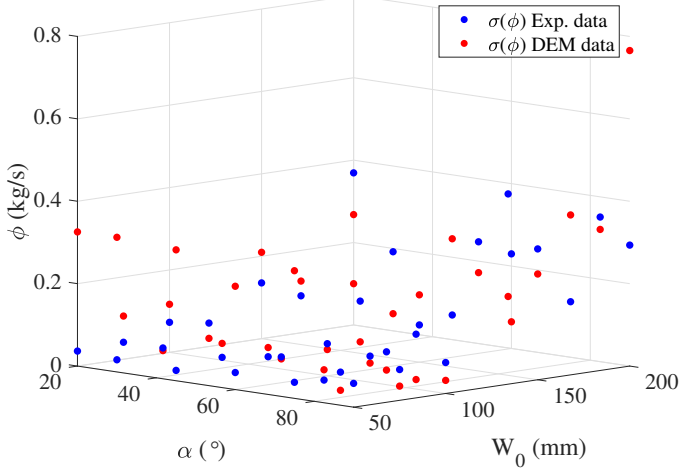
B.3. COMPARING DEM RESULTS AND EXPERIMENTS

The validation results in this study showed differences in predicted discharge rates between the DEM-model simulation results and experiments. Based on the calibrated DEM-model an overestimation of 2% was expected by the DEM-model compared to the experiments. However, this error seemed to be inconsistent throughout the design space as shown by the validation results. In Figure B.2 (a,b) we have shown the average discharge rate and its standard deviation based on the DEM-data and their equivalent experiments using five repetitions for the sampled design space along with the respective errors for each discharge opening and angle in Figure B.2 (c). As can be seen the results from the calibration is a 2% error at a 45-degree angle and 100 mm discharge opening. As can be seen for the other angles for the 100mm discharge-opening errors up to 6% are present. This means that if the DEM model is used to predict the discharge rate for a 20-degree angle and 100 mm discharge opening the result is 5% higher than the value obtained from the experiments. However, getting closer to the 75mm discharge opening leads to an underestimation of 5%. This means that significantly larger errors between DEM-model and experiment are present in different parts of the design space than expected from the calibration (Fransen et al., 2022). Combined with the introduced error by the DEM-based metamodel this can lead to additional errors in the different steps in the methodology. To prevent this, additional calibration experiments can be used to resemble the physics of the system.

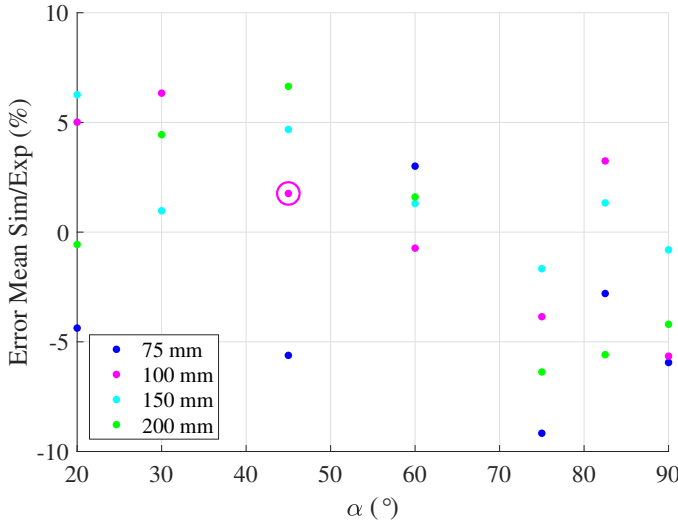
B



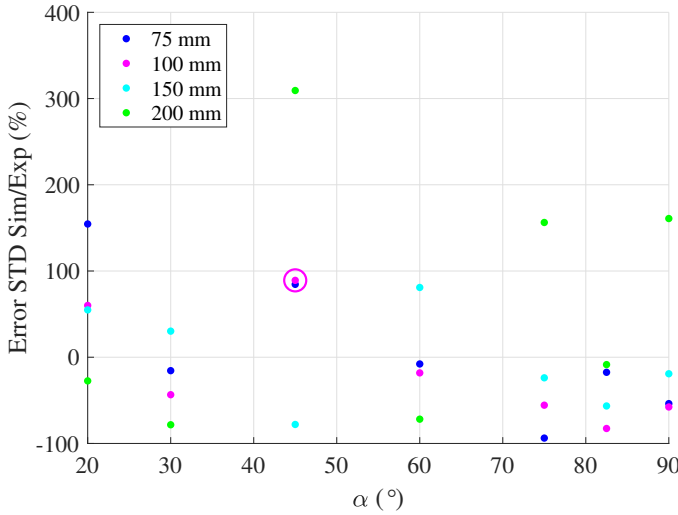
(a)



(b)



(c)



(d)

Figure B.2: DEM training data for metamodells (a) discharge rate (b) relative standard deviation discharge rate (c) mean error between simulation and experiment for the discharge rate (d) mean error between simulation and experiment for the standard deviation of the discharge rate, where the calibration results from [51] are shown by an additional circle in both (c,d)

REFERENCES

- [1] P. A. Cundall, *A discrete numerical model for granular assemblies*, Geotechnique , 47 (1979).
- [2] C. Coetzee, *Review: Calibration of the discrete element method*, Powder Technology **310**, 104 (2017).
- [3] C. Coetzee, *Calibration of the discrete element method: Strategies for spherical and non-spherical particles*, Powder Technology **364**, 851 (2020).
- [4] A. Jensen, K. Fraser, G. Laird, N. Karajan, Z. Han, H. Teng, J. Wang, M. T. Davidson, J. H. Chung, H. Teng, Z. Han, V. Le, M. A. Faraone, J. H. Chung, M. T. Davidson, P. O. Box, M. B. Cil, and K. Alshibli, *Improving the Precision of Discrete Element Simulations through Calibration Models*, 13 th International LS-DYNA Users Conference **7**, 405 (2014).
- [5] T. A. Simons, R. Weiler, S. Strege, S. Bensmann, M. Schilling, and A. Kwade, *A ring shear tester as calibration experiment for DEM simulations in agitated mixers - A sensitivity study*, Procedia Engineering **102**, 741 (2015).
- [6] L. Benvenuti, C. Kloss, and S. Pirker, *Identification of DEM simulation parameters by Artificial Neural Networks and bulk experiments*, Powder Technology **291**, 456 (2016).
- [7] N. Govender, D. N. Wilke, and S. Kok, *Blaze-DEMGPU: Modular high performance DEM framework for the GPU architecture*, SoftwareX **5**, 62 (2015).
- [8] H. Cheng, T. Shuku, K. Thoeni, P. Tempone, S. Luding, and V. Magnanimo, *An iterative Bayesian filtering framework for fast and automated calibration of DEM models*, Computer Methods in Applied Mechanics and Engineering **350**, 268 (2019).
- [9] H. Kureck, N. Govender, E. Siegmann, P. Boehling, C. Radeke, and J. G. Khinast, *Industrial scale simulations of tablet coating using GPU based DEM: A validation study*, Chemical Engineering Science **202**, 462 (2019).
- [10] P. Hartmann, H. Cheng, and K. Thoeni, *Performance study of iterative Bayesian filtering to develop an efficient calibration framework for DEM*, Computers and Geotechnics **141**, 104491 (2022).
- [11] S. Lommen, *Virtual prototyping of grabs: co-simulation of discrete element and rigid body models*, phd dissertation, (2016).

- [12] T. Roessler and A. Katterfeld, *Scaling of the angle of repose test and its influence on the calibration of DEM parameters using upscaled particles*, Powder Technology **330**, 58 (2018).
- [13] D. Schott, J. Mohajeri, J. Jovanova, S. Lommen, and W. de Kluijver, *Design framework for DEM-supported prototyping of grabs including full-scale validation*, Journal of Terramechanics **96**, 29 (2021).
- [14] R. Jin, X. Du, and W. Chen, *The use of metamodeling techniques for optimization under uncertainty*, Structural Multidisciplinary Optimization **116**, 99 (2003).
- [15] D. J. Lucia, P. S. Beran, and W. A. Silva, *Reduced-order modeling: New approaches for computational physics*, Progress in Aerospace Sciences **40**, 51 (2004).
- [16] P. Benner, M. Ohlberger, A. Cohen, and K. Willcox, *Model Reduction and Approximation: Theory and Algorithms*, Model Reduction and Approximation (2017), 10.1137/1.9781611974829.
- [17] S. Koziel and L. Leifsson, *Surrogate-Based Modeling and Optimization* (2010).
- [18] A. Quarteroni and G. Rozza, *Reduced Order Methods for Modeling and Computational Reduction* (2014) pp. 21–47.
- [19] G. Wang, *Review of metamodeling techniques in support of engineering design optimization*, Journal of Mechanical Design **129**, 370 (2007).
- [20] J. P. C. Kleijnen, *A comment on blanning's metamodel for sensitivity analysis the regression metamodel in simulation*, Interfaces **5**, 21 (1975), <https://doi.org/10.1287/inte.5.3.21>.
- [21] K. Wilde, M. Rucka, and J. Tejchman, *Silo music - Mechanism of dynamic flow and structure interaction*, Powder Technology **186**, 113 (2008).
- [22] K. Wilde, J. Tejchman, M. Rucka, and M. Niedostatkiewicz, *Experimental and theoretical investigations of silo music*, Powder Technology **198**, 38 (2010).
- [23] R. Balevi, I. Sielamowicz, Z. Mróz, and R. Ka, *Investigation of wall stress and out flow rate in a flat-bottomed bin : A comparison of the DEM model results with the experimental measurements*, Powder Technology **214**, 322 (2011).
- [24] R. J. Goodey, C. J. Brown, and J. M. Rotter, *Predicted patterns of filling pressures in thin-walled square silos*, Engineering structures **28**, 109 (2006).
- [25] R. J. Goodey, C. J. Brown, and J. M. Rotter, *Rectangular steel silos : Finite element predictions of filling wall pressures*, Engineering Structures **132**, 61 (2017).
- [26] Y. Wang, Y. Lu, and J. Y. Ooi, *A numerical study of wall pressure and granular flow in a flat-bottomed silo*, Powder Technology **282**, 43 (2015).
- [27] J. Carson and D. Craig, *Silo design codes : Their limits and inconsistencies*, Procedia Engineering **102**, 647 (2015).

- [28] M. Rhodes, *Introduction to particulate technology* (2008).
- [29] D. Schulze, *Powders and Bulk Solids* (2008).
- [30] A. Jenike, *Steady gravity flow of frictional-cohesive solids in converging channels*, (1964).
- [31] A. Jenike, *Storage and flow of solids. Bulletin No. 123; Vol. 53, No. 26, November 1964*, Bulletin of the University of Utah **53**, 209 (1976).
- [32] R. L. Michalowski, *Flow of granular media through a plane parallel/converging bunker*, Chemical Engineering Science **42**, 2587 (1987).
- [33] N. Wang, H. Lu, J. Xu, X. Guo, and H. Liu, *Velocity profiles of granular flows down an inclined channel*, International Journal of Multiphase Flow **110**, 96 (2019).
- [34] D. Höhner, S. Wirtz, and V. Scherer, *Experimental and numerical investigation on the influence of particle shape and shape approximation on hopper discharge using the discrete element method*, Powder technology **235**, 614 (2013).
- [35] D. Höhner, S. Wirtz, and V. Scherer, *A study on the influence of particle shape on the mechanical interactions of granular media in a hopper using the Discrete Element Method*, Powder Technology **278**, 286 (2015).
- [36] H. Tangri, Y. Guo, and J. S. Curtis, *Hopper discharge of elongated particles of varying aspect ratio: Experiments and DEM simulations*, Chemical Engineering Science: X **4**, 100040 (2019).
- [37] C. Slominski, M. Niedostatkiewicz, and J. Tejchman, *Application of particle image velocimetry (PIV) for deformation measurement during granular silo flow*, Powder Technology **173**, 1 (2007).
- [38] M. Mehdizad, L. Fullard, P. Galvosas, and D. Holland, *Quantitative measurements of flow dynamics in 3D hoppers using MRI*, Powder Technology **392**, 69 (2021).
- [39] R. J. Adrian and J. Westerweel, *Particle image velocimetry*, 30 (Cambridge university press, 2011).
- [40] N. Sanvitale and E. T. Bowman, *Using PIV to measure granular temperature in saturated unsteady polydisperse granular flows*, Granular Matter **18**, 1 (2016).
- [41] S. A. Stanier, J. Blaber, W. A. Take, and D. J. White, *Improved image-based deformation measurement for geotechnical applications*, Canadian Geotechnical Journal **53**, 727 (2016).
- [42] D. Fischer, B. Szabó, A. Ashour, R. Stannarius, Z. Kovács, T. Börzsönyi, and S. Wegner, *Flow of anisometric particles in a quasi-two-dimensional hopper*, Physical Review E **97** (2018), 10.1103/physreve.97.062904.
- [43] D. Gollin, W. Brevis, E. T. Bowman, and P. Shepley, *Performance of PIV and PTV for granular flow measurements*, Granular Matter **19**, 1 (2017).

- [44] P. A. Langston, U. Tüzün, and D. M. Heyes, *Discrete element simulation of internal stress and flow fields in funnel flow hoppers*, Powder Technology **85**, 153 (1995).
- [45] L. Sarno, A. Carravetta, Y. C. Tai, R. Martino, M. N. Papa, and C. Y. Kuo, *Measuring the velocity fields of granular flows – Employment of a multi-pass two-dimensional particle image velocimetry (2D-PIV) approach*, Advanced Powder Technology **29**, 3107 (2018).
- [46] L. Sarno, Y. C. Tai, A. Carravetta, R. Martino, M. Nicolina Papa, and C. Y. Kuo, *Challenges and improvements in applying a particle image velocimetry (PIV) approach to granular flows*, Journal of Physics: Conference Series **1249** (2019), 10.1088/1742-6596/1249/1/012011.
- [47] D. A. Steingart and J. W. Evans, *Measurements of granular flows in two-dimensional hoppers by particle image velocimetry . Part I : experimental method and results*, Chemical Engineering Science **60**, 1043 (2005).
- [48] A. M. Taylor-Noonan, D. Gollin, E. T. Bowman, and W. A. Take, *The influence of image analysis methodology on the calculation of granular temperature for granular flows*, Granular Matter **23**, 1 (2021).
- [49] C. González-Montellano, Á. Ramírez, E. Gallego, and F. Ayuga, *Validation and experimental calibration of 3D discrete element models for the simulation of the discharge flow in silos*, Chemical Engineering Science **66**, 5116 (2011).
- [50] R. O. Uñac, A. M. Vidales, O. A. Benegas, and I. Ippolito, *Experimental study of discharge rate fluctuations in a silo with different hopper geometries*, Powder Technology **225**, 214 (2012).
- [51] M. Fransen, M. Langelaar, and D. Schott, *Including stochastics in metamodel-based DEM model calibration*, Powder Technology **406**, 117400 (2022).
- [52] I. Cruz-Matías, D. Ayala, D. Hiller, S. Gutsch, M. Zacharias, S. Estradé, and F. Peiró, *Sphericity and roundness computation for particles using the extreme vertices model*, Journal of Computational Science **30**, 28 (2019).
- [53] G. Chen, *Surface wear reduction of bulk solids handling equipment using bionic design* (2017) p. 289.
- [54] E. Gallego, F. Ayuga, and C. Gonza, *Validation and experimental calibration of 3D discrete element models for the simulation of the discharge flow in silos*, Chemical Engineering Science **66**, 5116 (2011).
- [55] M. P. Fransen, M. Langelaar, and D. Schott, *Application of DEM-based metamodels in bulk handling equipment design : methodology and DEM case study*, Powder Technology **393**, 205 (2021).
- [56] J. Q. Gan, Z. Y. Zhou, and A. B. Yu, *A GPU-based DEM approach for modelling of particulate systems*, Powder Technology **301**, 1172 (2016).

- [57] G. Y. Liu, W. J. Xu, Q. C. Sun, and N. Govender, *Study on the particle breakage of ballast based on a GPU accelerated discrete element method*, Geoscience Frontiers **11**, 461 (2020).
- [58] G. Y. Liu, W. J. Xu, N. Govender, and D. N. Wilke, *A cohesive fracture model for discrete element method based on polyhedral blocks*, Powder Technology **359**, 190 (2020).
- [59] N. Guo and J. Zhao, *A coupled FEM / DEM approach for hierarchical multiscale modelling of granular media*, International Journal of Numerical Methods in Engineering **99**, 789 (2014).
- [60] N. Guo and J. Zhao, *Parallel hierarchical multiscale modelling of hydro-mechanical problems for saturated granular soils*, Computer Methods in Applied Mechanics and Engineering **305**, 37 (2016).
- [61] S. Lommen, D. Schott, and G. Lodewijks, *DEM speedup: Stiffness effects on behavior of bulk material*, Particuology **12**, 107 (2014).
- [62] S. Lommen, M. Mohajeri, G. Lodewijks, and D. Schott, *DEM particle upscaling for large-scale bulk handling equipment and material interaction*, Powder Technology **352**, 273 (2019).
- [63] D. S. Nasato, C. Goniva, S. Pirker, and C. Kloss, *Coarse graining for large-scale DEM simulations of particle flow - An investigation on contact and cohesion models*, Procedia Engineering **102**, 1484 (2015).
- [64] D. Forsström and P. Jonsén, *Calibration and validation of a large scale abrasive wear model by coupling DEM-FEM Local failure prediction from abrasive wear of tipper bodies during unloading of granular material*, Engineering Failure Analysis **66**, 274 (2016).
- [65] Q. J. Zheng, M. H. Xu, K. W. Chu, R. H. Pan, and A. B. Yu, *A coupled FEM / DEM model for pipe conveyor systems : Analysis of the contact forces on belt*, Powder Technology **314**, 480 (2017).
- [66] G. Barrios, R. de Carvalho, A. Kwade, and L. Tavares, *Contact parameter estimation for dem simulation of iron ore pellet handling*, Powder Technology **248**, 84 (2013).
- [67] G. Barrios and L. Tavares, *A preliminary model of high pressure roll grinding using the discrete element method and multi-body dynamics coupling*, International Journal of Mineral Processing, 32 (2016).
- [68] C. Coetzee, D. Els, and G. Dymond, *Discrete element parameter calibration and the modelling of dragline bucket filling*, Journal of Terramechanics **47**, 33 (2010).
- [69] G. Hess, C. Richter, and A. Katterfeld, *Simulation of the dynamic interaction between bulk material and heavy equipment*, The 12th International Conference on Bulk Materials Storage, Handling and Transportation (ICMBH) , pp. 427 436 (2016).

- [70] S. Lommen, D. Schott, and G. Lodewijks, *Multibody dynamics model of a scissors grab for co-simulation with discrete element method*, Conference proceedings CHOPS **40**, 177 (2012).
- [71] A. J. Morrison, I. Govender, A. N. Mainza, and D. J. Parker, *The shape and behaviour of a granular bed in a rotating drum using Eulerian flow fields obtained from PEPT*, Chemical Engineering Science **152**, 186 (2016).
- [72] J. Yoon, J. Park, C. Ahn, and J. Choi, *Co-simulation of mbd (multi body dynamics) and dem of many spheres using gpu technology*, In: Proceedings of Particle-Based Methods II - Fundamentals and Applications. International Center for Numerical Methods in Engineering, 778 (2011).
- [73] B. Besselink, U. Tabak, A. Lutowska, N. V. D. Wouw, and H. Nijmeijer, *A comparison of model reduction techniques from structural dynamics, numerical mathematics and systems and control*, Journal of Sound and Vibration **332**, 4403 (2013).
- [74] D. Barrasso, A. Tamrakar, and R. Ramachandran, *A reduced order pbm-ann model of a multi-scale pbm-dem description of a wet granulation process*, Chemical Engineering Science, 319 (2014).
- [75] F. Boukouvala, Y. Gao, F. Muzzio, and M. Ierapetritou, *Reduced-order discrete element method modelling*, Chemical Engineering Science **95**, 12 (2013).
- [76] Y.-d. Lang, A. Malacina, L. T. Biegler, S. Munteanu, J. I. Madsen, S. E. Zitney, and W. Virginia, *Reduced order model based on principal component analysis for process simulation and optimization*, Energy and Fuels **23**, 1695 (2009).
- [77] K. McBride and K. Sundmacher, *Overview of Surrogate Modeling in Chemical Process Engineering*, Chemie-Ingenieur-Technik **91**, 228 (2019).
- [78] A. Rogers and M. Ierapetritou, *Challenges and opportunities in modeling pharmaceutical manufacturing processes*, Computers and Chemical Engineering **81**, 32 (2015).
- [79] R. Furukawa, Y. Shiosaka, K. Kadota, K. Takagaki, T. Noguchi, A. Shimosaka, and Y. Shirakawa, *Size-induced segregation during pharmaceutical particle die filling assessed by response surface methodology using discrete element method*, Journal of Drug Delivery Science and Technology **35**, 284 (2016).
- [80] P. M. Pardalos, A. Zhigljavsky, and J. Žilinskas, *Springer Optimization and Its Applications 107 Advances in Stochastic and Deterministic Global Optimization* (2016).
- [81] J. Martin and T. Simpson, *Use of Adaptive Metamodeling for Design Optimization*, 9th AIAA/ISSMO Symposium on Multidisciplinary Analysis and Optimization, 1 (2012).
- [82] D. Gorissen and T. Dhaene, *A Surrogate Modeling and Adaptive Sampling Toolbox for Computer Based Design*, Journal of Machine Learning Research **11**, 2051 (2010).

- [83] H. Cheng, T. Shuku, K. Thoeni, and H. Yamamoto, *Probabilistic calibration of discrete element simulations using the sequential quasi-Monte Carlo filter*, Granular Matter **20**, 1 (2018).
- [84] J. P. C. Kleijnen, *Kriging metamodeling in simulation : A review*, European Journal of Operational Research **192**, 707 (2009).
- [85] T. W. Simpson, J. D. Peplinski, P. N. Koch, and J. K. Allen, *Metamodels for Computer-based Engineering Design : Survey and recommendations*, Engineering with Computers , 129 (2001).
- [86] C. E. Rasmussen and C. K. I. Williams, *Gaussian Processes for Machine Learning* (2006).
- [87] J. D. Gergonne, *The application of the method of least squares to the interpolation of sequences*, Historia Mathematica **1**, 439 (1974).
- [88] R. L. Hardy, *Multiquadric Equations of Topography and Other Irregular Surfaces*, Journal of Geophysical Research **76**, 1905 (1971).
- [89] N. Cressie, *The Origins of Kriging I*, Mathematical Geology **22**, 239 (1990).
- [90] D. G. Krige, *Journal of the Chemical Metallurgical & Mining Society of South Africa*, Journal of the Chemical Metallurgical & Society of South Mining Africa **52**, 119 (1951).
- [91] S. Lophaven, H. Nielsen, and J. Søndergaard, *DACE - A Matlab Kriging Toolbox, Version 2.0* (2002).
- [92] M. Urquhart, E. Ljungskog, and S. Sebben, *Surrogate-based optimisation using adaptively scaled radial basis functions*, Applied Soft Computing Journal **88**, 1 (2020).
- [93] M. Meckesheimer, A. J. Booker, T. B. Company, R. R. Barton, and T. W. Simpson, *Computationally inexpensive metamodel assessment strategies*, AIAA **40**, 2053 (2002).
- [94] T. Weinhart, L. Orefice, M. Post, M. P. van Schrojenstein Lantman, I. F. Denissen, D. R. Tunuguntla, J. M. Tsang, H. Cheng, M. Y. Shaheen, H. Shi, P. Rapino, E. Grannonio, N. Losacco, J. Barbosa, L. Jing, J. E. Alvarez Naranjo, S. Roy, W. K. den Otter, and A. R. Thornton, *Fast, flexible particle simulations — An introduction to MercuryDPM*, Computer Physics Communications **249**, 107129 (2020).
- [95] J. Brown, R.L., Richards, *Profile of flow of granules through apertures*, Transactions of the Institution of Chemical Engineers **38**, 243 (1960).
- [96] S. Luding, *Cohesive , frictional powders : contact models for tension*, Granular Matter **10**, 235 (2008).
- [97] F. Zamponi, *Mathematical physics: Packings close and loose*, Nature **453**, 606 (2008).

- [98] S. Luding, *About contact force-laws for cohesive frictional materials in 2D and 3D*, Proceedings issue: Behavior of Granular Media (2006).
- [99] M. Marigo and E. H. Stitt, *Discrete element method (DEM) for industrial applications: Comments on calibration and validation for the modelling of cylindrical pellets*, KONA Powder and Particle Journal **32**, 236 (2015).
- [100] M. J. Mohajeri, H. Q. Do, and D. L. Schott, *DEM calibration of cohesive material in the ring shear test by applying a genetic algorithm framework*, Advanced Powder Technology **31**, 1838 (2020).
- [101] M. Rackl and K. J. Hanley, *A methodical calibration procedure for discrete element models*, Powder Technology **307**, 73 (2017).
- [102] T. Roessler, C. Richter, A. Katterfeld, and F. Will, *Development of a standard calibration procedure for the DEM parameters of cohesionless bulk materials – part I: Solving the problem of ambiguous parameter combinations*, Powder Technology **343**, 803 (2019).
- [103] S. M. Derakhshani, D. L. Schott, and G. Lodewijks, *Micro – macro properties of quartz sand : Experimental investigation and DEM simulation*, Powder Technology **269**, 127 (2015).
- [104] M. Rackl and W. A. Günthner, *Biomass and Bioenergy Experimental investigation on the influence of different grades of wood chips on screw feeding performance*, Biomass and Bioenergy **88**, 106 (2016).
- [105] M. J. Mohajeri, W. de Kluijver, R. L. Helmons, C. van Rhee, and D. L. Schott, *A validated co-simulation of grab and moist iron ore cargo: Replicating the cohesive and stress-history dependent behaviour of bulk solids*, Advanced Powder Technology **32**, 1157 (2021).
- [106] C. Richter, T. Rößler, G. Kunze, A. Katterfeld, and F. Will, *Development of a standard calibration procedure for the DEM parameters of cohesionless bulk materials – Part II: Efficient optimization-based calibration*, Powder Technology **360**, 967 (2020).
- [107] C. M. Wensrich and A. Katterfeld, *Rolling friction as a technique for modelling particle shape in DEM*, Powder Technology **217**, 409 (2012).
- [108] S. Luding, *Anisotropy in cohesive, frictional granular media*, Journal of Physics Condensed Matter **17** (2005), 10.1088/0953-8984/17/24/017.
- [109] Y. C. Zhou, B. H. Xu, A. B. Yu, and P. Zulli, *Numerical investigation of the angle of repose of monosized spheres*, Physical Review E - Statistical Physics, Plasmas, Fluids, and Related Interdisciplinary Topics **64**, 8 (2001).
- [110] Y. Yan, R. Helmons, C. Wheeler, and D. Schott, *Optimization of a convex pattern surface for sliding wear reduction based on a definitive screening design and discrete element method*, Powder Technology **394**, 1094 (2021).

- [111] R. H. Byrd, J. C. Gilbert, and J. Nocedal, *A trust region method based on interior point techniques for nonlinear programming*, Mathematical Programming, Series B **89**, 149 (2000).
- [112] M. P. Fransen, M. Langelaar, and D. L. Schott, *Deterministic vs. robust design optimization using DEM-based metamodels*, Powder Technology **425**, 118526 (2023).
- [113] P. W. Cleary, *DEM simulation of industrial particle flows: Case studies of dragline excavators, mixing in tumblers and centrifugal mills*, Powder Technology **109**, 83 (2000).
- [114] P. Cleary, *Dem prediction of industrial and geophysical flows*, Particuology **8**, 106 (2010).
- [115] H. Q. Do, A. M. Aragón, and D. L. Schott, *A calibration framework for discrete element model parameters using genetic algorithms*, Advanced Powder Technology **29**, 1393 (2018).
- [116] C. Richter and F. Will, *Introducing Metamodel-Based Global Calibration of Material-Specific Simulation Parameters for Discrete Element Method*, Minerals **11** (2021).
- [117] R. T. Marler and J. S. Arora, *Survey of multi-objective optimization methods for engineering*, Structural and Multidisciplinary Optimization **395**, 369 (2004).
- [118] G. J. Park, T. H. Lee, K. H. Lee, and K. H. Hwang, *Robust design: An overview*, AIAA Journal **44**, 181 (2006).
- [119] E. J. Rykiel, *Testing ecological models: the meaning of validation*, Ecological Modelling **90**, 229 (1996).

NOMENCLATURE

Acronyms

AoM	Angle of Movement
AoR	Angle of Repose
BCA	Bulk Calibration Approach
BHE	Bulk Handling Equipment
CI	Confidence Interval
CoV	Coefficient of Variation
DEM	Discrete Element Method
GP	Gaussian Process
GPR	Gaussian Process Regression
IBM	Interpolation Based Metamodel
KPI	Key Performance Indicator
M	Mean
MBDO	Metamodel Based Design Optimization
MF	Model Fitting
ML	Machine Learning
MSE	Mean Squared Error
MV	Mean Variance
NRMSE	Normalized Root Mean Squared Error
P-P	Particle-particle
P-W1	Particle-Wall 1
P-W2	Particle-Wall 2
PR	Polynomial Regression
PSD	Particle Size Distribution

RBM	Regression Based Metamodel
VSA	Validation Set Approach

Greek Symbols

α	Hopper angle [°]
β	Angle of Repose [°]
ϵ_ϕ	Error between experimental and simulation results
η	Sampling density [–]
γ	Overall damping coefficient[–]
γ_r	Rotational damping coefficient[–]
γ_s	Sliding damping coefficient[–]
μ_r	Coefficient of rolling friction [–]
μ_s	Coefficient of sliding friction [–]
ν	Poisson ratio [–]
ϕ	Discharge rate[kg/s]
ϕ_e	Experimental discharge rate [kg/s]
ϕ_s	Simulated discharge rate [kg/s]
ϕ_{norm}	Normalized discharge rate[–]
ψ	Coefficient of variation (Chapter 3)[–]
ψ	Sphericity (Chapter 2)[–]
ψ	Squared exponential Gaussian (Chapter 5)[–]
ρ_b	Bulk density [kg/m ³]
ρ_{pe}	Experimental particle density [kg/m ³]
ρ_{ps}	Simulation particle density [kg/m ³]
ρ_p	Particle density [kg/m ³]
$\sigma_{\mu-s}$	Standard deviation of sliding friction coefficient [–]
σ_f	Metamodel hyper parameter [–]

Roman Symbols

a_i	Acceleration [m/s^2]
c_1	Metamodel hyper parameter [–]
c_2	Metamodel hyper parameter [–]
$c_i(x)$	Objective function
C_n	Coordination number [–]
C_u	Uniformity coefficient [–]
d	Hopper depth [mm]
d_{10}	10% particle size [mm]
d_{50}	Average particle size [mm]
d_{60}	60% particle size [mm]
d_{ei}	End point angle of repose calculation [m]
d_e	End point angle of movement calculation [m]
d_{si}	Start point angle of repose calculation [m]
d_s	Start point angle of movement calculation [m]
e	Void ratio [–]
E_b	Bulk modulus [MPa]
F	Force [N]
F_{imp}	Impact force [N]
$F_{imp} - norm$	Normalized impact force [–]
$f_i(x)$	Gaussian Process Regression metamodel [–]
$F_{loadcell}$	Loadcell force [N]
f_{rec}	Recording frequency [Hz]
g	Gravitational acceleration [m/s^2]
G_{DR}	GPR metamodel for discharge rate
H_f	Hopper fill height [m]
I	Identity matrix
K	Gramm matrix

$k(a, b)$	Correlation function
K_{i-e}	Experimental KPI value
K_{i-s}	Simulation KPI value
k_p	Particle contact stiffness [N/m]
k_r	Rotational contact stiffness [N/m]
k_t	Torsional contact stiffness [N/m]
k_w	Wall contact stiffness [N/m]
l	Metamodel hyper parameter [–]
m	mass [kg]
m_{eff}	Effective particle mass [kg]
r_{avg}	Average particle radius [m]
R_n	Roundness number [–]
t	Time [s]
t_c	Contact time [s]
$V(f^*)$	Variance function
v_i	Velocity [m/s]
v_y	Velocity in y-direction [m/s]
W_h	Hopper width [m]
W_o	Size of discharge opening [mm]
w_i	Objective weight
x	x-coordinate
y	y-coordinate
z	z-coordinate

Superscripts

◦	Degrees
---	---------

Subscripts

lb	lower bound
ub	upper bound

ACKNOWLEDGEMENTS

After a journey that started almost eight years ago, I am glad and proud to present this dissertation. Of course bringing this research to an end would not have been possible without the help and guidance of several individuals.

First of all, I would like to thank Prof. dr. ir. Dingena Schott and Prof. dr. ir. Matthijs Langelaar for their supervision and moral support during this project. They gave me the confidence to really shape this project and pursue the research gaps that presented themselves along the way. The expertise they both have in their respective fields resulted in interesting and fruitful discussions and new insights.

Next to my supervisors I would like to thank the members of the research group: Javad, Hamid, Raisa, Aaron, Ahmed, Ana, Jovana, and Zhaorui. During the PhD we have had regular group meetings where we discussed our scientific problems and helped each other where we could. I would also like to express my gratitude to the MTT department which funded this PhD project and the support staff that were always there to lend a helping hand. A special note is addressed to the multiscale modelling research group at Twente which supported me during the use of the Mercury DPM code. Individuals that deserve a special mention are Hongyang Cheng, Hao Shi, Anthony Thornton, and Thomas Weinhart whom I would like to thank for their support. In the future, I hope to collaborate on exciting scientific challenges with you all. Next to the direct colleagues in our research group there are a couple of people that I would like to thank for the essential coffee breaks and fun activities that kept moral high. Thank you, Lindert, Mike, Arnoud, Harsh, Johan, and Breno for these moments.

Of course the most important thing is support from your family and friends during such a process. I would like to thank you all for the moments where we talked about the other important things in life. However, there are a couple of people that deserve a special mention. Firstly, I would like to thank my parents Willem en Jacqueline for their support and for giving me the tools to cope with whatever comes my way. My sister Lisa and her husband Stijn for their moral support. I would also like to thank Brigitte for taking the time to have a look at some of my writing. Next, I would like to thank Guus and Marlies for giving me a place to take my mind of things when things seemed to go nowhere but also and eventually finish the last stretches of this project.

Last but not least, my wife Eline, thank you for your unconditional love and support. It was not always easy during this process but I am very grateful that you were there to support me along the way. I could not have done this without you by my side. When one journey ends there is always another one that begins and last June the most fantastic journey we could think of has started with the birth of our little Hanne. I cannot wait to see what the future has in store for us.

*Marc Fransen
Rotterdam, November 2024*

CURRICULUM VITÆ

Marc Patrick FRANSEN

28-02-1991 Born in Amstelveen, The Netherlands

EDUCATION

2003-2009 VWO, Alkwin Kollege, Uithoorn

2009-2013 Bachelor Mechanical Engineering
Delft University of Technology, the Netherlands

2013-2016 Master Mechanical Engineering
Delft University of Technology, the Netherlands
Track: Solid and Fluid Mechanics
Thesis: Eigenstrain reconstruction of residual stresses induced by selective laser melting

2017-2023 Doctor of Philosophy
Delft University of Technology
Thesis: Unravelling gravel: Including stochastic behaviour of granular materials in design of bulk handling equipment
Promotor: Prof. dr. ir. D.L. Schott
Promotor: Prof. dr. ir. M. Langelaar

EXPERIENCE

2022–present Researcher & Advisor, *Flood Defence Technologies*
Deltares, Delft, the Netherlands

2013–2014 Intern
Nationaal Lucht en Ruimtevaart laboratorium, Marknesse, the Netherlands

LIST OF PUBLICATIONS

JOURNAL PUBLICATIONS

4. **M.P. Fransen**, M. Langelaar, D.L. Schott, *Application of DEM-based metamodels in bulk handling equipment design: Methodology and DEM case study*, Journal of Powder Technology (2021).
3. **M.P. Fransen**, M. Langelaar, D.L. Schott, *Including stochastics in metamodel-based DEM model calibration*, Journal of Powder Technology (2022).
2. **M.P. Fransen**, M. Langelaar, D.L. Schott, *Deterministic vs. robust design optimization using DEM-based metamodels*, Journal of Powder Technology (2023).
1. **M.P. Fransen**, M. Langelaar, D.L. Schott, *Experimental study on flow induced hopper vibrations and the relation to geometry*, [Under review Granular Matter \(2024\)](#).

CONFERENCE PROCEEDINGS

1. M.P. Fransen, D.L. Schott *Metamodelling of structural design parameters affecting silo discharge performance*, [CHoPS 2018: 9th International Conference on Conveying and Handling of Particulate Solids - London, United Kingdom \(2018\)](#).

DATASETS

1. Hopper discharge experiments, (10.4121/fa7544d6-14fd-4372-a81f-e2e1b4a44832)

Propositions

accompanying the dissertation

UNRAVELLING GRAVEL

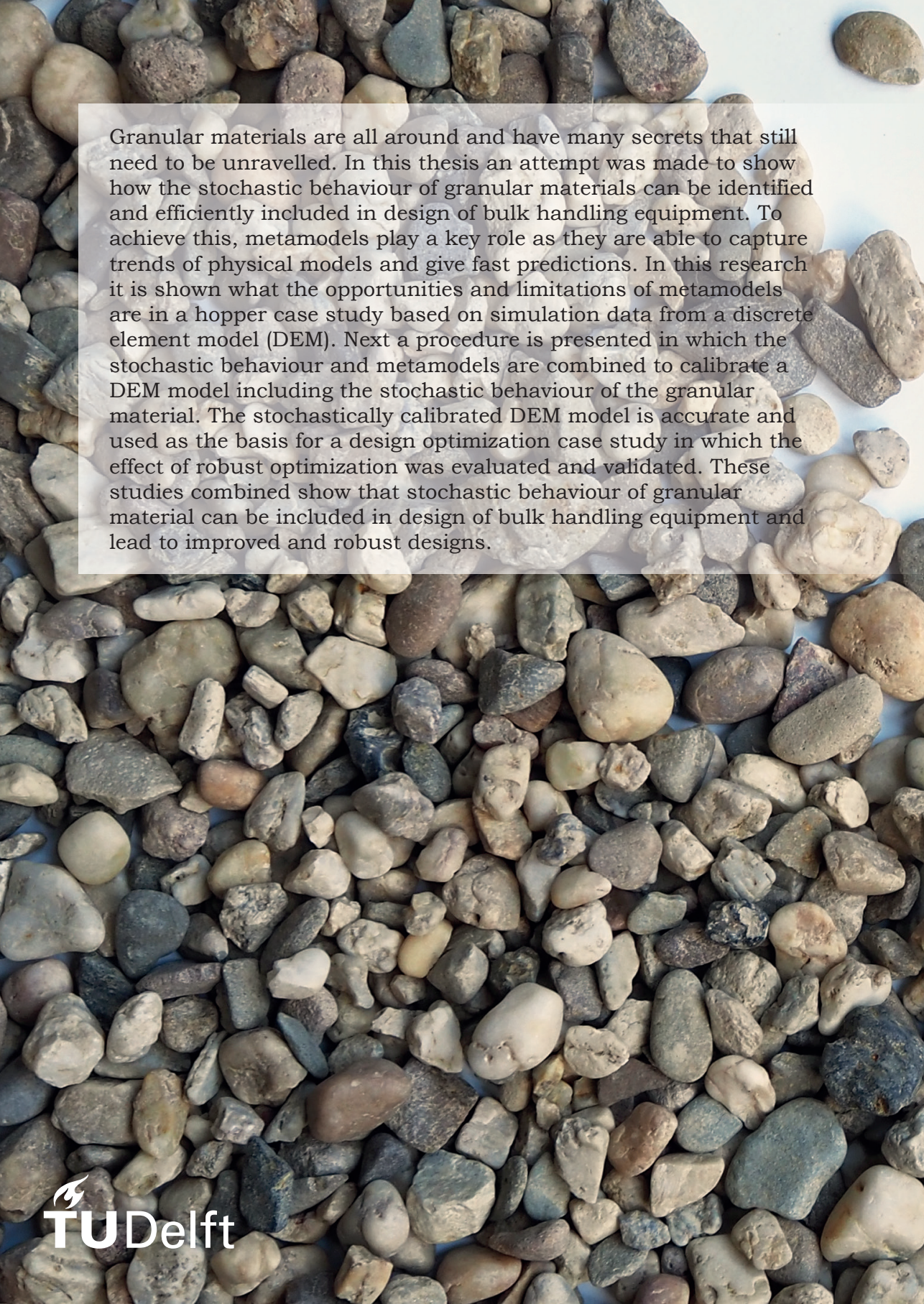
INCLUDING STOCHASTIC BEHAVIOUR OF GRANULAR MATERIALS IN DESIGN OF BULK
HANDLING EQUIPMENT

by

Marc Patrick FRANSEN

1. Stochastics of granular processes must always be included in the calibration of bulk materials and the design of bulk handling equipment to obtain reliable DEM models and equipment designs. (this proposition pertains to this dissertation)
2. Surrogate and metamodeling techniques in calibration of DEM models without hyperparameter optimization lead to incorrect predictions of calibration parameters. (this proposition pertains to this dissertation)
3. A DEM model calibrated using mean values gives accurate predictions for the mean behaviour of granular material but does not automatically predict the stochastic behaviour accurately. (this proposition pertains to this dissertation)
4. Machine learning and AI can only be used to their full potential if combined with human intelligence.
5. The interaction between equipment and granular materials is too often neglected in fundamental studies on particle behaviour even though it plays an important role.
6. Of all skills acquired during a PhD, the ability to transfer skills and knowledge to others is the most important one.
7. Society is like an avalanche of particles that interact, steering it in the right direction is difficult because of the uncertainties in all interaction properties.
8. More computing power leads to larger computations because we tend to increase the complexity of our simulations accordingly.
9. Funnelling your PhD topic down to its essentials is equally as important as bringing the results back to the surface.
10. Obtaining your doctorate is like walking through a forest and climbing a few challenging trees: reaching the tree tops makes you realize that the forest is even bigger than you thought.

These propositions are regarded as opposable and defensible, and have been approved as such by the promotors prof. dr. ir. D.L. Schott and prof. dr. ir. M. Langelaar.



Granular materials are all around and have many secrets that still need to be unravelled. In this thesis an attempt was made to show how the stochastic behaviour of granular materials can be identified and efficiently included in design of bulk handling equipment. To achieve this, metamodels play a key role as they are able to capture trends of physical models and give fast predictions. In this research it is shown what the opportunities and limitations of metamodels are in a hopper case study based on simulation data from a discrete element model (DEM). Next a procedure is presented in which the stochastic behaviour and metamodels are combined to calibrate a DEM model including the stochastic behaviour of the granular material. The stochastically calibrated DEM model is accurate and used as the basis for a design optimization case study in which the effect of robust optimization was evaluated and validated. These studies combined show that stochastic behaviour of granular material can be included in design of bulk handling equipment and lead to improved and robust designs.